Methods and challenges in STEM composition determination of III/V semiconductors via complementary multislice simulations

Dissertation

zur
Erlangung des Doktorgrades
der Naturwissenschaften
(Dr. rer. nat.)

dem
Fachbereich Physik
der Philipps-Universität Marburg

vorgelegt von

Lennart Josef Duschek, M.Sc.

aus

Fulda

Marburg/Lahn 2019

Table of Contents

1. Introduction

Semiconductor materials have had an enormous influence on our everyday lives since their appearance in industry in the middle of the twentieth century. Advances in science and technology play increasingly crucial roles in modern human society, with one factor being the rise of global connectivity through the internet and increasing use of mobile technology. The key words "Internet of Things" and "Industry 4.0" describe a trend that every modern piece of technology is connected to the internet and a wide range of data is collected through them. This development forecasts consequences, namely that the process of transmitting data via the internet is increasing in speed. Furthermore, every modern device includes a small, fast and efficient chipset that is based on semiconductors. The data collected from the devices is analyzed in large computing centers on a previously unseen scale. Machine learning companies attempt to identify unexplored patterns that can be used to increase their value on the market. In order for this progress to occur, the chipsets included in the devices must become smaller, faster and more efficient, and the speed of internet transmission must also be improved. The main components of these architectures are the countless servers that are currently located in all regions of the world, networked together via fiber optic cables that allow ever-increasing amounts of data to be transmitted, utilizing semiconductor lasers as a light source [1]. In addition, this development has led to a significant increase in electricity demand. Although the power consumption of devices can be reduced, power generation through renewable energies can also be enhanced. One example of a renewable energy source is solar cells with high conversion efficiencies. The successful and continuous improvement of devices such as solar cells [2] and laser devices [3, 4] depends on the ability to observe and describe the material properties as precisely as possible, in order for that understanding to serve as a basis for new developments. To understand how the optoelectronic properties of a semiconductor device are connected to the composition of a material, it is important to determine the material's composition as accurately as possible. It has been demonstrated that the composition distribution, even on an atomic level, has a significant influence on the optoelectronic properties of a device [5-7], and thus the need for a very precise technique to determine the composition is obvious. One widely-used method is high-resolution x-ray diffraction (HRXRD) in combination with the strain sensitive 004 reflex [3]. This technique determines the lattice constant of the material and uses this to calculate the composition of the material. Besides the high accuracy in the determination of the lattice constant and thus the composition, a 2D lateral resolution of the material is not provided. The reflexes are generated from a relatively large area of the material and thus represents the average composition of an area of around mm^2. Moreover, HRXRD is no longer applicable to semiconductor compounds that consist of more than three constituents. Tilli et al. developed a method that uses the quasi forbidden (002) reflex in

combination with the (004) reflex to determine the composition of a *Ga(N,As,P)* sample [8], but they found that this only works for very thin quantum well (QW) films.

In this task, the scanning transmission electron microscopy (STEM) has proven to be a powerful tool for the atomic scale analysis and characterization of crystalline specimens [9]. When combined with spherical aberration correctors, which were developed in the last two decades [10, 11], the resolution of STEM imaging can reach the sub-angstrom range [12, 13]. The high lateral resolution combined with intuitive interpretation in terms of Z-contrast has meant that STEM combined with a high angle annular dark field detector (HAADF) is a commonly applied tool in semiconductor analysis. The so-called Z-contrast of HAADF STEM images is very sensitive to the number and types of atoms present [14-16]. Nonetheless, to satisfy the increasing need for the local arrangements of atoms on an atomic scale, several factors must be considered to make electron microscopy a quantitative method [17-19]. The basis of accurate simulations is the multislice algorithm combined with the frozen phonon approach, which has been proven to reproduce experimental data accurately [20]. To bring simulated and experimental data on the same intensity scale, it is necessary to normalize the experimental data to the intensity of the impinging beam, e.g., via a detector scan [21]. Furthermore, it has been demonstrated that the sensitivity of the used detectors is not homogenous and must be applied to the simulated data [22, 23]. It could be proven that properties of the electron beam can also have a significant influence on the resulting image. The finite distribution of the electron beam can be included by a convolution of the results with an effective source size [24, 25]. Moreover, the energy spread of the accelerated electrons [26] determines the magnitude of chromatic aberration, which is introduced in section 2.5, and can be taken into account by summing over a weighted defocus series of the simulation [27, 28]. The topics of the effective source size and the chromatic aberration are covered in more detail in section 3.2. Amorphous layers on the sample surface, caused by the preparation, can have a severe influence on the resulting image intensity [29, 30]. The magnitude of this effect depends on the thickness of the sample. In addition, the effect of cross-scattering from neighboring atomic columns [31] depends on the sample thickness and the material itself, and can influence the HAADF intensity [32, 33].

This is only a brief overview of the factors that must be considered to achieve an agreement between experimental and simulated HAADF images. When all of the aforementioned influences are considered carefully, the comparison of experimental HAADF images and complementary multislice simulations can reveal quantitative information about the sample, such as thickness or elemental composition. It has been demonstrated that the composition distribution, even on an atomic level, has a significant influence on the optoelectronic properties of a device [5-7], and thus the need for a very precise technique to determine the composition is apparent. Composition inhomogeneity in QW layers at interfaces is especially interesting, and STEM is a highly effective tool to combine high lateral resolution

with quantitative information about the sample. An overview of existing techniques to determine sample composition by using simulated results is provided in section 3.3.

In the present work, different methods are explained that incorporate experimental effects into multislice simulations, e.g., elastic surface relaxation. This allows very precise multislice simulations to be conducted, which are the basis from which to determine atomically resolved composition distribution from STEM HAADF images. The technique to compare simulated intensities with experimental ones is examined in the course of this work, and precision – with a focus on single-atom accuracy – is analyzed in a simulation study. The proposed composition determination method is applied to experimental STEM images and the results are compared with commonly-used techniques, such as HRXRD. Furthermore, the usage of this method with regard to quaternary compounds is discussed and introduced with the example of *Ga(N,As,P)*.

This thesis is written in cumulative form and is structured as follows: chapter 2 introduces the most important concepts of STEM, which includes the electron-matter interaction and an explanation of the formation of a HAADF image. Chapter 3 covers the background of the applied methods in this thesis, namely the multislice formula and how to take the influence of temporal and spatial coherence into account. The research results are discussed and summarized in chapter 4. The chapter is subdivided into the implementation of the multislice algorithm, the influence of elastic surface relaxation on the STEM intensity, and finally the topic of composition determination. Chapter 5 summarizes the research results and provides an outlook on how to adapt the extended composition intensity method to multinary semiconductor systems by combining angle-resolved STEM [34] from dedicated angular regimes with dedicated multislice simulations. The publications that were created during the course of this work are reprinted in full in chapter 6.

2. Scanning Transmission Electron Microscopy

This chapter covers the basic principles of STEM, namely the key physical background and the general concepts that are used throughout this work.

Firstly, to provide a fundamental understanding, section 2.1 introduces the basic concepts of microscopy, followed by the electron-specimen-interaction that is important in the following chapter of this work. The method of HAADF is introduced in section 2.2, as this technique is of high importance for this thesis. Section 2.3 deals with the concept of electron channeling, which is also important to understand, since static atomic displacements – covered in section 2.4 – can cause de-channeling of the electrons. The chapter ends with a brief introduction of the most important lens aberrations, in section 2.5.

2.1. Physical Background

The idea to use electrons instead of conventional light as an illumination source is a result of the limited image resolution of light microscopes and humanity's desire to explore smaller and smaller objects. The resolution of a conventional light microscope is limited by the wavelength of visible light. Louis de Broglie first theorized that the electron had a wave-like characteristic in 1925 [35]. The wavelength of an electron is determined by the de Broglie wavelength, and is linked to the accelerating voltage (U) used to create the electron beam. Two research groups demonstrated the wave nature of electrons, independently from each other, by electron diffraction experiments in 1927 [36, 37]. The formula of Abbe [38] describes the resolution in a classical light microscope with $d = 0.61 \frac{\lambda}{n \sin \alpha}$, λ being the wavelength of the used radiation, n the refractive index of the viewing medium and α the semi-angle of collection of the magnifying lens. The wavelength of an accelerated electron can be calculated by

$$\lambda_R = \frac{h}{\sqrt{2m_0 eU(1 + \frac{eU}{2m_0 c^2})}},$$

(2.1)

with m_0 being the electron's rest mass, e the elementary charge, U the accelerating voltage, c the speed of light and h the Planck constant. The wavelength of an electron used in a microscope with an accelerating voltage of 200 kV can be calculated to 2.5 pm, whereas the wavelength of visible light is between 400 and 800 nm. It should be noted that equation (2.1) accounts for relativistic effects, since acceleration voltages above 100 kV are used. With such a small wavelength, the idea to use accelerated electrons as an illumination source became apparent, and was first proposed by Knoll and Ruska in 1932 [39]. For modern scientists, the STEM developed as an indispensable and versatile tool for the analysis of organic or inorganic samples. In this work, the focus is on semiconductor samples. With the

development of magnetic lens correctors [10, 11], the resolution of a modern STEM can reach a sub-angstrom range [12, 13, 32].

The following section summarizes the process of the electron-specimen interaction that is fundamental for STEM. The interaction of highly accelerated electrons with a specimen produces a wide variety of signals that can be used in analytical electron microscopy. A visual representation of the processes can be found in *Figure 2.1* a and can be categorized into two areas.

If the incident electron loses energy during the interaction process with the specimen, this is generally referred to as an inelastic process. This process can result in the emittance of x-rays or Auger electrons, which can be used to analytically characterize the specimen [40, 41]. Additionally, the energy loss can be analyzed to gain precise sample information, referred to as electron energy loss spectroscopy (EELS) [42]. Since mainly quasielastic processes contribute to STEM annular dark field (ADF) images, only this process is covered in more detail in the following chapter.
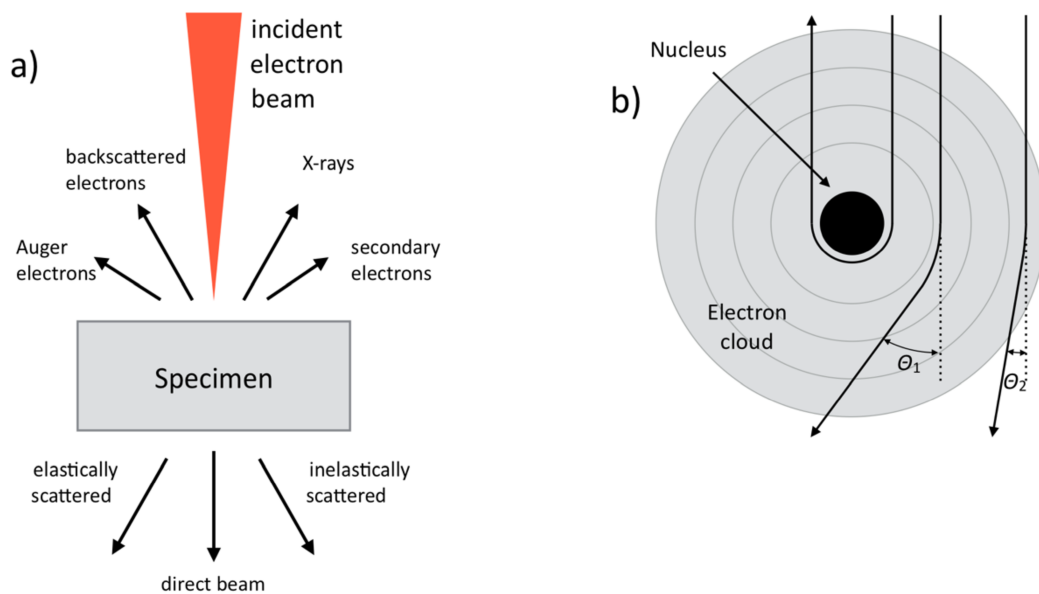

Figure 2.1: Figure a) illustrates the various signals that can occur during the electron-specimen interaction and can be used to characterize the investigated sample. Figure b) illustrates the two mechanisms by which an isolated atom can scatter a high-energy electron. The strong coulombic force between the positive atom nucleus and the incident electron results in high angle scattering θ_1 and may even evoke back scattering in rare cases ($\theta_1 > 180°$). The coulombic interaction between the electron cloud and the incident electron results in low angle scattering θ_2. These figures are adapted from [43].

In the case of elastic scattering, the total energy and the momentum of the incident electron are conserved after the scattering process. Since the electron is a low-mass and negatively charged particle, it can easily be deflected by other electrons from the atom cloud or the positive nucleus itself. The interaction of the electron with either the electron cloud or the nucleus is coulomb interaction. The main and most probable interaction is the repulsive force between the electron cloud and the incident electron, and results in low scattering angles. The coulomb attraction force between the nucleus and

the incident electron is large compared to electron-electron interaction, which occurs in the cloud. This results in high scattering angles and may even cause back scattering in rare cases (scattering angles of 180 °). It should be noted that both processes mentioned are not fully elastic, but the minimal energy loss can be neglected. The elastic interaction between the incident electron and the electrical field of the nucleus can be best described by Rutherford scattering [44]. Rutherford describes the differential cross section as follows:

$$d\sigma_R = \frac{e^4 Z^2}{16(4\pi\epsilon_0 E_0)^2} \frac{d\Omega}{\sin^4 \frac{\theta}{2}},$$ (2.2)

where Z is the atomic number, e is the elementary charge, E_0 is the kinetic energy of the particle, ϵ_0 is the dielectric constant and θ is the scattering angle. Since the scattering process occurs with electrons with a high kinetic energy, the relativistic wavelength of the electrons λ_R has to be taken into account and equation (2.2) must be adapted accordingly. Furthermore, the electrical field of the nucleus cannot be considered in isolation, but the electron cloud must also be considered. This is called the screening effect, and reduces the differential cross section and therefore the amount of scattering. A corrected screening parameter θ_0 is introduced and is given by

$$\theta_0 = \frac{0.117\, Z^{\frac{1}{3}}}{E_0^{\frac{1}{2}}}.$$

This modifies the Rutherford expression from (2.2) to

$$d\sigma_R = \frac{\lambda_R^4 Z^2}{64\, \pi^4\, a_0^2} \frac{d\Omega}{[\sin^2(\frac{\theta}{2}) + \frac{\theta_0^2}{4}]^2},$$

where a_0 is the Bohr radius. This expression describes the screened, relativistic, differential Rutherford cross section and gives the probability of the occurrence of a scattering event. The correct calculation of the differential cross section of an isolated atom is of importance when performing numerical simulations, which are addressed in chapter 3.1, and in which the atomic scattering factor $f(\theta)$ plays a significant role. The atomic scattering factor connects the wave nature of the electron beam to the differential elastic cross section by

$$|f(\theta)|^2 = \frac{d\sigma(\theta)}{d\Omega}.$$

This means that $f(\theta)$ is a measure of the amplitude of an electron wave that is scattered from an isolated atom. Moreover, $|f(\theta)|^2$ is proportional to the scattered intensity.

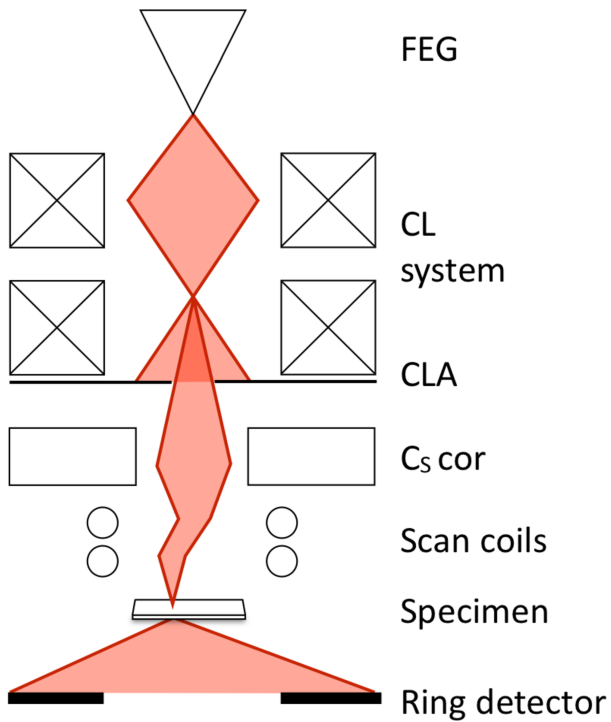## 2.2. High Angle Annular Dark Field Image Formation

Figure 2.2: The figure represents a schematic beam path in a STEM, equipped with a C_s-corrector. Only the fundamental components that are responsible for the image formation are depicted here. The figure is adapted from [43].

In a STEM, a focused electron probe is scanned over a specimen. The accelerated electrons interact with the specimen, as outlined in section 2.1. By analyzing the transmitted electrons, one can gather information about the specimen. This section outlines the operational mode of the ADF in a STEM, which only uses the elastically scattered electrons as input for the resulting specimen image. *Figure 2.2* depicts a schematic of the beam path when using a STEM in ADF mode, while only illustrating the main components for the image formation. All ADF images used in the scope of this work were acquired with a JEOL JEM 2200 FS, with two C_s correctors. The image process is described from the top to the bottom, starting with the Schottky field emission gun (FEG) as the source of electrons. Electrons are extracted by applying a high electric field to a heated tungsten wire (1700 K). With this, an electron beam with a high emission current can be formed. The upcoming lens system focuses the beam and may be used to change its intensity when combined with an aperture, and is referred to as a condenser lens (CL) system. The condenser lens aperture (CLA) blocks the outermost electrons, because electrons far away from the optical axis increase the lens aberrations. The aperture is adjustable and determines the convergence angle of the beam. Thereafter, the beam is transferred into the C_s-corrector of the microscope, which corrects the spherical aberrations of the beam. The most important lens aberrations are described in more detail in section 2.5. The C_s-corrector helps to form a very narrow electron probe, which significantly improves the resolution of the microscope. The C_s-corrector is a highly complex technical tool that increased the resolution of modern microscopes significantly [12, 13, 32]. The scan coils, depicted in *Figure 2.2*, are used to deflect the electron beam in a way that it can probe the specimen at distinct points. At every scan point, the beam rests for several microseconds (dwell-time) and a ring detector, located below the specimen, collects the transmitted electrons. The detector consists of an yttrium aluminum perovskite (YAP) scintillator and a light guide that connects the scintillator to a

photomultiplier. The detector integrates the electron signal (incoherently) over its complete range and thus delivers one intensity value for each scan point respectively. The specimen-detector distance is referred to as the camera length, and determines the inner detector angle by its geometry, while the outer detector angle is defined by the physical size of the detector. Different angular regions provide different information from the acquired electron signals. A projector lens system (not depicted here) can be utilized to virtually change the distance between specimen and ring detector, and thus the inner detector angle. The different angular regions are named the bright field (BF), which collects signals from 0 mrad to 10 mrad, and the dark field (DF), which is defined as every scattering angle above 10 mrad [43]. Furthermore, scattering angles above 50 mrad can be referred to as the HAADF. It should be noted that this definition is taken from [43] and is not consistent throughout the literature. A high inner detector angle is mainly necessary to consider signals from electrons that have been scattered through very high angles and thus provide an intensity that is proportional to Z^n – where $n < 2$ – and is connected to the actual value of the inner detector angle [45].

In summary, a STEM image is constructed by scanning the focused electron probe over the specimen and recording the transmitted intensity at each position of the probe. If the inner detector angle is sufficiently large, one can consider the measured signal to be an incoherent sum of the Rutherford scattering intensities of all the atoms irradiated by the electron beam. This means that the measured intensity in a STEM HAADF image is proportional to the average atomic number Z of the atomic column and the specimen thickness. This makes the results obtained from STEM intuitively interpretable in comparison to conventional transmission electron microscopy (TEM) images.

2.3. Electron Channeling

Since the STEM technique in this work is used solely with semiconductor crystals that are highly symmetrical, one effect that must be considered is called the channeling effect. This effect describes the fact that the intensity, collected by the detector, is at a maximum if the electron probe focuses on an atomic column that is highly ordered in the direction of the electron beam. A detailed and intuitive explanation for this effect was provided by D. v. Dyck [46]. In simple terms one can state that the electron beam interacts with the averaged potentials of the atoms situated in an atomic column as a 2D plane wave. The wave oscillates in the electron beam's direction, centered around the positive nuclei of the elements. Due to the positive electrostatic potential of the atoms, an atomic column acts as a guide or channel for the electrons. The electrons can scatter dynamically without leaving this channel and are thus strongly localized to the atomic columns. The wave function of the electron beam presents an amplitude that oscillates with the sample thickness, which decreases radially and symmetrically as its distance from the atomic column increases. The local maxima of the intensity of the wave function of the electron beam thus correspond to the positions of the atomic columns of the crystal lattice. A

loss of column intensity is associated with deviations of the atomic positions from the column. Thus, if a significant proportion of the atoms of a column are located at positions displaced from their lattice positions, the intensity distribution changes and the phenomenon of de-channeling occurs [47]. This leads to a loss of beam intensity on or at the atomic column, so that subsequent scattering events by atoms within the column result in lower intensity in comparison to the non-displaced case. The deviations of atoms from their lattice positions that evoke de-channeling can have multiple origins; e.g., crystal defects, substitute atoms, lattice plane bending, etc. The atomic displacements that are introduced by substitute atoms are discussed in the following section, 2.4. The bending of lattice planes due to the surface relaxation of thin TEM samples, and its effect on STEM intensity, are covered in chapter 4.2.

2.4. Static Atomic Displacements

The common phenomena of atomic displacements occur when working with compound semiconductors, such as *Ga(N,As)*, in which the elements on one sublattice (*N* & *As*) have significantly different sizes and covalent radii. The effect of the occurring static atomic displacements (SAD) on STEM HAADF is well-known and widely discussed in literature [48-50], and is briefly introduced in this section. A comprehensive simulation study of the effect of SAD on STEM HAADF can be found in the dissertation of R. Fritz [51], in which the order of magnitude of different material systems is investigated.

The displacement of atoms from the resting lattice positions occurs when an atom of the host material system is substituted with an atom of a different type. If the substitute atom has a significantly higher or lower atomic number, or a different covalent radius, the crystal lattice is disturbed. For example, consider *GaAs* as the host system and incorporate *N* on the group V lattice positions. When an *As* atom is replaced by a *N* atom, the bond length is changed significantly. For the directly adjacent Ga atoms, this change in environment leads to a changed resting position in the crystal lattice. The magnitude of this effect was simulated with a Valence Force Field (VFF) routine, implementing a Keating potential [52]. The results demonstrated a mean displacement of *Ga* atoms of approximately 35 pm. The size of this displacement clearly exceeds that of a thermally induced displacement, which is approximately 10 pm, calculated for room temperature (295 K). It should be noted that there are material systems, e.g., *Ga(P,As)*, in which the static displacements are in the range of the thermally induced displacements [51].

The presence of SAD in a crystalline specimen strongly affects the ADF intensity and its angular distribution. The symmetry of the crystal is broken and de-channeling is more likely to take place, depending on the material system and thus the magnitude of the static displacement. De-channeling increases the diffuse scattering, which increases the intensity in lower angular regions in the given example of incorporated *N* [49, 50].

2.5. Lens Aberrations

Similar to glass lenses in light microscopy, magnetic lenses used in electron microscopy also suffer from lens imperfections. The most striking aberrations are explained phenomenologically and are visualized in *Figure 2.3*.
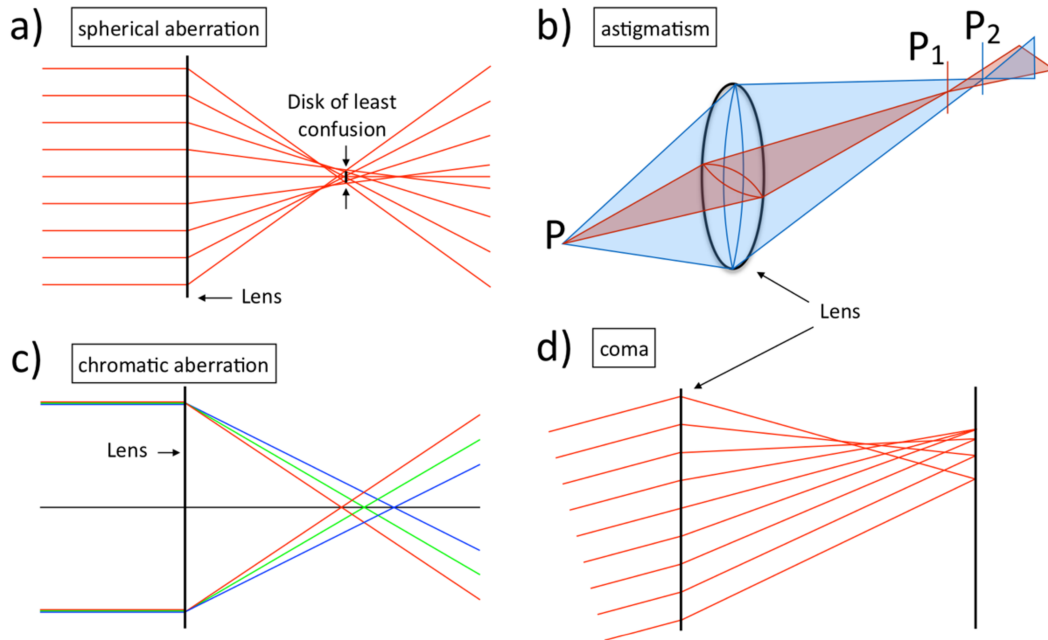

Figure 2.3: The figure depicts the main lens aberrations, namely (a) spherical aberration, (b) astigmatism, (c) chromatic aberration and (d) coma. The image is adapted from [53].

The achievable resolution of a conventional STEM is most strongly limited by the <u>spherical aberration</u>. This lens aberration describes the fact that off-axis beams are refracted more strongly or weakly than near-axis beams from the imperfect magnetic field of a lens. This means that different focal planes and image planes exist for these rays, as depicted in *Figure 2.3* (a). The strength of the spherical aberration is indicated by the spherical aberration coefficient C_S. Due to the nature of the Lorentz force, cylindrical magnetic lenses always have a positive C_S, so that off-axis rays are always more strongly refracted than near-axis rays. The factor C_S is defined as the distance between the Gaussian image plane (which refers to the ideal image plane) and the disk of least confusion. *Figure 2.3* (a) illustrates a schematic of the spherical aberration with the disk of least confusion marked. The spherical aberration blurs the image and thus degrades the resolution of details in the image. Unfortunately, the aberration is further exacerbated by the other lenses present in the instrument. Although Scherzer had already proposed various approaches for the correction of aberrations in 1947 [54], the first correctors could not be realized for scanning electron microscopes [55, 56] until almost 50 years later. The effect of these correctors is based on two hexapole lenses, in which the primary non-rotationally symmetric aberrations balance each other. However, the hexapoles also induce a rotationally symmetric C_S that is

contrary to the objective lens. The spherical aberration is proportional to the third power of the scattering angle of the electron beam and is thus also referred to as C_3. The next limiting aberration of this kind is the fifth-order spherical aberration, and its coefficient is referred to as C_5.

Astigmatism refers to the depiction of a point-shaped object as an extended rod. It is caused by inhomogeneities in the magnetic field of a lens, which are caused by its imperfectly cylindrical shape. A schematic of this aberration is illustrated in *Figure 2.3* (b). An electron originates from point P and enters the magnetic lens in the horizontal plane (red), resulting in its corresponding focal length focusing at Point P1. The focal length of an electron that enters the magnetic lens in the vertical plane (blue) will be longer (P2). This results in an elongated and distorted image of the object. However, astigmatism can be corrected by stigmator lenses, which are present in most conventional microscopes.

The chromatic aberration, quantified by the coefficient C_C, causes a lens to refract electrons of different energies to different values. Even with the use of FEG, an energy distribution ΔE of the emitted electrons around the intended accelerating voltage is unavoidable. Electrons with different kinetic energies will naturally experience different amounts of Lorentz force within the magnetic field of the lens. This leads to different focus points for the different energized electrons and results in a blurred image. C_c has the dimension of length and is proportional to $\Delta E/E_0$, where E_0 refers to the initial beam energy. A schematic of the aberration is illustrated in *Figure 2.3* (c).

The last aberration that is covered in this section is called coma, as illustrated in *Figure 2.3* (d). In this process, off-axis beam electrons that propagate through regions of the magnetic lens are focused at different positions, which are shifted relative to each other in the image plane. As a result, the spot size of each focus point is different, resulting in a spot with a tail-like character. This distortion is called coma or comic aberration, and shares its etymology with the astronomical term "comet".

3. Applied Methods

This chapter provides information about the multislice formalism that is implemented in the STEMsalabim software, whereas the software itself is introduced in chapter 4.1 as a part of the results in the course of this work. The key physical concepts that are necessary to be able to theoretically model a modern STEM and its interaction with specimens are introduced in section 3.1. Furthermore, this chapter presents an overview of the existing literature with regard to composition determination and the integration of experimental influences into STEM simulations. The final section in this chapter provides the reader with an overview of former publications and contextualizes the achievements presented in chapter 4.

3.1. The Multislice Formula

A modern STEM, as presented in chapter 2.2, is a very complex device. Theoretical modeling of the processes in this instrument should be as detailed as possible, but also only contain parts that have an influence on the results. The formalism that is most commonly used when simulating STEM HAADF images is the multislice formalism that was first introduced by Cowley [57] and Moodey [58] and further developed by Kirkland [59].

The basic concept of this formalism is the division of the simulated model, called the supercell, into thin slices with identical thicknesses dz in the electron beam direction. Each atomic potential contained in a slice is projected perpendicular to the beam direction on an x-y plane. To prevent the atomic potentials from overlapping, the dz must be chosen carefully. In a zincblende structure in the [010] view direction, the smallest dz that fulfills these conditions is one unit-cell. The incident probe wave function $\psi_0(x, y)$ firstly interacts with the projected potential of the first slice. The interaction process can be described by the slice's transmission function $t_j(x, y)$, where j denotes the number of the slice. After this interaction, the modified electron wave function propagates to the next slice $j+1$. This propagation is defined by a propagation function $p(k_x, k_y, dz)$, and is given in frequency space. This process is iteratively applied to all slices of the supercell, and the wave intensity is integrated and collected over a certain momentum range to simulate the ADF detector. The most important equations are summarized in the next paragraph. A detailed description of the formulae and the complete simulation process can be found in the work of Kirkland [60].

The highest spatial resolution could be achieved if the probe function of the illumination system of the microscope was point-like. As already discussed in the previous chapter, the quality, and more precisely, the diameter of the electron beam is determined by the lens aberrations. Hence, the incident probe wave function $\psi_0(k_x, k_y)$ for a focused electron beam in frequency space, resting at the scan position (x_p, y_p), is given by

$$\psi_0(k_x, k_y, x_p, y_p) = A(k_x, k_y)\exp\left[-i\chi + 2\pi i(k_x x_p + k_y y_p)\right]$$

Whereas the frequency and real space are connected via the inverse Fourier transformation $\mathcal{F}^{-1}$ and a normalization constant B:

$$\psi_0(x, y) = B\mathcal{F}^{-1}\left[\psi_0(k_x, k_y)\right].$$

$A(k_x, k_y)$ is the aperture function and is unity for all $|k| < \alpha_{max}$ and zero outside. α_{max} refers to the maximal angle of the CLA, with $\alpha = |k|$ as the polar angle. $\chi(k_x, k_y)$ is the aberration phase error and is defined as follows:

$$\chi(k_x, k_y) = \frac{\pi\alpha^2}{\lambda}\left(-\Delta f + C_a \cos(2\phi - 2\phi_a) + \frac{1}{2}C_s\alpha^2 + \frac{1}{3}C_5\alpha^4\right),$$

where ϕ is the azimuthal angle, Δf refers to the defocus, C_a is the two-fold astigmatism, ϕ_a refers to the two-fold astigmatism azimuthal angle, and C_s and C_5 represent the already introduced spherical aberration coefficients in the third- and fifth-order, respectively. The transmission function $t_j(x, y)$ for the jth slice can be written as

$$t_j(x, y) = \exp\left[i\sigma v_j(x, y)\right],$$

which includes the interaction parameter σ and the cummaltive atomic potential of all atoms, n, in the slice j. The interaction parameter is defined as

$$\sigma = \frac{2\pi\gamma m_0 e\lambda}{h^2}.$$

Here, m_0 is the rest mass and e the charge of an electron, γ is the Lorentz factor, and h is Planck's constant. The atomic potential $v_j(x, y)$ is the projected sum of each individual atomic potential in the slice:

$$v_j(x, y) = \sum_n v_n(x - x_n, y - y_n, z)dz.$$

The individual atomic potentials $v_n(\vec{|r|})$ are calculated from the atomic scattering amplitudes $f_n(|\vec{k}|)$ through the use of the first Born approximation:

$$v_n(|\vec{r}|) \propto \mathcal{F}^{-1}\left(f_n(|\vec{k}|)\right).$$

The scattering amplitudes can be parametrized using tabulated values for the element-specific parameters $a_{i,j}, b_{i,j}, c_{i,j}$ and $d_{i,j}$ and the following equation as described in Kirkland's work [60].

$$f_i(\vec{k}) = \sum_{j=1}^{3} \frac{a_{i,j}}{|k| + b_{i,j}} + \sum_{j=1}^{3} c_{i,j} \exp\left(-d_{i,j}|k|^2\right).$$

Details of the parametrization used within the presented STEMsalabim software can be found in the publication appended to this work.

A Fresnel propagator is applied to the transmitted electron wave to propagate the wave through free space to the next slice and is given by

$$p(k_x, k_y, dz) = \exp[-i\pi|k|^2 \lambda dz].$$

In summary, the interaction between the incident wave function and a slice can be written as

$$\psi_{j+1}(x, y) = \mathcal{F}^{-1}\{p_j(k_x, k_y, dz) \cdot \mathcal{F}[t_j(x, y)\psi_j(x, y)]\}.$$

STEMsalabim takes the thermal diffuse scattering (TDS) into account by applying the frozen lattice approximation to the atoms in the supercell. This approach calculates different atomic vibration (phonon) configurations by disturbing the atom's resting positions according to thermal vibrations. The perturbation of the lattice position is determined by a Gaussian distribution and the individual Debye-Waller factor of the element. The Debye-Waller factors of each element are temperature dependent and give a measure of the mean square displacement, which is in the range of Å^2. For the present work, the mean square displacements for the elements were taken from Schowalter et al. [61]. To resemble the interaction of the electron beam with the thermally disturbed lattice precisely, a sufficiently large number of unique frozen phonon configurations must be calculated and averaged incoherently at the end. This increases both the accuracy of the results and the computational time required. The exact number of necessary frozen phonon configurations depends on the material system and the thickness of the simulated sample. A simulation study for different material systems can be found in [62].

3.2. Temporal and Spatial Coherences

This section introduces the method used in this work to consider chromatic aberration and a finite source size in the multislice simulations. Moreover, the influence of amorphous layers that are

introduced by the sample preparation are discussed. The results presented here are summarized from the publication of Beyer et al. [63].

Using the example of a binary *GaP* sample, the influence of source size and shape, and chromatic aberration on the intensity of the HAADF is investigated. *GaP* is chosen as an example because of its inherently fixed composition and the relatively large difference in the two elements' atomic numbers. The contrast between these two elements in a unit-cell is higher than for materials with similar atomic numbers, and thus, the discussed effects can be more effectively visualized. The conclusions drawn from this rather simple material system can be further used for future evaluation of more complex material systems.

Even if the most important geometric aberrations, introduced in chapter 2.5, are taken into account in the multislice simulations, the resolution and contrast are found to be higher in the simulation compared to the experimental image. The publication of Beyer et al. [63] illustrates the importance of the aforementioned effects by calculating a 2D match between simulation and experiment. The effects are approached individually and the calculated differences between simulation and experiment are taken as a figure of merit. For a detailed description of the experimental setup and parameters, please refer to the publication [63].

The first reason for the discrepancy between simulation and experimental image is the chromatic aberration or energy distribution of the electron beam. The influence of chromatic aberration on the STEM ADF intensity has been previously investigated [27, 28]. Since different energies of electrons lead to different focus points, as demonstrated in chapter 2.5, the chromatic aberration is taken into account by summing over a simulated defocus series. The results from the different defocus values are then summed in a weighted way. The weight of each defocus is determined by a Gaussian distribution with a full width at half maximum of

$$\Delta z_{CC} = 2 \, C_c \frac{dE}{E_0} \sqrt{2log2} \, ,$$

where C_c refers to the chromatic aberration coefficient [27]. The determined coefficients for the utilized microscope, a JEOL JEM 2200 FS, are C_c of 1.5 mm and dE of 0.42 eV. A value for Δz_{CC} of 7.5 nm can thus be calculated. By simulating this defocus series, the relative error between simulation and experiment could be improved from 41.61% to 28.28%. It must be noted that this was evaluated at a sample thickness of approximately 28 nm, and the actual values are dependent on thickness.

Spatial coherence is related to source size, i.e., the electron emitter is not a point-like source but rather has finite dimensions. The form of the source is discussed controversially in literature as Gaussian or Lorentzian, and as combinations of both [25, 64]. The finite source size and beam broadening by amorphous layers were included in this work as a convolution of a 2D Lorentzian and Gaussian distribution to a simulation. Distributions were normalized to keep the mean of the image unchanged. The different shapes of the distributions led to different intensity distributions within a unit-cell. This

16

demonstrates the importance of a 2D analysis, because it is preferable to achieve a good agreement in the complete unit-cell, rather than only on the atom positions themselves. The distributions take the following form:

$$S_G = \exp\left(-\frac{x^2}{2\sigma} - \frac{y^2}{2\sigma}\right) \text{ and } S_L = \frac{\sigma}{(x^2 + y^2 + \sigma^2)^{\frac{3}{2}}},$$

where x and y are spatial coordinates and σ refers to the width of the distribution, in the order of nanometers.

In addition to the chromatic aberration, the Gaussian distribution is convoluted with the simulated image. The comparison with the experimental image exhibits a significant decrease in the relative error from 28.28% to 4.11%. The width of the distributions was varied to minimize the relative error. If one considers the results obtained by convoluting the Lorentzian distribution, an improvement of the error from 4.11% to 1.84% can be observed. This leads to the conclusion that a Lorentzian distribution best resembles the finite source size of the microscope, and is thus used for further analysis. To determine whether amorphous layers change this result, simulation cells with amorphous layers were created and analyzed equivalently to the simulation cells without amorphous layers. The layers were added to the top and the bottom of the sample supercell, respectively. They were created with the *Ideal Amorphous Solids* (IAS) software package [65, 66]. This algorithm generates amorphous materials without symmetrical elements. The density of the amorphous material was chosen to fit that of the crystalline *GaP* cell. These amorphous layers are generated during sample preparation and a detailed study can be found in [30]. The application of amorphous layers to the sample reduced the relative error to 1.39%. The width of the source distribution σ was determined to be 36 pm. This compensates for the finite electron source and the beam broadening by the amorphous layers.

The results from [63] are used throughout the course of this work, meaning that every simulation includes chromatic aberration and compensates for finite source size and amorphous layers through the combination of defocus series and convolution with a 2D Lorentzian distribution.

3.3. Synopsis of Existing Literature

In the last two decades, several approaches for quantitative composition mapping with HAADF STEM have been proposed [67-73]. This section presents a brief overview of the existing literature that addresses the topic of the extraction of quantitative compositional information from Z-contrast images by comparison to simulated results. Two main techniques are introduced: the analysis of the raw STEM intensities and the application of a statistical model to the STEM images.

In 2012, Grieb et al. determined the chemical composition of *GaNAs* QWs using STEM HAADF imaging in combination with the multislice simulations presented in [74]. They investigated *GaNAs* QW with an *N* concentration of between 1% and 5%. They took the SAD into account by relaxing supercells with a

VFF algorithm, and simulated the scattering intensity of the QW via multislice simulations as a reference set. To obtain the *N* concentration, they evaluated the normalized intensities by dividing the image into Voronoi cells, centered around atomic columns. The intensities were compared to the simulated reference set, and with this, a concentration could be assigned to every atomic column. Furthermore, they performed a strain state analysis and compared both results to HRXRD measurements. Additionally, they discussed the effect of surface relaxation on the HAADF intensities and the resulting composition fluctuation. The results obtained from the intensity method demonstrate an agreement with the HRXRD results and thus prove the validity of the method. Grieb et al. improved the method in their subsequent work [75], published in 2013, by using STEM images obtained from two different detector inner angles. They demonstrated that images that are received from lower detector angles are more sensitive to the lattice plane bending, due to elastic surface relaxation.

The same method was used by Kauko et al. in 2013 [76], by which they evaluated the *Sb* concentration in axial $Ga(As_{1-x}Sb_x)$ inserts of otherwise pure *GaAs* nanowires. The concentration was quantified by comparing the experimental image intensities that were normalized to the incident beam intensity with a simulated reference set. The multislice simulations were performed with the frozen lattice approach. Kauko et al. verified the composition analysis by comparing the results to energy dispersive x-ray spectroscopy (EDX).

In 2013, Pastore et al. published the results of a compositional analysis of $(In_xGa_{1-x})P$ layers used in a multijunction solar cell [77]. Again, the normalized experimental STEM HAADF intensities were compared to a simulated reference region. Mehrtens et al. published a composition analysis on $(In_xGa_{1-x})As/GaAs$ heterostructures and verified their findings with results from a lattice fringe analysis and from EDX [78]. The publications introduced here confirm that the intensity method is valid for a variety of ternary material systems.

Grieb et al. combined the intensities from the Z-contrast with the strain state of the sample to simultaneously determine *In* and *N* composition in a $(In_xGa_{1-x})(N_yAs_{1-y})$ QW structure, in 2014 [79]. With this, they were able to determine the composition of a quaternary material system with information obtained from two independent sources. The presented results were in accordance with the results from x-ray diffraction measurements and 3D atom probe tomography.

A different approach to gather quantitative information from HAADF STEM images has been presented in the work of S. van Aert et al. in multiple publications [80-83]. The calculation of a sufficiently large simulated reference set to compare the raw STEM intensities is very time consuming. S. van Aert et al. propose a model-based approach that is used to estimate the positions and the total intensity of the scattered electrons for every atomic column in a STEM HAADF image [80]. This model cannot be used to determine the absolute chemical composition without additional information, but is still useful to

extract important structural and chemical information, which then can be used to relatively quantify chemical compositions.

Instead of a time consuming model, a simplified, empirical, incoherent imaging model is proposed to describe HAADF STEM images. This simplified model is then used to estimate the positions and the total intensity of the scattered electrons for every atomic column from a HAADF STEM image. Although this model cannot be used to quantify the absolute chemical composition, it is demonstrated by means of accurate HAADF STEM image simulations to be useful to extract relevant structural and chemical information, which can then be used for the relative quantification of the chemical composition. When combining the model-based method with additional multislice simulations, it has been proven that the method can be extended from a relative toward an absolute quantification of chemical compositions from HAADF STEM images [81]. The model-based approach, without additional information from a multislice simulation, was successfully used to determine the exact number of atoms in crystalline nanoparticles [82, 83]. Recently, M. Alania et al. published a comparative study of the relationship between multislice frozen phonon simulations and the absorptive potential approach in terms of the integrated intensity and atomic column position measurement [84]. This study demonstrates that the frozen phonon approach provides more accurate results over the complete inner detector range, and also that it is more stable in terms of sample thickness.

In summary, it can be confirmed that reference sets that are calculated with the frozen phonon approach provide highly accurate results, taking all experimental effects into account. The method has been successfully applied to a variety of material systems and verified by commonly-used techniques, such as HRXRD and atom probe tomography.

The question of whether information should be extracted from the STEM images by taking the integrated intensities from a Voronoi cell, calculating the probe integrated scattering cross section [85], or using the atomic column position measurement model, cannot be answered conclusively.

4. Results

In this chapter, the achieved research results are discussed in detail. First, the implementation of the multislice algorithm in the STEMsalabim software package is outlined. This software is specifically designed to handle supercells with large lateral dimensions while maintaining a small memory footprint. Thereafter, the modeling of supercells with macroscopic elastic relaxation is explained. The influence of the resulting lattice plane bending on the STEM intensity in different angular regions is not negligible; therefore, it is important to understand the influence of the geometrical structure of the sample on the STEM intensity. Under consideration of the most important experimental influences, it can be assured that the multislice simulations exhibit a good agreement with experimental images. This leads to the expansion of a composition determination technique that has been established in the relevant literature [76, 79, 86]. Experimental STEM intensities are iteratively compared to a set of simulations with different compositions, and the best fit allows for a conclusion about the samples' composition. In the course of this chapter, the implementation of the intensity composition method is explained and a comprehensive simulation study indicates the capabilities and limitations of the method. With the capabilities in mind, the extended algorithm is presented through the example of three technological important semiconductor samples, and compared to composition profiles obtained from HRXRD.

All of the results that are presented here can be found in detail in the publications appended to this work.

4.1. Implementation of the Multislice Algorithm

STEMsalabim is a software package specifically designed for the purpose of simulating large amounts of cells, also called supercells, including parameter sweeps. It is adapted and optimized for use on a high-performance computing (HPC) cluster. The software package makes use of the message passing interface (MPI) and threads to supply an efficient and scalable parallelization of the calculations, while maintaining a small memory footprint. This enables an efficient calculation of model structures with large lateral dimensions. Furthermore, different atomic configurations, defocus values and phonon configurations [87, 88] are necessary for a comprehensive simulation set, and require fast and efficient simulation software.

Since 1980, STEM has become an indispensable tool for the quantitative analysis of crystalline samples. To extract quantitative information from experimental images, multislice simulations of the samples are often inevitable. The basic algorithm of the multislice formula, introduced in section 3.1, consists mainly of (inverse) Fourier transformations, and can be conducted efficiently with highly optimized discrete Fourier transformation packages. Furthermore, most of the simulation steps are independent of each other and can be parallelized. Therefore, the sheer amount of scanning points in one simulation

increases the computational effort needed. An example of a simple *GaP* simulation illustrates the number of multislice simulations. The example supercell has a size of 9 x 9 x 92 unit-cells, which corresponds to a cuboid structure with approximately 4.8 nm x 4.8 nm x 49.6 nm edge lengths. The slice thickness in the electron beam direction was chosen to be one unit-cell which ensures no overlapping atom potentials in [010] direction. The grid density was decided to be 360 nm^{-1}, resulting in a grid size of 1766 x 1766 points. The scanning area was chosen to be 3 x 3 unit-cells, and was sampled by 65 points in each direction. This led to 3640 scan points for each supercell slice. A full supercell simulation with one frozen phonon configuration and one defocus value resulted in 334,880 calculations. Multiplying this by 15 phonon configurations for each of the seven defocus values, more than 40 million calculations must be conducted in total; these are mostly (inverse) Fourier transformations. Additional parameter sweeps and different atom configurations of the cell increase the number of calculations drastically.

Since the available software [89-96] is mainly designed to work on desktop computers, a software package that is optimized for HPC clusters was developed. The software uses MPI and shared-memory threads to supply an efficient and scalable parallelization of the calculations, while maintaining a small memory footprint. The STEMsalabim software package implements the popular multislice algorithm developed by Kirkland [60, 97], which has already been covered in section 3.1. As illustrated above, for a simple simulation, millions of calculations must be done. Fortunately, the tasks can be parallelized over several computing nodes and the time can be reduced by using pre-calculated results. Every atomic potential $V_i(r)$ for every element within the sample can be calculated upfront and reused within the simulation. Furthermore, the Fresnel propagator (see section 3.1) can be calculated within one frozen phonon configuration if the slice thickness is kept constant. The transmission functions could also be cached for each individual defocus value, but calculating new atom positions increases the number of unique configurations. This helps in the convergence of the final results.

The parallelization scheme uses MPI to communicate between different computing nodes, and uses shared-memory threading architecture within one machine; this reduces the memory required within one machine drastically. Moreover, this reduces the number of total MPI processes and thus improves performance. With fewer MPI processes, less network activity occurs when reporting temporary results to the main MPI process. The resulting data is gathered on one machine within the threads and passed as a single chunk to the master MPI process. As mentioned previously, the main mathematical calculation that must be carried out is an (inverse) Fourier transformation. The popular FFTW library, which is designed to run on CPUs, is used in this context. Since the multislice simulations are independent of each other, they can be parallelized very efficiently, which leads to the nearly linear scaling behavior of the time versus the number of used computer cores. The simulation results are stored as binary data using NetCDF, which is based on the HDF5 library. The data can be read selectively from the file, which is a significant advantage with large result files.

To demonstrate the usability of the software and highlight the close resemblance of the experimental results, an example of a $Ga(As_{95.2\%}Bi_{4.8\%})$ sample is presented in *Figure 4.1*. The sample is approximately 32 nm thick. The experimental image was taken with a JEOL JEM 2200 TEM, operating at 200 kV with C_s = 2 µm and C_5 = 5 mm. The simulation used ten frozen lattice configurations for each of the seven defocus values used to incorporate chromatic aberration. The experimental image is presented in Figure 4.1, with the simulated $Ga(As_{95.2\%}Bi_{4.8\%})$ results depicted in the overlay, surrounded by the white dotted line. Both images have the same intensity scale, with intensities given in fractions of the impinging electron beam. An excellent agreement can be observed, both qualitatively and quantitatively. This is important to the quantitative analysis that is necessary to determine the composition of experimental images.
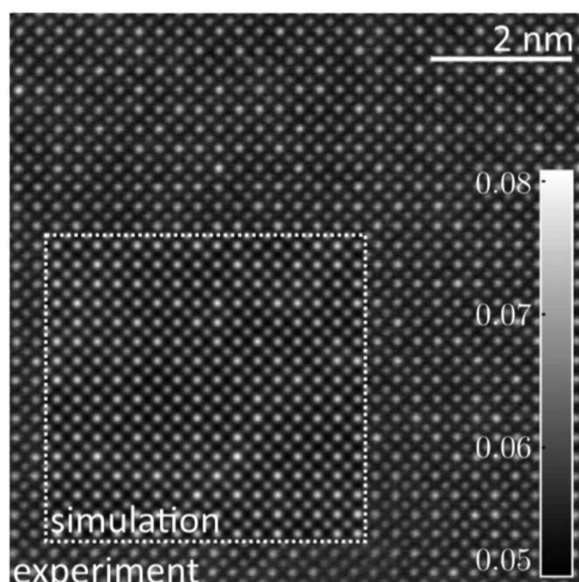

Figure 4.1: The figure presents an experimental STEM image of a 32 nm thin GaAs sample with a Bi composition of approx. 4.8%. The inset depicts the simulation result obtained from the associate multislice simulation conducted in STEMsalabim. Both images share the same intensity scale, which emphasizes the quantitative agreement between simulation and experiment. The figure is reproduced from [98].

This section has summarized the results from the publication, *"Stemsalabim: a high-performance computing cluster friendly code for scanning transmission electron microscopy image simulations of thin specimens"*. The full publication is appended to this thesis. The software package is a useful tool to efficiently simulate sets of simulation with varying parameters (e.g., atomic configurations) on an available HPC cluster. The memory efficiency of this software makes it possible to simulate large amounts of data in a reasonable timeframe. Therefore, a decent amount of phonon configurations or defocus values can be calculated efficiently. Since the code scales nearly linearly with the number of computing cores, it is easy to increase the speed of a simulation by horizontally scaling. The publication provides a more detailed overview of the different examples of applications. This also includes the simulation power that is required to study the effect of surface relaxation, which is covered in the next section.

4.2. Elastic Surface Relaxation

Modern semiconductor devices often consist of thin layers of multiple different material systems [2-4]. The interfaces in the device also contribute to the functionality of the device, e.g., the separation of charge carriers in "W"-type laser structures [4]. The publications "*Influence of surface relaxation of strained layers on atomic resolution ADF imaging*" [99] and "*Surface relaxation of strained Ga(P,As)/GaP heterostructures investigated by HAADF STEM*" [100] study the effect of elastic surface relaxation of thin TEM specimens on HAADF intensity.

A mismatch between the lattice constants of two different materials at an interface produces strain. One way to release this strain is via elastic relaxation. The strength of this effect is determined by the lattice mismatch between the two materials on either side of the interface. The stress relaxation in cubic bulk material is described as tetragonal distortion [101, 102]. The type of strain relaxation is also defined by the restricting dimensions of the sample. In a bulk material, the stress is relaxed in the direction of growth, or perpendicular to it. In the case of a TEM sample, one spatial dimension is thinned drastically in comparison to the other two. This allows the strain of the interface to be released via the surface of the sample. If the sample is very thin, this results in the deformation of the surface area and the bending of the atomic columns. These bent atomic columns have a significant influence on the STEM contrast. A large fraction of the HAADF STEM intensity is connected the channeling of the electrons via the atomic columns [46, 47] (see section 2.3). If the structure is modified, channeling is reduced and thus the local intensity is decreased drastically.

In the next paragraph, the influence of elastic surface relaxation on HAADF intensity is presented with the help of a model interface that consists of a *GaAs* QW sandwiched between *GaP* barriers. The interface is relaxed with a finite element (FE) algorithm and is used as supercell input for a STEM multislice simulation. The results are analyzed and the STEM ADF intensity is correlated to the lattice bending of the corresponding atomic column. The relatively high lattice mismatch of 3.7% of the model system was deliberately chosen to study an extreme case of surface relaxation. Moreover, an experimental sample is presented and demonstrates that the insights gained from the simulation study help to interpret results from experimental specimens.

The model used in the initial studies is a *GaP* substrate and *GaAs* QW, with varying parameters with regard to QW thickness *w* and sample thickness *t*. This material combination has a lattice mismatch of 3.7%, which is a high value for actual pseudomorphically grown layers. The results gained from these studies further an understanding of the effects of elastic surface relaxation in more complex materials, such as multinary semiconductors.

The structure of the sample is exemplarily depicted in *Figure 4.2*. When mentioning spatial measurements in this context, we refer to monolayers (ML) and not *nm*, since the metric dimensions in *nm* can change according to the deformation. The supercell is designed to contain a *GaP* layer with

a width of 376 ML (~50 nm) along the growth direction, i.e., the X-direction in *Figure 4.2*. Group V and group III are considered as individual ML. On top of the *GaP* substrate, a *GaAs* QW is placed with a varying width *w* of 22, 37 and 74 ML, which corresponds to approximately 3, 5 and 10 *nm*. The QW region is capped by a *GaP* layer that consists of 376 ML analogous to the bottom layer. The thickness in the electron beam direction *t*, i.e., the Z-direction, is also varied with the chosen thicknesses of 80, 184 and 376 ML, which translate approximately to 10, 25 and 50 *nm*. The sample thickness and the QW thickness *w* and *t* are chosen to fit the typical dimensions of a conventionally prepared TEM sample.

The model structure was first relaxed with an FE formalism implemented by the COMSOL software, which solves the equations of linear elastic theory [103]. The structure is initially created as a continuous medium and then divided into small regions. Irreversible plastic deformation is neglected, since the focus is on pseudomorphic growth. Due to the lattice mismatch that originates from the different lattice constants, the *GaAs* layer is set to a condition of hydrostatic pressure. Establishing the boundary conditions decides the way in which relaxation occurs. If the Z- and Y-direction are considered to be infinite, the well-known effect of tetragonal distortion takes place, as is depicted in *Figure 4.2* (b), in which the stress is released via deformation of the lattice constant only in the X-direction. By changing these conditions so that the Z- and X-direction are free, and assuming a periodicity in the Y-direction, the stress is released in a deformation at the surface. The structure deforms according to the chosen boundary conditions and the elastic properties that are introduced in an anisotropic manner and taken from [104]. The relaxation is visualized in *Figure 4.2* (c), in which the displacement of the atoms is multiplied by a factor of 5 to create a better visualization for the reader. The result of the FE algorithm is a displacement field that indicates the extent of the displacement of an atom from its resting position. This displacement field is used to transfer the atom displacements from the FE simulation to a supercell decorated with the specific atoms. This atomistic supercell is further refined using a VFF approach [105] to also include the microscopic forces between the different material systems on the interface.
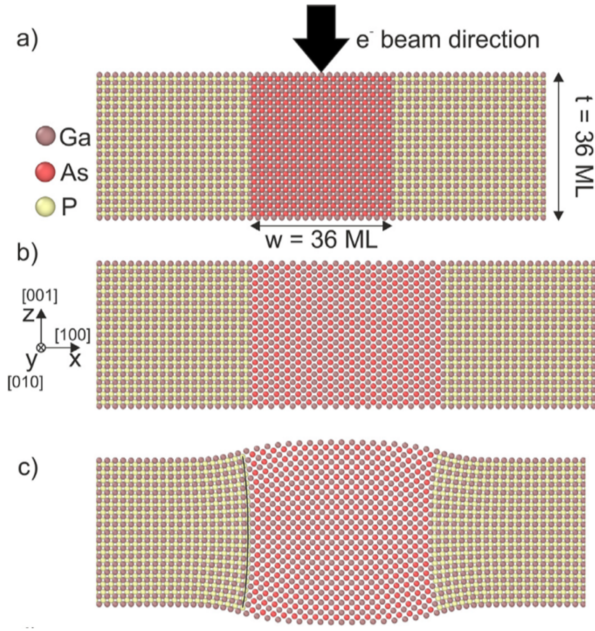
Figure 4.2: The figure presents a structural model of a GaAs QW embedded in a GaP matrix in the unrelaxed form (a), relaxed with neglected (b) and considered surface relaxation (c). The displacement of the atoms is multiplied by a factor of 5 for better visualization. The image is reproduced from [99].

The resulting atomistic macroscopic relaxed supercells are used as an input for ADF STEM multislice simulations. This process is automated and carried out for all possible combinations of QW and sample thickness *w* and *t.* Since this is a very time consuming computation process, a highly efficient optimized multislice code is used. The STEMsalabim software package, which has already been introduced, is used. All simulations are conducted with a defocus series to consider the effect of chromatic aberration. For each of the seven defocus values, ten individual phonon configurations are carried out and averaged. To simulate the effect of the source distribution, as explained above, all simulations are convoluted with a Lorentzian distribution with a width of 38 *nm*. This ensures a good fit between simulation and experiment and enables extraction of data comparable to experimental results. To quantify the simulation results, the lateral mean square displacement M can be defined as

$$M_i = \sum_{k=1}^{N} \frac{(x_k - \overline{x}_i)^2}{N} + \sum_{k=1}^{N} \frac{(y_k - \overline{y}_i)^2}{N},$$

where $\overline{x}_i$ and $\overline{y}_i$ are the mean x and y coordinates of the atomic column and N denotes the number of atoms in the column. *Figure 4.3* summarizes a portion of the results from the simulation study conducted in "*Influence of surface relaxation of strained layers on atomic resolution ADF imaging*" [99]. The results of nine combinations of *w* and *t* are displayed. The black line represents the mean square displacement of the simulation cell along the X-direction. It is displayed on a common Y scale, which is determined by the highest value present in the simulation study. The red solid line represents the simulated STEM intensity of group III atomic columns. To enable a comparison of the different sample structures, all intensities were normalized to the intensity of pure *GaP* at the according thickness.

Therefore, the intensity change is comparable within completely different sample structures. The STEM intensities were collected by circular averaging of the intensities around an atomic column position with a diameter of 25 *pm*. The circular averaging approach was chosen over the PICS method [85], which uses Voronoi cells, because it is more sensitive to the bent lattice planes. The shaded red area in *Figure 4.3* (a) marks the region in which the *GaAs* QW starts.
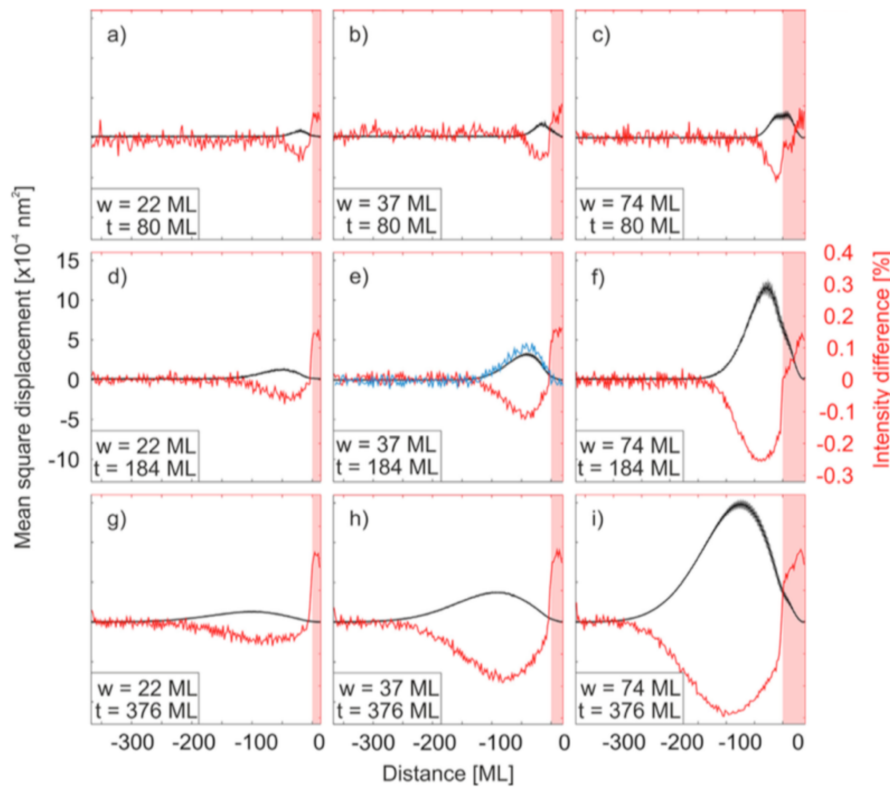

Figure 4.3: The figure illustrates the results obtained from the systematic variation of the geometrical properties of the structural model. The QW width w increases from left to right, whereas the sample thickness t increases from the top to the bottom. The mean square displacement M of the atoms is represented by the black line, corresponding to the left y axis. The red line represents the normalized group III intensity (read right y axis). The blue curve in subfigure (e) represents the intensity difference between the relaxed surface and the tetragonal distorted supercell. All subfigures share the same y axis. The image is reproduced from [99].

The most important result obtained from the simulation study is the perfect correlation between the mean square displacement (M) of the atoms and the simulated STEM intensity difference, summarized in *Figure 4.3*. The results clearly demonstrate that the greatest value of M evokes the greatest drop in intensity. Furthermore, the X values of the maximum M value and the intensity change correlate perfectly. The blue line in *Figure 4.3* (e) illustrates the intensity change that corresponds to the surface relaxation. The values are calculated by normalizing the change in intensity to the unrelaxed model structure: $(I_{unrelaxed} - I_{relaxed})/I_{unrelaxed}$. This highlights the fact that the change in intensity can be attributed solely to the lattice bending of the model structure.

Furthermore, the simulation study suggests that an increasing QW thickness w, and keeping the sample thickness t fixed, leads to a higher maximum displacement. Following the results of the study vertically – meaning a fixed QW width w and an increase in sample thickness t – leads to the observation that the magnitude of the displacements increases drastically. This also increases the range of the effect in the X-direction; compare *Figure 4.3* (c) and (i). This is important information when choosing reference regions in experimental images.

Especially when correlating the STEM intensity to the elemental composition of a sample, it is important to know the present effects on the intensity that originate from the sample geometry. The study demonstrates that if the displacement field extends significantly into the QW area, the shape of the intensity curve is altered accordingly. This can lead to a misinterpretation in terms of elemental composition and thus to changes in segregation curves, etc.

In the example of the model structure *GaP/GaAs/GaP*, the effect of the surface relaxation can be clearly visualized. The conclusions drawn from this study can be transferred to real TEM specimens with some additions. Any additional present SADs (e.g., that are introduced by substitutional atoms) in the material can superimpose the effect of lattice bending. The lattice distortion evoked by a substitutional atom, such as N in *GaAs*, can have values of approximately 9 *pm*, whereas the mean square displacement is in the range of 12 *pm.* Both lattice distortions lead to de-channeling of the electrons and shifting intensity from high to low detector collection angles. Furthermore, composition fluctuations in heterostructures will influence the lattice bending. The lattice bending will influence the HAADF intensity and thus the composition determination. This means that the problem must be solved self-consistently. Since the mean square displacement is directly connected to the intensity reduction in STEM images, computationally cheap FE simulations can support the process of correctly interpreting the intensity results. This summary represents a small fraction of the comprehensive study on surface relaxation presented in [99].

The application of knowledge gained through the study summarized above is presented in the publication "*Surface relaxation of strained Ga(P,As)/GaP heterostructures investigated by HAADF STEM*" [106]. Therefore, a *GaP/Ga(P,As)/GaP* heterostructure specimen was investigated via STEM and complementary multislice simulations were carried out, including the full relaxation process with FE simulation and VFF.

The experimental STEM image is depicted in *Figure 4.4* (a). The smaller figures (b) to (e) present detailed magnifications of the atomic columns in the barrier of the structure (b) and near the interface between the barrier and QW (d). An elongation of the atomic columns is visible, which is caused by the surface relaxation and the resulting lattice plane bending. Consequently, the intensity is not as distinct on the atomic columns, but blurred in the background of the image.
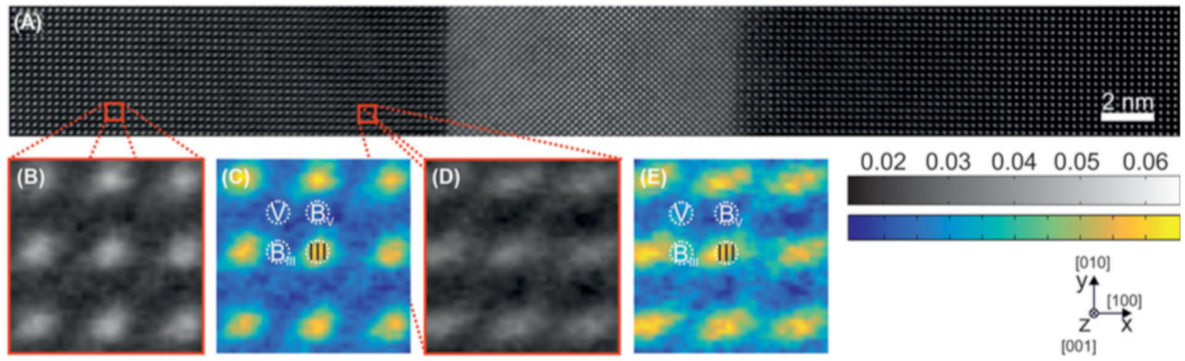
Figure 4.4: The figure presents an experimental high-resolution HAADF STEM image from a Ga(P,As) QW embedded in a GaP matrix (A). A magnified unit-cell at a relatively long distance from the interface is depicted in (B) and with different colors in (C). (D) and (E) depict a unit-cell that is relatively close to the QW region to illustrate the effect of the surface relaxation on the shape of the atomic columns. The atomic columns near to the interface exhibit elongation compared to the atomic columns that are distant to the interface. The image is reproduced from [106].

The QW consists of a *Ga(P,As)* compound with 65.9% *As*, determined by HRXRD. To model the effect of surface relaxation, a model structure was created that resembled the geometric dimensions of the experimental specimen, with a QW width of 12 *nm* and a sample thickness of 22 *nm*. The model structure was relaxed via FE simulations by applying the linear elastic theory and a VFF routine. Furthermore, the model structure was used as an input cell for the STEM HAADF simulation, adapting the experimental parameters obtained from the electron microscope used to acquire the image. *Figure 4.5* (a) presents a purely tetragonal relaxed image, in which the surface relaxation is suppressed by restricting the degrees of freedom in the FE simulation. *Figure 4.5* (b) depicts the fully surface relaxed cell. It should be noted that the experimental image in *Figure 4.5* (a) is plotted on the same intensity scale – representing the fraction of the impinging electron beam – as *Figure 4.5* (b), which means that there is not only a qualitative matching of the results but also a quantitative one.
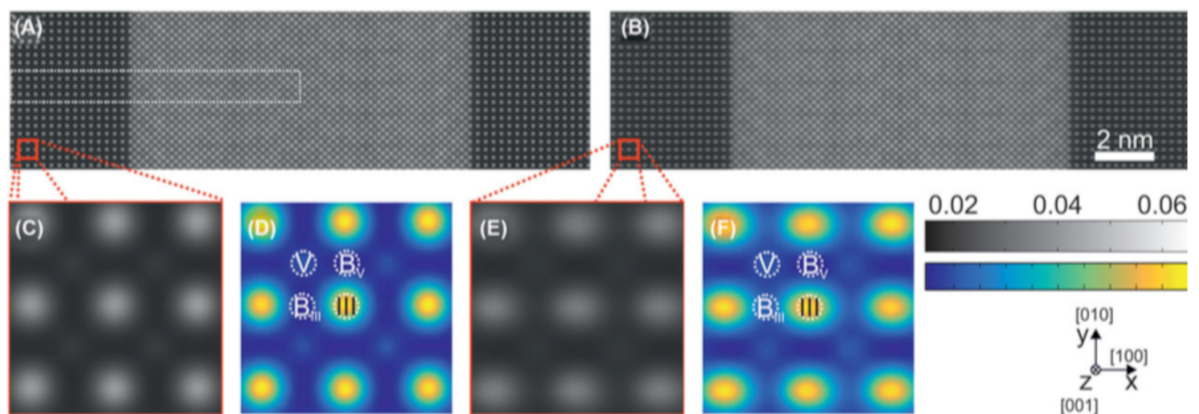

Figure 4.5: The figure presents HAADF images obtained from multislice simulations, in which the supercell is tetragonally distorted (A), and from a fully relaxed supercell (B). Enlarged regions from both images are depicted in (C) & (D) and (E) & (F) respectively. An elongation of the atomic columns is visible in the enlarged images (E) & (F), and resembles the effect of the surface relaxation on the shape of the atomic columns that was observed in the experimental image. The figure is reproduced from [106].

Figure 4.5 (c) illustrates a detailed section from the tetragonal relaxed cell, and displays perfectly round atomic columns. *Figure 4.5* (e), however, illustrates the same section from a surface relaxed cell, and displays elongated atomic columns. This is the same effect, originating from lattice plane bending, that was observed in the experimental image in *Figure 4.5* (a). This demonstrates that the FE simulation combined with the multislice simulation closely resembles the effect of surface relaxation. Comparing the experimental data presented in *Figure 4.4* to the simulated data from *Figure 4.5* yields a very good agreement.

For a quantitative analysis, intensity profiles across the QW are investigated, and are presented in *Figure 4.6* (a). Furthermore, the effect of the surface relaxation on the measurable lattice constant is determined and presented in *Figure 4.6* (b). In addition, the *As* concentration is calculated via STEM intensity or lattice constant by assuming a linear dependence, for simplicity.
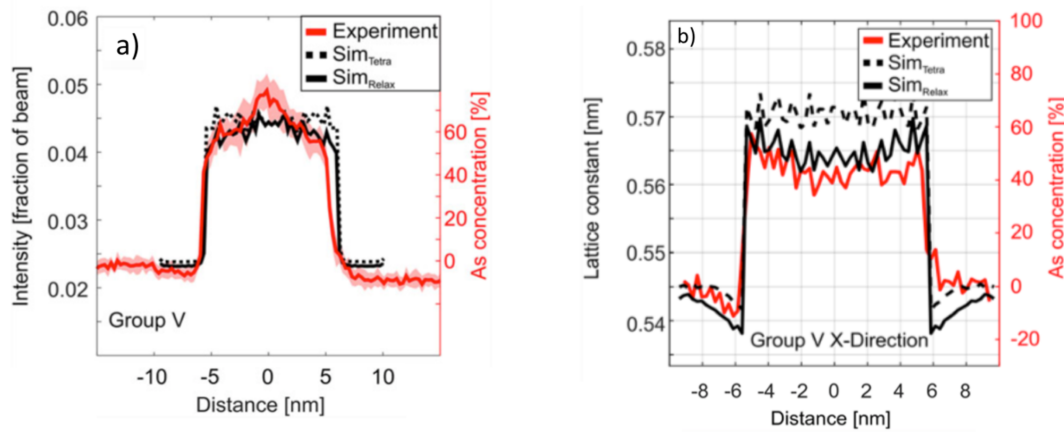

Figure 4.6: Subfigure (a) illustrates the intensity profile obtained from the experimental STEM image (red). Furthermore, the intensities gathered from the fully relaxed (solid black) and tetragonal relaxed (dotted black) simulations are plotted. The right y axis indicates the calculated As concentration, assuming a linear correlation between the intensity and the As content. Subfigure (b) illustrates the analysis of the lattice constant in the X-direction. Also in this subfigure, the solid red line represents the experimental lattice constants. Furthermore, the lattice constants obtained from the tetragonal distorted (dotted black) and fully relaxed (solid black) simulations are displayed. The As concentration is again calculated by assuming a linear correlation between the lattice constant and the As concentration. The figures are reproduced from [106].

Figure 4.6 (a) illustrates the intensity values obtained from the experimental image, and from the tetragonal relaxed and fully relaxed simulations. The profile for the tetragonal relaxed simulation nearly resembles a box profile. The right y axis indicates the *As* content, and a small variation around the desired value of 65.9% is noticeable. The profile derived from the surface relaxed simulation demonstrates a good agreement with the profile from the experimental image. They both exhibit an intensity gradient at the interface of the QW, which could possibly be misinterpreted as composition fluctuation. It is worth mentioning that some of these effects can be compensated using the PICS method [107]; however, this work focuses on the study of the relaxation effect.

The analysis of the lattice constant of the sample reveals a different side of the effect of surface relaxation. The lattice constant was determined by calculating the distance to the next neighbor of the

respective atomic column, and by averaging and dividing them into their respective X- and Y-components. The distances were calibrated using the (004) spots in the Fourier transformed image of the *GaP* barrier. Once again, the lattice constant of the tetragonal distorted cell displays a nearly box-like profile. The lattice constant profiles of the experiment and the fully surface relaxed simulation demonstrate a good agreement. The lattice constant exhibits a significant dip at the interface of the QW, and also in the middle of it. This is due to the lattice plane bending, and can again be misinterpreted as a change in composition. This would lead to a calculated *As* composition of around 40%, which differs significantly from the actual composition of 65.9%. The method of calculating the composition is inherently sensitive to the positions of lattice plane bending, which is why it was chosen to illustrate the greatest influence that the surface relaxation can possibly have.

Overall, the simulated results demonstrate a very good agreement with the experimental results. This strengthens the fact that the FE and VFF simulations that were conducted resemble the state of the experimental specimens very precisely. This increases the possibility to describe experimental specimens precisely via simulations, and helps in the estimation and differentiation between chemical changes and geometrical relaxation.

All of the results summarized here are presented in more detail in the publications appended to this work [99, 106].

4.3. Composition Determination

In the preceding paragraphs, important experimental influences were presented which must be accounted for in multislice simulations in order for them to resemble experimental STEM images correctly. Due to the consideration of chromatic aberration, source size, detector sensitivity, TDS, etc., it is possible to achieve excellent agreement between the experimental intensities and simulated ones. The ability to achieve perfect agreement between simulated and experimental samples, with a given composition, can be used to draw conclusions about samples with unknown compositions, with the assistance of simulated results. The general procedure is to compare the STEM intensities from the undefined samples to the simulated intensity of a reference set, applications of which can be found in the relevant literature [76, 79, 86].

In the following section, the used technique is outlined. However, the focus lies on the improvements that are made to the method, including the previously mentioned experimental influences. With all improvements implemented, a comprehensive simulation study is presented in order to provide an understanding of the theoretical capabilities of the extended technique presented here. A special focus is devoted to the potential of the method with regard to single-atom accuracy. The accuracy of the extended method is illustrated with three different technically important semiconductor samples. The results presented in this paragraph are summarized from the publications "*Composition determination*

of semiconductor alloys towards atomic accuracy by HAADF-STEM" [108] and "*Composition determination of multinary III/V semiconductors via STEM HAADF multislice simulations*" [109].

The following three samples were used as examples in this case: a *(Ga$_{80\%}$In$_{20\%}$)As* QW structure between *GaAs* barriers, which is referred to as sample I, a *Ga(P$_{40\%}$As$_{60\%}$)* QW structure between *GaP* barriers, which is referred to as sample II, and a strained *SiGe* multi-QW heterostructure that was grown via low-energy plasma-enhanced chemical vapor deposition (LEPECVD) on a Si (001) substrate [110], which is referred to as sample III.

For each sample, a complementary simulation set is generated that is in turn used to generate a relationship between STEM HAADF intensity and the number of substitute atoms. To achieve this, structure models are created with the dimensions of 5 x 5 unit-cells in X- and Y-directions and 80 unit-cells in the Z-direction, which denotes the electron beam direction. The lateral dimensions are chosen carefully to cover a large lateral range, in order to simultaneously improve the accuracy of statistics and limit the simulation effort. The thickness is in the range of conventional prepared STEM samples. The ternary alloys are generated by randomly replacing atoms in the base matrix (e.g. *GaAs* for sample I) with the substitute atom (*In* for sample I). The compositions of the structure models are varied between 0% and 100% of the substitute atom in steps of 5%. The corresponding lattice constants for the resulting compounds are calculated by Vergard's law [111, 112], using the binary lattice constants of the underlying materials (*GaAs* and *InAs* for sample I). The final atom positions are calculated by taking SADs into account, since they can have a significant influence on the STEM intensity, as already indicated in chapter 2.4.

All multislice simulations are carried out with STEMsalabim, as already introduced in section 4.1. Every supercell is calculated with seven defocus values and ten individual phonon configurations. Thus, one simulation set contains 1,400 individual multislice simulations. For the analysis, the source distribution and detector sensitivity are taken into account.

The Voronoi intensity [19, 113] obtained from the simulated STEM HAADF images is correlated with the number of substitute atoms in the model structure for every atomic column. Since simulated results are processed, the exact number of substitute atoms present in every atomic column is given by design. Each simulation, viewed in [010] projection, has 100 atomic columns, from which 81 are chosen for the analysis. The outermost atomic columns are neglected to prevent artifacts due to non-closed Voronoi cells. *Figure 4.7* (a) to (c) depict the resulting correlations between Voronoi intensity and number of substitute atoms for the three sample material systems (*(Ga$_{1-x}$In$_x$)As* , *Ga(P$_x$As$_{1-x}$)* and *Si$_{1-x}$Ge$_x$*). The data is gathered from every simulation present in a simulation set. The blue dots in *Figure 4.7* (a) to (c) represent the raw intensity data plotted versus the number of substitute atoms obtained from the simulations. All of the illustrated correlation functions are evaluated exemplarily for a chosen thickness of 15 *nm*. The red dots indicate the mean Voronoi intensity for a fixed number of substitute atoms. The

"error bars" mark the maximum overlap of the standard deviations for different numbers of substitute atoms. In other words, if the maximum of the standard deviation of one specific number overlaps with the minimum of the next higher number, the uncertainty is one atom. This is also an indication of the highest precision that is possible for this material system to achieve at a certain thickness, with the chosen detector inner angles.
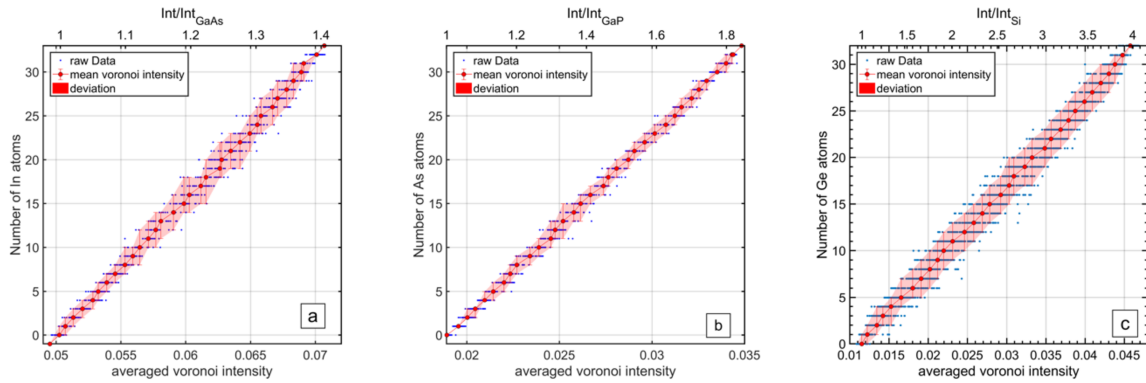

Figure 4.7: The figure presents the intensity composition relationships for all corresponding samples, I – III. The blue dots mark the averaged Voronoi intensity of every atomic column of each concentration set. The red markers illustrate the mean intensity for every atom count, and the error bars mark the overlap of the standard deviations, which is the maximum precision achievable. The second x-axis indicates the intensity normalized to the barrier material. With this, a quantitative comparison between all samples is possible. All figures are calculated for a total thickness of 32 atoms. The image is reproduced from [108].

It is noticeable that every material system displays a nearly linear correlation with a positive slope between Voronoi intensity and the number of substitute atoms. This is due to the fact that a lighter element is always substituted with a heavier one in these three examples, and thus the mean atomic number Z of the atomic column is increased.

When applying such a method, it is always crucial to determine its accuracy and limitations. For this, a simulation study is conducted to check the accuracy of the composition determination. An artificial *(Ga,In)As* sample with an *In* concentration of 20% is used as input to check the accuracy of the algorithm. To improve the accuracy of statistics, ten uniquely random element configurations are generated and used as input. The artificial input samples are treated as samples with unknown composition, and the composition of every atomic column from the artificial samples is determined. Since the input is artificial, the number of substitute atoms on every column is known exactly. With this, the difference between the calculated result from the algorithm and the real number of substitute atoms can be determined. If the calculated number of substitute atoms matches the real number, the atomic column is considered to be correct. By this method, a percentage of correct atomic columns can be determined and further analyzed as a function of sample thickness *t*.
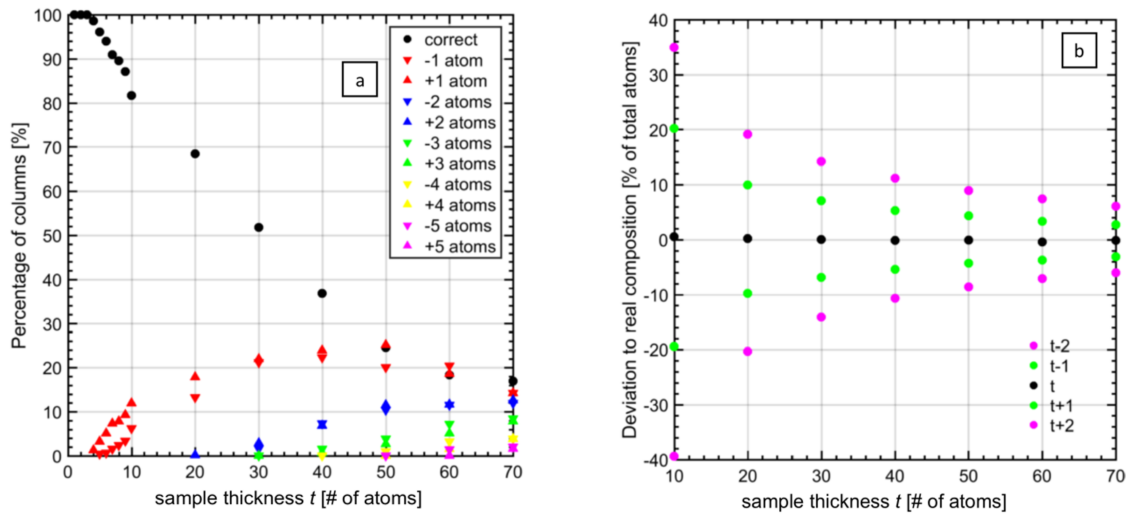
Figure 4.8: Subfigure (a) illustrates the percentage of atomic columns in which the composition was determined to be correct (black dots) or incorrect by 1-5 atoms (colored triangles), versus the sample thickness t. The analysis was conducted for an artificial input (Ga,In)As sample with 20% In. Subfigure (b) illustrates the deviation of the calculated composition to the real composition versus the sample thickness t. It also illustrates the influence of the assumed sample thickness on the deviation. If the sample thickness is assumed to be correct, the deviation from the real composition is very small; in the range of 0.4%. Even with a sample thickness that is incorrect by one (green) or two atoms (magenta), the deviation is centered symmetrically around zero. This image is reproduced from [108].

Figure 4.8 (a) illustrates the percentage of correctly determined atomic columns from a sample set of 810 examined atomic columns. Moreover, a deviation of up to five atoms between the calculated substitute atoms and the real number of substitute atoms was extracted, and is visualized by the colored triangles depicted in *Figure 4.8* (a). The percentage of correctly determined atomic columns (black dots) starts at 100% at a sample thickness of one atom, and remains constant up to a sample thickness of three atoms. At a higher sample thickness, the deviation of one atom increases. An additional deviation of two atoms arises a sample thickness of 30 atoms. All higher atom deviations increase according to the sample thickness. It is noticeable that the deviation in a positive and negative direction originates symmetrically from the statistical nature of the deviation. The analysis demonstrates that it is not possible to determine the number of substitute atoms correctly if the sample is thicker than three atoms. Nevertheless, the negative and positive deviations of the calculated number of substitute atoms are symmetrically distributed. This means that the mean number of determined substitute atoms is always correct. This is visualized in *Figure 4.8* (b), in which the deviation of the calculated sample composition from the real sample composition is plotted versus the sample thickness. The black dots represent the deviation from the real composition (20% *In*), assuming the correct sample thickness for every investigated atomic column. It can be noted that there is only a very small deviation from the real composition over the total range of investigated sample thicknesses. The maximal deviation is 0.5% at a sample thickness of ten atoms, which results in either a 20.5% or 19.5% determined Indium content.

Although the number of substitute atoms determined for the individual atomic columns may vary by a few atoms, the mean composition is still highly accurate.

So far, all of the analyses assume that the sample thickness is determined correctly. A falsely determined assumed thickness changes the relationship between the intensity and substitute atoms drastically. *Figure 4.8* (b) illustrates the results of a study that focused on the deviation of assumed sample thickness. The green triangles represent the deviation from the real composition with one atom difference in assumed sample thickness. This raises the error to ± 20% at a sample thickness of ten atoms. With two atoms, the deviation rises to ± 35% deviation from the real composition. The values decrease with increasing sample thickness t. The most important fact that can be deduced from this investigation is that the deviation is symmetrically distributed around zero. This means that although the deviation from the real composition is not zero, the positive and negative composition fluctuations are likely to cancel out when over- or underestimating the thickness in experimental images, due to statistics. Only a systematic over- or underestimation of the actual thickness will lead to significant deviations.

With the capabilities and limitations of the extended method in mind, three applications of three technologically important semiconductor samples are presented in two different ways. Color-coded maps visualize the calculated number of the substitute atoms in a 2D map in *Figure 4.9*. This view demonstrates the high lateral resolution of the method while also revealing local composition fluctuations in the sample. This is helpful to determine whether the homogeneity of the QW is as desired. *Figure 4.9* (a) to (c) present the 2D composition maps of the three samples. For a detailed discussion of the individual composition distribution, please refer to the paper appended to this work [108].
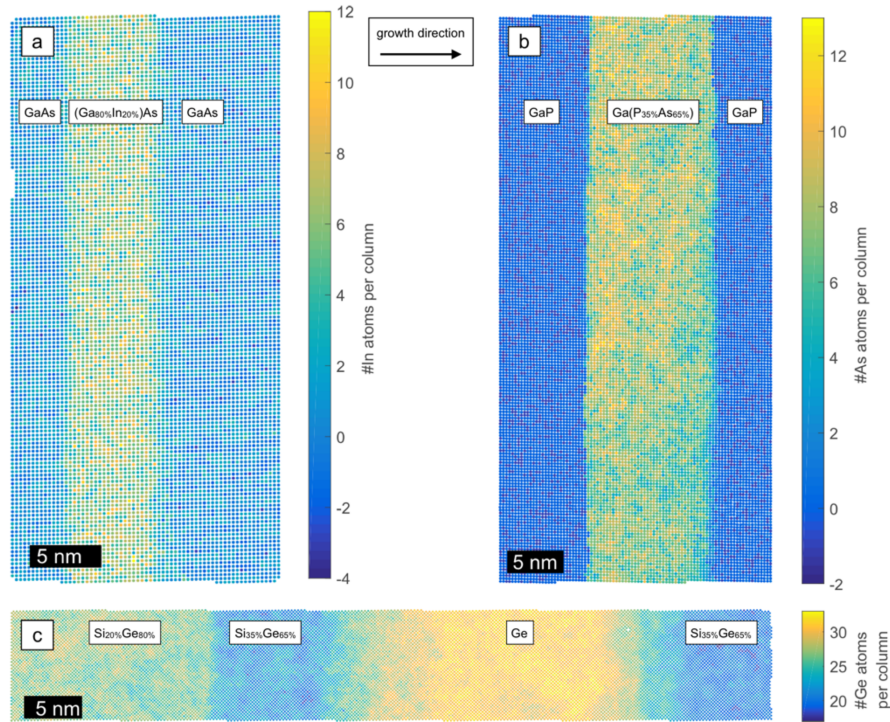
Figure 4.9: Composition maps of all three samples. The number of substitute atoms per atomic column is given for (a) the group III sublattice of sample I, (b) the group V sublattice of sample II, and for (c) sample III. Note that the thickness of each atomic column differs and is in the range of 25-31 atoms for sample I, 8-18 atoms for sample II and 29-34 atoms for sample III. This was taken into account for composition determination. This image is reproduced from [108]*.*

The well-established HRXRD method is a macroscopic technique to determine the mean composition over a relatively large area. Therefore, the results of these two methods are not directly comparable. One way to compare the accuracy of the presented extended method to that of HRXRD is with a line-scan of the composition parallel to the growth direction from left to right. For this, all compositions from the 2D composition maps, depicted in *Figure 4.9*, are averaged perpendicular to the growth direction to obtain a line profile. This inherently eliminates the characteristics of the lateral resolution but makes it possible to compare it to the results from HRXRD. *Figure 4.10* (a) to (c) illustrate the line profiles of the different methods for the three experimental samples. The solid red line depicts the composition line-scan obtained from the STEM intensities. The shaded red area illustrates the deviation of the composition perpendicular to the growth direction. The solid black line depicts the schematic line-scan deduced from the HRXRD values, or from the desired concentration in the case of sample III (*Figure 4.10* [c]). The blue line illustrates the results obtained from the lattice constant analysis using the experimental STEM images. Local lattice constants can be calculated from the positions of the atomic columns. These can then be converted into compositions by assuming a linear correlation. More details of this method can be found in [114] and [108].
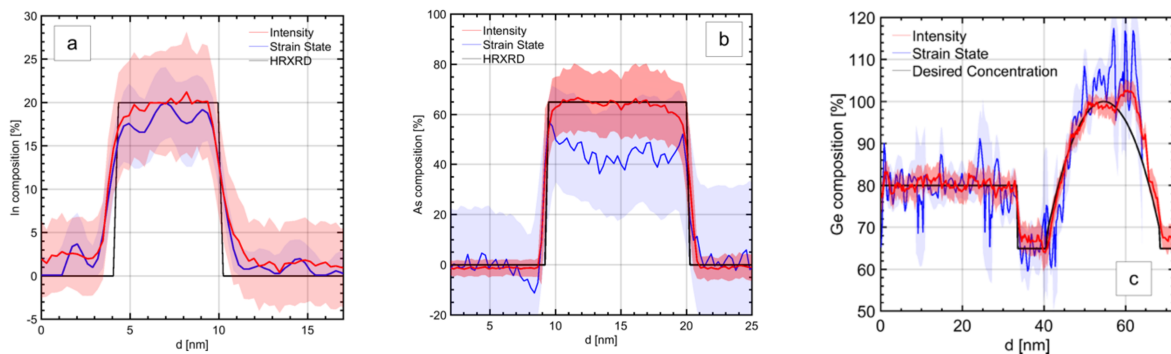
Figure 4.10: The figures present line scans of the calculated compositions from the three investigated samples; (a) (Ga,In)As, (b) Ga(P,As) and (c) SiGe. The solid red line represents the composition across the QWs that were obtained from the intensity method. The blue line represents the composition profile, calculated from the local lattice constants combined with linear interpolation. The black line represents the results from the HRXRD measurements and serve as a reference. The images are reproduced from [108].

The intensity method demonstrates a good agreement with the composition profiles deduced from HRXRD. The deviation perpendicular to the growth direction is not negligible, which underlines the fact that the composition is not completely homogenously distributed within in the area of the QW. The composition obtained from the lattice constant analysis demonstrates a deviation in composition that can be attributed to elastic surface relaxation. For a detailed discussion of this effect, please refer to the paper, "*Surface relaxation of strained Ga(P,As)/GaP heterostructures investigated by HAADF STEM*" [100], which is appended to this work.

The extended composition determination method was also used to determine composition profiles of *(Ga,In)As/Ga(As,Sb)/(Ga,In)As* "W"-type QW heterostructures to investigate the surface segregation and interaction of *In* and *Sb*. The results of this work are summarized in the work of P. Kükelhan, in "*Segregation at interfaces in "W"-type quantum well heterostructures explored by atomic resolution STEM*"[115].

The analysis and application of the extended intensity method demonstrates that it is a valuable technique to determine unknown compositions from STEM HAADF experimental images. The composition line profiles, depicted in *Figure 4.10*, that are obtained from the extended intensity method demonstrate a good agreement with the well-established HRXRD technique. The lateral resolution, however, is as precise as one atomic column. In addition, the determination of the number of substitute atoms toward single-atom accuracy is an improvement on other techniques. The technique correlates compositional with geometrical information about the investigated sample in only one STEM HAADF image. It is important to consider the accuracy and limitations of this method when using it. The simulation study illustrates that a perfect determination of substitute atoms is only possible for very thin samples. In the presented case for $(Ga_{80\%}In_{20\%})As$, it was only possible up to a sample thickness of three atoms. This is solely due to the statistical fluctuations of the STEM intensity that originate from

different height distributions of the substitute atoms, and inherently limits the resolution of this technique.

Furthermore, the method is not only suitable for ternary/binary semiconductor samples, but can also be expanded to multinary semiconductor samples. In the appended paper, "*Composition determination of multinary III/V semiconductors via STEM HAADF multislice simulations*", the basis of the method is extended and is presented in the example of *Ga*(*N,As,P*). This challenging material system inherits a mixture of substitute atoms on one sublattice and a large effect of SADs evoked by the incorporation of nitrogen.

The expansion of the method involves combining STEM images from multiple detector regions. The angular intensity distribution of the elements in *Ga*(*N,As,P*) is not identical. Since nitrogen evokes localized lattice distortions, the scattering mechanism of the material system is altered. As already indicated in chapter 2.4, lattice distortion obstructs the channeling effect of the electrons. This results in an increased intensity in lower angular regions when working with materials that contain *N*. Thus, the intensity from lower angular regions allows a conclusion to be drawn about the *N*-content. The high angular region is mostly unaffected, since *N* is a light element compared to *As*, and the scattered intensity in high angles is comparatively low. Thus, the angular regions are differently sensitive to different elements. *Figure 4.11* (a) illustrates the simulated STEM intensity of *GaAs* and $Ga(N_{15\%}As_{85\%})$ versus the detector inner angle. The *Ga(N,As)* material system exhibits a significantly increased intensity in the lower angular regions up to ~50 mrad. The study in the appended publication [116] used this characteristic feature and combined three different angular regions to present a benchmark of three different *Ga(N,As,P)* concentrations. The basis of the adaption to multinary material systems is to identify the cumulative best fit between experimental intensities and simulated intensities to all angular regions. This ensures that the effects of all substitute elements are taken into account. The global minimum between the simulations and the input then determines the concentration of the material. *Figure 4.11* (b) presents the resulting deviation map of a *Ga(N,As,P)* input with 15% *N* and 20% *P*. The two axes represent the *P* and *N* content accordingly. The color illustrates the normalized total deviation of all angular regions combined. A global minimum is visible in the deviation map, which indicates the most probable concentration. This adaption to multinary material systems, and especially to materials that contain *N*, combines the knowledge of angular resolved STEM presented by K. Müller-Caspary [34] and the extended intensity method summarized in [109] and [108].
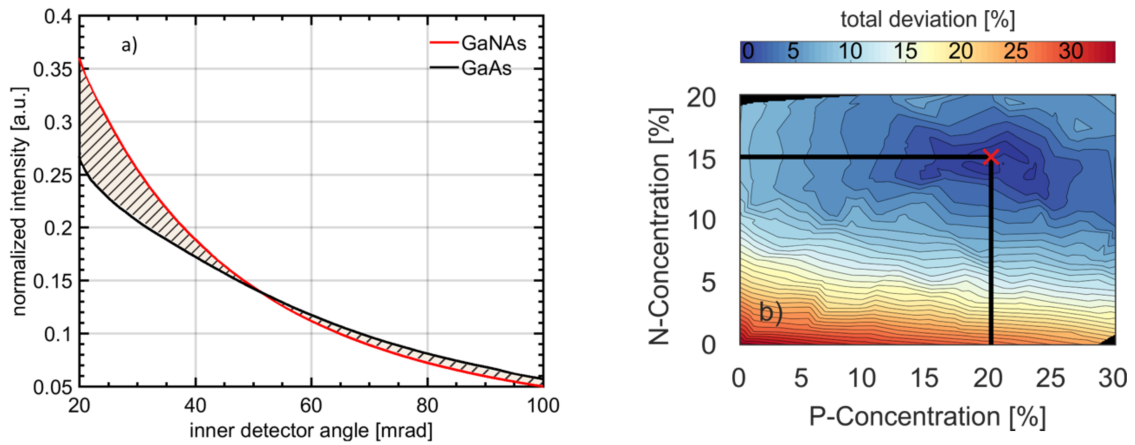
Figure 4.11: Subfigure (a) presents the normalized STEM intensities of Ga(N,As) with 15% N and GaAs versus the inner detector angle. The intensity of Ga(N,As) is higher in lower angular regions compared to pure GaAs. This effect is caused by SADs and can be used to gather information about the N-content from lower angular regions. Subfigure (b) illustrates the deviation results obtained from three different angular regions of a Ga(N,As,P) sample that contains 15% N and 20% P. The minimum in the map indicates the most probable fit between input intensities and the reference simulation set. Image (b) is reproduced from [116].

Furthermore, Kükelhan, et al. recently published a study [117] with a more advanced method to determine the composition of quaternary III/V bismuth-containing semiconductors; they use the cross-scattering between the two group III and group V sublattices of *(Ga,In)(As,Bi)* on *GaAs*, and *(Ga,In)(As,Bi)* on *InP*.

5. Summary and Outlook

The successful and continuous improvement of modern semiconductor devices depends significantly on the ability to observe and describe the material properties as precisely as possible, in order for that understanding to serve as a basis for new developments. Complex semiconductor devices, such as multijunction solar cells [2] and laser devices [3, 4], consist of multilayer structures and a combination of multinary material systems. Not only are the geometrical parameters of the system important to characterize, but the chemical composition also plays a crucial role in the functionality of the device. The STEM offers an effective combination of lateral resolution, i.e., sub-angstrom, and quantitative methods to gain insight into the material. Complementary simulations are essential to gain quantitative information from the investigated sample structure.

In the course of this thesis, a workflow was developed to precisely model a real-world electron microscope sample. This included accounting for the most important experimental influences on efficient multislice simulations.

An implementation of Kirkland's commonly-used multislice algorithm was realized in the STEMsalabim software package [98] and explained in chapter 4.1. The software was specifically adapted and optimized for HPC clusters with a multi-CPU architecture. This enables the user to simulate samples with large lateral dimensions and perform important parameter sweeps within a reasonable timeframe. The mixture of different semiconductor material systems in multilayer structures can induce stress at the interfaces where the magnitude is connected to the lattice mismatch of the two compounds. With very thin TEM samples, the stress is relaxed via elastic surface relaxation. The surface of the samples deforms elastically and the atomic lattice planes from the material bend from their resting positions. The resulting bent lattice planes provoke the electrons to de-channel, influencing the collected STEM ADF intensity. The effect itself, in addition to its influence on the STEM HAADF, is presented and explained in chapter 4.2. The simulation study modeled sample structures of *GaP/GaAs/GaP* with varied geometrical parameters and relaxed the structures by a FE algorithm. Multislice simulations were then performed with the relaxed supercells as input. It could be demonstrated that the mean square displacement of the atomic lattice planes is directly connected to the STEM ADF intensity. This enables computationally demanding multislice simulations to be exchanged with cheap FE simulations to still obtain an effective overview of the effect of surface relaxation. The simulation method was then adapted and applied to an experimental sample of *GaP/Ga(As,P)/GaP*. The simulated structure quantitatively matched with the experimental findings. This emphasizes the quality and precision of the FE simulations.

With the knowledge that the intensity of multislice simulations demonstrates a very good agreement with experimental intensities, a known method for composition determination was extended to achieve

high lateral resolution and single-atom accuracy. The basis was to compare the experimental intensities to a simulated composition set, and determine the best match. The accuracy of the method was investigated in detail, and it was determined that a perfect agreement can only be achieved with very thin TEM samples. This is due to the way in which the intensities from materials with substitute elements are created. The statistical distribution of substitute atoms in the material leads to a spread in intensities for a given composition, due to the different possible Z-height configurations for this atomic column [118]. Since the simulation set inherits the statistical nature of the height distribution of the substitute atoms by design, the effect on the STEM intensity is taken into account. The simulation study demonstrated that on average, the statistical composition errors eventually cancel out, and thus the mean error of composition is symmetrically distributed around zero. Furthermore, the application of the method to three technologically important samples, namely *(Ga,In)As*, *Ga(P,As)* and *SiGe*, demonstrated a very good agreement with the widely-used HRXRD technology. The extended intensity method also provided a greatly improved 2D resolution of one atomic column.

Furthermore, it is also possible to apply the extended method to determine unknown semiconductor compositions via STEM intensity in multinary semiconductors. This was illustrated with a *Ga(N,As,P)* model system in [109], and with *(Ga,In)(As,Bi)/GaAs* and *(Ga,In)(As,Bi)/InP* in [119]. The enhanced method makes use of the increased STEM intensity, in lower angular regions, generated by the lattice distortion due to *N* atoms in the lattice. This allows conclusions to be drawn about the *N*-content of the material. The higher angle intensity is mainly sensitive to the *As* content, and hence the individual chemical compositions can be determined individually.

In summary, a comprehensive workflow has been developed and presented that includes experimental influences such as elastic surface relaxation, a finite source size and amorphous materials. All of this combined makes it possible to quantitatively investigate experimental STEM images via multislice simulations. An advantage of this technique is that no additional methods need to be used, and only STEM HAADF images and simulations are necessary.

Some general improvements for future work are discussed in the following paragraphs. Firstly, the simulation of amorphous materials could be prevented if the residual amorphous materials on the experimental samples could be decreased significantly. This would drastically improve the general quality of the experimental images [120].

The speed of the calculations within the STEMsalabim software package could be improved by adapting the code to run on graphical processing units (GPU). A GPU is optimized for graphics problems, and consists of thousands of smaller efficient cores that are designed to handle multiple tasks simultaneously. The very large number of Fourier transformations that occur during a multislice simulation could be conducted on GPUs [96].

Simulated STEM intensities exhibit a significant discrepancy in low angular regions in relation to experimental data [121], and there are some indications that this may be due to inelastic scattering events [34]. Currently, only elastic scattering events are taken into account by STEMsalabim. Techniques that take the inelastic effects into account have already been presented [88, 120], and could improve the quality of the simulations with regard to angular intensity distribution.

A further improvement would be the use of a pixelated detector that records the complete angular intensity distribution of every scan point, rather than the cumulative incoherent sum. If the angular intensity distribution could be present for every scan point of the experimental data, improved fitting methods could be applied to each pixel. This would increase the precision of simulation-based fitting methods greatly [121-123].

The statistical distribution of substitute atoms in the multislice simulations leads to a spread in intensities for a given composition of an atom, due to the different possible Z-height configurations for this atomic column. Therefore, a mean intensity value was assigned, along with an associated width of the intensity distribution. The width of this intensity distribution determined the minimum uncertainty associated with any composition determination, and is primarily influenced by atomic column thickness, due to the increasing number of possible atomic configurations. Every method that relies on comparing simulated intensities to experimental images is sensitive to the assumed or calculated sample thickness. Especially when the goal is to achieve single-atom accuracy, a falsely assumed sample thickness can have a significant effect. With the use of a pixelated detector, position averaged convergent beam electron diffraction (PACBED) patterns could be evaluated, and PACBEDs could be easily recorded at every scan position, thus creating a very precise thickness map of the sample [126].

6. Publications of this Work

Composition determination of semiconductor alloys towards atomic accuracy by HAADF-STEM

L. Duschek , P. Kükelhan , A. Beyer, S. Firoozabadi, J.O. Oelerich, C. Fuchs, W. Stolz, A. Ballabio, G. Isella, K. Volz

Abstract

This paper presents a comprehensive investigation of an extended method to determine composition of materials by scanning transmission electron microscopy (STEM) high angle annular dark-field (HAADF) images and using complementary multislice simulations. The main point is to understand the theoretical capabilities of the algorithm and address the intrinsic limitations of using STEM HAADF intensities for composition determination. A special focus is the potential of the method regarding single-atom accuracy. All-important experimental parameters are included into the multislice simulations to ensure the best possible fit between simulation and experiment. To demonstrate the capabilities of the extended method, results for three different technical important semiconductor samples are presented. Overall the method shows a high lateral resolution combined with a high accuracy towards single-atom accuracy.

The authors' contributions:

My contribution to this publication was the development and implementation of the algorithm used to determine the concentration of the experimental STEM images. Furthermore I wrote the software to supervise and initiate the multislice simulations used for this work. The experimental STEM images used in this publication were recorded by P. Kükelhan, A. Beyer, S. Firoozabadi. The Si/Ge samples were grown and provided by A. Ballabio and G. Isella. A. Beyer, K. Volz and P. Kükelhan helped interpreting the data. All co-authors helped to improve the manuscript that was written by P. Kükelhan and myself.
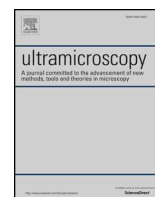
Composition determination of semiconductor alloys towards atomic accuracy by HAADF-STEM

L. Duschek[a], P. Kükelhan[a], A. Beyer[a],[*], S. Firoozabadi[a], J.O. Oelerich[a], C. Fuchs[a], W. Stolz[a], A. Ballabio[b], G. Isella[b], K. Volz[a]

[a] Materials Science Center and Faculty of Physics, Philipps-Universität Marburg, Hans-Meerweinstraße 6, Marburg, Germany
[b] L-NESS, Dipartimento di Fisica, Politecnico di Milano Polo di Como via Anzani, 42 22100 Como Italy

A B S T R A C T

This paper presents a comprehensive investigation of an extended method to determine composition of materials by scanning transmission electron microscopy (STEM) high angle annular darkfield (HAADF) images and using complementary multislice simulations. The main point is to understand the theoretical capabilities of the algorithm and address the intrinsic limitations of using STEM HAADF intensities for composition determination. A special focus is the potential of the method regarding single-atom accuracy. All-important experimental parameters are included into the multislice simulations to ensure the best possible fit between simulation and experiment. To demonstrate the capabilities of the extended method, results for three different technical important semiconductor samples are presented. Overall the method shows a high lateral resolution combined with a high accuracy towards single-atom accuracy.

1. Introduction

In the last two decades, scanning transmission electron microscopy (STEM) developed into a very important characterization tool for atomic analysis of crystalline specimens [1,2]. Using high angle annular dark field (HAADF) detectors, this technique can provide directly interpretable atomic resolution images where the measured intensity is highly sensitive to the type and the number of atoms [3–5]. Since the electron-matter interaction as well as the image formation process have been understood in detail, it is nowadays possible to reproduce experimental images via numeric simulations [6]. Through the combination of experimental aberration corrected STEM HAADF images and complementary multislice simulations it is possible to extract important information about the sample such as the thickness, chemical composition or strain fields [7–10]. Since semiconductor devices such as lasers or transistors become constantly smaller, there is an increasing need for the local arrangements of atoms on an atomic scale. To gain such quantitative insights from crystalline structures, a lot of work has been performed to make electron microscopy a quantitative method [6]. Combining all knowledge of the past years of research, several methods have been proposed to gain quantitative information from crystalline samples [11–13]. Van Aert and coworkers have published significant work in the field of statistical model-based quantitative

characterization of a $La_{0.7}Sr_{0.3}MnO_3$-$SrTiO_3$ interface [14–17]. Also Grieb et al. demonstrated quantitative composition determination for the samples of Ga(N,As) [18,19] and (Ga,In)(N,As) [10,20,21], using the averaged intensities from STEM multislice simulations and comparing them to experimental images.

This work focuses on the composition determination of ternary III/V and binary group IV semiconductor alloys with atomic precision. The technique to compare experimental intensities with simulated intensities known from literature [10,18,21,22] is extended in this work. All influencing experimental parameters are included and a detailed analysis of the used simulated supercells opens up the possibility to push the precision to single-atom accuracy. This is shown using a detailed simulation study. The evaluation scheme is applied to experimental images of technologically relevant semiconductor samples. The experimental samples are the following: $(Ga_{1-x}In_x)As$ quantum wells (QW) are investigated, potentially being part of a 'W'-type or a multi QW heterostructure used in an infrared laser device [23]. Furthermore a $Ga(P_{1-x}As_x)$ QW structure is analyzed that might be used as a barrier in several different laser designs. Additionally a $Si_{1-x}Ge_x$ QW heterostructure is investigated, where the Ge fraction x is varied in the attempt of obtaining a parabolic confining potential [24]. Especially in devices as lasers, transistors, solar cells and photodetectors a detailed knowledge of the element´s local distribution is a key factor in the

---

* Corresponding author.
  E-mail addresses: lennart.duschek@physik.uni-marburg.de (L. Duschek), andreas.beyer@physik.uni-marburg.de (A. Beyer).

optimization process. This work shows, how to determine the exact composition of atomic columns in a ternary/binary alloy with the detailed analysis of STEM HAADF multislice simulations, using the STEMsalabim package [25].

Following this introduction, the samples used as well as the experimental equipment used is explained in detail in Section 2. Furthermore, the complementary simulations used to evaluate the data will be outlined. In Section 3, the method itself is described and explained in detail followed by plots of the resulting intensity composition relationships. A detailed analysis of the limitations with regards to single atom accuracy is the focus of the next paragraph.

Section 4 starts with the description of the raw experimental data. The determination of the local thicknesses is described afterwards, as it is different for every sample used and has an important role in the quantitative analysis. The results are presented in color coded 2D composition maps of the investigated samples that have a lateral resolution of one atomic column. Furthermore line scans in growth direction are presented and compared to well established methods for composition determination such as high resolution X-ray diffraction (HRXRD) and lattice constant analysis. For the latter technique, the lattice constant is derived from the experimental images and combined with Vegard's law and tetragonal distortion due to pseudomorphic growth to determine the composition.

At the end, a discussion points out the potential of single-atom accuracy of the method and the role of experimental influences is assessed.

2. Methods and experiment

The investigated samples include a $(Ga_{1-x}In_x)As$ quantum well (QW) structure between GaAs barriers, which will be referred to as sample I, as well as a $Ga(P_xAs_{1-x})$ quantum well structure between GaP barriers, which will be referred to as sample II. Both of these samples were grown for TEM investigations via metalorganic vapor phase epitaxy (MOVPE) using an AIXTRON AIX 200 GFR reactor (Gas Foil Rotation) (Aixtron SE, Herzogenrath, Germany). Sample I was grown on an exactly oriented, semi-insulating GaAs (001) substrate at a growth temperature of 550 °C [23]. The (Ga,In)As QW structure is 6.1 nm wide with an In concentration of 20%, derived from HRXRD.

Sample II was grown on an exactly oriented, semi-insulating GaP (001) substrate at a growth temperature of 550 °C. The Ga(P,As) QW layer has a width of 11.7 nm and the As content is about 65.5% which was determined by HRXRD [26].

Sample III is a strained SiGe multi-quantum well heterostructure, which was grown via low-energy plasma-enhanced chemical vapor deposition (LEPECVD) on a Si (001) substrate [27]. The buffer layer on which the QW structures are grown, consists of a 2 μm thick $Si_{0.2}Ge_{0.8}$ layer on top of a 11 μm linearly graded buffer [28]. 15 QW layers with a width of 30 nm are grown with a Ge concentration graded between 65% and 100% in a parabolic manner. In this work, only the first QW of the sample is investigated.

All samples were conventionally prepared for cross-sectional TEM investigations in [010] direction. Mechanical grinding and polishing was carried out for all samples utilizing an Allied MULTIPREP system (Allied High Tech Products, Inc., Rancho Dominguez, CA, United States). The final thinning and polishing was done by Ar-ion milling with a precision ion polishing system (model 691 Gatan, Inc., Pleasanton, CA, United States) until electron transparency was achieved. The acceleration voltage of the Ar-ions was progressively reduced from 5 kV to 1.2 kV to limit the amorphous surface layers and damage of the thin specimen. The inclination angle of the ion beam used was 6° resulting in a wedge shape of the TEM samples, which can be seen as a thickness gradient in the STEM images. All samples were treated in a plasma cleaner (model 1020 E. A. Fischione Instruments, Inc., Export, PA, United States) before inserting them into the microscope.

All HAADF measurements shown here were carried out in a double C_s-corrected JEOL JEM 2200FS (JEOL Ltd., Tokyo, Japan) operating at 200 kV acceleration voltage. The annular dark-field detector used (JEOL EM-24590YPDFI) detected electrons scattered to an annular range that was determined for each image using the method proposed by LeBeau and Stemmer [29] namely measuring the physical shadow of the detector on a CCD camera to determine the inner detector angle. For sample I the detector ranges were 63–252 mrad, for sample II 74–174 mrad and for sample III 68–272 mrad. A condenser aperture with a size of 40 μm diameter was used, which led to a semi-convergence angle of 21 mrad of the probe. To improve the signal-to-noise-ratio and to reduce the effect of sample drift on the image, each STEM image is the average of multiple images with a short dwell time (3 μs). The images have been aligned with the Smart Align software [30]. Furthermore the image intensity was normalized to the intensity of the impinging beam applying the approach described in [31]. The peak positions of the atomic columns were found by the 2D peak finding program PeakPairs [12].

2.1. Complementary STEM HAADF simulations

To gain quantitative information from the STEM HAADF images, complementary contrast simulations are necessary. All steps described in the next paragraph are equivalent for the samples introduced above. Structure models were created with dimensions of 5×5 unit cells in X- and Y- direction and with 80 unit cells in Z-direction (electron beam direction). The ternary/binary alloys were generated by randomly replacing atoms in the base matrix (e.g. GaAs for sample I) with the substitute atom (e.g. In for sample I). The lattice constant for the corresponding resulting compound material was calculated by Vegards law [32,33]. The composition of the cells was chosen between 0% and 100% in steps of 5% for all three samples. The atom positions for sample I & II were relaxed via a force field, using a Keating potential as described by Rubel et al. [34,35]. This has been done to acknowledge the static atomic displacements (SADs), caused by the different atom sizes and electronegativity [36]. It has already been shown in literature that SADs have a significant influence on the HAADF intensities in STEM [8]. Sample III has not been relaxed in the same way because the differences in covalent radii and electronegativities between Si and Ge are minor compared to the other two systems investigated.

Then these cells were used as input for the simulation software, called STEMsalabim [25], that was used for this investigation. This software package is designed for highly parallelized simulations on high-performance computer clusters and implements the multislice algorithm presented by Kirkland in [37,38]. A more detailed description on the technical implementation and scaling of the code can be found in [25]. Thermal diffuse scattering (TDS) was taken into account using the frozen lattice approach [39], where the atomic positions get displaced statistically (Gaussian distribution) from their resting positions. To include chromatic aberration, a defocus series of 7 defocus values was calculated for every individual simulation cell as described in [40–43]. For each defocus value, 10 phonon configurations were simulated, resulting in 70 individual phonon configurations for one simulation cell. In addition, the detector sensitivity was determined and applied to all simulations as proposed by LeBeau et al. in [44]. The finite source size as well as beam broadening by amorphous layers were included by convoluting a two dimensional Lorentzian distribution to the simulation of the form:

$$S_L = \frac{\sigma}{(x^2 + y^2 + \sigma^2)^{3/2}},$$

where x and y are the spatial coordinates and σ describes the width of the distribution. This step is crucial to match simulation intensities as closely as possible to the experimental images as described in [40]. A detailed explanation on the choice of the width parameter sigma of the Lorentzian function will be given in a later chapter. All simulation

Table 1

Experimental parameters of the used electron microscope. All the parameters were used for the complementary multislice simulations.

Electron beam energy	200 kV
Aperture angle	21 mrad
C_s	2 µm
C_5	5 mm
C_C	1.5 mm
ΔE	0.42 eV

parameters were carefully chosen to fit the experimental setup and are summarized in Table 1.

3. Results

This chapter presents the steps necessary to determine the composition of the investigated samples using HAADF-STEM images and complementary multislice simulations. First, the method itself is explained and it will be shown how the *intensity composition relationships* are extracted from the multislice simulations. The capabilities of the extended method are highlighted afterwards and the intrinsic limitations towards single-atom accuracy are pointed out. Thereafter, the raw experimental STEM images are introduced which are used to demonstrate the composition determination method. Several parameters have to be taken into account to match the simulated STEM intensity to the experimental intensities. The various important parameters are addressed in the upcoming section. Since the thickness determination plays a crucial role to gain accurate results, three different methods to consider thickness locally are explained and demonstrated using the experimental images. Three technologically important semiconductor samples are used to present the method. The color coded 2D composition with a lateral resolution of one atomic column are explained in detail. Line scans are compared to established methods such as HRXRD and lattice constant analysis.

3.1. Intensity composition relationship

The foundation of the method described is to find the dependency between the STEM HAADF intensity and the number of included substitute atoms. Since the method should be as accurate as possible, the analysis is carried out for every atomic column. The first step for analyzing the simulated concentration set is to retrieve STEM HAADF images from the raw simulation data. The experimental parameters needed for this, i.e. sample thickness, detector angles or the sigma parameter of the Lorentzian distribution, can be determined with the method explained in an upcoming chapter. For every STEM image created from the simulated concentration set, the atomic column positions are extracted from the simulation cell and divided into group III and group V (or group IV respectively). The Voronoi intensity [13,45] is determined and correlated to the number of substitute atoms in the column. Since simulated results are processed, the count of substitute atoms in every atomic column is given by design. The value pair of Voronoi intensity and number of substitute atom is determined for every column in every simulation of the concentration set. With this, a dependency between number of substitute atoms and Voronoi intensity is build up gradually. Fig. 1a–c shows the dependencies for a fixed thickness of 32 atoms in total and experimentally used detector angles, as stated in previous chapter, for all three samples used in this work. It is important to derive the *intensity composition relationships* for every column thickness present in the experimental image to be able compare it to every column individually. Every blue dot visible in Fig. 1a–c represents an intensity – number of atoms value pair derived from a simulation of the concentration set. It is noticeable in the plots that there is a deviation in intensity for one fixed number of substitute atoms. For example: for 10 In atoms embedded in GaAs with 32 atoms thickness,

the Voronoi intensity ranges from 0.055 to 0.057. This effect is caused by the different heights of the substitute atoms in the crystal in reference to the defocus of the electron beam [46,47]. As already mentioned above, the distribution of the substitute atoms' coordinates is random and thus also the height. Crosstalk between atomic columns can affect the intensity on a specific column as well [48,49]. These two effects are the main reasons why there is a deviation in the Voronoi intensity for a specific amount of substitute atoms. These inherent statistical fluctuations influence the corresponding STEM HAADF images and therefore introduce a fundamental limitation of the achievable accuracy of the composition determination. In addition to this theoretical limit, in experimental STEM HAADF measurements where additional noise is present, the achievable accuracy may be reduced. Further on, the Voronoi intensity as well as the standard deviation is calculated for each number of substitute atom. The red markers in Fig. 1a–c depicts the mean Voronoi intensity for a fixed number of substitute atom. The "errorbars" mark the maximum overlap of the standard deviations for different numbers of substitute atoms. In other words, if the upper maximum of the standard deviation of one specific number overlaps with the minimum of the next higher number, the uncertainty is one atom. This also represents the highest precision possible for each atom number of a specific material. All three sample materials, used in this work, show a maximum precision error of ± 2 atoms at a total thickness of 32 atoms. The deviation in the Voronoi intensity is influenced by the elements, which build up the material, as well as the total thickness and the detector range of interest.

The dependencies that follow from the analysis, described above will be called intensity composition relationship in the following. Each intensity composition relationship depicted in Fig. 1a–c shows an increasing, nearly linear behavior of the Voronoi intensity with increasing number of substitute atoms. This is because a lighter element is substituted with a heavier one and thus increasing the mean atomic number Z of the column. The slope of the plot depends on the atomic number of the substitute atom as well as the difference to the replaced atom, since heavier elements have a higher influence on the STEM HAADF intensity. To visualize this effect more clearly, a second *x*-axis has been plotted in Fig. 1a–c. There, the plotted intensities were normalized to the surrounding base material, i.e. GaAs for sample I, GaP for sample II and Si for sample III. The limits of the axis reflect the slope of the plot. This means that the intensity difference between pure GaAs and InAs (Fig. 1a) or pure GaP and GaAs (Fig. 1b) is smaller than the difference between pure Si and pure Ge (Fig. 1c). Comparing sample I and II, it is noticeable that the points of pure GaAs do not match in Voronoi intensity. This is due to the different inner detector angles (63 mrad for sample I and 74 mrad for sample II), which affects the intensity strongly. The inner detector angles of sample I and III were 63 mrad and 68 mrad and thus are more comparable. The second axis in Fig. 1c ranges from 1 to 4, whereas the limits of the second axis in Fig. 1a only range from 1 to 1.4. The drastic difference in this limits originates, amongst others, from the different sample structure (diamond, zincblende) of the samples. Since the substitute atoms in the diamond SiGe sample occupy both fcc sub lattices, the fractional compositions of Ge actually reflect twice the absolute number of substitute atoms compared to the zincblende case.

3.2. Capabilities and limitations the method

In the following paragraph, the capabilities and limitations of the presented method are investigated. The subject is the overall accuracy with a special focus on accuracy towards single-atom detection. For this, simulated STEM images with known composition and thickness are used as input. The resulting number of substitute atoms that are determined by the algorithm proposed are verified by the supercell used as input. This is used to derive a percentage of exactly determined atomic columns. Furthermore, the number of columns that differ by a certain number of substitute atoms are extracted and are examined. The
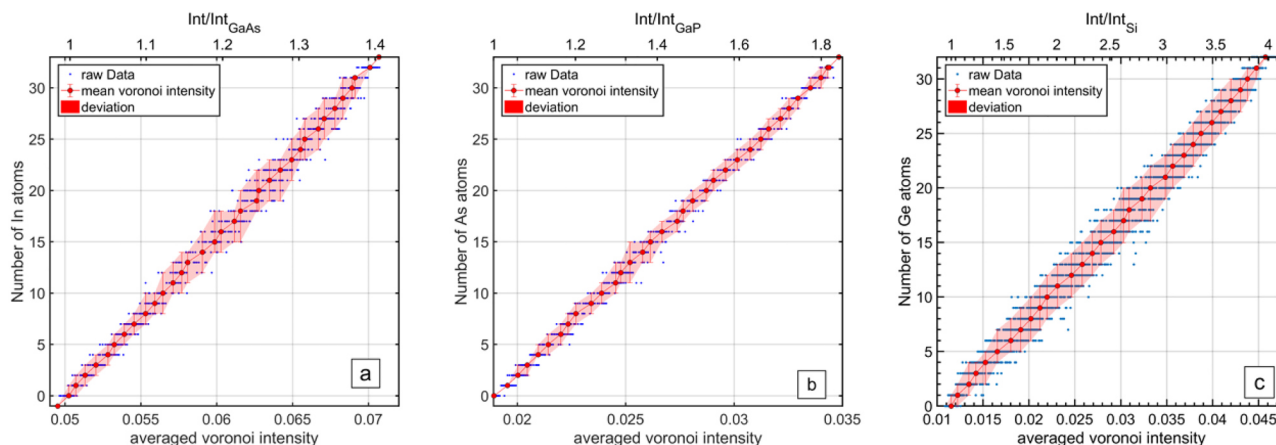
Fig. 1. The figure shows the *intensity composition relationships* for all corresponding samples I and III. The blue dots mark the averaged Voronoi intensity of every atomic column of each concentration set. The red markers illustrate the mean intensity for every atom count, whereas the "errorbars" mark the overlap of the standard deviations, which is the maximum precision achievable. The second *x*-axis shows the intensity normalized to the barrier material. With this a quantitative comparison between all samples is possible. All figures were calculated for total thickness of 32 atoms. (For interpretation of the references to color in this figure legend, the reader is referred to the web version of this article.)
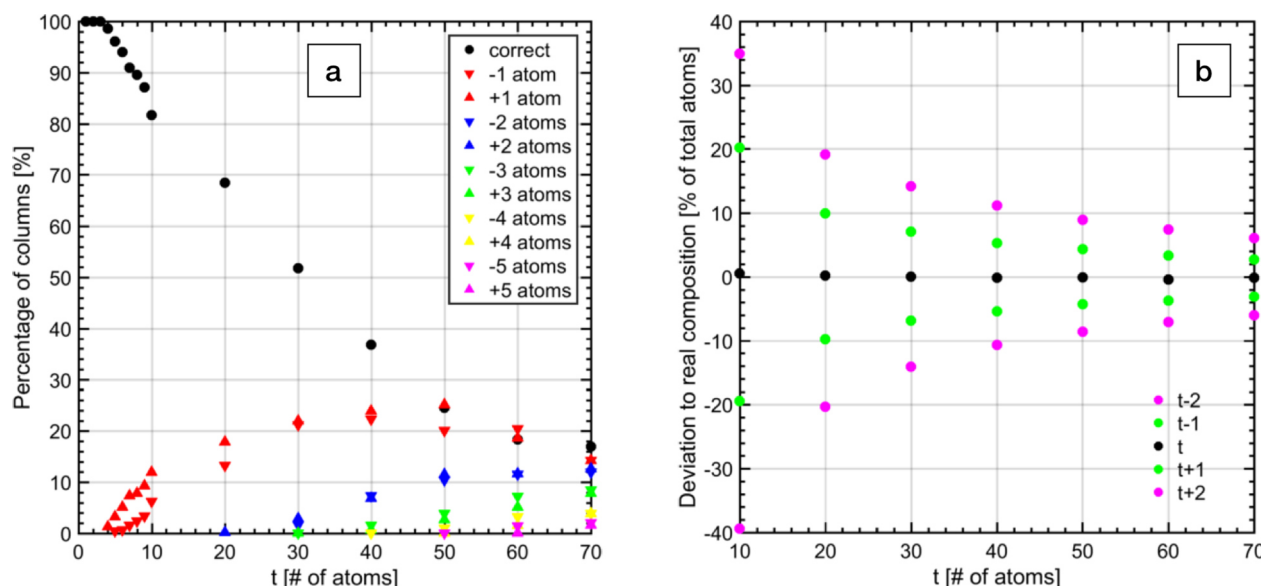
Fig. 2. Percentage of correctly determined atomic columns versus the sample thickness *t* for (Ga,In)As with 20% In concentration (a). With increasing sample thickness, the percentage of correctly determined atomic columns decreases and the number of atomic columns, off by several atoms increases. The number of underestimated columns is nearly the same as the number of overestimated columns, resulting in the correct average composition for all thicknesses. Subfigure (b) shows the deviation of the real composition determined from all atomic columns (810 in total) versus sample thickness. Assumed sample thickness affects the deviation of real composition. The composition deviation is symmetrically distributed around 0, which means that the mean concentration stays mainly correct.

benchmark will be exemplarily done with GaInAs with 20% indium content incorporated. To improve statistics, 10 simulations are used as input with random atom configurations. This ensures, that the benchmark covers a decent amount of indium atoms distributed in e-beam direction. The individual simulations are 5 × 5 unit cells in lateral dimensions which leads to 81 group III atomic columns, edge columns excluded. Overall, the 10 simulations then add up to 810 examined atomic columns. The analysis was also carried out for varying sample thickness. Fig. 2a depicts the results from the benchmark. The y-axis shows the percentage of atomic columns that are either determined correctly or differ by one or up to five substitute atoms. The percentage of atomic columns is plotted against the sample thickness *t* presented in number of atoms in e-beam direction. The black dots depict the number of correctly determined atomic columns, meaning that the exact amount of substitute atoms resulted from the algorithm. The differently colored triangles show the fraction of atomic columns, where the result

is off by one or up to five atoms, according to the legend. The upwards facing triangles represent deviation in the positive direction whereas the downwards facing triangles show negative deviation.

The plot, seen in Fig. 2a starts at 1 atom thickness and 100% correctly determined atomic columns. This is not relevant for experimental cases but important to check for the correct operation of the algorithm. The exact number of substitute atoms can be determined correctly on each atomic column up to a sample thickness of 3 atoms. At 10 atoms thickness, the percentage of exactly determined atomic columns drops to 82% with a deviation in one atom of 13% in positive direction and 5% in negative direction. From statistics, these values should be equal since overestimation of the In content is as likely as underestimation according to Fig. 1a. The discrepancy observed is most likely caused by insufficient statistics at a thickness of only 10 atoms. For higher thicknesses, the errors are distributed nearly symmetrically around zero.
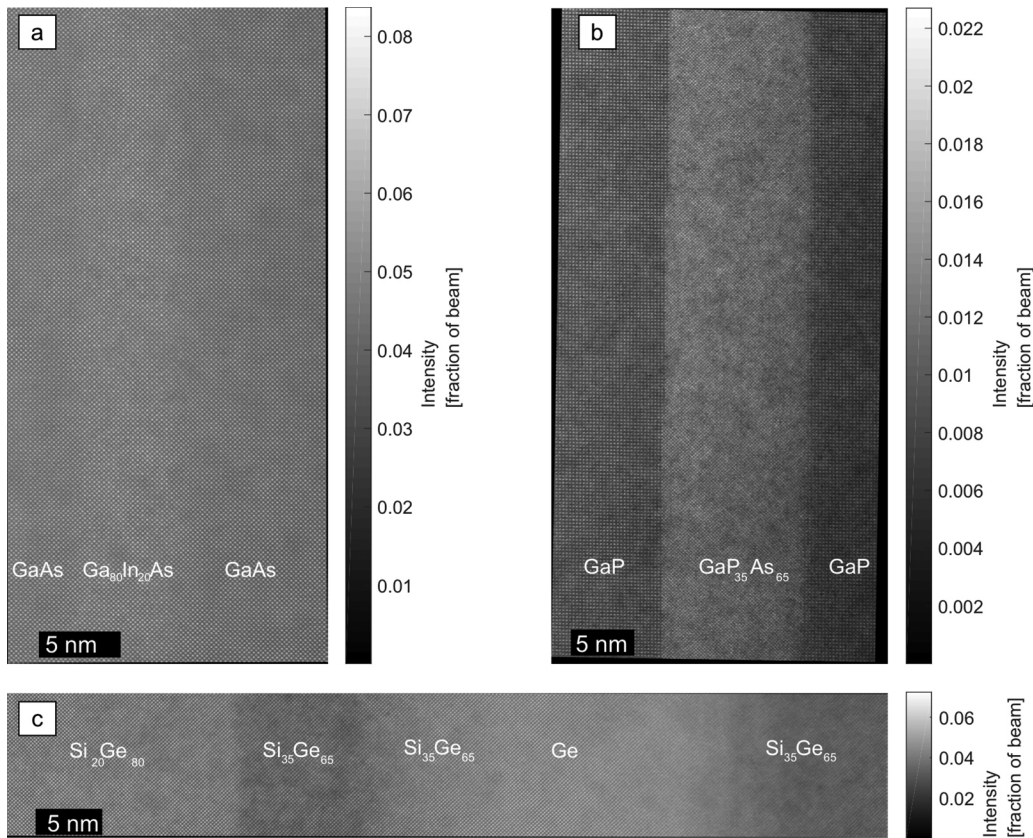
Fig. 3. STEM images of all three samples normalised to the impinging electron beam. (a) Sample I, a (Ga,In)As)-QW between GaAs barriers. (b) Sample II, a Ga(P,As)-QW between GaP barriers. (c) Sample III, SiGe with different Ge concentrations. Growth direction is from left to right.

With increasing thickness *t*, the percentage of exactly determined atomic columns drops and the percentage of atomic columns with some atoms deviation increases accordingly. Up to a sample thickness of 50 atoms the maximum deviation is in the range of 2 atoms. At thicknesses higher than 50 atoms, a small fraction of atomic columns are determined with a deviation of 3 atoms or higher.

To check how the atomic deviations influences the total determined composition of the sample, Fig 2b shows the deviation from the real composition in percent versus the sample thickness *t*. The black dots represent the deviation from real composition if the correct thickness is assumed. The deviation from the real composition starts at 0.5% at 10 atoms thickness and decreases with increasing sample thickness down to 0.1% at 50 atoms thickness. This means, that the mean of the determined atomic columns is still very accurate with a deviation under 0.5% for (Ga,In)As with 20% indium and thicknesses below 70 atoms. The deviation from real composition is given in absolute percentage, i.e. a deviation of 0.5% would mean that In content 19.5% or 20.5% would be determined instead of the 20% being present in reality.

If the assumed thickness of the sample is incorrect by 1 or two atoms, deviation from the real composition increases. The green dots, depict the total deviation with a thickness error of 1 atom. The deviation increases tremendously to 20% whilst still remaining centered symmetrically around 0% deviation. The deviation starts at (±) 20% indium concentration at 10 atoms sample thickness. This deviation decreases with increasing sample thickness down to (±) 3% at 70 atoms thickness. With a thickness error of two atoms the deviation starts at (±) 37% at 10 atoms thickness and decreases down to (±) 6% at 70 atoms thickness whilst also remaining symmetrically distributed around 0%.

This analysis summarizes the capability of the composition determination via STEM HAADF intensities using the example of (Ga,In)As with 20% indium concentration. The accuracy of the method is determined mainly by the thickness of the sample and the slope of the intensity composition relationship (compare Fig. 1). The steeper the

slope is, the higher is the accuracy of the intensity method.

The analysis shows that the precision of correct determined number of atoms is higher at thinner samples. The thicker the sample is, the higher is the deviation in determined number of substitute atoms. Nevertheless, it can be said that the deviation is in the range of 1–2 atoms per atomic column. Furthermore, the analysis of the mean composition determined from the atomic columns shows a negligible deviation from the real composition for all investigated thicknesses *t* at a correctly assumed sample thickness. This stresses the fact, that calculating the correct sample thickness is crucial for the composition determination. If the assumed thickness is off by one or two atoms, it has a tremendous effect on the composition determination. However, since the deviations are symmetrically around zero when over/underestimating the thickness, they are likely to cancel out in experimental images due to statistics. This will be shown in later paragraphs.

3.3. Collocation of raw experimental data

With the capabilities of the presented method in mind, the next paragraph addresses the application on experimental samples. A $(Ga_{1-x}In_x)As$ quantum well (QW) is investigated, potentially being part of a 'W'-type or a multi QW heterostructure used in an infrared laser device. Furthermore, a $Ga(P_{1-x}As_x)$ QW structure, that might be used as a barrier in several different laser designs is investigated. Moreover, a $Si_{1-x}Ge_x$ QW heterostructure is investigated, where the Ge fraction *x* is varied in the attempt of obtaining a parabolic confining potential. [24]

For all three samples, STEM images were acquired under HAADF conditions. These are shown in Fig. 3. Due to the dominant Z-contrast under HAADF conditions, the different QWs are clearly visible within the respective barriers. For all samples the substituting atoms are heavier than the atoms in the matrix (i.e. In (49) vs. Ga (31), As (33) vs. P (15) and Ge (32) vs. Si (14)), therefore the QW appears brighter than the matrix material in all cases.

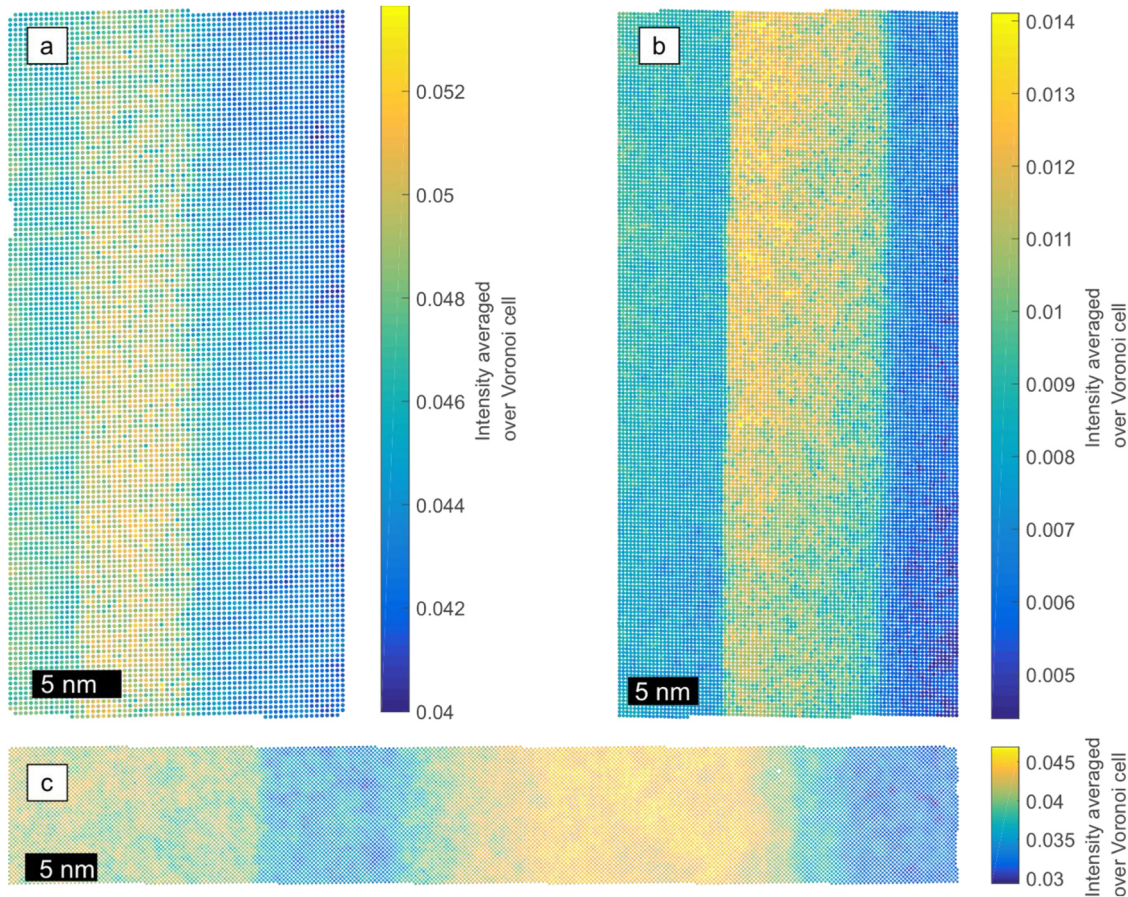For a quantitative analysis of these raw STEM images, intensities are

Fig. 4. Intensity maps showing the intensities of every atomic column averaged using Voronoi cells. For sample I (a), only the group III sub lattice is shown, for sample II (b) only the group V lattice is shown. In (c), all atomic columns of sample III are shown. Growth direction is from left to right.

evaluated by Voronoi cells and assigned to every atomic column [21,45]. In a Voronoi cell, every pixel is belonging to its closest atomic column and for every column the intensity of the appropriate pixels is averaged. These Voronoi intensities have the advantage of being robust regarding most experimental influences [45] especially including surface relaxation that is important for our samples [50]. Using these Voronoi cells, Voronoi intensity maps are created as shown in Fig. 4. For clarity, only the sub lattice on which the composition change is taking place is shown in the Voronoi intensity map. This is the group III sub lattice for sample I (Fig. 4a), the group V sub lattice for sample II (Fig. 4b) and the group IV lattice for sample III (Fig. 4c) which is the only lattice present in this sample. To determine the influence of cross scattering to neighboring columns and show the thickness gradient (see later chapter), additionally Voronoi intensity profiles are shown for the group III and V sub lattices in the case of sample I and II and for group IV for sample III (Fig. 5).

3.4. Matching of simulation and experiment

To determine the composition of semiconductor alloys by intensity comparison of experiment and simulation, the simulation has to reproduce the experiment as closely as possible. Considering the influences mentioned above, a parameter for the Lorentzian convolution of the simulation remains to be determined. This takes into account the size of the electron source [40].

The adaption of the simulation to the experiment has to take place in a region with known composition, i.e. the barrier, and at the correct thickness.

In sample I, this adaption is done for GaAs. Here, for every peak of

one sub lattice the surrounding unit cell is found and the average experimental unit cell (AEUC) of GaAs is generated as shown in Fig. 6a. For the simulated image of GaAs, which has a size of 5×5 unit cells, the average simulated unit cell (ASUC) is also calculated (Fig. 6b). Now, the most suitable thickness – that is number of atoms – for the simulation is chosen so that the mean intensity of the ASUC is matching the mean intensity of the AEUC. As the composition is the same in both experiment and simulation, thickness is the decisive parameter for matching both. A thickness intensity relationship can be obtained by evaluating the ASUC for different thicknesses. This relationship and the best fitting thickness are shown in Fig. 6d.

At this thickness, a Lorentzian convolution of the simulated image is performed using a range of different widths of the Lorentzian. Minimizing the total deviation between AEUC and ASUC for all pixels, the correct width $\sigma = 0.049\,nm$ is found. The resulting ASUC with correct thickness and width σ is shown in Fig. 6b. A pixel wise 2D representation of the relative difference between both AEUC and ASUC is presented in Fig. 6c already showing the good overall agreement. To get an exact comparison of both images, they are aligned using the software SmartAlign [30] beforehand. The good agreement between experiment and simulation is also supported by a diagonal line scan across both ASUC and AEUC plotted in Fig. 6e. The difference in 2D pixel wise intensity between the experimental and simulated intensity can be calculated to 1.6% in this case for GaAs in sample I.

The corresponding figures for sample II and sample III, respectively, can be found in the supplements. Here, a difference between experimental and simulated 2D pixel wise intensity of 1.1% (GaP in sample II) and 1.4% ($Si_{0.2}Ge_{0.8}$ in sample III) is achieved.
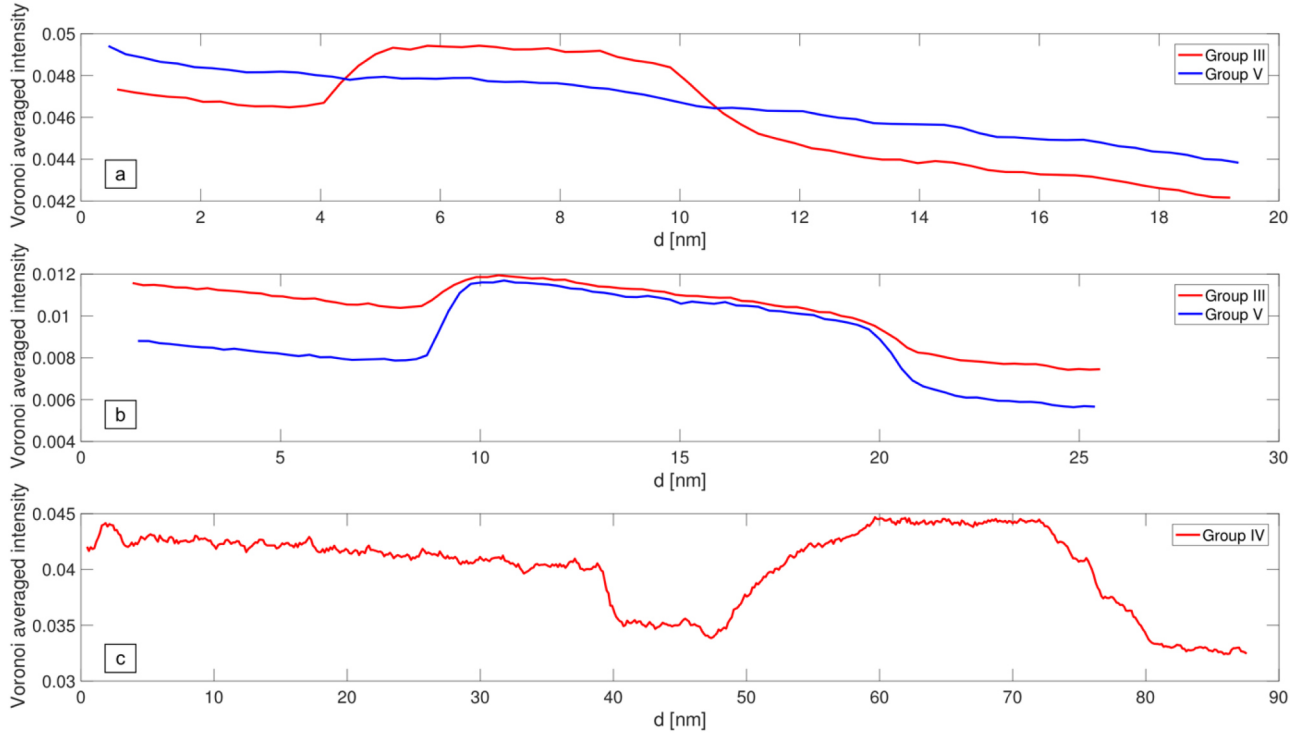
Fig. 5. Voronoi averaged intensity profiles of all three samples. In (a) and (b) both sub lattices of sample I ((Ga,In)As-QW in GaAs barrier) and sample II (Ga(P,As)-QW in GaP barrier) are shown. The intensity profile for sample II (SiGe-QW in SiGe barrier) is shown in (c). Growth direction is from left to right.

3.5. Local thickness determination

In this way, suitable parameters for a matching between experiment and simulation were determined. To be able to find the composition of every atomic column, for each column the thickness, i.e. the number of

atoms in this column, has to be specified. A determination of the thickness is only possible with a known composition of the atomic column. In order to assign a thickness to a column with unknown composition, thickness information about the material itself or the surrounding atomic columns are necessary. There are several
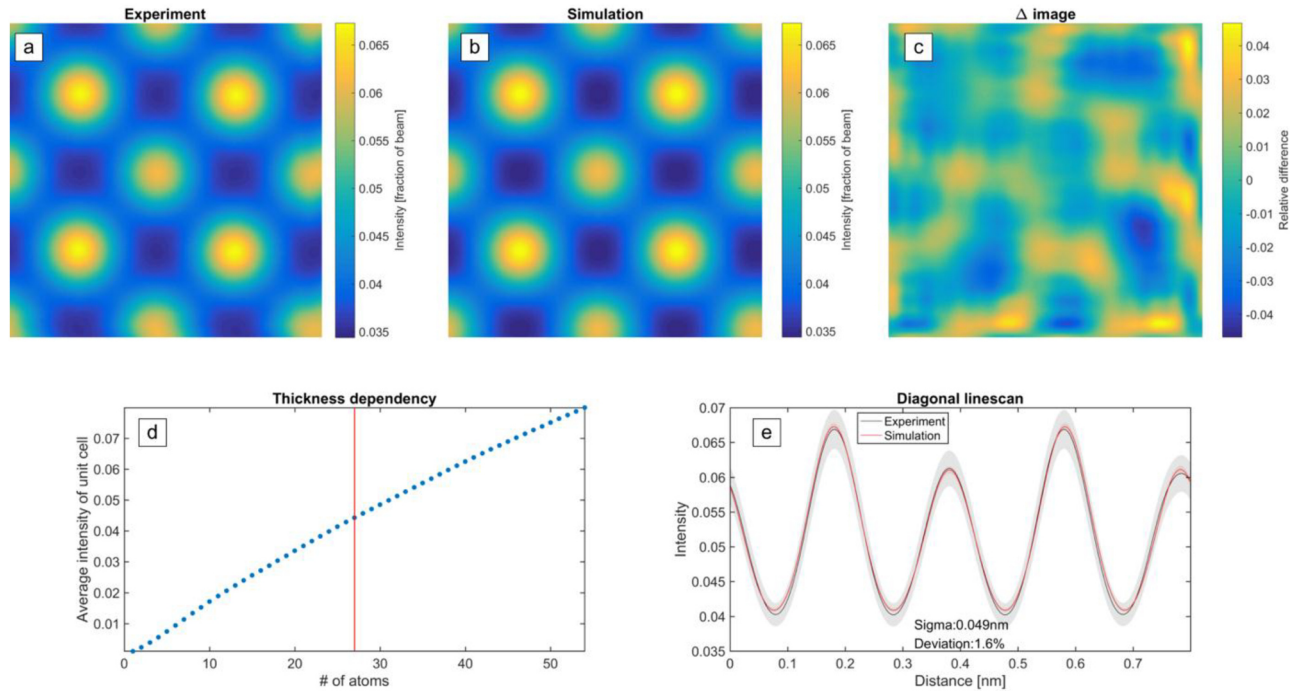
Fig. 6. Adapting simulation to experiment for GaAs. The correct thickness is found by matching the unit cell averaged intensities with the simulated thickness intensity relationship shown in (d). The respective unit cells are shown in (a) and (b) for experiment and simulation, respectively. By choosing a suitable width for the Lorentzian convolution, representing the source size, both show a good agreement as proven in 1D by a diagonal line scan (e) across both images as well as in 2D by difference image (c), normalized to the intensity of the simulated unit cell. A deviation in Voronoi intensity of only 1.6% was achieved.
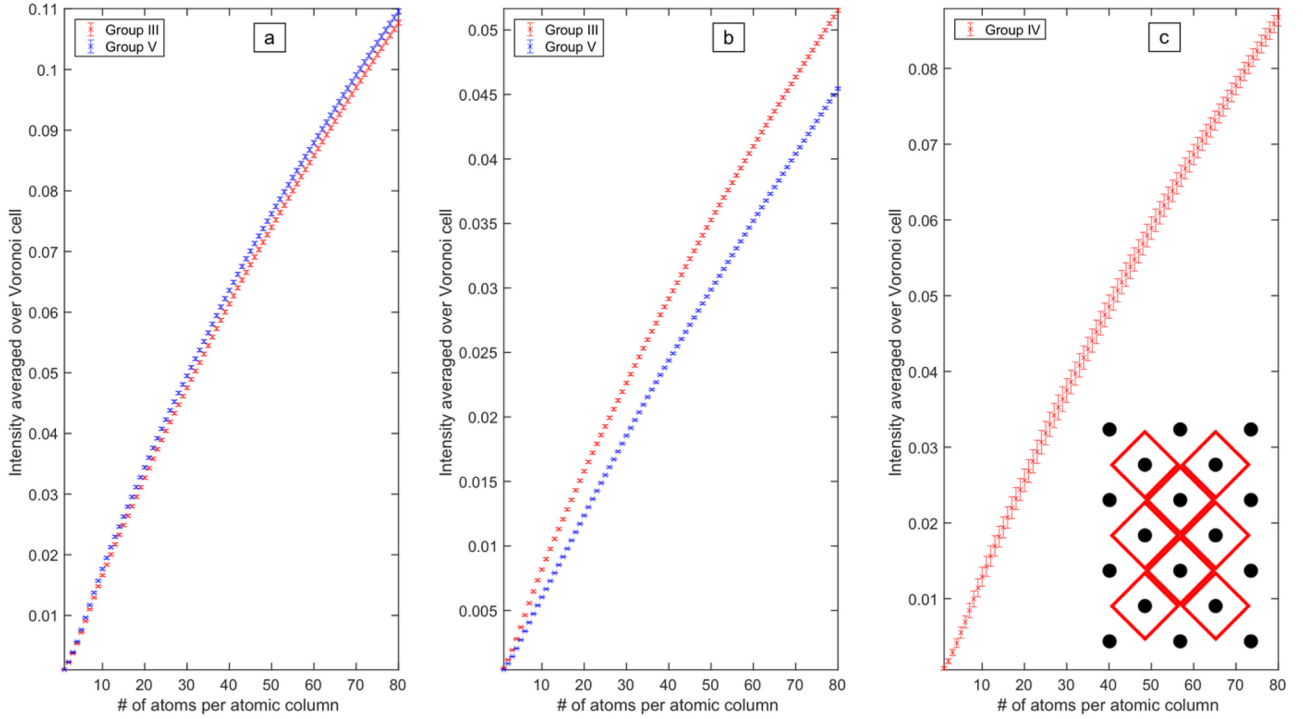
Fig. 7. Thickness dependencies for Voronoi intensities. The different barrier materials are presented: GaAs in (a), GaP in (b) and $Si_{0.2}Ge_{0.8}$ in (c). The inset in (c) illustrates the concept of the Voronoi cell.

possibilities to do so, which will be explained for the different samples in the following.

In sample I, there is a composition change on one sub lattice only, as group V columns are consisting of As in the barrier and the QW region. In contrast, the group III sub lattice composition is changing across the sample: there is only Ga in barrier regions but Ga and In in the QW region. Since the sample is thin enough (thickness determined by unit cell average is 27 atoms), there is no substantial influence of one sub lattice on the other during the electron scattering process, i.e. there is no cross scattering. This assumption is supported by the line plots depicted in Fig. 5(a) and (b). Comparing subfigure (a) to subfigure (b), one can see the clear effect of cross scattering in subfigure (b) but not in (a). Therefore, the group V sub lattice can be used to determine the thickness of the sample. The intensity is compared to simulated Voronoi intensities, As in the case of sample I (see Fig. 7a), and the suitable thickness is assigned. Since finally the thickness of group III sub lattice atomic columns is needed, for every group III column the thickness of the 4 neighboring group V columns is averaged and assigned to the group III column. The resulting thickness map of group III atomic columns only is shown in Fig. 8a. Thicknesses are ranging from 25 to 33 atoms per column. This thickness gradient is induced by the preparation method as explained earlier. The thickness map shows a reasonable thickness distribution considering the last preparation step of Ar ion milling.

In sample II, the composition change is also taking place on one sub lattice only. Here, group III atomic columns consist of Ga atoms everywhere, while group V atomic columns consist of P atoms in the barrier regions and P and As in the QW. As can be seen in Fig. 5b, cross scattering plays a more important role in this sample. Thus, even if the composition stays constant on the group III sub lattice it cannot be used for a thickness determination in the QW. Instead, the thickness in the QW region is interpolated by fitting a plane to the intensities of the group V columns in the barrier. There, the original intensities of every column are taken for thickness determination while in the QW region the intensities are interpolated. The QW region is found by setting an

intensity threshold for gradient normalized column intensities. Intensities above this threshold are then assigned to the QW region. The intensities assigned to each peak are then compared to the thickness dependent simulated P intensities and the thicknesses are determined. In Fig. 8b the resulting thickness map for the group V sub lattice is shown. Thicknesses range from 8 to 18 atoms per column. In the interpolated region, the small length scale features are necessarily gone but the fitted plane is the best approximation of the thickness in this region.

In sample III, there is only one sub lattice on which Si and Ge concentration are changing. Additionally, there is no region consisting only of Si or pure Ge. Instead, there is a region where the Ge concentration is nominally 80%. However, as can be seen from the intensity profile (see Fig. 5c) the intensity is also fluctuating in this region suggesting that the concentration may not be constant here. Therefore, only a mean concentration of 80% Ge is assumed. A plane is fitted to the linear decreasing region (see Fig. 5c) and intensities are assigned to the columns based on this plane both in the buffer layer of $Si_{0.2}Ge_{0.8}$ and in the region of unknown composition. This technique is only suitable if the reference region is large enough (40×40 nm in this case) and shows a linear behavior. Using a simulation of $Si_{0.2}Ge_{0.8}$ and its mean Voronoi intensity, thicknesses are specified for every column. Hence, extrapolation is used to determine local thicknesses in this sample. The thickness map resulting is shown in Fig. 8c where the thickness ranges from 29 to 35 atoms per column.

3.6. Composition maps

With the composition intensity relationships explained above, the experimental Voronoi intensities can now be converted to a composition of the corresponding material. For this, every atomic column's intensity is compared to its corresponding *intensity composition relationship*. For this, the local thickness of every column is used and its corresponding *intensity composition relationship* is calculated. This ensures that no intensity that originates from thickness is mistaken for
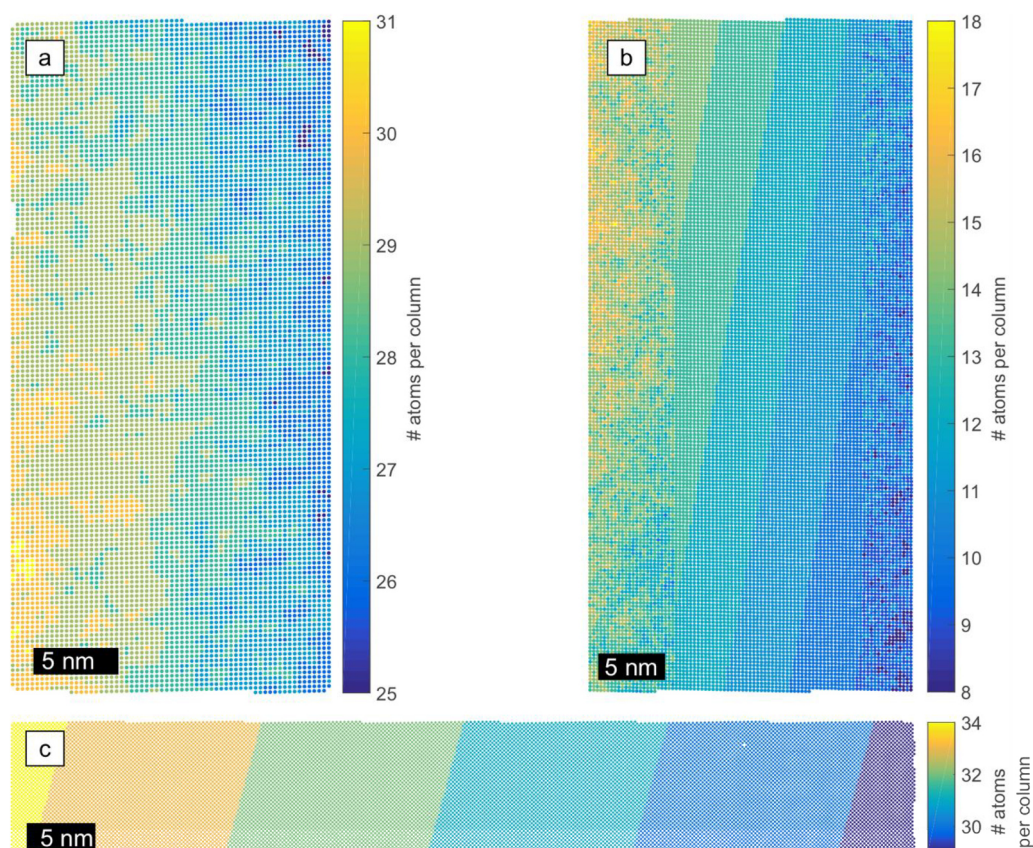
Fig. 8. Thickness maps for all three samples. In (a), the thicknesses in atoms per column are given for the group III sub lattice of sample I. For sample II, thicknesses of the group V sub lattice are shown in (b). In (c) the thicknesses of the atomic columns of sample III are presented. Growth direction is from left to right.
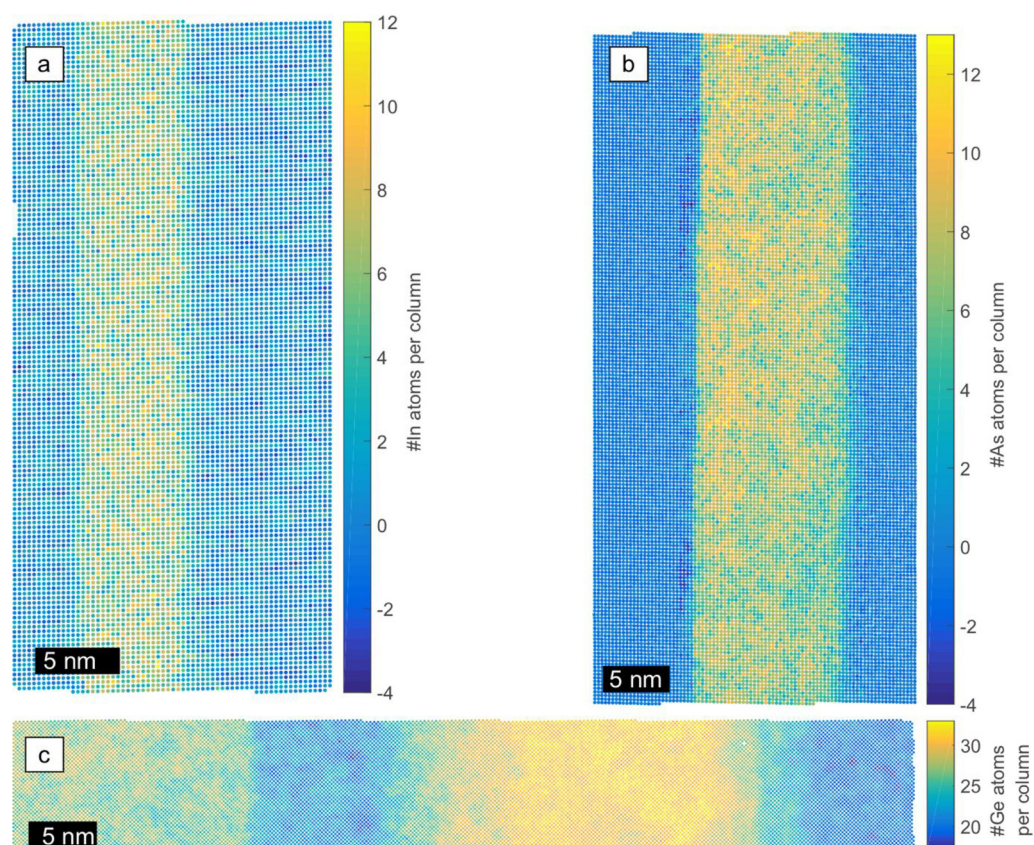

Fig. 9. Composition maps of all three samples. The number of substitute atoms per atomic column is given for the group III sub lattice of sample I (a), the group V sub lattice of sample II (b) and for sample III (c). Note, that the thickness of each atomic column differs as indicated in the thickness maps in Fig. 6. This was taken into account for composition determination.
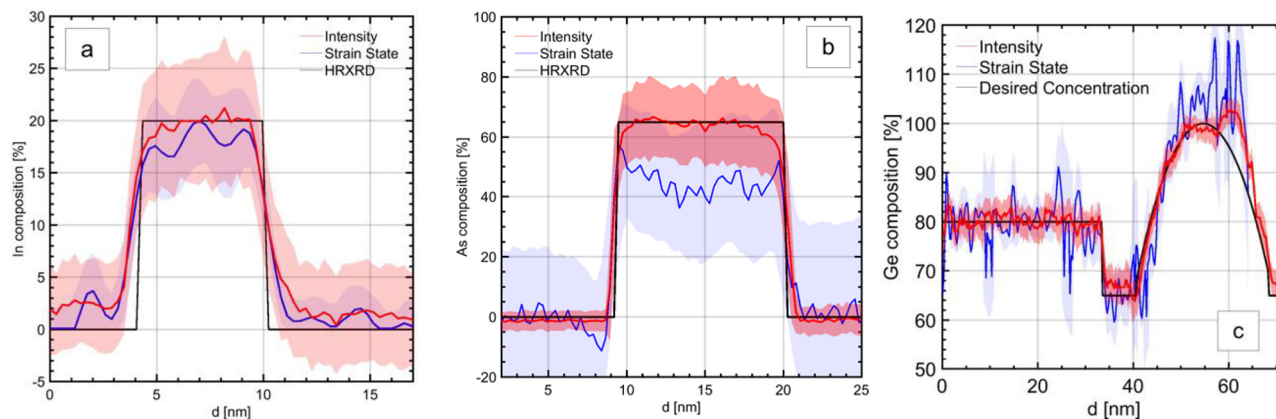
Fig 10. Horizontal line scans, acquired by averaging the 2D maps perpendicular to the growth direction. Sample I is depicted in (a) where the red line represents the composition derived from the intensity method, the solid blue line originates from the strain state, calculated from the local lattice constant and the black line visualizes the output of HRXRD measurements. Sample II is visualized in (b) and sample III in (c). The red and blue shaded areas depict the concentration standard deviation perpendicular to the growth direction. (For interpretation of the references to color in this figure legend, the reader is referred to the web version of this article.)

composition variation. The Voronoi intensities can now be converted into the corresponding number of substitute atoms. Fig. 9a shows the color coded 2D composition map of sample I. The GaAs barrier is clearly visible with a mean number of In atoms of 0 which increases up to a maximum of 12 in the QW region. The local thickness in the QW region ranges between 27 and 29 atoms in total. The mean number of In atoms in the QW area is around 6 which translates to a composition of 20% In. Additionally to the 2D map, Fig. 10a shows a line scan in growth direction of sample I. This is done by averaging the composition of the atomic columns perpendicular to the growth direction. In this way, the results of the different methods can be compared more easily. The red solid line represents the composition determined by the intensity method, explained above. The shaded area around the solid line is not the accuracy of the method but rather the composition deviation perpendicular to growth direction. The deviation of the composition in the GaAs barrier material as well as in the QW region is around ± 5%. Additionally an offset in the pure GaAs barrier of ∼ 1.5% is visible. The black line in Fig. 10a shows the geometry retrieved from HRXRD with a QW width of 6.1 nm and an In composition of around 20%. Furthermore, the concentration derived from the lattice constant analysis of the sample is visualized with the blue line. The In concentration was calculated via the local lattice constant, derived from the image and combining Vegard's law with tetragonal distortion due to pseudomorphic growth. This method is considerably more sensitive to the surface relaxation of the sample. An increase of the concentration in the upper barrier region of the QW is visible which is due to the elastic surface relaxation of the sample. The concentration deviation along the QW is smaller than for the intensity method with ± 4%. Nevertheless, the composition derived from the intensity method is in good agreement with the composition derived from HRXRD.

The effect of the noise from the experimental intensity can be seen in the GaAs barrier in Fig. 9a. The mean concentration of In atoms in the GaAs is zero, but due to the noise, the minimum of the calculated In atoms is negative. Surface damage introduced during the preparation of the sample enhances the effect.

Fig. 9b shows the 2D composition maps for sample II. The GaP barrier is clearly visible and distinguishable from the QW region. The number of As atoms in the barrier is around 0 with a total number of group V atoms of 10 − 18. The number of As atoms increases to maximum of 13 atoms in the QW with a local thickness between 11 and 16 total atoms. Fig. 10b shows the corresponding line scans for sample II. The composition line scan (red) derived from the intensity method shows a very good agreement with the sample geometry derived from HRXRD (black). The parameters of the QW, according to XRD are

11.7 nm width with an As concentration of 65.5%, which is also reproduced by the intensity method. The concentration deviation is small in the barrier region and increases to around ± 4% in the QW area. This is due to the averaging of the intensities perpendicular to the growth direction. The distribution of atoms in a QW consisting of a compound semiconductor is not completely homogeneous, which leads to different compositions on the atomic columns. The composition deviation in the barrier is small and results from the intensity deviation, introduced by surface damage. The concentration profile derived from the lattice constant (blue line) shows a prominent discrepancy with the HRXRD profile (black). The concentration in the QW is between 40% and 50%. Due to the sample geometry, the elastic surface relaxation is very prominent. The intensities, derived from the Voronoi cells compensate the elastic relaxation very well, which is why the influence is not present, whereas the lattice constant is influenced tremendously. A detailed description how the elastic surface relaxation influences the lattice constant and thus the concentration derived from it can be found in.

Fig. 9c depicts the 2D composition map for sample III. The sample geometry is different than the one of sample I & II. The barrier consists of a $Si_{0.35}Ge_{0.65}$ alloy grown on the relaxed $Si_{0.2}Ge_{0.8}$ buffer. In the QW region the Ge content increases gradually in a parabolic form to 100% Ge. The composition drops back to $Si_{0.35}Ge_{0.65}$ after the QW area. The Ge content profile is such to ensure strain balance between the tensile strained barrier regions and the compressively strained QW regions. This geometry cannot be clearly distinguished from that a conventional box like QW by means of X-ray diffraction, therefore the nominal parabolic profile has been estimated from the calibrated deposition rate and alloy composition at varying precursor gas fluxes. The relaxed buffer material with $Si_{0.2}Ge_{0.8}$ is visible in the 2D color map from Fig. 9c with a total number of atoms between 35 and 33. The drop to $Si_{0.35}Ge_{0.65}$ is clearly visible with a number of Ge atoms between 19 and 22 with a total number of atoms of 32. The QW area with a higher Ge concentration is clearly visible whereas the parabolic form is not clearly distinguishable. The highest point of the parabola consists of 32 Ge atoms with a total number of 32 atoms. After the QW region, the Ge concentration drops back to 20 atoms with a thickness between 29 and 30 atoms in total. The line scans in Fig. 10c visualize the desired sample geometry more in detail. The concentration derived from the intensity method fluctuates around 80% of Ge in the barrier and the drop to 65% is clearly visible. The intensity method shows a small offset of around 3% to the desired sample geometry. The increase to 100% Ge is visible and peaks at around 102% Ge, which is due to the deviation of the Voronoi intensity. The drop in Ge concentration after the QW results in

a Ge concentration of 68%. The concentration derived from the lattice constant shows an enormous fluctuation around the desired concentration (black). This underlines that the proposed intensity method is more stable in comparison to the composition derived from the lattice constant.

4. Discussion

In this paragraph, we discuss composition determination by comparing simulated and experimental STEM intensities with regards to its extension towards single-atom accuracy. First, a general assessment of the method and its capabilities is done. Then, the application to experimental STEM images and accompanying influences are assessed.

Composition determination by comparing STEM intensities is based on the assumption that a certain composition of an atomic column leads to a unique intensity. In this work, Voronoi intensities [21] are considered. However, due to different possible z-height configurations of the substitute atom(s) inside the atomic column different intensities result. This leads to the intensity distribution for a given composition shown in Fig. 1. For the composition determination, the whole intensity distributions are reduced to a mean intensity that reflects a certain composition. The intensity distributions lead to the statistical character of the composition determination that is inherent in the composition intensity relationships of STEM experiments.

Therefore, the overlap of the intensity distributions determines the accuracy of the composition determination. To be more exactly, it is that overlap of the intensity distributions that is closer to the mean intensity of another composition. This is referred to as overlap from now on. In this work, an estimation of this accuracy was done with help of standard deviations of the intensity distributions. With this, 68% of the atomic columns are considered. An assessment of the error for all atomic columns can be done with the simulation study performed for the example of (Ga,In)As.

Atomic columns that have a z-height configuration leading a "non-overlap intensity" are determined correctly. If an atomic column has an intensity that is part of the overlap to another composition, its composition is not determined correctly.

The overlap of the intensity distributions and hence the accuracy of composition determination depends on the material system, the number of substitute atoms in an atomic column and its thickness. The HAADF-STEM images used for this study exhibit strong Z-contrast. Consequently, if the difference between the atomic number of the substitute atom and the replaced atom is higher, the overlap between different intensity distributions is smaller. Therefore, the achievable accuracy depends decisively on the studied material system and for example for Ga(As,Bi), where the difference in atomic number is $\Delta Z = 50$, the accuracy of composition determination is higher than for (Ga,In)As where the difference in atomic number is only $\Delta Z = 18$. For a higher number of substitute atoms in an atomic column, there are more possible arrangements of these substitute atoms and therefore a larger overlap of intensity distributions. If the number of total atoms in an atomic column is higher, this leads to more possible z-height configurations and a larger overlap between intensity distributions.

The influence of thickness can be clearly seen in the simulation study on (Ga,In)As. With increasing thickness, the percentage of atomic columns for which the composition was determined correctly decreases since the overlap of intensities increases. From a statistical point of view, this means that there is certain probability that the composition of a given atomic column is determined correctly. This probability depends on the material system and the composition and decreases with increasing thickness.

The errors in composition determination increase with increasing thickness since there is overlap with more compositions. However, overall these errors cancel out on average, since plus and minus deviations are equally frequent independently of the thickness. Consequently, the overall composition is determined very accurately at

every thickness for the investigated sample size.

For the application to an experimental STEM image, all experimental parameters are determined and all influences are treated carefully. Since the evaluation method solely relies on STEM HAADF intensities, every potential influence on the intensities has to be understood very precisely. In the following, the influences of local thickness, amorphous layers, detector angles, clustering of substitute atoms and surface relaxation are discussed.

As already apparent during the evaluation, the thickness of each atomic column has a major influence on its intensity. In the simulation study for (Ga,In)As, it is found that below thicknesses of 30 atoms it is impossible to determine the correct number of In atoms if the thickness is of by one atom. At higher thicknesses, the probability of correct composition determination becomes almost equally likely for wrong thicknesses.

The process of sample preparation where Ar ion milling is used as a final step leads to thickness variation within the field of view of one image. Therefore, the thickness of each atomic column has to be considered locally. Several options to do so have been introduced tailored to the demands of different samples. These demands depend on experimental sample thickness and present atomic columns/regions with known composition that can be used as reference for thickness determination. If the assumption for the thickness of an atomic column is wrong, this will lead to a locally wrong composition. However, the deviations in composition for under- and overestimated thickness of an atomic column cancel at every thickness. Hence, for the experiment contributions from wrong thicknesses will cancelout, leading to an overall correctly determined composition as shown for the three samples.

Thickness determination is realized by comparison of experimental intensities to simulation resulting in a certain number of atoms per atomic column. In the simulation, only crystalline material is considered. However, due to sample preparation there are amorphous layers on top and bottom of the sample. For the case of GaAs based material, an amorphous layer of 3.5 nm was found on both sides of the sample [51]. These amorphous layers lead to two main effects: One is beam broadening [40] and the other one is different intensity compared to only crystalline material [52] leading to a thickness determination deviating from only crystalline material.

The beam broadening caused by the upper amorphous layer leads to a two-dimensional redistribution of intensity in the image, which is the same effect as caused by the finite source size. As this is taken into account by a Lorentzian convolution, the width of this convolution will increase due to the amorphous layers and lead to a higher effective source size.

Since the thickness is determined via intensity comparison to simulation which only considers crystalline material, this crystalline thickness is overestimated. The real crystalline thickness is smaller: Considering the intensity of amorphous material to be about 50% [53] of crystalline material, the real crystalline thickness would be about 3.5 nm smaller than the one determined by intensity comparison. The real crystalline thickness is not considered in this case but could be taken into account by for example measuring position averaged convergent beam electron diffraction (PACBED) patterns [53]. However, since there is still a linear relationship between thickness and intensity there is only a minor influence by the amorphous layers present due to our sample preparation. Amorphous and crystalline material seems to behave similar despite of the different compositions present. This is supported by the good agreement of the presented composition results to other methods.

Additionally, to these two main effects, the amorphous layers are probably also causing the non-zero concentration of substitute atoms in the barrier of samples I and II (see Fig. 10). In the case of sample I, the In concentration is slightly higher than zero (~2%, ~0.5 atoms per column), in sample II As concentration is slightly smaller than zero (~1.3%, ~0.2 atoms per column). This will be explained in the

following with the example of Fig. 6.

In Fig. 6, the adaption of simulation to experiment for GaAs is shown. In the diagonal line scan, the central peak is a Ga peak (group III), while both neighboring peaks are As peaks (group V). Using the best possible adaption of the simulation to the experimental image, the group III intensity is slightly underestimated by simulation, while the group V intensity is slightly overestimated. In the case of GaP (see SI), the simulation is overestimating both group II and group V peaks. This leads to a small amount of In that increases the intensity of group III atomic columns being necessary to match experiment and simulation for sample (~1.3% intensity increase per substitute In at 27 atoms thickness). For sample II, a small negative concentration of As that decreases the intensity of group V atomic columns gives the best match between simulation and experiment in GaP (~5.8% intensity decrease per negative substitute As at 14 atoms thickness). While these deviations in adapting simulation to experiment cause the non-zero concentrations of substitute atoms in the barriers of samples I and II, the deviations themselves are probably caused by the two main effects of amorphous layers on intensity evaluations that are differing thickness and differing effective source size discussed above.

A possible solution to deal with the residual amorphous layers is to use very low kV ion milling to remove them [54]. This is work in progress, which should improve both adaption of simulation to experiment and composition determination.

However, amorphous layers are most influential on STEM intensities in a lower angular detector range. This is also the case for inelastic scattering and diffuse scattering caused by SADs. While the two former ones are not considered in simulation, SADs are taken into account. However, since the angular range used for the measurements is in the HAADF regime all three effects do not contribute majorly.

Detector angles were determined following the ansatz from [29]. Thickness determination is performed assuming this certain angular range of the detector. Since these thicknesses and the same angular range are used for composition determination, final compositions are relatively robust against small angle deviations.

The distribution of substitute atoms within the supercells that are used for simulations is done statistically in both the x–y-plane and their z-height within one atomic column. The distribution of substitute atoms in the x–y-plane only influences the Voronoi averaged intensities of atomic columns if the sample exceeds a certain thickness so that cross scattering comes into play. However, for samples that show clustering effects in the x-y-plane and are quite thick this assumption of statistical distribution leads to a wrong treatment of the influence of neighboring atomic columns on the intensity. This is only a minor effect while clustering in z-direction would have a larger influence. Here, the statistical distribution of substitute atoms leads to the intensity distribution and its mean value for a certain number of atoms per atomic column (see Fig. 1). If there is clustering in z-direction, the mean intensity of an atomic column will deviate from the one determined by evaluation of the simulated super cells. However, for all samples investigated no clustering effects are expected. Indeed, for a similar structure as sample I it was already shown that In atoms are statistically distributed [55].

Surface relaxation was shown to have a possibly severe influence on HAADF-STEM images [26,50]. It changes not only the intensity in the QW region but also in the barrier. Thus, it can be difficult to find a suitable reference for quantitative evaluations. However, the influence of surface relaxation on composition determination by intensity evaluation is decreased by the use of Voronoi cells [45]. To fully treat surface relaxation and its influence on composition determination is very complex since it is a self-consistent problem for both intensity evaluations and strain state analysis.

The composition determined by strain state analysis is severely influenced by surface relaxation [26] in the case of sample II (Fig. 10b) where the lattice mismatch of barrier and QW is the highest for the three samples investigated. Here, strain state analysis gives lower compositions than both other methods. However, in general the overall accuracy of the composition determination where a single-atom ansatz is chosen is also very good experimentally. This is confirmed by the comparisons to XRD and strain state analysis results.

5. Summary

In this paper, an extension of the established procedure that is used to determine compositions of materials by comparing STEM multislice simulations to experimental images is presented. A special focus lies on the comprehensive investigation of the capabilities and limitations of the extended method presented and the question whether single-atom accuracy is achievable. With the help of a simulation study on (Ga,In)As, the extended technique was benchmarked by calculating the percentage of correctly determined atomic columns as a function of assumed sample thickness. The results show that a correct determination of the composition of all atomic columns is possible up to a sample thickness of 3 atoms only. Above a sample thickness of 3 atoms, locally a deviation in composition of one atom is visible. Above 30 atoms sample thickness, the fraction of atomic columns which have a composition deviation of one atom or above increases substantially. This inaccuracy is caused by the fact that there is a certain intensity range for a fixed number of substitute atoms caused by the different z-heights of the substitute atoms as well as their local environment. Accordingly, the intensities for different number of substitute atoms overlap, leading to an over- or underestimation of the local composition. Since, over- and underestimation of the composition is as likely, the global composition, however, is determined very accurately.

Furthermore, the simulation study showed that the assumed sample thickness is a crucial parameter when determining compositions. With a correctly assumed thickness, the mean total deviation is below 0.5% for the example of (Ga,In)As with 20% indium. Moreover, the analysis of intentionally wrong chosen thicknesses shows that the resulting deviation in composition is symmetrical around zero. This means, that the errors in global composition determination again cancel out, since plus and minus deviations are equally frequent independently of the thickness. With the capabilities of the evaluation method in mind, three technologically important semiconductor samples, namely (Ga,In)As QW, a Ga(P,As) and a SiGe QW, were used to prove the applicability of the method. The concentration resulting from the intensity method presented here shows a good agreement with HRXRD measurements and strain state analysis. However, it has the advantages of atomic lateral resolution and insensitivity to surface relaxation. Of course, in the future this allows to investigate samples, which cannot be characterized accurately by XRD, e.g. due to gradients in the composition or interface roughness present.

Supplementary materials

Supplementary material associated with this article can be found, in the online version, at doi:10.1016/j.ultramic.2019.02.009.

References

[1] O.L. Krivanek, M.F. Chisholm, V. Nicolosi, T.J. Pennycook, G.J. Corbin, N. Dellby, M.F. Murfitt, C.S. Own, Z.S. Szilagyi, M.P. Oxley, S.T. Pantelides, S.J. Pennycook, Atom-by-atom structural and chemical analysis by annular dark-field electron microscopy, Nature 464 (March (7288)) (2010) 571–574.

[2] P.D. Nellist, M.F. Chisholm, N. Dellby, O.L. Krivanek, M.F. Murfitt, Z.S. Szilagyi, A.R. Lupini, A. Borisevich, W.H. Sides, S.J. Pennycook, Direct sub-angstrom imaging of a crystal lattice, Science (80-.) 305 (September (5691)) (2004) 1741.

[3] A. Singhal, J.C. Yang, J.M. Gibson, STEM-based mass spectroscopy of supported Re clusters, Ultramicroscopy 67 (June (1–4)) (1997) 191–206.

[4] P.M. Voyles, D.A. Muller, J.L. Grazul, P.H. Citrin, H.-J.J.L. Gossmann, Atomic-scale imaging of individual dopant atoms and clusters in highly n-type bulk Si, Nature 416 (April (6883)) (2002) 826–829.

[5] S.J. Pennycook, L.A. Boatner, Chemically sensitive structure-imaging with a scanning transmission electron microscope, Nature 336 (December (6199)) (1988) 565–567.

[6] J.M. LeBeau, S.D. Findlay, L.J. Allen, S. Stemmer, Quantitative atomic resolution scanning transmission electron microscopy, Phys. Rev. Lett. 100 (May (20)) (2008) 206101.

[7] S.J. Pennycook, D.E. Jesson, High-resolution Z-contrast imaging of crystals, Ultramicroscopy 37 (August (1–4)) (1991) 14–38.

[8] V. Grillo, E. Carlino, F. Glas, Influence of the static atomic displacement on atomic resolution Z-contrast imaging, *Phys. Rev. B – Condens. Matter Mater. Phys.* 77 (5) (2008).

[9] V. Grillo, The effect of surface strain relaxation on HAADF imaging, Ultramicroscopy 109 (November (12)) (2009) 1453–1464.

[10] A. Rosenauer, K. Gries, K. Müller, A. Pretorius, M. Schowalter, A. Avramescu, K. Engl, S. Lutgen, Measurement of specimen thickness and composition in AlxGa1–xN/GaN using high-angle annular dark field images, Ultramicroscopy 109 (August (9)) (2009) 1171–1182.

[11] L. Jones, Quantitative ADF STEM: acquisition, analysis and interpretation, IOP Conf. Ser. Mater. Sci. Eng. 109 (1) (2016) 012008.

[12] P.L. Galindo, S. Kret, A.M. Sanchez, J.Y. Laval, A. Yáñez, J. Pizarro, E. Guerrero, T. Ben, S.I. Molina, The Peak Pairs algorithm for strain mapping from HRTEM images, Ultramicroscopy 107 (November (12)) (2007) 1186–1193.

[13] J.M. LeBeau, S.D. Findlay, L.J. Allen, S. Stemmer, Standardless atom counting in scanning transmission electron microscopy, Nano Lett 10 (November (11)) (2010) 4405–4408.

[14] A. De Backer, G.T. Martinez, A. Rosenauer, S. Van Aert, Atom counting in HAADF STEM using a statistical model-based approach: methodology, possibilities, and inherent limitations, Ultramicroscopy 134 (November) (2013) 23–33.

[15] A. De wael, A. De Backer, L. Jones, P.D. Nellist, S. Van Aert, Hybrid statistics-simulations based method for atom-counting from ADF STEM images, Ultramicroscopy 177 (June (2017) 69–77.

[16] S. Van Aert, A. De Backer, G.T. Martinez, B. Goris, S. Bals, G. Van Tendeloo, A. Rosenauer, Procedure to count atoms with trustworthy single-atom sensitivity, Phys. Rev. B - Condens. Matter Mater. Phys. 87 (Feburary (6)) (2013) 064107.

[17] G.T. Martinez, A. Rosenauer, A. De Backer, J. Verbeeck, S. Van Aert, Quantitative composition determination at the atomic level using model-based high-angle annular dark field scanning transmission electron microscopy, Ultramicroscopy 137 (Feburary) (2014) 12–19.

[18] T. Grieb, K. Müller, R. Fritz, V. Grillo, M. Schowalter, K. Volz, A. Rosenauer, Quantitative chemical evaluation of dilute GaNAs using ADF STEM: avoiding surface strain induced artifacts, Ultramicroscopy 129 (June) (2013) 1–9.

[19] T. Grieb, K. Müller, R. Fritz, M. Schowalter, N. Neugebohrn, N. Knaub, K. Volz, A. Rosenauer, Determination of the chemical composition of GaNAs using STEM HAADF imaging and STEM strain state analysis, Ultramicroscopy 117 (June) (2012) 15–23.

[20] T. Grieb, K. Müller, E. Cadel, A. Beyer, M. Schowalter, E. Talbot, K. Volz, A. Rosenauer, Simultaneous Quantification of Indium and Nitrogen Concentration in InGaNAs Using HAADF-STEM, Microsc. Microanal. 20 (December (06)) (2014) 1740–1752.

[21] A. Rosenauer, T. Mehrtens, K. Müller, K. Gries, M. Schowalter, P. Venkata Satyam, S. Bley, C. Tessarek, D. Hommel, K. Sebald, M. Seyfried, J. Gutowski, A. Avramescu, K. Engl, S. Lutgen, Composition mapping in InGaN by scanning transmission electron microscopy, Ultramicroscopy 111 (July (8)) (2011) 1316–1327.

[22] T. Grieb, K. Müller, R. Fritz, M. Schowalter, N. Neugebohrn, N. Knaub, K. Volz, A. Rosenauer, Determination of the chemical composition of GaNAs using STEM HAADF imaging and STEM strain state analysis, Ultramicroscopy 117 (June) (2012) 15–23.

[23] C. Fuchs, A. Beyer, K. Volz, W. Stolz, MOVPE growth of (GaIn)As/Ga(AsSb)/(GaIn)As type-II heterostructures on GaAs substrate for near infrared laser applications, J. Cryst. Growth 464 (April) (2017) 201–205.

[24] A. Ballabio, "Germanium and SiGe epitaxial growth for mid-infrared applications.", Dissertation, Italy 2018.

[25] J.O. Oelerich, L. Duschek, J. Belz, A. Beyer, S.D. Baranovskii, K. Volz, STEMsalabim: a high-performance computing cluster friendly code for scanning transmission electron microscopy image simulations of thin specimens, Ultramicroscopy 177 (June) (2017) 91–96.

[26] A. Beyer, L. Duschek, Jü. Belz, J.O. Oelerich, K. Jandieri, K. Volz, Surface relaxation of strained Ga(P,As)/GaP heterostructures investigated by HAADF STEM, J.

[27] C. Rosenblad, H.R. Deller, A. Dommann, T. Meyer, P. Schroeter, H. von Känel, Silicon epitaxy by low-energy plasma enhanced chemical vapor deposition, J. Vac. Sci. Technol. A 16 (October (5)) (1998) 2785–2790.

[28] S. Marchionna, A. Virtuani, M. Acciarri, G. Isella, H. von Kaenel, Defect imaging of SiGe strain relaxed buffers grown by LEPECVD, Mater. Sci. Semicond. Process. 9 (August (4–5)) (2006) 802–805 SPEC. ISS..

[29] J.M. LeBeau, S. Stemmer, Experimental quantification of annular dark-field images in scanning transmission electron microscopy, Ultramicroscopy 108 (November (12)) (2008) 1653–1658.

[30] L. Jones, H. Yang, T.J. Pennycook, M.S.J. Marshall, S. Van Aert, N.D. Browning, M.R. Castell, P.D. Nellist, Smart Align—a new tool for robust non-rigid registration of scanning microscope data, Adv. Struct. Chem. Imaging 1 (December (1)) (2015) 8.

[31] D.S. He, Z.Y. Li, A practical approach to quantify the ADF detector in STEM, J. Phys. Conf. Ser. 522 (June (1)) (2014) 012017.

[32] K.T. Jacob, S. Raj, L. Rannesh, Vegard's law: a fundamental relation or an approximation? Int. J. Mater. Res. 98 (September (9)) (2007) 776–779.

[33] W. Li, M. Pessa, J. Likonen, Lattice parameter in GaNAs epilayers on GaAs: deviation from Vegard's law, Appl. Phys. Lett. 78 (May (19)) (2001) 2864–2866.

[34] O. Rubel, I. Németh, W. Stolz, K. Volz, Modeling the compositional dependence of electron diffraction in dilute GaAs- and GaP-based compound semiconductors, Phys. Rev. B - Condens. Matter Mater. Phys. 78 (August (7)) (2008) 075207.

[35] P.N. Keating, Effect of invariance requirements on the elastic strain energy of crystals with application to the diamond structure, Phys. Rev. 145 (May (2)) (1966) 637–645.

[36] T.G. Ramesh, S. Ramaseshan, Determination of the static displacement of atoms in a binary alloy system using anomalous scattering, Acta Crystallogr. Sect. A 27 (November (6)) (1971) 569–572.

[37] E.J. Kirkland, Advanced Computing in Electron microscopy: Second Edition, Springer, 2010.

[38] E.J. Kirkland, Image simulation in transmission electron microscopy, Simulation (2006) 1–14.

[39] B.D. Forbes, A.J. D'Alfonso, S.D. Findlay, D. Van Dyck, J.M. LeBeau, S. Stemmer, L.J. Allen, Thermal diffuse scattering in transmission electron microscopy, Ultramicroscopy 111 (December (12)) (2011) 1670–1680.

[40] A. Beyer, J. Belz, N. Knaub, K. Jandieri, K. Volz, Influence of spatial and temporal coherences on atomic resolution high angle annular dark field imaging, Ultramicroscopy 169 (October) (2016) 1–10.

[41] C. Dwyer, R. Erni, J. Etheridge, Method to measure spatial coherence of sub-angstrom electron beams, Appl. Phys. Lett. 93 (July (2)) (2008) 021115.

[42] C. Dwyer, R. Erni, J. Etheridge, Measurement of effective source distribution and its importance for quantitative interpretation of STEM images, Ultramicroscopy 110 (8) (2010) 952–957.

[43] D. Nguyen, S. Findlay, J. Etheridge, The spatial coherence function in scanning transmission electron microscopy and spectroscopy, Ultramicroscopy 146 (2014) 6–16.

[44] S.D. Findlay, J.M. LeBeau, Detector non-uniformity in scanning transmission electron microscopy, Ultramicroscopy 124 (January) (2013) 52–60.

[45] H. E, K.E. MacArthur, T.J. Pennycook, E. Okunishi, A.J. D'Alfonso, N.R. Lugg, L.J. Allen, P.D. Nellist, Probe integrated scattering cross sections in the analysis of atomic resolution HAADF STEM images, Ultramicroscopy 133 (October) (2013) 109–119.

[46] J. Belz, A. Beyer, L. Nattermann, K. Volz, On the effects of column occupancy and static atomic disorder on the analysis of chemical ordering in Ga(P(1-x)Bix) compounds, Microsc. Microanal. 23 (July (S1)) (2017) 1474–1475.

[47] K.H.W. van den Bos, L. Janssens, A. De Backer, P.D. Nellist, S. Van Aert, The atomic lensing model: new opportunities for atom-by-atom metrology of heterogeneous nanomaterials, Ultramicroscopy (December) (2018).

[48] J. Fertig, H. Rose, Resolution and contrast of crystalline objects in high-resolution scanning transmission electron microscopy, Optik (Stuttg) 59 (1981) 407–429.

[49] P.D. Nellist, S.J. Pennycook, Incoherent imaging using dynamically scattered coherent electrons, in *Ultramicroscopy* 78 (1–4) (1999) 111–124.

[50] A. Beyer, L. Duschek, J. Belz, J.O. Oelerich, K. Jandieri, K. Volz, Influence of surface relaxation of strained layers on atomic resolution ADF imaging, Ultramicroscopy 181 (October) (2017) 8–16.

[51] J. Belz, A. Beyer, T. Torunski, W. Stolz, K. Volz, Direct investigation of (sub-) surface preparation artifacts in GaAs based materials by FIB sectioning, Ultramicroscopy 163 (2016) 19–30.

[52] K.A. Mkhoyan, S.E. Maccagnano-Zacher, E.J. Kirkland, J. Silcox, Effects of amorphous layers on ADF-STEM imaging, Ultramicroscopy 108 (July (8)) (2008) 791–803.

[53] T. Grieb, M. Tewes, M. Schowalter, K. Müller-Caspary, F.F. Krause, T. Mehrtens, J.M. Hartmann, A. Rosenauer, Quantitative HAADF STEM of SiGe in presence of amorphous surface layers from FIB preparation, Ultramicroscopy 184 (2018) 29–36.

[54] R.R. Cerchiara, P.E. Fischione, J. Liu, J.M. Matesa, A.C. Robins, H.L. Fraser, A. Genc, Raising the standard of specimen preparation for aberration-corrected TEM and STEM, Micros. Today 19 (01) (2011) 16–19.

[55] P. Kükelhan, A. Beyer, C. Fuchs, M.J. Weseloh, S.W. Koch, W. Stolz, K. Volz, Atomic structure of 'W'-type quantum well heterostructures investigated by aberration-corrected STEM, J. Microsc. 268 (December (3)) (2017) 259–268.

Composition determination of multinary III/V semiconductors via STEM HAADF multislice simulations

L. Duschek, A. Beyer, J. O. Oelerich, and K. Volz,

Abstract

Knowledge of the microscopic elemental composition of multinary III/V semiconductor materials is crucial to the development of functionalized opto-electronic devices. Well-proven composition analysis methods, such as high-resolution x-ray diffraction (HRXRD), fail to determine the elemental composition when more than three atomic species are involved. In this work we propose a procedure for the composition analysis of multinary III/V semiconductors at atomic resolution using high angle annular dark field (HAADF) scanning transmission electron microscopy (STEM) image simulations. Our method exploits the dependence of HAADF-STEM image intensities on the atomic number and static atomic displacements (SAD) at different detector inner angles. Here, we describe the proposed method in detail using Ga(NAsP) as an example multinary material.

The authors' contributions

The algorithm was developed and implemented by me. A. Beyer and J. O. Oelerich supported the development of the algorithm. All authors contributed to the interpretation of the data as well as improved the manuscript written by me.

Composition determination of multinary III/V semiconductors via STEM HAADF multislice simulations

Lennart Duschek, Andreas Beyer[*], Jan Oliver Oelerich, Kerstin Volz

Materials Science Center and Faculty of Physics, Philipps-Universität Marburg, Hans-Meerweinstraße 6, 35032 Marburg, Germany

A B S T R A C T

Knowledge of the microscopic elemental composition of multinary III/V semiconductor materials is crucial to the development of functionalized opto-electronic devices. Well-proven composition analysis methods, such as high resolution X-ray diffraction (HRXRD), fail to determine the elemental composition when more than three atomic species are involved. In this work we propose a procedure for the composition analysis of multinary III/V semiconductors at atomic resolution using high angle annular dark field (HAADF) scanning transmission electron microscopy (STEM) image simulations. Our method exploits the dependence of HAADF-STEM image intensities on the atomic number and static atomic displacements (SAD) at different detector inner angles. Here, we describe the proposed method in detail using Ga(NAsP) as an example multinary material.

© 2017 Elsevier B.V. All rights reserved.

1. Motivation

A key issue in the development process of any novel functional material, e.g. a new compound semiconductor material or a device, is to gather information about the exact composition as well as elemental distribution on atomic length scales. For ternary materials, the method of choice to obtain laterally averaged information is high resolution X-ray diffraction (HRXRD) [1], where the elemental composition is determined via the lattice constant of the material by assuming Vegards law [2,3]. For quaternary layers where the former is not possible, Tilli et al. proposed a method that uses the (002) reflection's peak intensity of a single XRD measurement combined with the strain of the layer, to determine the composition of Ga(NAsP) layers with layer thicknesses up to 30 nm [4]. The quantitative analysis of scanning transmission electron microscopy (STEM) images has made a big progress over the last two decades [5–8]. A comparison of the mean intensity from STEM high angle annular dark field (HAADF) images with STEM multislice simulations [9] can also reveal the elemental composition of the TEM specimen [10–12], as well as give information about chemical homogeneity in ternary alloys [10,13,14] at nanometer length scales. The latter technique uses the fact that the intensity of a STEM image is proportional to the mean atomic number Z of the atom species [15–17]. With an aberration corrected microscope, this technique is also suitable for quantifying material

composition at atomic length scales [10,18]. Müller-Caspary et al. recently showed the use of angular resolved high resolution STEM to determine the N composition in a Ga(NAs) [19] multi-quantum well structure. The rather straight-forward interpretation of the so-called Z-contrast images becomes complicated for quaternary or even more-component semiconductor alloys, which are essential to achieve the desired band-gap/lattice constant combination for many semiconductor devices, e.g. (GaIn)(NAs) or (GaIn)(NAsSb) for solar cells [20]. The images obtained from STEM measurements are always a projection of the crystal's atomic potentials in the electron (e^-) beam direction. For atomic columns containing more than two different elements, the ADF intensity is ambiguous as an increasing amount of a low-Z element can always be compensated by a decrease of a heavier atomic species, preserving the mean atomic number. A method where the additional information required to quantify the composition in not atomically resolved STEM HAADF images comes from the measurement of the strain state of the quantum well, is presented by Grieb et al. in Ref. [21] with the example of (GaIn)(NAs). For this material system, it would in principle also be possible to derive the atomic composition on each sublattice, group III as well as group V, from high resolution STEM images, since each sublattice of this quaternary alloy consists only of a mixture of two atomic species. However, the method cannot be applied if one sublattice is composed of more than two atom species.

In this work, we propose a new procedure for the compositional analysis of multinary semiconductor alloys. This procedure aims to find the best fit between experimental and simulated high resolution STEM images, and allows for more than two elements

on one atomic column. Here we will focus on the procedure itself without providing application examples, which will be subject of upcoming publications. The method exploits the different behavior of the scattered intensity at the positions on and off the atomic columns (in the background), respectively, and at different detector inner angles in simulated ADF images. We apply the procedure to the model system $Ga(N_xAs_{100-x-y}P_y)$, a III/V semiconductor with a cubic zinc-blende crystal structure, the composition mixture solely occurs on the group V sublattice. It is important to note that the N incorporated in the material evokes crystal distortions called static atomic displacements (SAD) that have influence on the ADF intensity [22]. The SAD are the key to our method as we will show in the next section. The Ga(NAsP) material system was chosen as an example, as it has a tremendous application potential in the integration of optically active photonic devices on Silicon substrates [23–25]. However, the method presented here can be applied to any multinary crystalline material, where composition affects the scattered intensity at distinct spatial positions and/or at different detector angles.

2. Method

In the method presented here, we compare HAADF STEM intensities from a set of multislice STEM simulations, split into group III, V and background (BG) positions, i.e. the positions between the atomic columns. The set contains numerous simulations with systematically varied N and P composition for the chosen example of Ga(NAsP).

The super cells used for the multislice simulations were 5×5 unit cells (approx. 2.5 nm $\times$ 2.5 nm) wide and have a thickness of up to 60 unit cells (approx. 30 nm) in the electron beam direction, fitting in the typical thickness range of conventionally prepared TEM specimens of around 15 nm–30 nm. Both the N and the P atoms were distributed randomly on the group V lattice positions of a GaAs matrix and the resulting cell was relaxed via a valence force field (VFF) routine [26]. Structural relaxation is important when trying to match simulations as closely as possible to the real specimen. The SAD have a huge influence on the local intensity distribution [27] and thus are a key element for this technique. To underpin this statement the complete procedure will also be carried out with a simulation set built from unrelaxed super cells. The numerical simulations were performed with the STEM-salabim software package [28] based on the multislice algorithm of Kirkland [29,30]. This software package is designed for highly parallelized simulations on high-performance computer clusters. A more detailed description on the technical implementation and scaling of this code can be found in Ref. [28]. Thermal diffuse scattering (TDS) was taken into account using the frozen lattice approach [31], where the atomic positions get displaced statistically (Gaussian distribution) from their resting positions. Geometric aberrations were chosen to fit the parameters of a spherical aberration corrected microscope, namely the JEOL JEM-2200 FS, with $C_S = 2$ μm, $C_5 = 5$ mm, $\Delta f = -2$ nm, and a convergence semi-angle of 24 mrad. Chromatic aberration was taken into account with a defocus series as proposed in Ref. [32–35]. A two dimensional Lorentzian function with a full width at half maximum of 36 pm was convoluted with the image to model the source size of the electron gun [32]. Furthermore the detector sensitivity was determined and applied to the simulation as proposed by LeBeau et al. in Ref. [7]. This was done to match the simulations as closely as possible to experimental STEM images.

The sampling of the simulation set was chosen to be in the range of experimentally reasonable compositions of N (0–20%) and P (0–30%) with a step size of 2%, resulting in 150 single concentration steps. For each concentration point, a defocus series with 7 defoci and 10 phonon configurations (TDS), was calculated. A new
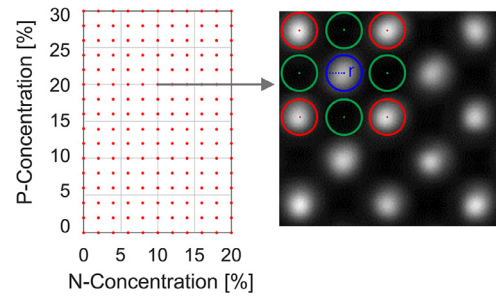

Fig. 1. A scheme of the composition set is depicted on the left side. Every red mark represents a full STEM multislice simulation. With given parameters an image can be formed, as displayed on the right side with examples of group III (red), V (blue), and BG column positions (green), and integration radius r. (For interpretation of the references to color in this figure legend, the reader is referred to the web version of this article.)

set of phonon configurations was used for each defocus, resulting in 70 independent phonon configurations for each concentration point. With this, a total of 10,500 simulations was performed. Each result was stored as a compressed binary file using NetCDF [36]. To save disk space, the phonon configurations for each defocus were averaged leading to a file size of approx. 500 MB per simulation. The total amount of file space covered by the complete simulation set sums up to roughly 750 GB. The simulation time for one concentration point parallelized over 128 computing nodes was about 11 h. Assuming that the simulation time scales almost linearly, the simulation time on a single desktop PC with 8 computing cores would take 26,400 h or approximately 3 years. With the computational resources of a mid-sized cluster, on the other hand, the total simulation time for the whole concentration map is about 2 weeks, since many simulations can run simultaneously. Besides the long simulation time, the file size of one concentration point is about 4 GB which means that only one file at a time fits into the memory of a common desktop computer with 8 GB of RAM. By using the principle of selective data loading and parallelizing this step to the 8 threads of a modern desktop machine, a processing time of approx. 5 min was achieved to gather information from the whole simulation set.

3. Results

In the following paragraph, we will first explain the transformation of the multislice simulation set into *composition maps* that represent the integrated STEM intensity on distinct spatial positions. Afterwards we will discuss the simulated *composition maps*, built from the unrelaxed as well as the relaxed super cell set, for a high angular range of $\theta_{in-out} = 71 - 174$ mrad which will we be referred to be the HAADF regime from now on. We will then investigate the *composition maps* for a low angular range, namely $\theta_{in-out} = 34 - 136$ mrad and will refer to this as low angle ADF (LAADF) regime. In the LAADF regime we will also look at the *composition maps* built from the unrelaxed and the relaxed super cell set with a focus on the angular dependence of the SAD effect. In the end, *composition maps* will be combined and a sanity check of the presented algorithm with three exemplarily chosen $Ga(N_xAs_{100-x-y}P_y)$ compositions is performed.

The basis of the presented method is a set of simulations with systematically varied N - P concentration as explained in the previous section. Every red mark in Fig. 1 represents a full STEM multislice simulation. With given simulation parameters, including the detector range θ_{in-out} and sensitivity θ_{sen}, chromatic as well as geometric aberrations, and sample thickness *t*, a HAADF image is formed. The atomic column positions are found by a 2D peak finding algorithm, implemented in a custom MATLAB script and di-
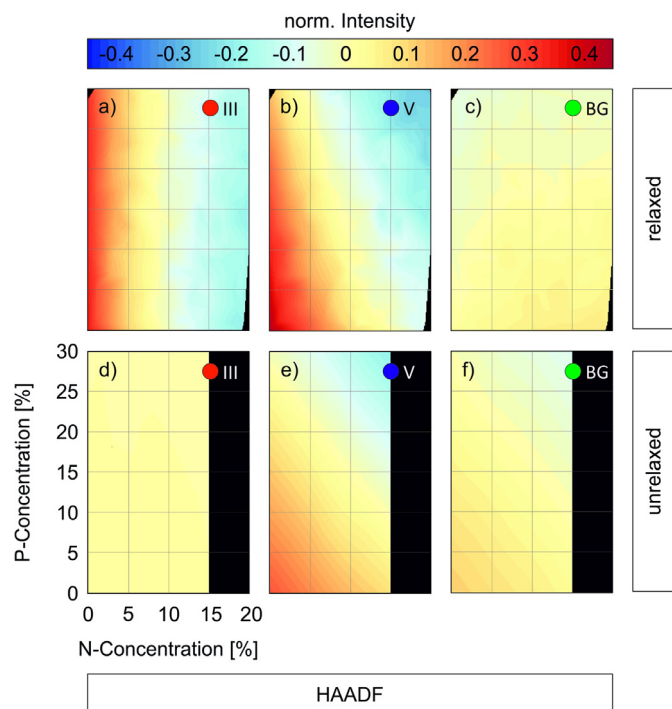
Fig. 2. Normalized composition maps for the different atom column positions (III, V) as well as the background (BG) for $\theta_{in-out} = 71 - 174$ mrad derived from the relaxed (a)–(c) and unrelaxed (d)–(f) super cells are shown. The values of the color scale represent the relative deviation of the scattered intensity of a single composition point to the mean value of the map. The composition axes from subfigure (d) correspond to all subfigures in the figure. (For interpretation of the references to color in this figure legend, the reader is referred to the web version of this article.)

vided into group III and V atomic column positions. Afterwards, the BG positions are determined by finding the center of mass between 4 neighboring atomic columns (Fig. 1).

The intensity of the different atomic columns is obtained by averaging the intensity values in a fixed radius r around the column position. The radius r is chosen in a way that it is big enough to cover the major part of the atomic column but does not interfere with the surrounding peak integrations. In this work an integration radius of 24 pm was chosen. By averaging the integrated column intensities over approx. 160 columns, three independent mean intensity values $\bar{I}_{III}(N,P)$ for group III, $\bar{I}_V(N,P)$ for group V, and $\bar{I}_{BG}(N,P)$ for the background positions are obtained for each N, P concentration. Applying this procedure to every simulation in the simulation set, with otherwise fixed parameters, three independent maps $I_{III, V, BG}$ are created which we will call *composition maps* from now on. Fig. 2(a)–(c) visualizes all three *composition maps* for a fixed θ_{in-out} with the help of color-coded maps. First we want to focus on the influence of N and P concentration on the STEM intensity. To visualize the effect of the composition on the intensity of the different atomic column positions, it is easier to look at the normalized intensities of the *composition map* rather than the absolute intensities. The normalized intensity of a *composition map*, using the example of a group V column, is calculated via:

$$\frac{\bar{I}_V(N,P)}{\text{mean}(I_V)} \ .$$

Fig. 2(a)–(c) shows the normalized *composition maps* of group III (a), group V (b), and BG positions (c). Since the sampling of the maps is finite (2%), the intensity between two composition points is linearly interpolated. All *composition maps* depicted in Fig. 2 are built for the HAADF regime. A strong influence of the N composition on the relative intensity deviation is noticeable for

the group III column, which is counter-intuitive since it consists of Ga only, while the influence from the P concentration is negligible. This feature is an immediate consequence of the SAD effect and is in very good agreement with the expectation. An N atom on the group V sublattice distorts the crystal locally, resulting in smaller bond lengths to its neighbors. Therefore, the Ga atoms bound to the N atom get distorted from their resting position. Consequently the channeling effect [37] of the beam on a well-aligned atomic column is drastically reduced and the total column intensity of the group III sublattice is spread to a wider region. Keeping the integration radius r constant, the integrated intensity gets smaller accordingly. With increasing N concentration, this effect becomes stronger and the corresponding group III column intensity decreases. Additionally, the mean atomic number Z on the group V sublattice decreases when the N and the P composition increases, and consequently the group V column intensity decreases. This can be observed in the map of group V depicted in Fig. 2(b). The BG intensity, shown in Fig. 2(c), shows no significant N–P dependency. Distortions induced by N mainly lead to increased diffuse scattering at lower angular regions [38], hence, we also do not expect any influence on the BG for the detector range chosen for Fig. 2.

From the previous observations, we conclude that the SAD effect projects information about a group V element (N) on the group III lattice intensity. This splits the information from one mixed sublattice to different spatial positions and thus enables us to investigate a material system like Ga(NAsP). In fact, if we would neglect the SAD effect or choose a multinary material system without SAD effect, the information about the individual elements would be mixed on one sublattice. To prove that the SAD effect is responsible for the behavior of the group III, a simulation set with unrelaxed Ga(NAsP) super cells was created. The set was sampled coarser with steps of 5% in N and 10% in P – direction. Fig. 2(d)–(f) shows the three *composition maps* built from the unrelaxed super cells. The impact of N on the group III intensity, observed in Fig. 2(a), is not visible anymore in the unrelaxed *composition map* in (d). Since the concentration change solely happens on the group V lattice, this is the only map where we can find the influence of N and P concentration on the intensity. Map (e) is nearly identical to the one observed in Fig. 2(b), representing the decreasing mean atomic number Z of the group V sublattice. Because of TDS, the BG map (f) also follows the decreasing mean atomic number Z. This means that a composition quantification is impossible with the maps built from the unrelaxed super cells. As local distortions evoke an increase of diffuse scattering in lower angular regions, hence, we will investigate the corresponding maps, relaxed and unrelaxed, for the LAADF regime, in the following.

Fig. 3(a)–(c) shows the *composition maps* for the LAADF regime built from the relaxed super cells. The course of the group III map for the low detector inner angle is very similar to the map of the large detector inner angle. Also group V (b) shows the same trend that is observed in Fig. 2(b). However, it should be pointed out that the color scale of the maps changes. The largest deviation from the mean value can be found at the background positions (c). This drastically depends on the N – composition which can be attributed to the SAD effect. The Ga atoms are shifted away from their ideal column position to the off-column positions. The on-column intensity is spread in a wider region, adding more intensity to the background. With increasing N content the group III intensity decreases and more intensity is scattered into the background, which is especially visible in low angle regions. To underpin this finding, we will present the corresponding *composition maps* derived from the unrelaxed cells in the following, where we do not expect the previous behavior of the group III intensity, since every atom is still on its resting position in the crystal. The *composition maps* built from the unrelaxed simulation set for the LAADF regime are depicted in Fig. 3(d)–(f). No significant changes com-
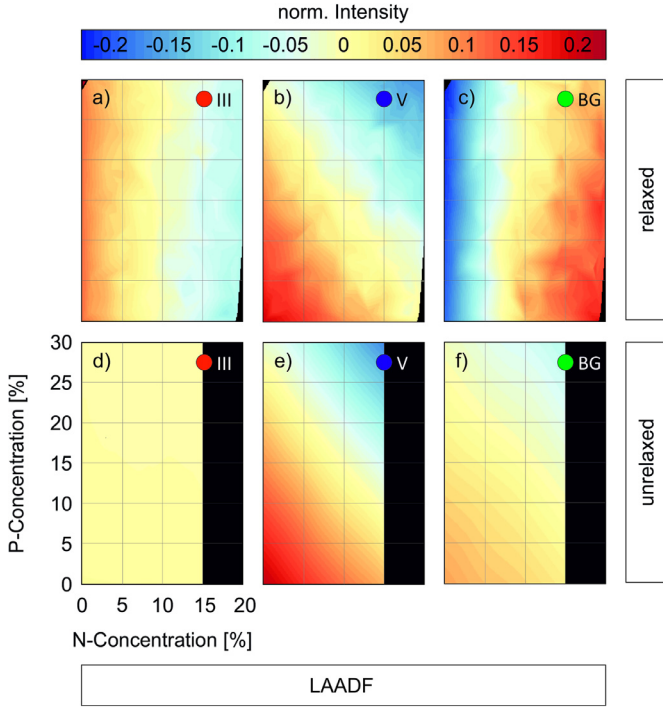
Fig. 3. Normalized composition maps for the different atomic column positions (III, V) as well as the background (BG) for $\theta_{in-out} = 34 - 136$ mrad derived from the relaxed (a)–(c) and unrelaxed (d)–(f) super cells are shown. The Background shows a much stronger influence on the N–composition compared to Fig. 2. The composition axes from subfigure (d) correspond to all subfigures in the figure. (For interpretation of the references to color in this figure legend, the reader is referred to the web version of this article.)

pared to the *composition maps* built from the unrelaxed simulation set shown in Fig. 2(d)–(f) are noticeable except that the color scale is slightly different. The change of intensity still occurs on the group V lattice only, originating from the change of mean atomic number Z by intermixing from N and P with As. To sum up the observations gained from Figs. 2 and 3, we saw that the lattice distortion evoked by N yields information about a group III element on group III positions. Furthermore, information about the N concentration can be extracted from the off-column positions at low detector angles. Also, the intensity scales with the percentage of the element that is responsible for the lattice distortion. This enables us to determine the N and P concentration independently from each other.

In the following paragraph, we want to present an algorithm that combines the gained information from different column position as well as from different θ_{in-out} to determine the composition of the sample.

The main goal of the algorithm is to find the smallest deviation between input values $\bar{I}_{III,V,BG}^{exp}(\theta_{in-out})$ and the *composition maps* $I_{III,V,BG}(\theta_{in-out})$. Therefore, the first step is to build the *deviation maps* for the individual *composition maps* via:

$$I_{III}^\Delta(\theta_{in-out}) = \frac{|I_{III}(\theta_{in-out}) - \bar{I}_{III}^{exp}(\theta_{in-out})|}{I_{III}(\theta_{in-out})}.$$

Fig. 4 shows the *deviation maps* $I_{III,V,BG}^\Delta$ for exemplarily chosen input values $\bar{I}_{III,V,BG}^{exp}(\theta_{in-out})$ obtained from a $Ga(N_5As_{75}P_{20})$ simulation for the HAADF as well as the LAADF regime with a thickness chosen to be 20 nm. When using real STEM images the sample thickness has to be determined very carefully to account for thickness difference caused by sample preparation. Many different methods have been proposed to determine the sample thickness, for example by comparing HAADF intensity to adequate multislice
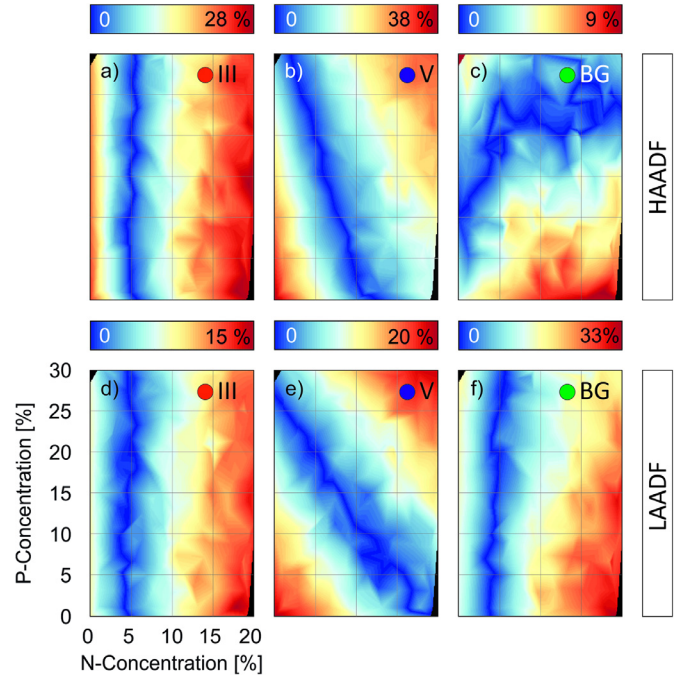

Fig. 4. The deviation maps for an example $Ga(N_5As_{75}P_{20})$ composition are displayed for the individual atomic columns in the HAADF (a) – (c) as well as the LAADF (d) – (f) regime. The color scale represents relative deviation between the input values and the corresponding composition map. The composition axes from subfigure (d) correspond to all subfigures in the figure. (For interpretation of the references to color in this figure legend, the reader is referred to the web version of this article.)

simulations [12] or using electron energy loss spectroscopy (EELS) [39]. The color scale in Fig. 4 now represents the relative deviation between the input value and the *composition maps*, starting at 0 (in dark blue) for perfect agreement.

Map I_{III}^Δ(HAADF) (a) shows the smallest deviation for an N concentration of approx. 5% which is independent of the P concentration. The same behavior can be seen in the I_{III}^Δ(LAADF) (d) map. With this information, we certainly know that the input intensities have to come from a material with approx. 5% N but have no information about the P content up to now. The Maps from I_V^Δ(HAADF) (b) and I_V^Δ(LAADF) (e) both show the smallest deviation on a diagonal line with slightly different slopes but both crossing the 20% P point. If we would now combine the maps from I_{III}^Δ(HAADF) & I_{III}^Δ (LAADF) (a) & (d) and I_V^Δ(HAADF) & I_V^Δ (LAADF) (b) & (e) without the I_{BG}^Δ (c) & (f), the information would be sufficient to determine the input composition to 5% N and 20% P. But this is just the case for the example of Ga(NAsP) with N having a tremendous influence on these maps. Additional information will enhance the accuracy of the determination. Thus, we define the *total deviation map* I_{total}^Δ as follows:

$$I_{total}^\Delta = \frac{\sum_{j=1}^M I_{III}^\Delta(\theta_j) + I_V^\Delta(\theta_j) + I_{BG}^\Delta(\theta_j)}{3 \cdot M},$$

where the used detector ranges are represented by $\theta_1 \dots \theta_M$. There is the option of weighting the individual *deviation maps* $I_{III,V,BG}^\Delta$ with respect to each other, which will be tackled in further studies. This *total deviation map* now represents the combined relative deviations between the input values $\bar{I}_{III,V,BG}^{exp}(\theta_{in-out})$ and the *deviation maps* $I_{III,V,BG}^\Delta(\theta_{in-out})$ for different detector ranges. In this *total deviation map* we can now identify the global minimum of all individual maps at once, which gives us the N and P concentration with the best agreement between input values and individual *deviation maps*. To check if the algorithm is self-consistent, a sanity check was performed, with the results of I_{total}^Δ depicted
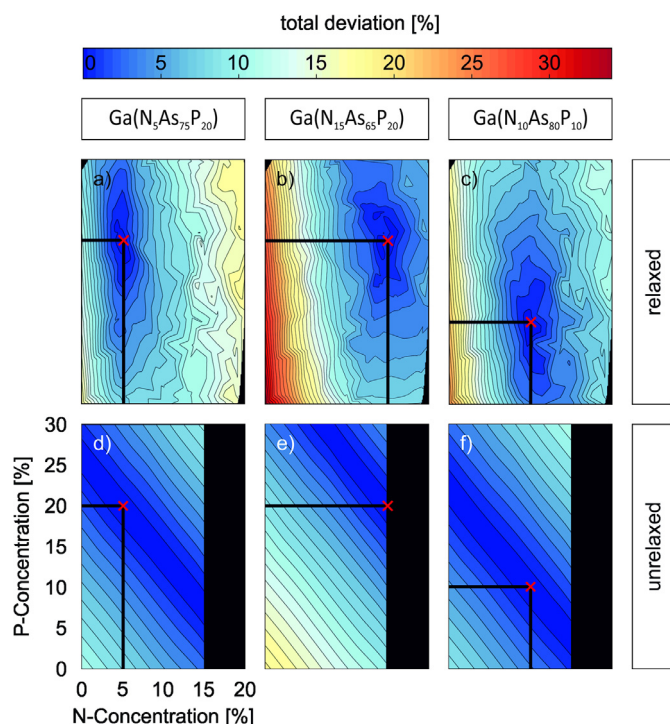
Fig. 5. Sanity Check of the algorithm with three different input compositions. The total deviation maps show a minimum area of total deviation around the input composition. The red cross marks the global minimum of the map and thus the calculated N-P composition. The black lines represent plateaus with 1% error steps. The composition axes from subfigure (d) correspond to all subfigures in the figure. (For interpretation of the references to color in this figure legend, the reader is referred to the web version of this article.)

in Fig. 5. For this check, simulated images for fixed N-P compositions, namely $Ga(N_5As_{75}P_{20})$ (a) & (d), $Ga(N_{15}As_{65}P_{20})$ (b) & (e) and $Ga(N_{10}As_{80}P_{10})$ (c) & (f), were created and treated like experimentally acquired images. The maps I_{total}^Δ are depicted as contour plots with a spacing of 1%, which means that every N-P point included in a colored plateau surrounded by a black line has the same total deviation from the input values within a tolerance of 1%. This leads to distinct areas, which represent N-P compositions that differ around a chosen uncertainty. The red crosses represent the total minima of the map obtained using the procedure described above. Fig. 5(a)–(c) shows I_{total}^Δ, created with the relaxed *composition maps*. The total minima of the maps (a)–(c) show perfect agreement with the chosen input compositions, which demonstrates that the algorithm is self-consistent. The area around the global minimum is elongated elliptically, with a larger radius in the P-axis with approx. 4% uncertainty and a smaller radius along the N-axis with approx. 2% uncertainty. This indicates that the P content is harder to determine accurately compared to the N content, due to the bigger difference in atomic number and the SAD induced by N.

The sanity check was also performed with the *composition maps* built from the unrelaxed super cells with the resulting *total deviation maps* I_{total}^Δ depicted in Fig. 5(d)–(e). A very broad diagonal stripe that represents 1% uncertainty around the input composition is visible in every map. This means that every composition within that stripe is equally possible for this set of input values. Since the group III and BG intensities (Fig. 2(d) & (f)) from the *composition maps* created from the unrelaxed super cells show no significant dependency on the N or P content, the *total deviation maps* I_{total}^Δ are dominated by the course of the group V maps (Fig. 2(e)). With this intensity information it is not possible to determine the composition of a material with different elements mixed on one sub-

lattice accurately. Furthermore, the overall gradient of the maps built from the unrelaxed super cell set, shown in Fig. 5(d)–(f), is less steep than the maps created with the relaxed super cell set depicted in Fig. 5(a)–(c).

In summary, the sanity check performed with the *composition maps* built from the relaxed super cells shows that it is possible to determine the concentration of a quaternary semiconductor alloy with STEM image intensities, even when the intermixing of the atoms solely happens on one sublattice. This is possible because the SAD effect evoked by N projects information about a group V element (N) onto the group III sublattice.

Of course, the algorithm will be applied to experimental images in the future with the goal to gain highly resolved information on the composition for quaternary semiconductor alloys.

4. Summary

In this work, we presented a method to determine the composition of a quaternary III/V semiconductor alloy by comparing its HAADF STEM images to a set of STEM image simulations with systematically varied elemental composition. The simulation cells were prepared carefully, including VFF relaxation to account for SAD effects. Due to the high number of simulations needed for a profound simulation set, the simulations had to run on a high performance computing cluster. For the model system Ga(NAsP), the N atoms change the group III column intensity provoked by the SAD effect, since this behavior is not visible using unrelaxed simulation cells. With the information from the group III sublattice and the group V sublattice, it is already possible to determine the composition. Additional measurements, especially at lower detector angular ranges, improve the accuracy of the method presented here. Therefore, we combined *deviation maps* $I_{III,V,BG}^\Delta$ from multiple θ_{in-out} to take care of all dependencies at once. In the end, we presented a successful sanity check with three exemplarily chosen Ga(NAsP) alloys to check whether our algorithm is self-consistent. With this we could show that it is possible to determine the concentration of a quaternary semiconductor alloy via STEM images at atomic resolution without further information from any supplementary method. This method has great potential to be implemented in the standard workflow when investigating semiconductor alloys with STEM.

References

[1] L. De Caro, C. Giannini, L. Tapfer, Determination of the lattice strain and chemical composition of semiconductor heterostructures by high-resolution x-ray diffraction, J. Appl. Phys. 79 (1996) 4101, doi:10.1063/1.361773.
[2] W. Li, M. Pessa, J. Likonen, Lattice parameter in GaNAs epilayers on GaAs: deviation from Vegard's law, Appl. Phys. Lett. 78 (2001) 2864–2866, doi:10.1063/1.1370549.
[3] S. Raj, Vegard's law: a fundamental relation, Int. J. Mat. Res. 98 (2007) 776–779.
[4] J.M. Tilli, H. Jussila, K.M. Yu, T. Huhtio, M. Sopanen, Composition determination of quaternary GaAsPN layers from single X-ray diffraction measurement of quasi-forbidden (002) reflection, J. Appl. Phys. (2014) 115, doi:10.1063/1.4878939.
[5] D.O. Klenov, S.D. Findlay, L.J. Allen, S. Stemmer, Influence of orientation on the contrast of high-angle annular dark-field images of silicon, (n.d.). doi:10.1103/PhysRevB.76.014111.
[6] J.M. Lebeau, S.D. Findlay, L.J. Allen, S. Stemmer, Quantitative atomic resolution scanning transmission electron microscopy, Phys. Rev. Lett. 100 (2008) 1–4, doi:10.1103/PhysRevLett.100.206101.
[7] J.M. LeBeau, S. Stemmer, Experimental quantification of annular dark-field images in scanning transmission electron microscopy, Ultramicroscopy 108 (2008) 1653–1658, doi:10.1016/j.ultramic.2008.07.001.

[8] A. Rosenauer, K. Gries, K. Müller, A. Pretorius, M. Schowalter, A. Avramescu, K. Engl, S. Lutgen, Measurement of specimen thickness and composition in Alx Ga1 - x N / GaN using high-angle annular dark field images, Ultramicroscopy 109 (2009) 1171–1182, doi:10.1016/j.ultramic.2009.05.003.

[9] J.M. Cowley, a.F. Moodie, The scattering of electrons by atoms and crystals. I. A new theoretical approach, Acta Crystallogr 10 (1957) 609–619, doi:10.1107/S0365110X57002194.

[10] T. Grieb, K. Müller, R. Fritz, M. Schowalter, N. Neugebohrn, N. Knaub, K. Volz, A. Rosenauer, Determination of the chemical composition of GaNAs using STEM HAADF imaging and STEM strain state analysis, Ultramicroscopy 117 (2012) 15–23, doi:10.1016/j.ultramic.2012.03.014.

[11] T. Grieb, K. Müller, R. Fritz, V. Grillo, M. Schowalter, K. Volz, A. Rosenauer, Quantitative chemical evaluation of dilute GaNAs using ADF STEM: avoiding surface strain induced artifacts, Ultramicroscopy 129 (2013) 1–9, doi:10.1016/j.ultramic.2013.02.006.

[12] A. Rosenauer, K. Gries, K. Müller, A. Pretorius, M. Schowalter, A. Avramescu, K. Engl, S. Lutgen, Measurement of specimen thickness and composition in Alx Ga1 - x N / GaN using high-angle annular dark field images, Ultramicroscopy 109 (2009) 1171–1182, doi:10.1016/j.ultramic.2009.05.003.

[13] T. Wegele, A. Beyer, P. Ludewig, P. Rosenow, L. Duschek, K. Jandieri, R. Tonner, W. Stolz, K. Volz, Interface morphology and composition of Ga(NAsP) quantum well structures for monolithically integrated LASERs on silicon substrates, J. Phys. D Appl. Phys. 49 (2016) 75108, doi:10.1088/0022-3727/49/7/075108.

[14] N. Knaub, A. Beyer, T. Wegele, P. Ludewig, K. Volz, Quantification of Bi distribution in MOVPE-grown Ga(AsBi) via HAADF STEM, J. Cryst. Growth 433 (2016) 89–96, doi:10.1016/j.jcrysgro.2015.10.007.

[15] S.J. Pennycook, Z-contrast stem for materials science, Ultramicroscopy 30 (1989) 58–69, doi:10.1016/0304-3991(89)90173-3.

[16] A. Rosenauer, M. Schowalter, STEMSIM - A new software tool for simulation of STEM HAADF Z-contrast imaging, Microsc. Semicond. Mater. 2007 (2008) 170–172 Springer P, doi:10.1007/978-1-4020-8615-1_36.

[17] S.J. Pennycook, D.E. Jesson, High-resolution Z-contrast imaging of crystals, Ultramicroscopy 37 (1991) 14–38, doi:10.1016/0304-3991(91)90004-P.

[18] A. Rosenauer, T. Mehrtens, K. Müller, K. Gries, M. Schowalter, P. Venkata Satyam, S. Bley, C. Tessarek, D. Hommel, K. Sebald, M. Seyfried, J. Gutowski, A. Avramescu, K. Engl, S. Lutgen, Composition mapping in InGaN by scanning transmission electron microscopy, Ultramicroscopy 111 (2011) 1316–1327, doi:10.1016/j.ultramic.2011.04.009.

[19] K. Müller-Caspary, O. Oppermann, T. Grieb, F.F. Krause, A. Rosenauer, M. Schowalter, T. Mehrtens, A. Beyer, K. Volz, P. Potapov, Materials characterisation by angle-resolved scanning transmission electron microscopy, Sci. Rep. 6 (2016) 37146, doi:10.1038/srep37146.

[20] D.B. Jackrel, S.R. Bank, H.B. Yuen, M.A. Wistey, J.S. Harris, A.J. Ptak, S.W. Johnston, D.J. Friedman, S.R. Kurtz, Dilute nitride GaInNAs and GaInNAsSb solar cells by molecular beam epitaxy, J. Appl. Phys. 101 (2007), doi:10.1063/1.2744490.

[21] T. Grieb, K. Müller, E. Cadel, A. Beyer, M. Schowalter, E. Talbot, K. Volz, A. Rosenauer, Simultaneous quantification of indium and nitrogen concentration in InGaNAs using HAADF-STEM, Microsc. Microanal. 20 (2014) 1740–1752, doi:10.1017/S1431927614013051.

[22] V. Grillo, K. Mueller, K. Volz, F. Glas, T. Grieb, A. Rosenauer, Strain, composition and disorder in ADF imaging of semiconductors, J. Phys. Conf. Ser. 326 (2011) 12006, doi:10.1088/1742-6596/326/1/012006.

[23] S. Liebich, M. Zimprich, A. Beyer, C. Lange, D.J. Franzbach, S. Chatterjee, N. Hossain, S.J. Sweeney, K. Volz, B. Kunert, W. Stolz, Laser operation of Ga(NAsP) lattice-matched to (001) silicon substrate, Appl. Phys. Lett. 99 (2011) 1–4, doi:10.1063/1.3624927.

[24] B. Kunert, K. Volz, J. Koch, W. Stolz, Direct-band-gap Ga (NAsP)-material system pseudomorphically grown on GaP substrate, Appl. Phys. Lett. 88 (2006) 182108.

[25] S. Wirths, R. Geiger, N. Von Den Driesch, G. Mussler, T. Stoica, S. Mantl, Z. Ikonic, M. Luysberg, S. Chiussi, J.M. Hartmann, Lasing in direct-bandgap GeSn alloy grown on Si, Nat. Photonics 9 (2015) 88–92.

[26] P.N. Keating, Effect of invariance requirements on the elastic strain energy of crystals with application to the diamond structure, Phys. Rev. 145 (1966) 637–645, doi:10.1103/PhysRev.145.637.

[27] V. Grillo, E. Carlino, F. Glas, Influence of the static atomic displacement on atomic resolution Z-contrast imaging, Phys. Rev. B 77 (2008) 1–6, doi:10.1103/PhysRevB.77.054103.

[28] J.O. Oelerich, L. Duschek, J. Belz, A. Beyer, S.D. Baranovskii, K. Volz, STEMsalabim: A high-performance computing cluster friendly code for scanning transmission electron microscopy image simulations of thin specimens, Ultramicroscopy 177 (2017) 91–96, doi:10.1016/j.ultramic.2017.03.010.

[29] E.J. Kirkland, Advanced computing in electron microscopy, J. Appl. Cryst. 32 (1999) 378–379.

[30] E.J. Kirkland, Image simulation in transmission electron microscopy, Simulation (2006) 1–14.

[31] B.D. Forbes, A.J. D'Alfonso, S.D. Findlay, D. Van Dyck, J.M. LeBeau, S. Stemmer, L.J. Allen, Thermal diffuse scattering in transmission electron microscopy, Ultramicroscopy 111 (2011) 1670–1680, doi:10.1016/j.ultramic.2011.09.017.

[32] A. Beyer, J. Belz, N. Knaub, K. Jandieri, K. Volz, Influence of spatial and temporal coherences on atomic resolution high angle annular dark field imaging, Ultramicroscopy 169 (2016) 1–10, doi:10.1016/j.ultramic.2016.06.006.

[33] C. Dwyer, R. Erni, J. Etheridge, Method to measure spatial coherence of subangstrom electron beams, Appl. Phys. Lett. 93 (2008), doi:10.1063/1.2957648.

[34] C. Dwyer, R. Erni, J. Etheridge, Measurement of effective source distribution and its importance for quantitative interpretation of STEM images, Ultramicroscopy 110 (2010) 952–957, doi:10.1016/j.ultramic.2010.01.007.

[35] D.T. Nguyen, S.D. Findlay, J. Etheridge, The spatial coherence function in scanning transmission electron microscopy and spectroscopy, Ultramicroscopy 146 (2014) 6–16, doi:10.1016/j.ultramic.2014.04.008.

[36] Unidata, Network common data form (NetCDF), (2016). doi:10.5065/D6H70CW6.

[37] V. Grillo, The effect of surface strain relaxation on HAADF imaging, Ultramicroscopy 109 (2009) 1453–1464, doi:10.1016/j.ultramic.2009.07.010.

[38] V. Grillo, K. Mueller, K. Volz, F. Glas, T. Grieb, A. Rosenauer, Strain, composition and disorder in ADF imaging of semiconductors, J. Phys. Conf. Ser. 326 (2011) 12006, doi:10.1088/1742-6596/326/1/012006.

[39] R.F. Egerton, M. Malac, EELS in the TEM, J. Electron Spectros. Relat. Phenomena 143 (2005) 43–50, doi:10.1016/j.elspec.2003.12.009.

Segregation at interfaces in "W"-type quantum well heterostructures explored by atomic resolution STEM

P. Kükelhan, A. Beyer, L. Duschek, C. Fuchs, S. Firoozabadi, J. O. Oelerich, W. Stolz, K. Volz

Abstract:

Surface segregation and interaction effects of *In* and *Sb* in *(Ga,In)As/Ga(As,Sb)/(Ga,In)As*- "W"-type quantum well heterostructures ("W"-QWHs) are investigated by high angle annular dark field scanning transmission electron microscopy with atomic resolution. "W"-QWHs are a promising candidate for type-II laser applications in telecommunications and have been grown by metal organic vapour phase epitaxy on *GaAs* substrate. The composition is determined with atomic resolution and accuracy by comparison to complementary contrast simulations. From composition profiles, an altered segregation in "W"-QWHs in comparison to single *(Ga,In)As* and *Ga(As,Sb)* quantum wells grown on *GaAs* is detected. *In* and *Sb* are clearly influencing each other during the growth, including blocking effects of *In* incorporation by *Sb* and vice versa. Especially, growth rate and total amount of *Sb* incorporated for *Ga(As,Sb)* are decreased by *In* being present.

The authors' contributions

I developed and implemented the algorithm used to determine the concentration of the experimental STEM images in this publication. Furthermore P. Kükelhan and I performed the simulation of the large amount of multislice data. The images used in this publication were recorded by P. Kükelhan. All co-authors helped to improve the manuscript written by P. Kükelhan.

Surface relaxation of strained Ga (P,As)/GaP heterostructures investigated by HAADF STEM

A. Beyer, L. Duschek, J. Belz, J. O. Oelerich, K. Jandieri, and K. Volz,
Journal of Microscopy, vol. 268, no. 3, pp. 239–247, 2017.

Abstract:

The surfaces of thin transmission electron microscopy (TEM) specimens of strained heterostructures can relax. The resulting bending of the lattice planes significantly influences high-angle annular dark field (HAADF) measurements. We investigate the impact by evaluating the intensities measured at the atomic columns as well as their positions in high-resolution HAADF images. In addition, the consequences in the diffraction plane will be addressed by simulated position averaged convergent beam electron diffraction (PACBED) patterns. The experimental column intensities and positions acquired from a strained Ga(P,As) quantum well (QW) embedded in a in a GaP matrix agree very well with frozen phonon contrast simulations, if the surface relaxation is taken into account by finite element relaxation. Neglecting the surface relaxation the As content of the QW can be significantly underestimated. Taking the effects into account correctly, we find that the lower interface of the investigated Ga(P,As) QW is atomically abrupt whereas the upper one is smeared out.

The authors' contributions

J. Belz together with K. Jandieri developed the workflow of the macroscopic elastic relaxation of thin TEM supercells. My contribution was the help with the seamless integration in the available workflow as well as technical support with the algorithm. The multislice simulation that were used in the publication were done by me. The analysis of the simulated data was done by me and together with A. Beyer we did the interpretation of the data. All co-authors helped to improve the manuscript written by A. Beyer.

Surface relaxation of strained Ga(P,As)/GaP heterostructures investigated by HAADF STEM

ANDREAS BEYER [iD], LENNART DUSCHEK, JÜRGEN BELZ, JAN OLIVER OELERICH, KAKHABER JANDIERI & KERSTIN VOLZ

Materials Science Center and Faculty of Physics, Philipps-Universität Marburg, Marburg, Germany

Summary

The surfaces of thin transmission electron microscopy (TEM) specimens of strained heterostructures can relax. The resulting bending of the lattice planes significantly influences high-angle annular dark field (HAADF) measurements. We investigate the impact by evaluating the intensities measured at the atomic columns as well as their positions in high-resolution HAADF images. In addition, the consequences in the diffraction plane will be addressed by simulated position averaged convergent beam electron diffraction (PACBED) patterns.

The experimental column intensities and positions acquired from a strained Ga(P,As) quantum well (QW) embedded in a in a GaP matrix agree very well with frozen phonon contrast simulations, if the surface relaxation is taken into account by finite element relaxation. Neglecting the surface relaxation the As content of the QW can be significantly underestimated. Taking the effects into account correctly, we find that the lower interface of the investigated Ga(P,As) QW is atomically abrupt whereas the upper one is smeared out.

Introduction

Aberration corrected scanning transmission electron microscopy (STEM) has become an essential method in the field of materials science (Nellist *et al.*, 2004; Krivanek *et al.*, 2010). In particular, the high-angle annular dark field (HAADF) technique was proven to be a valuable tool in addressing complex heterostructures due to the easily interpretable Z contrast (Pennycook, 1989). Such heterostructures consist of various materials and therefore are usually strained (Tan *et al.*, 2016; Wang *et al.*, 2016; Xu *et al.*, 2016).

When an electron transparent transmission electron microscopy (TEM) sample is prepared from such a strained

heterostructure, the strain partially relaxes at the free surface (Gibson & Treacy, 1984; Treacy *et al.*, 1985; De Caro *et al.*, 1995). This leads to a deformation at the surface and more importantly, a bending of the lattice planes. The strength of the bending depends on the sample geometry, that is the sample thickness and the widths of the constituent layers (Treacy *et al.*, 1985). The finite element (FE) formalism can be used to model the displacement fields for a given sample geometry (Rosenauer *et al.*, 2006; De Caro *et al.*, 1997). The mistilt angle of the lattice planes with respect to perfect zone axis conditions can serve as a measure for the strength of the lattice plane bending (Grillo, 2009) as well as the lateral mean square displacement M of the atomic columns. The value M_i for the i-th column is determined via:

$$M_i = \sum_{k=1}^{N} \frac{(x_k - \bar{x}_i)^2}{N} + \sum_{k=1}^{N} \frac{(y_k - \bar{y}_i)^2}{N}, \qquad (1)$$

where $\bar{x}_i$ and $\bar{y}_i$ are the mean x and y coordinates of the respective atomic column, x_k and x_k are the coordinates of the k-th atom in this column and N denotes the number of atoms in this column.

This bending significantly influences the intensity in conventional high-resolution (HR) TEM imaging (De Caro *et al.*, 1997) as well as the positions of the atomic columns in the HR image, which influences strain mapping of strained quantum wells (Bierwolf *et al.*, 1993; Jouneau *et al.*, 1994; Walther *et al.*, 1995; Tillmann *et al.*, 2000) and islands (Tillmann *et al.*, 1996). Because the atoms along a column are no longer perfectly aligned, the channelling conditions change and the HAADF intensity will be influenced as well (Grillo, 2009). More to the point, the dechannelling effect of the electrons (Amali *et al.*, 1997; Perovic *et al.*, 1993; Cowley & Huang, 1992; Huang, 1947; Grillo, 2009) leads to a clear intensity deterioration at a strained interface (Yu *et al.*, 2004; Beyer *et al.*, 2017; Grillo, 2009). The intensity change observed in simulated HAADF images across a strained GaP/GaAs interface perfectly correlates with the lateral displacement M (Beyer *et al.*, 2017). This can impede the characterisation of a sample,

Correspondence to: Andreas Beyer, Materials Science Center and Faculty of Physics, Philipps-Universität Marburg, Hans-Meerweinstraße 6, 35032 Marburg, Germany. Tel +49 6421 28 25704; fax +49 6421 28935; e-mail: andreas.beyer@physik.uni-marburg.de

because the intensity change introduced by the surface relaxation can easily be misinterpreted as change of the chemical composition.

Often, the effect of surface relaxation is counter-balanced by averaging the intensity of an atomic column over a certain area, for example the Voronoi cell of each column, and therefore attributing the dechannelled intensity back to the respective column (Rosenauer *et al.*, 2011; E *et al.*, 2013). However, because surface relaxation not only leads to a redistribution of the intensity in real space but also in reciprocal space, some intensity is scattered into lower angles. Therefore, even applying an averaging approach, intensity dips at the interface are observed (Grieb *et al.*, 2012), which could be compensated by combining measurements with different angular scattering ranges (Grieb *et al.*, 2013).

However, all averaging approaches may hide some information, which was present in atomic resolution HAADF images. Especially for materials consisting of elements with different properties, for example covalent radius or electronegativity, the introduced displacements of the atoms and the resulting change in intensity of the atomic columns are important. The correct treatment of the surface relaxation effects allows the investigation of the interfaces in more complex materials, where such additional static atomic displacements (SADs) are present, for example Ga(N,As) in GaP, (Ga,In)(N,As) in GaAs (Grieb *et al.*, 2014) or (Ga,In)N in GaN (Rosenauer *et al.*, 2011). Recently we examined the effects of surface relaxation theoretically by simulated atomic resolution HAADF and low-angle annular dark field (LAADF) images (Beyer *et al.*, 2017).

Here we use the example of Ga(P,As) quantum wells (QWs) embedded in GaP to visualise these effects in experiments. We will show the influence of surface relaxation in real space by investigating the atomic column intensities as well as their positions in HAADF measurements. The impact on the scattering distribution in reciprocal space will be discussed via simulated position averaged convergent beam electron diffraction (PACBED) patterns. Furthermore, we will discuss the implications of the surface relaxation for different (S)TEM methods. We will show that the contrast simulations, taking into account the bending of the lattice planes, resemble the experiment very well.

Experimental

Ga(P,As) multi-QWs were grown via metalorganic vapour phase epitaxy (MOVPE) on GaP(100) substrate. The layer width of 11.7 nm and the As content of 65.5% were determined by modelling the 400 X-ray diffraction (XRD) rocking curves acquired in a Panalytical X′Pert Pro system (PANalytical GmbH, Kassel-Waldau, Germany). The elastic constants and lattice parameters used were taken from (Vurgaftman *et al.*, 2001).

The TEM specimens were prepared by mechanical polishing utilising an Allied MULTIPREP system (Allied High Tech Products, Inc., Rancho Dominguez, California, United States). The crystallographic [001] direction was chosen as viewing direction. Subsequent argon ion milling was carried out in a GATAN PIPS (Gatan, Pleasanton, California, United States) until electron transparency was achieved. Hereby, the voltage was progressively reduced from 5 kV to a final value of 1.2 kV to minimise amorphous surface layers and damage of the thin specimens.

HAADF measurements were carried out in a double C_S-corrected JEOL JEM 2200FS (JEOL [Germany] GmbH Freising, Germany) operating at 200 kV. An annular detector range from 73 to 174 mrad and a probe semiconvergence angle of 24 mrad were used. Series of 20 individual images were acquired and aligned nonrigidly using the Smart-Align software (Jones *et al.*, 2015) to improve the signal-to-noise ratio. The image intensity was normalised to the intensity of the impinging beam applying the approach described in (He & Li, 2014). The TEM sample thickness was determined to be 22 nm by comparing the normalised intensity in reference regions sufficiently far away (>20 nm) from the bent QW with adequate image simulations, as successfully performed for example in Beyer *et al.* (2016b).

In order to account for the effect of surface relaxation, super cells modelling the sample geometry were created and relaxed via FE applying linear elastic theory. In these cells abrupt interfaces between barrier and QW were assumed. Within the QW the two different elements present on the group V sublattice, that is P and As, were distributed randomly. Due to the discrete number of atoms in the super cell, the As content is 65.9% instead of the 65.5%, which was determined via XRD. Additional SADs, caused by the two different elements, were taken into account by a subsequent valence force field (VFF) relaxation (Keating, 1966). A model of the central part of the surface relaxed super cell is shown in Figure 1(A). Periodic boundary conditions were applied along the y axis, whereas the cell was allowed to expand along the x and z directions. For the given sample geometry this results in a bulging out of the QW of $\Delta z \sim 0.35$ nm and a mistilt $\alpha \sim 10$ mrad of the formerly straight lattice planes. In the right half of Figure 1(A), the calculated displacements were multiplied by a factor of 5 for better visualisation. Because the sample thickness (22 nm) and the QW width (12 nm) are in a similar range, the surface relaxation is very prominent, as predicted for this case (Treacy *et al.*, 1985). The lateral mean square displacement of each lattice plane was calculated according to Eq. (1). The variation of the displacement across the QW is drawn in Figure 1(B). In the centre of the QW the lateral displacement is zero, because the forces of the two opposing interfaces cancel out. Across the interfaces the displacements rise to a maximum of $\sim 6 \times 10^{-4}$ nm^2 at a distance of ~ 4 nm away from the respective interface. Far away from the interfaces (>10 nm) the displacements decrease to zero again, which cannot be seen in the smaller section shown here. For the purely tetragonally distorted super cell, periodic boundary conditions were applied
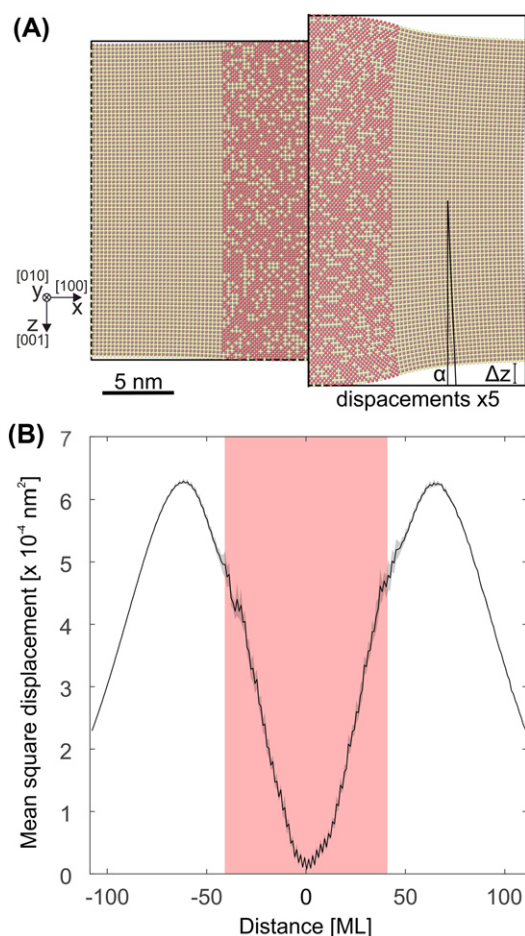
Fig. 1. Model of the surface relaxed super cell (A). In the right half of the image, the calculated displacements are multiplied by a factor of 5 for visualisation purposes. The derived displacements across the quantum well calculated according to Eq. (1) are drawn in (B).

along y and z, only expansion along the x axis was allowed. Both constructed super cells, a purely tetragonally distorted one as well as an additionally surface relaxed one, served as input for multislice simulations. To this end, we used the frozen phonon approach implemented in the STEMsalabim package (Oelerich *et al.*, 2017). Hereby, 7 different defoci with 10 independent phonon configurations were calculated to account for chromatic aberration and thermal diffuse scattering. The simulated images were convoluted by a Lorentzian source distribution with a width of 45 pm. Performing this simulation procedure, a nearly perfect agreement between simulation and experiment could be achieved for GaP (Beyer *et al.*, 2016a). Theoretical PACBED patterns were derived by averaging 400 simulated CBED patterns from one unit cell of the respective super cell.

Results

Here, we will illustrate the occurring effects using an experimental HAADF image. We will show that the experimental

features are also found in the simulated images with good quantitative agreement. A quantitative comparison between simulation and experiment will be carried out for the intensities as well as the strain. In addition, we will discuss the scattering redistribution in the reciprocal space.

Figure 2 shows a high-resolution HAADF image of the Ga(P,As) QW grown on GaP substrate. The [100] growth direction is oriented along the x axis and the electron beam transmits through the sample along the z axis, that is the crystallographic [001] direction. The As containing layer can be identified by its brighter contrast with respect to the surrounding GaP barriers due to its larger mean atomic number. The centre of the QW was tilted into zone axis condition utilising the convergent diffraction pattern. It is worth noting that the orientation alignment has to be carried out carefully, because the bending of the lattice planes results in apparent changes of the sample orientation across the field of view. A TEM sample thickness of 22 nm was derived by comparing the experimental intensity of the GaP barrier to thickness dependent frozen phonon simulations. At a sufficiently large distance from the QW (>10 nm), the Ga columns appear nearly circular symmetric with some residual astigmatism and the image exhibits a high contrast, which can be seen in more detail in the enlarged section shown in Figure 2(B) and in false colour in Figure 2(C), where the low-intensity features are better visible. The positions of the group III and V atomic columns are marked by circles. Due to the lower scattering power, the P atomic columns are barely visible. Two positions situated horizontally between two group III or two group V columns are marked by B_{III} and B_V, respectively. In this part of the image B_{III} and B_V appear equivalent. In contrast to this region, the Ga columns in the direct vicinity of the interface (<3 nm) appear blurred and elongated along the x direction. In combination with the aforementioned residual astigmatism, the atomic columns appear slightly inclined with respect to the x axis. An enlarged view of a unit cell from this region is depicted on a greyscale and in false colour in Figures 2(D) and (E), respectively. The 4-fold symmetry seems to be broken and the B_{III} and B_V positions are no longer equivalent. Taking a closer look at the QW itself reveals that the atomic columns appear blurred close to the upper and the lower interface, whereas the central part appears sharp. This change in the image contrast across the interface (i.e. sharp at a large distance from the QW (>10 nm)⇔ blurred at the interface⇔ sharp in the centre of the QW) follows the variations in displacements which are expected across the structure (c.f. Fig. 1B).

However, in the experimental image it is not possible to prove that the changing image contrast and the elongated lattice planes are introduced by the lattice plane bending, because the surface relaxation will always be present. Complementary simulations, however, allow this because both purely tetragonally distorted and surface relaxed structures can be used as inputs. For illustration a model of the surface relaxed super cell is shown in Figure 1(A).
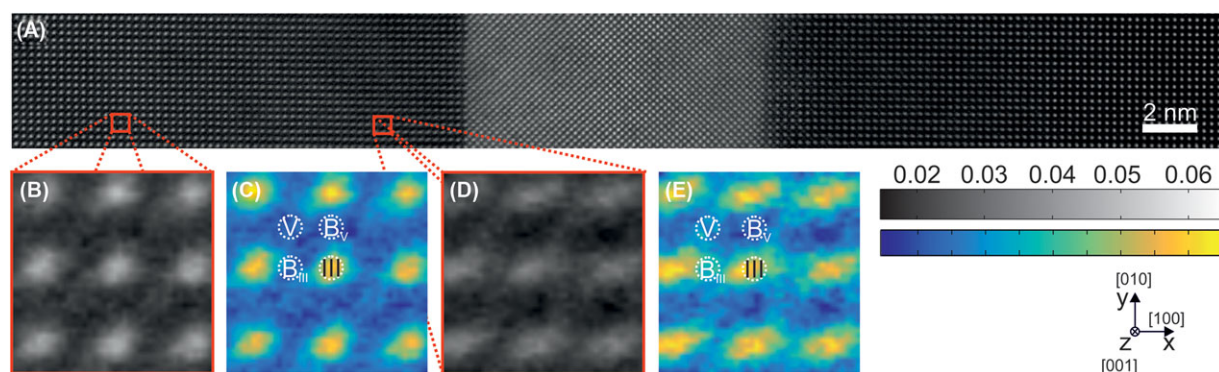
Fig. 2. Experimental high-resolution HAADF image of Ga(P,As) quantum well framed by GaP in [001] projection (A). A unit cell of the undistorted region far away (>10 nm) from the interface is shown in (B). The same section is shown in false colour in (C). An analogous region close to the interface is shown in greyscale and false colour in (D) and (E), respectively. The positions of the group III and V atomic columns are marked by circles. In addition, the positions that are situated horizontally between two group III or two group V columns are marked by B_{III} and B_V, respectively
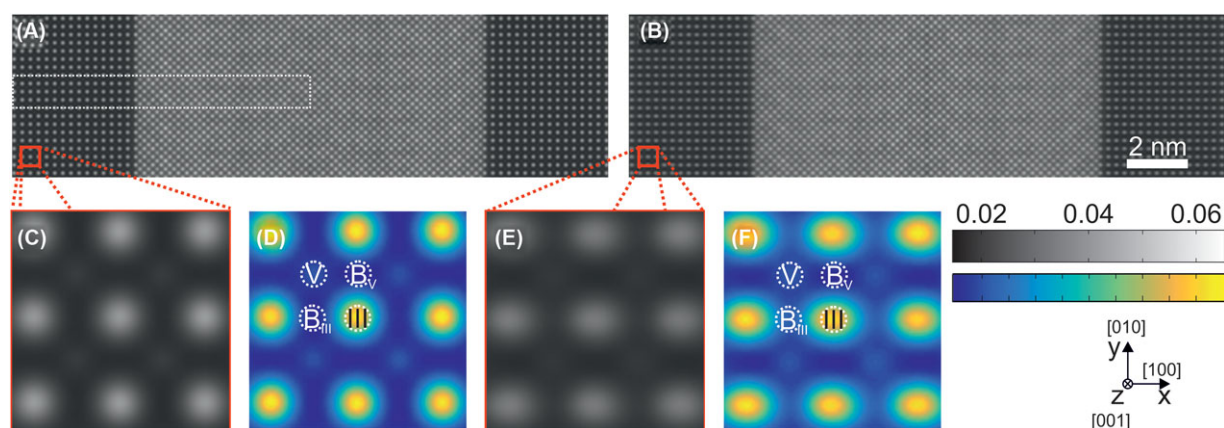

Fig. 3. Simulated HAADF images derived from a purely tetragonally distorted and the additionally surface relaxed super cell are shown in (A) and (B), respectively. Enlarged regions from both images are depicted in greyscale and false colour in (C) and (D) and (E) and (F), respectively. The positions of the group III and V atomic columns are marked by circles. In addition, the positions that are situated horizontally between two group III or two group V columns are marked by B_{III} and B_V, respectively

The simulated images derived from the purely tetragonally distorted and the surface relaxed cell with a sample thickness of 22 nm are shown in Figures 3(A) and (B), respectively. The white rectangle in Figure 3(A) indicates the simulated region, the simulations were mirrored vertically and repeated along the y axis for better resemblance of the experimental data.

Comparing Figures 3(A) and (B), the reduced contrast in the latter becomes obvious. This can be seen in more detail in the enlarged unit cells shown in Figures 3(C) and (E) and the corresponding false colour images in Figures 3(D) and (F). Again, the positions which are situated horizontally between two group III or two group V columns are marked by B_{III} and B_V, respectively. Although the atomic columns of the purely tetragonally distorted cell in Figures 3(C) and (D) appear perfectly round, the columns of the surface relaxed cell in Figures 3(E) and (F) appear significantly elongated along the x direction. The two different background positions

B_{III} and B_V show different intensity. Comparing the simulations of Figure 3 to the experimental data presented in Figure 2 yields a very good qualitative agreement.

In the following, the simulation and experiment will be compared quantitatively using intensity profiles across the QW. Figure 4 depicts the respective profiles for the different positions within a unit cell, that is the group III atomic columns (Fig. 4A), the group V atomic columns (Fig. 4B) and the background positions in between the columns (Fig. 4C). The intensity value of each atomic column is derived by averaging the intensity across a circular region with a diameter of 25 pm around the column centre, to compensate for inaccuracies in the determination of the peak centres. The size of the averaging circles is indicated by dashed circles depicted for example in Figure 3(D). Subsequently the intensity of a lattice plane is derived by averaging the intensities of the associated atomic columns. The shaded area indicates the standard deviation of the intensity across the atomic columns of a lattice plane.
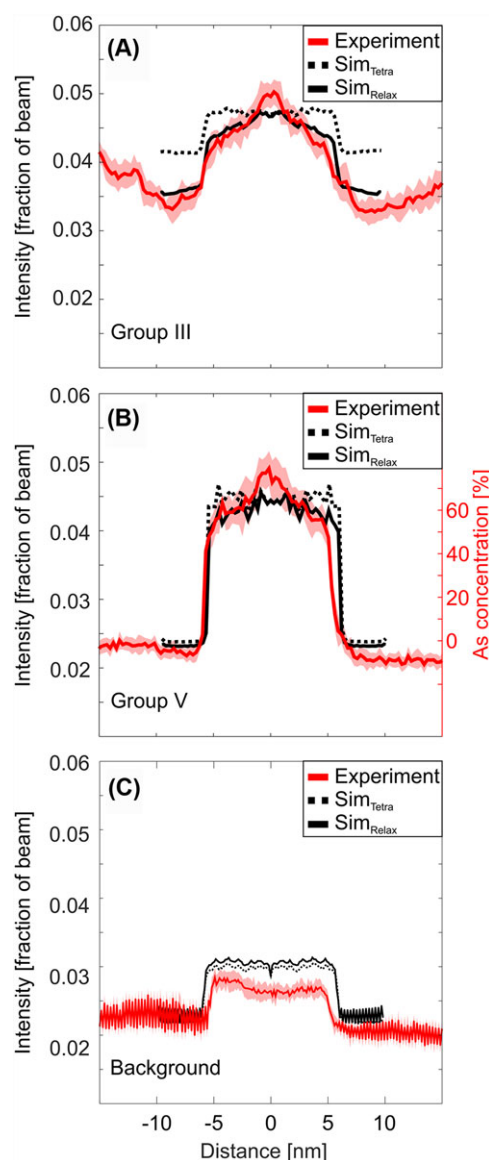
Fig. 4. The red lines indicate the experimental intensity profiles across the quantum well derived at the positions of the group III atomic columns (A), the group V atomic columns (B) and the background positions in between the columns (C). The simulated intensities for the surface relaxed case are drawn as a solid black lines. The simulated intensity derived from the purely tetragonally distorted cell is drawn as dashed black line for comparison.

The intensity profiles of the group III sublattice in Figure 4(A) illustrate the influence of the lattice plane bending best, because the lattice sites are occupied by Ga only throughout the whole structure. Because the chemical composition remains constant across the QW, the changes in intensity are caused by the plane bending mainly. We find that the simulated intensity derived from the surface relaxed super cell (solid black line) is up to 20% reduced compared to the intensity derived from the purely tetragonally distorted cell (dashed

black line). The maximum deviation can be found in the barrier, ~ 10 nm away from the centre of the QW, where the atoms are displaced the most (c.f. Fig. 1B). The displaced atoms lead to dechannelling of the electron beam (Huang, 1947; Cowley & Huang, 1992; Perovic *et al.*, 1993; Amali *et al.*, 1997; Grillo, 2009) and accordingly to a reduced HAADF intensity at the positions of the atomic columns (Yu *et al.*, 2004; Grillo, 2009; Beyer *et al.*, 2017). Additionally, the displaced atomic columns lead to increased Huang scattering into low angles (Huang, 1947; Cowley & Huang, 1992). The influence of the surface relaxation on the angular dependence of the scattering will be discussed in more detail below. The experimental curve (red line) closely resembles surface relaxed simulation (solid black line). The lack of correspondence between the experiment and the simulation at the upper interface is not caused by missing factors in the simulation but actual properties of the sample and will be discussed later.

The simulated intensity of the group V sublattice derived from the purely tetragonally distorted super cell (dashed black line in Fig. 4B) nearly resembles a box profile. The slight intensity variations within the QW region are due to the fact that the chemical composition fluctuates around the mean As content of 65.9%. The right y axis indicates the corresponding As concentration. For reasons of simplicity a linear dependence of the intensity on the composition was assumed, which has shown to be valid for thin samples (Van Aert *et al.*, 2009). In contrast, the profile derived from the surface relaxed super cell (solid black line in Fig. 4B) significantly differs from a box profile. Close to the interfaces the intensity is clearly reduced because of the displaced atomic columns. The resulting intensity gradient could be misinterpreted as a composition gradient. According to the right y axis an As content of only $\sim 50\%$ would be present at the interface. We emphasise that there are procedures to partially compensate for the observed intensity loss, for example the probe integrated scattering cross sections (PICS) approach (E *et al.*, 2013). Nevertheless, in this manuscript we want to highlight the influences of the surface relaxation. As stated in the introductory section, averaging approaches can fail for materials, in which additional SADs are present, for example Ga(N,As).

Also on the group V sublattice, the profile derived from the surface relaxed super cell (solid black line) resembles the experimental curve (red line) very well and shows some sample related deviations at the upper interface.

The intensity in the background is strongly influenced by the surface relaxation as well (Fig. 4C). The intensity of the purely tetragonally distorted simulation (dashed black line) follows a box profile following the different amounts of thermal diffuse scattering in GaP and Ga(P,As). The surface relaxation and the resulting bent lattice planes break the 4-fold symmetry, therefore there are two different intensity values of the background depending on whether there are two neighbouring Ga or P atomic columns along the x direction (compare e.g. Fig. 2F).

This manifests as intensity oscillations in the simulated background profile (solid black line) as well as the experimental profile (red line). Additionally, a slight intensity increase is observable at the edges of the QW in the simulation as well as in the experiment.

In general there is a very good agreement between the experiment and the simulations taking into account the lattice plane bending for all three observed positions. However, some distinct discrepancies can be found. First, a small intensity gradient is present in the experimental profiles, which is due to the wedge shape that is caused by the sample preparation. Second, at the upper interface the experimental profile is less steep than the simulation, where an abrupt composition profile was assumed. This might be caused by the thickness gradient and a corresponding asymmetric surface relaxation. However, we think that the change in thickness (<2 nm across the >25 nm field of view) is not sufficient to significantly alter the intensity profiles. This means that the upper interface is not atomically abrupt but intermixed. Both factors contribute to the notable asymmetry of the experimental profiles. It is worth noting that this asymmetry was not retrieved by the XRD measurements, where also a prefect box-like profile was assumed. Assuming a composition gradient in the simulated XRD profile could improve the fit to the experimental data.

The surface relaxation may not only influence the HAADF intensities, but also the positions of the atomic columns. The magnitude of this effect is investigated in the following.

To this end, the positions of the atomic columns in the simulated data were derived directly from the respective super cell by omitting the z coordinate and averaging the x and y coordinates of the atoms belonging to one atomic column. In the case of the experimental images, the corresponding positions were determined via the Peak Pairs software (Galindo *et al.*, 2007).

In each case the distances to the four next neighbour columns were determined, averaged and split into the components along the x and y axis, respectively. The distances were calibrated using the 4 0 0 spots in the FFT of the GaP region below the QW. We decided to only use the spots along the x direction because this is the fast scan direction in the experimental images which is less influenced by sample drift and scan distortions (Grieb *et al.*, 2012). The resulting curves utilising the positions of the group III and the group V atomic column are shown in Figures 5(A) and (B), respectively. As expected the determined lattice constants are almost identical for both sublattices, therefore we will discuss the observations on the basis of the group III lattice only. The right y axis indicates the As content, which was derived by combining Vegard's law with the tetragonal distortion due to pseudomorphic growth.

In analogy to the previous intensity evaluation, the lattice constant evaluation of the purely tetragonally distorted simulation (dashed black line in Fig. 5A) nearly follows a box profile. The lattice constant of 0.57 nm in the QW is in good agreement with the values derived from the XRD measure-
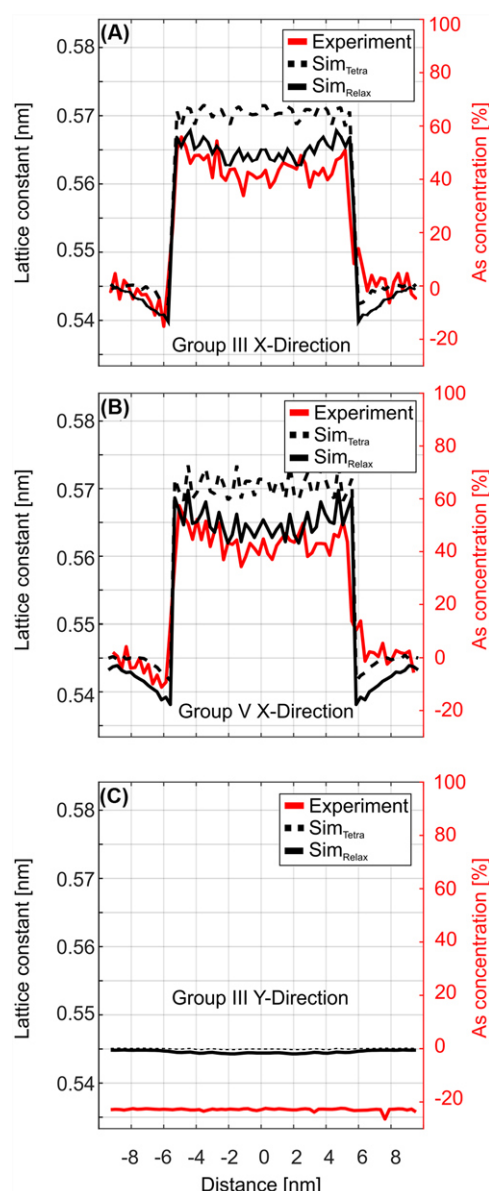

Fig. 5. Variation of the out-of-plane lattice constant across the QW derived from the group III (A) and group V (B) atomic column positions of the experimental image (red lines) and the surface relaxed simulation (solid black lines). The values derived from the purely tetragonally distorted cell are drawn as dashed black lines. The corresponding evaluation of the in-plane lattice constant is shown in (C).

ment. The small indents before and after the QW are caused by atom displacements at the interface due to the VFF relaxation, which was carried out for all simulated super cells, to account for the SADs introduced by the mixture of As and P atoms on the group V sublattice.

The lattice constants derived from the surface relaxed cell (solid black curve) are significantly altered. The previously observed dip at the interfaces becomes more pronounced. Additionally, the lattice constant in the centre of the QW is drastically reduced. This is due to the fact that a fraction of

the strain energy stored in the system is relaxed due to the additional free surface. Similar to the case of the intensity evaluation this change can be misinterpreted as a change of composition. According to the right y axis, the As content in the centre of the QW would be around 50% instead of the actual content of 65.9%. Again, the agreement between experiment (red curve) and surface relaxed simulation (solid black curve) is very good except for the upper interface. As discussed for the intensity curves, this discrepancy is caused by the intermixed upper interface.

We emphasise that the standard deviation of the experimental lattice constant is in the range of 15 pm, which is rather high compared to the difference in lattice constant between GaP and Ga(P,As), which is around 25 pm. The accuracy could be improved by increasing the sampling in the images to improve peak finding and by averaging over a larger number of images to reduce the impact of drift and scan distortions. Recently, accuracies in the range of 1% were reported in the determination of lattice constants via STEM (Yankovich *et al.*, 2014; Jones *et al.*, 2017). Here we did not add error bars to the graphs to retain clarity. As stated before, the evaluation of the out-of-plane lattice constant using the group V lattice (Fig. 5B) leads to similar results.

The analogue evaluation of the perpendicular y direction is shown in Figure 5(C). As expected for pseudomorphic growth, the in-plane lattice constant remains constant across the QW. In the simulations the absolute value is 0.545 nm, that is that of the GaP substrate. The value derived from the experiment is reduced by ~ 8 pm which is most likely caused by a compression of the y axis due to sample drift. To compensate for this the image could be rectified or the effect of drift could be reduced by intentionally varying the fast scan direction during the STEM measurements (Sang & LeBeau, 2014; Jones *et al.*, 2015). However, this small discrepancy is not important in our case, because the lattice constant along y is constant over the field of view.

After discussing the influences of the surface relaxation in the real space we finally address the reciprocal space as well. We do this via simulated PACBED patterns. The simulated patterns derived from a unit cell of the purely tetragonally distorted and a unit cell of the surface relaxed super cell for a specimen thickness of 22 nm are depicted in Figure 6(A) (top and bottom halves, respectively). The angular range is from 0 to 300 mrad. The bright field disc with a radius of 24 mrad is distinctly visible in the centre as well as the Kikuchi bands expected from the [001] crystal orientation. Comparing the two simulations, it becomes apparent that the surface relaxed PACBED (bottom) is blurred with respect to the purely tetragonally distorted one (top). Because the bending of the lattice planes induced by the surface relaxation is not isotropic, the PACBED pattern is no longer 4-fold symmetric. This can be seen faintly at the bright field disc as well as at the first-order Laue zone (FOLZ). The FOLZ is clearly visibly as a bright ring in the lower segment of the surface relaxed pattern (high-
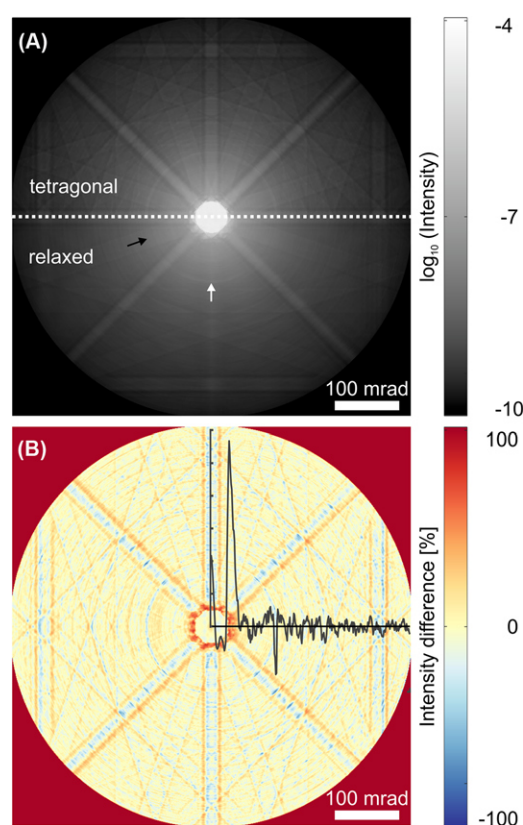

Fig. 6. Simulated PACBED patterns derived from one unit cell of the purely tetragonally distorted (top) and the surface relaxed (bottom) super cell (A). The difference between the two simulations is shown in false colour in (B). The black line represents the radial average of the difference.

lighted by white arrow), whereas it vanishes in the left segment of the pattern (highlighted by dark arrow). The observable asymmetry between the left and right half of the pattern could be used in experiments to judge whether significant lattice plane bending is present. This break of symmetry can also be very important for differential phase contrast (DPC) measurements, because the effects caused by the surface relaxation can be misinterpreted as electric fields at the interface.

The blurring of the pattern becomes even more obvious in the difference plot, which is shown in false colour in Figure 6(B). The difference values I_{Diff} were derived via $I_{\text{Diff}} = (I_{\text{Surf}} - I_{\text{Tetra}})/I_{\text{Surf}}$, where I_{Surf} and I_{Tetra} are the intensities from the surface relaxed and the purely tetragonally distorted simulation, respectively. The broadening of the Kikuchi bands is clearly visible by the red edges and blue centre of each band. The horizontal bands do not show up in the difference plot at all which implies they are not affected by the surface relaxation. Because periodic boundary conditions still apply along the y direction, no lattice plane bending is present. In the centre of the pattern an increased intensity is observable. This is caused by additional Huang scattering (Huang, 1947) and agrees well with the 'expansion of the diffraction pattern' for

example observed at dislocations (Cowley & Huang, 1992). The asymmetry of the pattern can be seen in the difference plot as well.

The radial average across the difference plot is shown as black line in Fig. 6(B). Most prominently the increased intensity at low scattering angles is visible. In LAADF images, where this angular region is detected, the increased intensity leads to a bright line at the strained interfaces (Grillo *et al.*, 2011; Grieb *et al.*, 2012; Beyer *et al.*, 2017). Additionally, the reduced intensity at FOLZ is visible in the radial average as well. So far we only addressed the reciprocal space via simulations, however, our theoretical findings could be compared to nanobeam diffraction experiments (Müller-Caspary *et al.*, 2015) or to actual CBED patterns acquired across the strained QW due to the recent developments in the field of fast pixelated detectors (Chen *et al.*, 2016).

In summary, there is a significant influence of the surface bending on the different STEM measurements presented. There are several possibilities to address these effects and minimise their impact. First, an optimum sample thickness can be chosen according to the QW width (Treacy *et al.*, 1985; Beyer *et al.*, 2017). For a fixed sample geometry, adequate evaluation schemes have to be applied, which attribute the dechannelled intensity back to the respective atomic column, for example the PICS approach (E *et al.*, 2013), or make use of measurements with different angular scattering ranges (Grieb *et al.*, 2013). Last but not least, the expected displacements can be modelled, for example by FE, to decide whether the surface relaxation will be crucial and to localise the distorted regions. Moreover, the displacement fields can be used to compensate the deteriorated intensity or to create super cells which reflect the actual sample geometry (Rosenauer *et al.*, 2006; Beyer *et al.*, 2017).

Conclusion

The surface relaxation of thin TEM specimens of commensurately strained heterostructures leads to a bending of the lattice planes. In HR HAADF measurements the intensities of the atomic columns are decreased wherever bending is present. In the case of a compressively strained QW, the distances of the atomic columns in the quantum well are reduced by the relaxation in comparison to the purely tetragonally distorted crystal. FE can be used to model the bending. The simulated HAADF images of a Ga(P,As) QW embedded in GaP are in good agreement with the experiments. Ignoring the effect of surface relaxation can lead to misinterpretation of data. Taking it into account, we find that the lower interface of the investigated sample is atomically abrupt, whereas the upper one is smeared out. The simulated PACBED patterns verify that the surface relaxation leads to additional scattering into low angles. Moreover, the Kikuchi bands belonging to bent planes broaden and the 4-fold symmetry is broken. The latter effect can be utilised to detect the presence of lattice plane bending.

The occurring effects can be accounted for by the appropriate choice of the sample geometry and the evaluation schemes or by the modelling of the surface relaxation.

References

Van Aert, S., Verbeeck, J., Erni, R., Bals, S., Luysberg, M., van Dyck, D. & van Tendeloo, G. (2009). Quantitative atomic resolution mapping using high-angle annular dark field scanning transmission electron microscopy. *Ultramicroscopy* **109**, 1236–1244.

Amali, A., Rez, P. & Cowley, J.M. (1997). High angle annular dark field imaging of stacking faults. *Micron* **28**, 89–94.

Beyer, A., Belz, J., Knaub, N., Jandieri, K. & Volz, K. (2016a). Influence of spatial and temporal coherences on atomic resolution high angle annular dark field imaging. *Ultramicroscopy* **169**, 1–10.

Beyer, A., Duschek, L., Belz, J., Oelerich, J.O., Jandieri, K. & Volz, K. (2017). Influence of surface relaxation of strained layers on atomic resolution ADF imaging. *Ultramicroscopy* **181**, 8–16.

Beyer, A., Straubinger, R., Belz, J. & Volz, K. (2016b). Local sample thickness determination via scanning transmission electron microscopy defocus series. *J. Microsc.* **262**, 171–177.

Bierwolf, R., Hohenstein, M., Phillipp, F., Brandt, O., Crook, G.E. & Ploog, K. (1993). Direct measurement of local lattice distortions in strained layer structures by H R E M. *Ultramicroscopy* **49**, 273–285.

De Caro, L., Giuffrida, A., Carlino, E. & Tapfer, L. (1995). Elastic stress relaxation in HRTEM specimens of strained semiconductor heterostructures and its influence on the image contrast. *Microsc. Microanal. Microstruct.* **6**, 465–472.

De Caro, L., Giuffrida, A., Carlino, E. & Tapfer, L. (1997). Effects of the elastic stress relaxation on the HRTEM image contrast of strained heterostructures. *Acta Crystallographica Sect. A Found. Crystallogr.* **53**, 168–174.

Chen, Z., Weyland, M., Ercius, P. *et al.* (2016). Practical aspects of diffractive imaging using an atomic-scale coherent electron probe. *Ultramicroscopy* **169**, 107–121.

Cowley, J.M. & Huang, Y. (1992). De-channelling contrast in annular dark-field STEM. *Ultramicroscopy* **40**, 171–180.

E, H., MacArthur, K.E., Pennycook, T.J., Okunishi, E., D'Alfonso, A.J., Lugg, N.R., Allen, L.J. & Nellist, P.D. (2013). Probe integrated scattering cross sections in the analysis of atomic resolution HAADF STEM images. *Ultramicroscopy* **133**, 109–119.

Galindo, P.L., Kret, S., Sanchez, A.M. *et al.* (2007). The Peak Pairs algorithm for strain mapping from HRTEM images. *Ultramicroscopy* **107**, 1186–1193.

Gibson, J.M. & Treacy, M.M.J. (1984). The effect of elastic relaxation on the local structure of lattice-modulated thin films. *Ultramicroscopy* **14**, 345–349.

Grieb, T., Müller, K., Cadel, E., Beyer, A., Schowalter, M., Talbot, E., Volz, K. & Rosenauer, A. (2014). Simultaneous quantification of indium and nitrogen concentration in InGaNAs using HAADF-STEM. *Microsc. Microanal.* **20**, 1740–1752.

Grieb, T., Müller, K., Fritz, R., Grillo, V., Schowalter, M., Volz, K. & Rosenauer, A. (2013). Quantitative chemical evaluation of dilute GaNAs using ADF STEM: avoiding surface strain induced artifacts. *Ultramicroscopy* **129**, 1–9.

Grieb, T., Müller, K., Fritz, R., Schowalter, M., Neugebohrn, N., Knaub, N., Volz, K. & Rosenauer, A. (2012). Determination of the chemical composition of GaNAs using STEM HAADF imaging and STEM strain state analysis. *Ultramicroscopy* **117**, 15–23.

Grillo, V. (2009). The effect of surface strain relaxation on HAADF imaging. *Ultramicroscopy* **109**, 1453–1464.

Grillo, V., Mueller, K., Volz, K., Glas, F., Grieb, T. & Rosenauer, A. (2011). Strain, composition and disorder in ADF imaging of semiconductors. *J. Phys.: Conf. Ser.* **326**, 1–10.

He, D.S. & Li, Z.Y. (2014). A practical approach to quantify the ADF detector in STEM. *J. Phys.: Conf. Ser.* **522**, 1–4.

Huang, K. (1947). X-ray reflexions from dilute solid solutions. *Proc. R. Soc. A: Mathemat., Phys. Eng. Sci.* **190**, 102–117.

Jones, L., Wenner, S., Nord, M., Ninive, P.H., Løvvik, O.M., Holmestad, R. & Nellist, P.D. (2017). Optimising multi-frame ADF-STEM for high-precision atomic-resolution strain mapping. *Ultramicroscopy* **179**, 57–62.

Jones, L., Yang, H., Pennycook, T.J., Marshall, M.S.J., Van Aert, S., Browning, N.D., Castell, M.R. & Nellist, P.D. (2015). Smart Align—a new tool for robust non-rigid registration of scanning microscope data. *Adv. Struct. Chem. Imag.* **1**, 1–16.

Jouneau, P.H., Tardot, A., Feuillet, G., Mariette, H. & Cibert, J. (1994). Strain mapping of ultrathin epitaxial ZnTe and MnTe layers embedded in CdTe. *J. Appl. Phys.* **75**, 7310–7316.

Keating, P.N. (1966). Effect of invariance requirements on the elastic strain energy of crystals with application to the diamond structure. *Phys. Rev.* **145**, 637–645.

Krivanek, O.L., Chisholm, M.F., Nicolosi, V. *et al.* (2010). Atom-by-atom structural and chemical analysis by annular dark-field electron microscopy. *Nature* **464**, 571–574.

Müller-Caspary, K., Oelsner, A. & Potapov, P. (2015). Two-dimensional strain mapping in semiconductors by nano-beam electron diffraction employing a delay-line detector. *Appl. Phys. Lett.* **107**, 1–4.

Nellist, P.D., Chisholm, M.F., Dellby, N. *et al.* (2004). Direct sub-angstrom imaging of a crystal lattice. *Science (New York, N.Y.)* **305**, 1741.

Oelerich, J.O., Duschek, L., Belz, J., Beyer, A., Baranovskii, S.D. & Volz, K. (2017). STEMsalabim: a high-performance computing cluster friendly code for scanning transmission electron microscopy image simulations of thin specimens. *Ultramicroscopy* **177**, 91–96.

Pennycook, S.J. (1989). Z-contrast stem for materials science. *Ultramicroscopy* **30**, 58–69.

Perovic, D.D., Rossouw, C.J. & Howie, A. (1993). Imaging elastic strains in high-angle annular dark field scanning transmission electron microscopy. *Ultramicroscopy* **52**, 353–359.

Rosenauer, A., Gerthsen, D. & Potin, V. (2006). Strain state analysis of InGaN/GaN – sources of error and optimized imaging conditions. *Physica Status Solidi (a)* **203**, 176–184.

Rosenauer, A., Mehrtens, T., Müller, K. *et al.* (2011). Composition mapping in InGaN by scanning transmission electron microscopy. *Ultramicroscopy* **111**, 1316–1327.

Sang, X. & LeBeau, J.M. (2014). Revolving scanning transmission electron microscopy: correcting sample drift distortion without prior knowledge. *Ultramicroscopy* **138**, 28–35.

Tan, H., Furlan, A., Li, W. *et al.* (2016). Highly efficient hybrid polymer and amorphous silicon multijunction solar cells with effective optical management. *Adv. Mater.* **28**, 2170–2177.

Tillmann, K., Lentzen, M. & Rosenfeld, R. (2000). Impact of column bending in high-resolution transmission electron microscopy on the strain evaluation of GaAs/InAs/GaAs heterostructures. *Ultramicroscopy* **83**, 111–128.

Tillmann, K., Thust, A., Lentzen, M. *et al.* (1996). Determination of segregation, elastic strain and thin-foil relaxation in InxGa-1-x As islands on GaAs(001) by high resolution transmission electron microscopy. *Philos. Magaz. Lett.* **74**, 309–315.

Treacy, M.M.J., Gibson, J.M. & Howie, A. (1985). On elastic relaxation and long wavelength microstructures in spinodally decomposed InxGa1−x.AsyP1−y epitaxial layers. *Philos. Magaz. A.* **51**, 389–417.

Vurgaftman, I., Meyer, J.R. & Ram-Mohan, L.R. (2001). Band parameters for III–V compound semiconductors and their alloys. *J. Appl. Phys.* **89**, 5815–5875.

Walther, T., Boothroyd, C.B. & Humphreys, C.J. (1995). Strain relaxation induced local crystal tilts at Si/SiGe interfaces in cross-sectional transmission electron microscope specimens. *Inst. Phys. Conf. Ser.* **146**, 11–16.

Wang, N., Cheng, L., Ge, R. *et al.* (2016). Perovskite light-emitting diodes based on solution-processed self-organized multiple quantum wells. *Nat. Phot.* **10**, 699–704.

Xu, Q., Ji, Y., Krut, D.D., Ermer, J.H. & Escarra, M.D. (2016). Transmissive concentrator multijunction solar cells with over 47% in-band power conversion efficiency. *Appl. Phys. Lett.* **109**, 1–4.

Yankovich, A.B., Berkels, B., Dahmen, W. *et al.* (2014). Picometre-precision analysis of scanning transmission electron microscopy images of platinum nanocatalysts. *Nat. Commun.* **5**. http://www.nature.com/doifinder/10.1038/ncomms5155

Yu, Z., Muller, D.A. & Silcox, J. (2004). Study of strain fields at a-Si/c-Si interface. *J. Appl. Phys.* **95**, 3362–3371.

Influence of surface relaxation of strained layers on atomic resolution ADF imaging

A. Beyer, L. Duschek, J. Belz, J. O. Oelerich, K. Jandieri, and K. Volz

Ultramicroscopy, vol. 181, pp. 8–16, 2017.

Abstract

Surface relaxation of thin transmission electron microscopy (TEM) specimens of strained layers results in a severe bending of lattice planes. This bending significantly displaces atoms from their ideal channeling positions which has a strong impact on the measured annular dark field (ADF) intensity.

With the example of GaAs quantum wells (QW) embedded in a GaP barrier, we model the resulting displacements by elastic theory using the finite element (FE) formalism. Relaxed and unrelaxed super cells served as input for state of the art frozen phonon simulation of atomic resolution ADF images.

We systematically investigate the dependencies on the samples' geometric parameters, i.e. QW width and TEM sample thickness, by evaluating the simulated intensities at the atomic columns' positions as well as at the background positions in between. Depending on the geometry the ADF intensity can be affected in a range several nm from the actual interface.

Moreover, we investigate the influence of the surface relaxation on the angular distribution of the scattered intensity. At high scattering angles we observe an intensity reduction at the interface as well as in the GaP barrier due to de-channeling. The amount of intensity reduction at an atomic column is directly proportional to its mean square displacement. On the contrary we find a clearly increased intensity at low angles caused by additional diffuse scattering. We discuss the implications for quantitative evaluations as well as strategies to compensate for the reduced intensities.

The authors' contributions

The algorithm to relax the surface strain in thin strained TEM samples was developed by J. Belz and K. Jandieri. I supported the implementation of the algorithm. Furthermore all multislice simulations, in particular the systematic parameter sweeps, were carried out by myself. The manuscript was written by A. Beyer, whereas the part of "Materials and methods" was written by me. All co-authors helped interpret the data and improve the manuscript.

Influence of surface relaxation of strained layers on atomic resolution ADF imaging

Andreas Beyer*, Lennart Duschek, Jürgen Belz, Jan Oliver Oelerich, Kakhaber Jandieri, Kerstin Volz

Materials Science Center and Faculty of Physics, Philipps-Universität Marburg Hans-Meerweinstraße 6, 35032 Marburg, Germany

ARTICLE INFO

ABSTRACT

Surface relaxation of thin transmission electron microscopy (TEM) specimens of strained layers results in a severe bending of lattice planes. This bending significantly displaces atoms from their ideal channeling positions which has a strong impact on the measured annular dark field (ADF) intensity.

With the example of GaAs quantum wells (QW) embedded in a GaP barrier, we model the resulting displacements by elastic theory using the finite element (FE) formalism. Relaxed and unrelaxed super cells served as input for state of the art frozen phonon simulation of atomic resolution ADF images.

We systematically investigate the dependencies on the sampleś geometric parameters, i.e. QW width and TEM sample thickness, by evaluating the simulated intensities at the atomic columnś positions as well as at the background positions in between. Depending on the geometry the ADF intensity can be affected in a range several nm from the actual interface.

Moreover, we investigate the influence of the surface relaxation on the angular distribution of the scattered intensity. At high scattering angles we observe an intensity reduction at the interface as well as in the GaP barrier due to de-channeling. The amount of intensity reduction at an atomic column is directly proportional to its mean square displacement. On the contrary we find a clearly increased intensity at low angles caused by additional diffuse scattering. We discuss the implications for quantitative evaluations as well as strategies to compensate for the reduced intensities.

© 2017 Elsevier B.V. All rights reserved.

1. Introduction

Modern devices often consist of multilayer structures, see e.g. [1–3]. Therefore, interfaces between different materials become increasingly important as their actual structure and chemical composition can determine the physical properties and efficiency of devices.

Aberration corrected high angle annular dark field (HAADF) scanning transmission electron microscopy (STEM) has become one of the leading techniques in the investigation of nanoscale materials [4,5], since a spatial resolution below one Angstrom is feasible. Moreover, quantitative agreement between simulation and experiment can be achieved if all decisive parameters are taken into account [6]. The dominant factors are the sensitivity of the annular dark field (ADF) detector [7,8], the partial spatial [9,10] and temporal coherences [6,11] and artefacts introduced by the sample preparation, e.g. amorphous layers [12].

At the interface of two materials additional challenges arise, as the lattice constants of the two materials forming the interface are commonly different. This is particularly relevant in the case of heteroepitaxy. In the special case of cubic materials, pseudomorphic growth takes places and the lattice mismatch results in the well-known tetragonal distortion, as long as a critical layer thickness is not exceeded. When a thin transmission electron microscopy (TEM) sample of a strained heterostructure is prepared, the stress can be relieved elastically, due to the additional free surface [13,14]. Depending on the lattice mismatch and the elastic constants, this results in the deformation of the TEM sample and the bending of the previously straight lattice planes [15]. This effect can be modeled by elastic theory [16]. Utilizing finite element (FE) calculations this model can be used to calculate the deformation fields occurring for actual sample geometries [13,16,17]. The tremendous effect of the bent lattice planes on conventional high resolution (HR) TEM imaging was studied e.g. in [13,16,18]. Although STEM, and especially high angle ADF, are regarded as less sensitive towards strain compared to conventional TEM, a distinct intensity deterioration at strained interfaces was found for uncorrected STEM microscopy [15,19] and explained by a de-channeling effect of the electrons [15,20–23]. Therefore, composition profiles

---

* Corresponding author.
   E-mail address: andreas.beyer@physik.uni-marburg.de (A. Beyer).

across interfaces and the actual interface structure cannot be determined straight forwardly. An accepted scheme to encounter this effect in HAADF measurements is to sum the scattered intensity over a certain lateral area e.g. the Voronoi cells of the atomic columns [24] like in the probe integrated scattering cross sections (PICS) method [25]. This method attributes the intensity scattered away from the atomic columns back to the column positions and therefore partially compensates for the effect of de-channeling.

In this paper we systematically study the influence of the lattice plane bending on simulated atomic resolution ADF images. To this end we intentionally choose evaluation schemes to visualize the occurring effects, i.e. evaluating the column intensities rather than Voronoi averaged intensities. To model the surface relaxation, we use super cells of heterostructures that are relaxed via an FE method using linear elastic theory. In addition, the actual interfaces are relaxed using Valence Force Field (VFF) [26] routine, minimizing the total energy of the cell. The resulting cells are then used as input for STEM multislice simulations. As material system we choose a 2 dimensional GaAs quantum well (QW) embedded in a GaP matrix. Yet the relaxation procedure could also be adapted for non-planar structures like e.g. embedded quantum dots.

We choose this system for the simplicity of having two binary constituents with fixed compositions. Therefore, no additional static atomic displacements (SADs) resulting from different properties of the constituents are expected and we can focus on the macroscopic relaxation rather than elemental distribution, because the whole group III sublattice is occupied by Ga atoms only. Additionally, the lattice mismatch between GaP and GaAs is 3.7%, which is a rather high value for actual pseudomorphically grown layers. Nevertheless, thin pseudomorphic layers can indeed be successfully grown [27]. A profound understanding of the occurring effects on the basis of this simple model system allows to address the interfaces in more complex materials, where additional SADs are present, like e.g. Ga(NAs) in GaP, (GaIn)(NAs) in GaAs [28] or (GaIn)N in GaN [24].

Since the elastic surface relaxation is a geometrical effect, we will systematically vary the geometrical parameters, i.e. the QW width and the sample thickness. In order to quantify the effect on actual imaging we will vary the angular detection range resembling high and low angle ADF measurements. Finally, we will propose conditions allowing for the quantification of the chemical composition across the interface of a strained heterostructure at the atomic scale.

2. Materials and methods

In this study several super cells with different geometries were created. The structure of the super cells is exemplarily depicted in Fig. 1 and will be described in the following. The two materials considered, GaP and GaAs, crystallize in zinc blende structure and therefore exhibit cubic symmetry. At first a GaP layer with a width of 376 monolayers (ML) (i.e. ~50 nm) along the "growth" direction x was created. Please note that here we regard group III and group V as individual ML, which might differ from the literature where often the bilayer of GaP is regarded as one ML. Since the absolute lengths in nm will change due to the subsequent relaxation, we will stick to monolayers as a length scale, which simplifies comparing data derived from relaxed and unrelaxed cells, respectively. On top of this virtual GaP substrate, a GaAs QW with a width w of either 22, 37 or 74 ML is created, which translates to a width of approximately 3, 5 and 10 nm, respectively. The QW is followed by another 376 ML of GaP. One has to keep in mind that the Ga columns at the interface have neighboring P columns as well as As columns and therefore could be ambiguously attributed to the GaP or to the GaAs layer. For reasons of consistency we define the first As containing layer in x direction as the start of the quan-
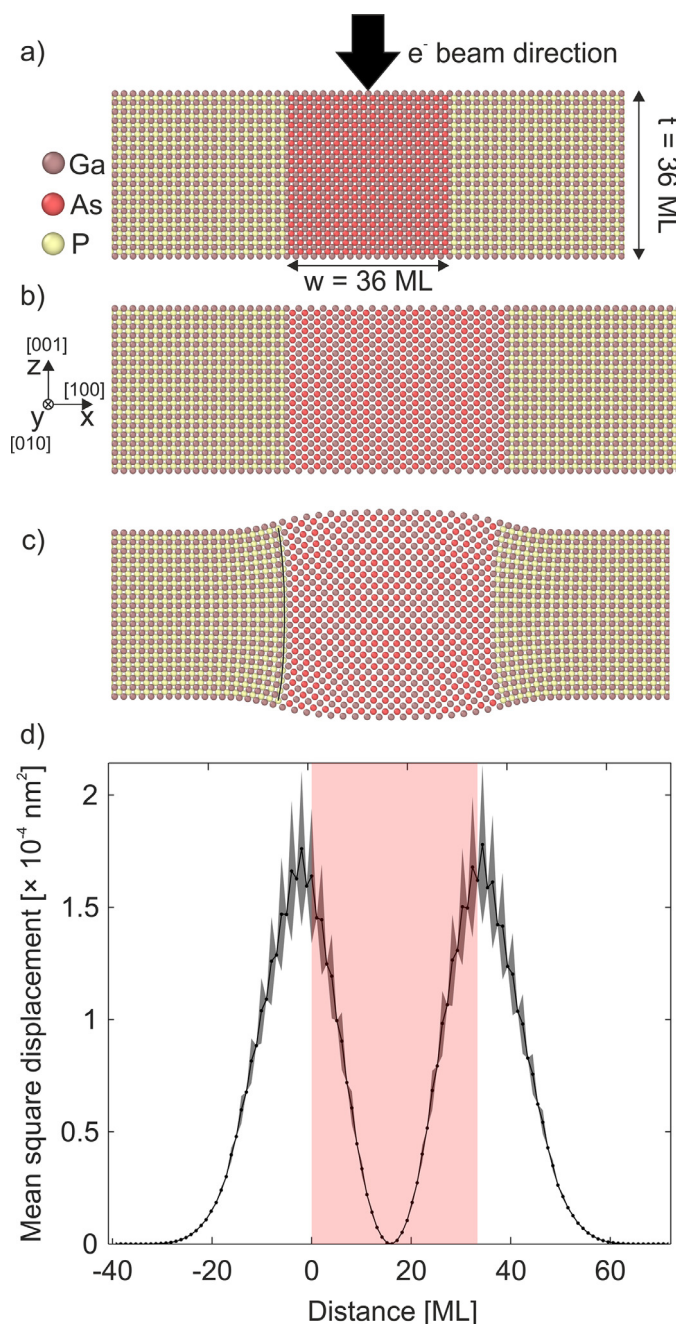

Fig. 1. Structural model of an unrelaxed GaP/GaAs heterostructure a). The direction of the electron beam is z. The same super cell after FE relaxation neglecting and allowing surface relaxation is shown in b) and c), respectively. For a better visualization of the effects, the displacement of the atoms is multiplied by a factor of 5. The bending of lattice planes is quantified via the mean square displacement depicted in d). The shaded red area indicates the position of the quantum well. The slight asymmetry is caused by the free top surface in positive x direction. (For interpretation of the references to colour in this figure legend, the reader is referred to the web version of this article.)

tum well and the first Ga layer which has neighboring P as end of the well. The thickness t with respect to the electron beam (along z-direction) is varied for all of the three above mentioned structures with the chosen values of 80, 184 and 376 ML (approximately 10, 25 and 50 nm). In addition, the y-direction is constructed to be periodic, therefore infinite in extension. This resembles the thin foil geometry of an actual TEM sample in cross-sectional measurements. The crystallographic directions of the cubic system are chosen to coincide with the reference system, therefore the epitaxial

growth direction [100] is along the x-direction. The z-direction is transmitted by the electron beam and is identical to the [001] direction of the zinc blende crystal. For one structure the crystallographic [011] direction was chosen as viewing direction, to investigate the influence of the zone axis on the observed effects.

These initial super cells are relaxed in a two-step process. At first, the geometry is created as a continuous medium. The total structure is divided in smaller regions which are the basis for FE calculations solving the equations of linear elastic theory [16]. Since only complete pseudomorphic growth is considered, plastic deformation is neglected. The GaAs layer is set up in a condition of hydrostatic pressure, according to the lattice mismatch resulting from the free lattice constants. This procedure results in the well-known tetragonal distortion in epitaxial heterostructures when both x- and y-directions are nearly infinite (see Fig. 1b)).

Since the super cells are designed to be finite in both growth and transmission direction as well as periodic in y-direction the appropriate boundary conditions are chosen. It is noteworthy, that the x-direction is not considered to be periodic but fixed to the substrate and free at the top surface.

After relaxation of the initial stress due to the applied hydrostatic pressure the structure deforms according to the boundary conditions and the elastic properties which introduced in a fully anisotropic manner and taken from [29]. In a second step, a super cell with actual atom decoration is created and the displacement field due to relaxation is applied. This atomistic super cell is then refined using a VFF approach using the mesoscopic deformation as starting parameters. We have observed excellent agreement between the simulated surface deformation and experimental atomic force microscopy measurements in the case of (GaIn)(NAs) on GaAs [30].

To reduce the time needed for the relaxation, highly optimized molecular dynamics/energy minimization codes (such as LAMMPS [31]) could be used. To this end the Keating potential used in VFF has to be implemented like it was done e.g. in [32].

In addition to the GaP/GaAs heterostructures, hypothetical structures were created, where the GaP was replaced by GaAs while retaining the lattice constant of GaP. These structures serve as a reference to separate between the influence of the chemical composition and the lattice plane bending on the ADF intensity.

The derived relaxed as well as unrelaxed super cells served as input for ADF STEM multislice simulations in the frozen phonon (FP) approach [33] utilizing the STEMsalabim software [34]. This software package is based on the multislice code of Kirkland [35] and is optimized to perform well on highly parallelized computing clusters. Since the effect of elastic surface relaxation is of considerable length, as will be shown in detail in the next section, the image simulation of large areas is mandatory and the use of efficient simulation software inevitable. The simulation parameters were chosen to model a probe C_S-corrected JEOL JEM 2200FS microscope operating at 200 kV. A convergence semi-angle of 24 mrad was set and residual geometric aberrations of $\Delta f = -2$ nm, $C_S = 2$ μm and $C_5 = 5$ mm were assumed. The angular detection range of the ADF detector was varied systematically. For each sample geometry a defocus series consisting of 7 weighted defoci centered on the optimum defocus was calculated to model the effect of chromatic aberration [6]. For each defocus 10 individual phonon configurations were averaged. In each configuration, the atoms were randomly displaced with mean square displacements of 6.36×10^{-05} nm^2 and 7.73×10^{-5} nm^2 for P and As and 7.17×10^{-5} nm^2 and 9.09×10^{-5} nm^2 for Ga in GaP and GaAs, respectively, according to their Debye-Waller factors from [36]. A Lorentzian source distribution with a width of 38 pm was applied to the simulations according to [37] modeling the effect of spatial incoherence. Considering these parameters, 2 dimensional quantitative agreement between simulation and experiment was

achieved [37]. This allows the extraction of meaningful data from the simulation at each position, e.g. at the position of the atomic columns and the regions in between.

3. Results

We will start with an introduction of the observable effects and the used nomenclature. For an exemplarily chosen combination of QW width w and TEM sample thickness t we will demonstrate the influence of lattice plane bending on HR STEM images of strained interfaces and discuss the impact on the angular dependence of the scattering process. We will systematically investigate the influence of the sampleś geometric properties, i.e. w and t on the surface relaxation and the resulting ADF images. On a final stage we will derive parameters which enable the quantification of strained interfaces.

Fig. 1a) shows a structural model of the initial QW structure with a width of w = 36 ML, without any relaxation method applied. The TEM sample thickness with respect to the impinging electron beam is t = 36 ML. This is rather thin for an actual TEM sample but can be readily created by low energy ion milling [38] and serves the illustration of the occurring effects. The tetragonally distorted super cell depicted in Fig. 1b) was retrieved by applying periodic boundary conditions along y and z, whereas the cell was allowed to relax along x. For a better visualization of the effect, the displacement of the atoms is multiplied by a factor of 5. The additional surface relaxation of the thin TEM sample was accounted for by allowing the FE relaxation along x and z and retaining the periodicity along the y direction only. The resulting super cell is drawn in Fig. 1c). Again the displacement of the atoms is multiplied by a factor of 5 for visualization purposes. With mean square atom displacements in the range of 10^{-4} nm^{-2}, the magnitude of the surface relaxation is rather large. For comparison, the maximum displacements caused by phonons at room temperature is 9.09×10^{-5} nm^{-2} for As. Due to the additional free surface the QW expands along the z direction. This bulging was investigated e.g. [39,40] and directly measured via atomic force microscopy (AFM) in [30]. At this stage we want to note that in the case of tensile strained materials, analogously an indentation is formed at the free surface.

The fact that the lattice planes are no longer perfectly aligned with respect to the impinging electron beam but are bent, is more important for the imaging in TEM than the deformation of the surface along the z axis. One bent lattice plane in the left GaP barrier is highlighted with a black line in Fig. 1c). The center part of the QW remains straight as the strain of the two opposite interfaces compensates. Moreover, a reduction of the elongation along the x axis can be observed, which results from the relaxation at the additional free surface. The magnitude of the lattice plane bending can be quantified via the resulting mistilt angle as done e.g. in [15], or via the lateral mean square displacement M of each atomic column. The value M_i for the i-th column is determined via:

$$M_i = \sum_{k=1}^{N} \frac{(x_k - \overline{x_i})^2}{N} + \sum_{k=1}^{N} \frac{(y_k - \overline{y_i})^2}{N}, \tag{1}$$

where $\overline{x_i}$ and $\overline{y_i}$ are the mean x and y coordinates of the respective atomic column and N denotes the number of atoms in this column. It is noteworthy that any displacement along the z axis is not taken into account here. Moreover, the second y dependent sum is zero in the case of surface relaxation due to the periodic boundary conditions along this direction, whereas in the case of non-planar structures like quantum dots the sum will be non-zero. The course of the displacements across the QW of this example structure is drawn in Fig. 1d). The red shaded area indicates the position of the QW. The origin of the x axis is chosen at the lower

interface of the QW. Here and in the following, the shaded area around the curve denotes the standard deviation calculated for the lattice planes along the y direction. In the GaP barrier on the left hand side M has values in the order of 10^{-9} nm^2 which is in the order of the numerical noise. Towards the interface, M increases by 5 orders of magnitude to a maximum value of 1.7×10^{-4} nm^2, yielding a displacement of 13 pm. As the deformation is compensated for the QW center, M drops to zero and rises near the upper interface. Besides a slight asymmetry, caused by the free top surface in positive x direction, the mean displacement is analogous to the lower surface. It is worth noting that the static atomic displacements (SADs) introduced by the lattice plane bending are comparable to those of substitutional atoms like N introduced in GaAs, which are ~30 pm for a single Ga-N bond and ~9 pm for a TEM sample containing 3% of N [41,42]. The SADs resulting from this change of composition also have been shown to have a significant effect on TEM and STEM imaging [41,43].

In the following we will investigate the effect of the aforementioned bending on ADF imaging. Therefore, we create super cells consisting of t = 184 ML (~25 nm) in z direction and a QW layer width w = 38 ML. Besides the surface relaxed super cell, we model a purely tetragonally distorted QW layer. The resulting HAADF image of the tetragonally distorted super cell is shown in Fig. 2a). To model HAADF imaging conditions the simulated intensity was integrated over an angular range of 74-174 mrad. To minimize the calculation effort, the actual width of the simulated region in y direction was one unit cell, as marked by the dashed rectangle in Fig. 2a). The simulated image was repeated periodically along the y-axis for presentation afterwards. To further reduce the simulation time, the GaP barrier on the right hand side was omitted, as the effects which are studied are anyhow almost symmetrical (cf. Fig. 1d)).

The analogue simulations for the surface relaxed super cell can be found in Fig. 2b). Both images are aligned to each other with respect to the lower interface. Qualitatively the images look very similar, even on a common intensity scale. Hence, the significant influence of the relaxation on the intensity will be highlighted via the following quantitative evaluation. To this end the group III lattice and the group V lattice will be evaluated separately. The corresponding intensity profiles were derived by averaging the intensity in a circle with a diameter of 25 pm (= 2.9 pixels) around each atomic column. We decided for this averaging approach rather than a summing approach, like e.g. the frequently used PICS method [25], because the intensity averaged around the column positions is more sensitive with respect to the tilted lattice planes. For the determination of the chemical composition across an interface this sensitivity is commonly regarded as a disadvantage, but for our study it is actually advantageous, since the effect of bending shall be investigated and the chemical composition is fixed anyways. The understanding of the bending in this model system allows to address interfaces in more complex materials, where additional SADs, e.g. induced by Nitrogen, are present. However, it should be noted that the circular averaging approach is more sensitive to the actual aberrations, especially the probe size. To account for this, reasonable values for an aberration corrected STEM were assumed [37]. The evaluation analogue to Fig. 2 but applying the PICS procedure is shown in Fig. S3 to allow the comparison of our results to others from the literature. As expected the effect of the lattice plane bending is partially compensated for in the PICS approach.

Additionally to the group III positions (Fig. 2c)) and the group V positions (Fig. 2d)), the positions between the atomic columns, i.e. the background (BG) positions, are evaluated (Fig. 2e)). The respective positions are marked in the unit cell shown as inset in Fig. 2c). From a simple point of view one would not expect that the QW is visible in the intensity profile of the group III lattice
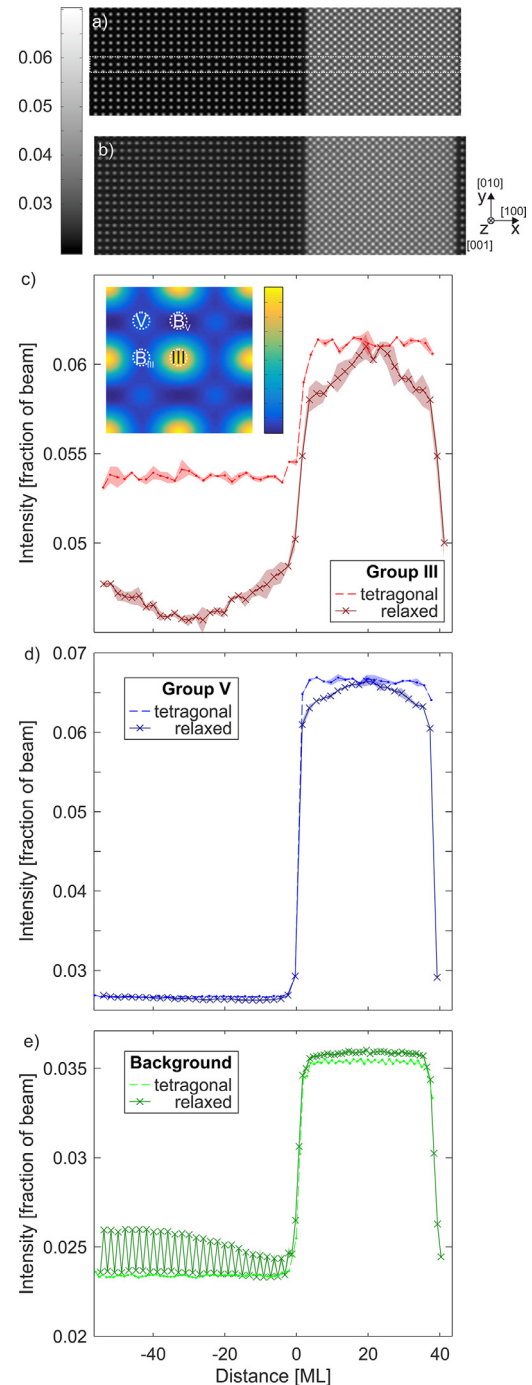

Fig. 2. Simulated ADF images of a tetragonally distorted a) and surface relaxed super cell b) in high angle regime (74-174 mrad). The intensity profiles of the group III sublattice positions are drawn in c) for the tetragonally distorted (broken red line) and relaxed (solid dark red line) super cell. Analogous graphs for the group V sublattice and the background positions are drawn in d) and e), respectively. (For interpretation of the references to colour in this figure legend, the reader is referred to the web version of this article.)

(Fig. 2c)), since the sublattice is occupied exclusively by Ga atoms throughout the entire heterostructure. However, the QW is clearly visible in the profile derived from the tetragonally distorted super cell (broken red line) by its higher intensity. This contrast can be caused by several reasons, i.e. the different interatomic distances of GaP and GaAs, the different Debye-Waller factors of Ga in GaP and GaAs and most prominently by the increased background intensity caused by the neighboring heavy columns. This "cross-talk" could be removed by background subtraction [44,45] or deconvolu-

tion [46]. Here we stick to the raw data as the influence of surface relaxation should be investigated. It is worth noting at this stage that even at the tetragonally distorted interface the STEM intensity does not switch digitally between the one of GaP and GaAs under realistic imaging conditions. Rather a transition over 4 ML (2 group III + 2 group V) is observable. This is caused by the finite probe size due to residual geometric aberrations as well as chromatic aberration and the finite source size. Additionally, broadening of the beam within the ~25 nm thick sample smears out the intensity profile. This highlights the necessity of adequate image simulations for the quantitative interpretation of experimental images.

For comparison, the corresponding profile for the surface relaxed super cell is drawn as solid dark red line in addition to the unrelaxed profile in Fig. 2c). The influence on the intensity is rather significant. The intensity in the GaP barrier is reduced by approximately 15%. Moreover, an intensity gradient across the QW is observable, ending in the same intensity for relaxed and unrelaxed profiles directly at the center. The intensity reduction occurs due to the displaced atomic columns and the resulting de-channelling [20,21] as will be investigated quantitatively later on. The analogue evaluation for the group V sublattice is shown in Fig. 2d). The difference between the intensity from the tetragonally distorted (broken blue line) and the surface relaxed (solid dark blue line) cell is most prominent in the region of the QW, where the intensity decreases by approximately 9%. This is of particular importance as the intensity gradient could be misinterpreted as a change in chemical composition across the QW. In contrast to the group III sublattice, the group V intensities in the GaP barrier seem to be rather unaffected by the relaxation. This is most likely due to the already very low intensity of the P columns. Dependent on the imaging conditions and the sample thickness the P intensity rises above the background level or not [37]. We assume that the effect of the lattice plane bending on the group V intensities will be more distinct in materials where there is not such a big difference in atomic numbers, e.g. (GaIn)As in GaAs. This assumption was verified exemplarily by evaluating a virtual structure, where the P atoms in GaP were replaced by As retaining the displacement field of GaAs in GaP (cf. Fig. S1).

The intensity evaluation of the background positions is shown in Fig. 2e). Here, the QW is clearly visible due to its increased intensity in the profile derived from the tetragonally distorted super cell (broken green line). This intensity rise (~1% of the impinging beam) is caused by the additional TDS of the heavy As columns, in analogy to the evaluation of the group III sublattice. The first thing that catches the eye in the corresponding relaxed profile (solid dark green line) is the intensity undulation in the GaP barrier. This reveals a different intensity depending on whether the position is situated between two group-III (B_{III}) or two group-V atoms (B_V) in growth direction x, which can be seen in more detail in the false color plot of a magnified unit cell shown as inset in Fig. 2c). This can be explained by the different amount of intensity de-channeled from the bent group III and group V atomic columns, respectively. The intensity at the B_{III} positions is significantly increased, as intensity from the neighboring bent Ga columns is present. In contrast to that, the intensity of the B_V positions is rather unaffected and the shape of the profile is retained. This can be understood since the intensity from the neighboring P columns is very low. For the virtual GaAs/GaAs structure the intensity on both background positions is increased and the intensity undulation between B_{III} and B_V is reduced drastically (cf. Fig. S1).

All in all, the total intensity is reduced resulting in the dark contrast at the interface in non-atomically resolved images as described e.g. in [15].

The quantitative correlation between intensity reduction and displacements M will be investigated in the following. To this end,
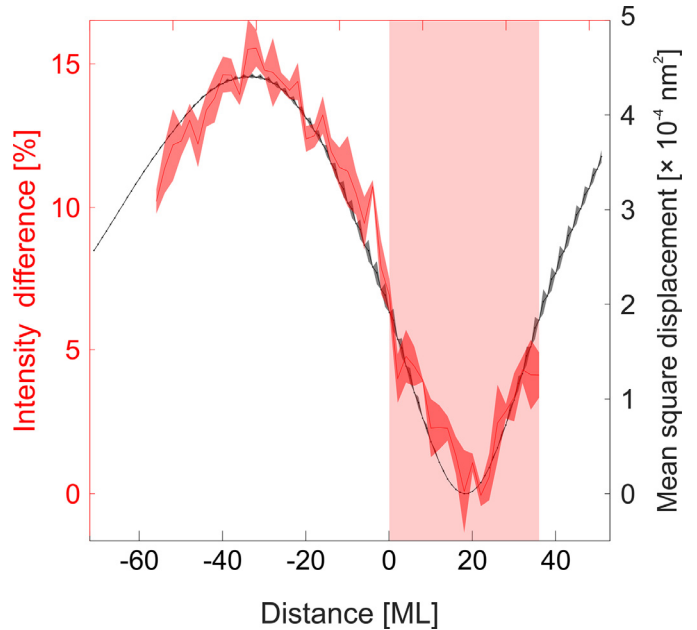

Fig. 3. Intensity difference of the relaxed and unrelaxed super cell for the group III sublattice (red line). The corresponding mean square displacement M of the atomic columns is drawn as black line. The shaded red area indicates the position of the quantum well. (For interpretation of the references to colour in this figure legend, the reader is referred to the web version of this article.)

we will use the group III columns because here the effect of the lattice plane bending can be seen most clearly. We have plotted the intensity difference derived from the relaxed and unrelaxed super cell ($I_{unrelaxed}$-$I_{relaxed}$)/$I_{unrelaxed}$ as red line in Fig. 3 as a quantitative measure for the impact of the lattice plane bending. The plot illustrates the course of the intensity discussed above, i.e. a decreased intensity in the barrier and a gradient across the QW. We want to note here that the maximum intensity change of around 17% is located in the GaP barrier at x = −34 ML which is several nm away from the actual interface. This has strong implications for experiments, as these regions are often used as a reference as will be discussed in Section 3.2.

We want to emphasize that in our simulations a finite source size and chromatic aberration were taken into account. In case of fully coherent simulations neglecting these effects, the influence of the lattice plane bending on the intensity is even more severe, which can be seen in the corresponding evaluation shown in Fig. S2. The intensity ratio is increased by a factor of 2.9 resulting in the unrelaxed intensity being up to 60% higher than relaxed one. Therefore, the discussed effects will be even more important for the next generation of aberration corrected microscopes. The profile of the atoms´ displacements across the heterostructure is drawn as black line in Fig. 3. This curve exhibits the same shape as the intensity ratio, with a distinct maximum of 4.4×10^{-4} nm^2 (i.e. 21 pm displacement) in the barrier at x = −34 ML and zero displacement at x = 18 ML, i.e. the center of the QW. The two curves correlate perfectly with a proportionality factor c of 3.4×10^4%/nm^2, which was derived by dividing the red curve by the black one. In other words a displacement of 10 pm will result in an intensity change of 3.4% and to change the intensity by 1% the column has to be displaced by 5 pm. As mentioned before the effect is more pronounced in the coherent simulation, where a proportionality of $c^{III}_{coh} = 9.9 \times 10^4$%/nm^2 was found. A similar correlation was found for the group V sublattice in coherent simulations, in which the P intensity rises above the background level in GaP and in the virtual GaAs/GaAs heterostructure (cf. Fig. S1).
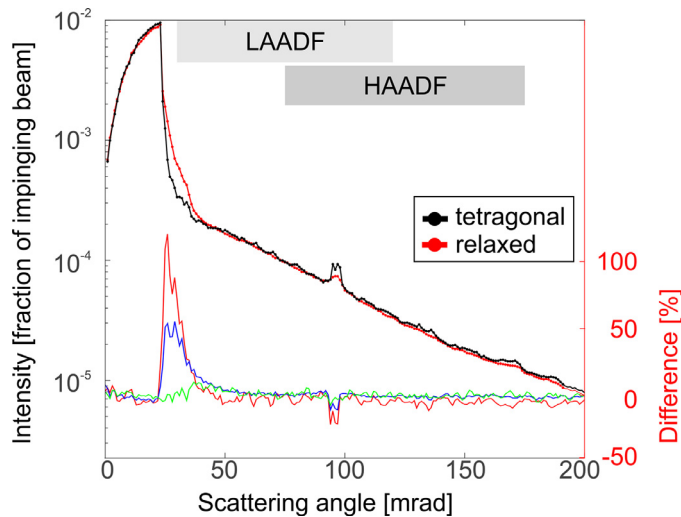
Fig. 4. Angular dependence of the scattered intensity for the tetragonally distorted (black data points) and surface relaxed super cell (red data points). Please read left y axis. The differences are drawn for the whole cell (blue line) and the lattice planes exhibiting the highest (red line) and lowest (green line) displacements, respectively. Please read right y axis. (For interpretation of the references to colour in this figure legend, the reader is referred to the web version of this article.)

With the knowledge of this proportionality constant, simulations neglecting the effect of lattice plane bending could be adapted or experimental images could be corrected to compensate for the bending effects. This is particularly beneficial as the necessary FE simulations are computationally cheap, whereas FP ADF multislice simulations are very demanding, see e.g. [47]. In order to give a measure for the relevant timescales, we choose the largest heterostructure considered in this study, i.e. a 360 ML thick sample containing an 80 ML thick GaAs QW. While the FE relaxation of the super cell was done in minutes, the HAADF simulation took 42 h on 256 cores for one defocus and full set of phonons. The speed of the relaxation can be further increased, if efficient parallel energy minimization codes like LAMMPS are used. Moreover, the strength and the range of the lattice plane bending strongly depends on the actual sample geometry (see chapter 3.2), therefore, more or less each STEM measurement of a strained interface has to be simulated independently, which makes a systematic compensation approach on basis of the FE relaxation even more favorable.

However, the exact value of the proportionality constant c depends on the applied imaging conditions, especially the used detector range, as well as sample parameters. A systematic study of the influencing factors is, however, beyond the scope of this work and will be performed in the future.

The remaining question, where the "missing" intensity is going to will be answered in the following.

3.1. Angular dependence

Already before we highlighted the similar magnitude of the atom displacements caused by the surface relaxation and caused by the incorporation of elements with different covalent radii, e.g. N in GaAs. For Ga(NAs) it has been shown that the consideration of the SADs induced by N is essential for the explanations of contrast reversals [41]. Due to the increased diffuse Huang scattering [22,23], low angle ADF (LAADF) measurements can be used to detect even small amounts of N in GaAs [48]. Therefore, one can expect a significant angular dependence in the case of surface relaxation, too.

To investigate this, the scattered intensity is drawn against the scattering angle in Fig. 4. The angular ranges used for retrieving

the images in Fig. 2 (HAADF) and 5 (LAADF), respectively, are highlighted by grey rectangles. The reference curve derived from the tetragonally distorted super cell is represented by the black data points (read left y axis). The corresponding dependence derived from the surface relaxed super cell is represented by red data points. Both curves run parallel for most angles, they only differ at two distinct angular ranges. This can be seen in more detail in the difference plots shown in the lower part of Fig. 4. The blue curve depicts the intensity difference, i.e. $(I_{relaxed}-I_{unrelaxed})/I_{relaxed}$, derived from the whole super cell. The right y axis quantifies the deviation in percent. At low angles (∼25-50 mrad) the intensity of the relaxed cell is increased significantly by around 50%. The bent (disordered) lattice planes result in additional diffuse Huang scattering. Additionally, a drop of intensity is visible at around 100 mrad, which is the region of the first order Laue zone (FOLZ). This reduction is not surprising as the disorder is expected to smear out the Bragg reflections. To underpin that this intensity change is caused by the bent lattice planes, the analogue difference plots are drawn for the most distorted plane only (red line) and the undistorted plane in the center of the QW (green line). Indeed, the intensity difference is severe (∼100% at low angles) for the bent plane and almost negligible at the undistorted one.

To summarize the angular dependence briefly, intensity at high scattering angles is reduced by de-channeling caused by the displacements, whereas the intensity at lower angles is increased due to diffuse Huang scattering [22,23].

The consequences of this angular dependence for ADF imaging using different angular ranges, i.e. different camera lengths, is summarized in Figs. 2 and 5. In analogy to Fig. 2, the simulated images of the tetragonally distorted as well as the surface relaxed super cell are depicted for the LAADF regime (35–140 mrad) in Fig. 5a) and b), respectively. We choose this angular region because recent studies show quantitative agreement between FP simulations and experimental data for scattering angles above 35 mrad, whereas for lower angles significant discrepancies were observed [49]. The influence of the lattice bending on the intensity will be quantified via the intensity profiles depicted in Fig. 5c)-e). Despite the expectable change of the intensity scale, the intensity profiles extracted from the unrelaxed super cell (broken lines) look similar to the ones derived at high scattering angles (compare Fig. 2), i.e. a nearly abrupt intensity transition from GaP to GaAs is visible. However, the intensity profiles derived from the relaxed super cells (dark solid lines) drastically differ from the ones of the unrelaxed cell as well as from the analogue profiles derived at high scattering angles (compare Fig. 2). For explanatory reasons we will detail the differences on the basis of the background intensity depicted in Fig. 5e) at first. The intensity is clearly increased at the positions at which the lattice planes are strongly bent. This results in an intensity curve in the shape of the letter M, which is complementary to the shape observed at high scattering angles. Once more an undulation of the intensity is observable in the GaP caused by the large Z difference of Ga and P. This distinct BG intensity also overlays the profiles of group III (Fig. 5c)) and V (Fig. 5d)) and partially compensates for the intensity loss on the column positions. The intensity increase observed at the background positions is even higher for lower scattering angles. Assuming for example an angular detector range from 30-120 mrad, the background intensity becomes dominating leading to the M-shape being observable on the group III and V sublattices as well. In total, at low scattering angles an intensity increase is observable at the interfaces like already shown in for uncorrected STEM measurements [41,48].

3.2. Variation of geometrical parameters

As already stated before, the lattice plane bending drastically complicates the derivation of quantitative data from strained inter-
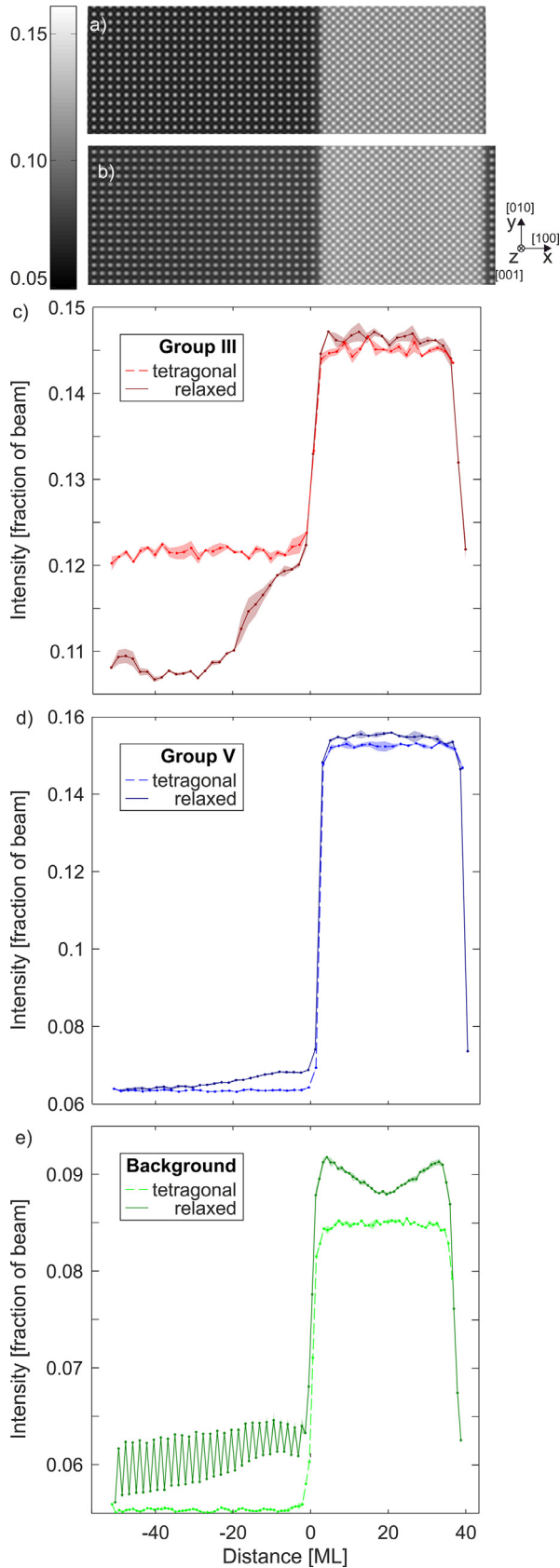
Fig. 5. Simulated ADF images of a tetragonally distorted a) and surface relaxed super cell b) in low angle regime (35-140 mrad). The intensity profiles of the group III sublattice positions are drawn in c) for the tetragonally distorted (broken red line) and relaxed (solid dark red line) super cell. Analogous graphs for the group V sublattice and the background positions are drawn in d) and e), respectively. (For interpretation of the references to colour in this figure legend, the reader is referred to the web version of this article.)

faces. At the previously discussed example structure, the maximum distortion was situated several nm away from the actual interface. In the following we will study how this depends on the sample geometric properties, namely QW width w (along x=[100] direction) and TEM sample thickness t (along z=[001] direction).

The results from 9 different sample geometries are summarized in Fig. 6. The QW width w increases from left to right from 22 to 37 and 74 ML. The position of the QW is marked by the red shaded area. Analogously the values for t increase from top to bottom, from 80 to 184 and 375 MLs, respectively. Like in the previous chapters we will look at the simulated STEM intensity on the group III column across the interface (red lines, read right y axis) as well as the mean square displacement for each corresponding atom column (black lines, read left y axis) in the following. To be able to compare samples with different thicknesses, the intensities are normalized to the intensities of pure GaP with the corresponding thickness, following the equation $I_{norm} = (I-I_{GaP})/I_{GaP}$. The mean square displacements for the different super cells are drawn on a common y scale which is determined by the highest values present, i.e. the values for the thickest sample and the widest QW (Fig. 6i)). In this super cell the maximum total strain energy which is proportional to $w \times t$ is accumulated.

For all super cells displayed, there is a perfect correlation between the displacements and the change of intensity: Firstly, the x position of the maximum displacement coincides with the maximum intensity drop. Secondly, the higher the displacement values, the more severe the intensity reduction. The quality of the correlation is highlighted exemplarily by the blue graph in Fig. 6e), which represents the intensity difference caused by the relaxation, i.e. $(I_{unrelaxed}-I_{relaxed})/I_{unrelaxed}$ in analogy to Fig. 3. Moreover, there are several other interesting trends visible, which will be discussed on the basis of the displacements first.

At a fixed TEM sample thickness (e.g. Fig. 6a)-c)), the thinner the QW, the smaller the maximum displacement. In addition, the x position of the maximum shifts away from the actual interface which may be explained by a compensation effect of the opposing interfaces.

Another observation is that for thicker TEM samples (e.g. from c) to f) and i)), the displacement field shifts away from the interface and broadens. For example in cell i), the maximum of the displacement is at x=-75 ML and it is still present at x=-250 ML. The long range of the displacement field again points out the necessity of large super cells and highly parallelized STEM simulations. For the two thicker QWs, also the magnitude of the displacement rises with increasing TEM sample thickness. This is not apparent for the thinnest QW (a), d) and g)), most likely due to a compensation of the effects of the opposing interfaces. It is worth noting that the degree of surface relaxation is reduced if the sample is thinned along [011] instead of [001]. A comparison between the two zone axes for a sample geometry comparable to the one evaluate in Fig. 6a) can be found in Fig. S4. A disadvantage of the [011] zone axis is that the distance between the group III and V atomic columns is smaller in this projection, therefore cross talk is more likely.

Finally, the two main consequences of the plane bending for ADF measurements will be highlighted briefly. Firstly, whenever the displacement field significantly reaches into the QW (see e.g. Fig. 6i)), the shape of the intensity curve is significantly altered from a box profile. If not accounted for, this can lead to a misinterpretation in terms of chemical composition. This means a thicker sample may be more favorable because the intensity drop is shifted into the barrier. Secondly, the bending significantly reaches into the barrier. This is of special importance as these regions often serve as reference for e.g. sample orientation, determining the chemical composition of the QW or during strain mapping, as they are regarded as undisturbed. For both problems, the computation-
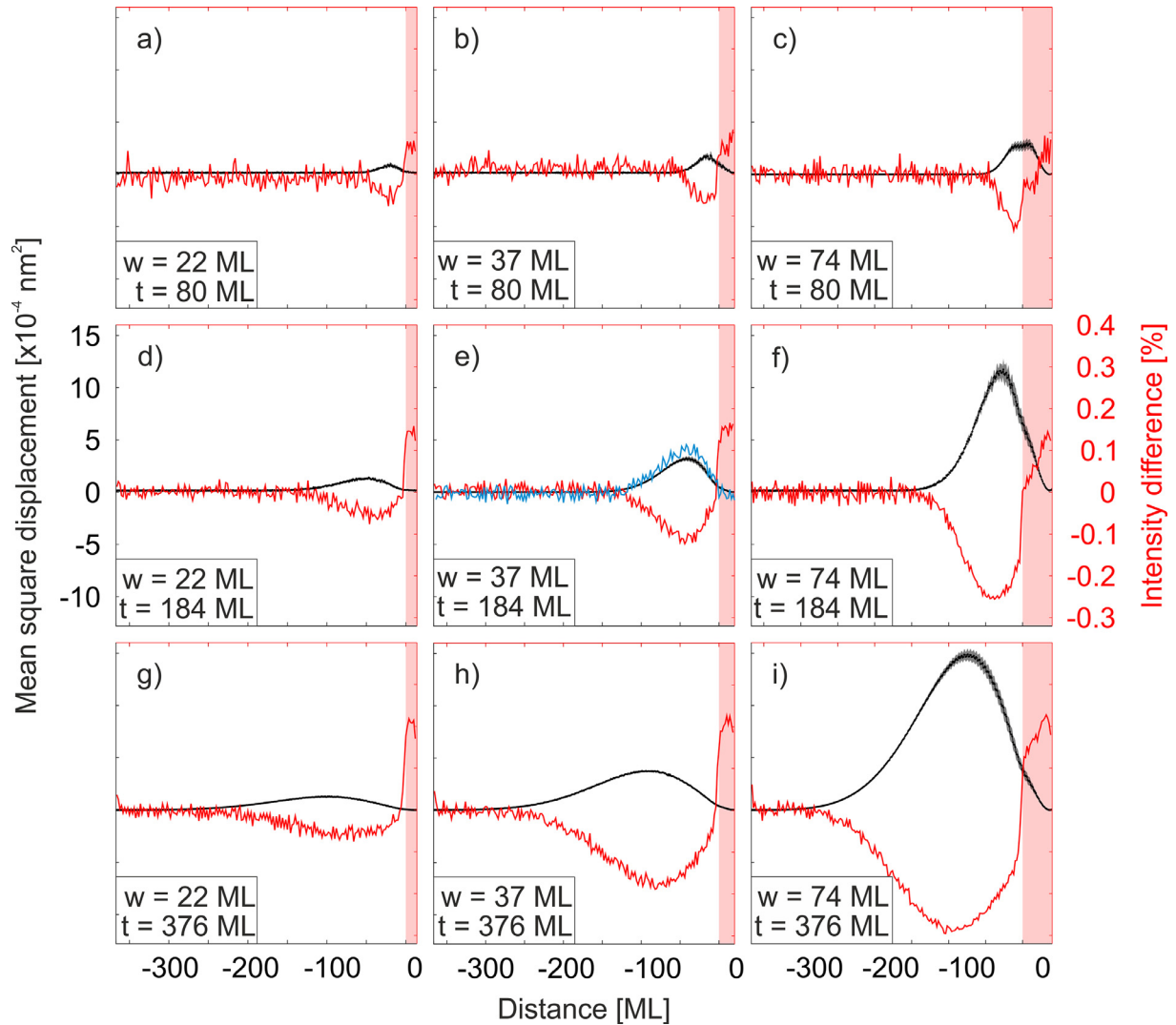
Fig. 6. Systematic variation of the sampleś geometric properties. The quantum well width w increases from left to right, whereas the TEM sample thickness increases from top to bottom. The displacements of the atomic columns are drawn as black lines (read left y axis). The normalized group III intensities are drawn as red lines (read right y axis). The shaded red area indicates the position of the quantum well. The blue curve in e) represents the intensity difference between the surface relaxed and tetragonally distorted super cell. (For interpretation of the references to colour in this figure legend, the reader is referred to the web version of this article.)

ally cheap FE relaxation can be used to localize the distorted regions, find undisturbed ones or on a final stage even to correct "spoiled" data. Anyhow, for real samples, some additional factors have to be considered. Firstly, any additionally present SADs (e.g. introduced by substitutional atoms) superimpose the effect of lattice bending giving rise to additional de-channeling. But since in our approach the FE and the VFF relaxations are performed consecutively, both effects may be differentiated from one another. Secondly, for heterostructures in which the chemical composition fluctuates the composition will influence the bending and the bending will influence the determination of the composition. This means, the problem has to be solved self-consistently. In this case, the average composition will be a good starting point for the simulation of the bending. The average composition can be determined from unbent regions, e. g. the center part of the QW.

4. Conclusions

Lattice plane bending significantly influences ADF images of strained interfaces. This impedes an accurate orientation of the sample, the quantitative evaluation of intensities as well as strain mapping.

Where and how much sample is bent can be estimated from FE relaxation of adequate super cells. FP simulations reveal a reduced intensity in HAADF images caused by de-channeling of electrons from the atomic column positions. Simultaneously, additional diffuse scattering takes place at the bent lattice planes resulting in an increased intensity at low scattering angles. Simulations neglecting the influence of chromatic aberration reveal that the discussed effects will be even more important for the next generation of aberration corrected microscopes.

The intensity reduction of an atomic column in HAADF measurements is directly proportional to its mean square displacement. The computationally cheap FE relaxation can be used to localize the distorted regions and on a final stage even to correct the reduced intensity, whereby a quantitative evaluation of the chemical composition across the interface becomes feasible.

Supplementary materials

Supplementary material associated with this article can be found, in the online version, at doi:10.1016/j.ultramic.2017.04.019.

References

[1] Q. Xu, Y. Ji, D.D. Krut, J.H. Ermer, M.D. Escarra, Transmissive concentrator multijunction solar cells with over 47% in-band power conversion efficiency, Appl. Phys. Lett. 109 (2016) 193905, doi:10.1063/1.4967376.

[2] H. Tan, A. Furlan, W. Li, K. Arapov, R. Santbergen, M.M. Wienk, M. Zeman, A.H.M. Smets, R.A.J. Janssen, Highly efficient hybrid polymer and amorphous silicon multijunction solar cells with effective optical management, Adv. Mater. 28 (2016) 2170–2177, doi:10.1002/adma.201504483.

[3] N. Wang, L. Cheng, R. Ge, S. Zhang, Y. Miao, W. Zou, C. Yi, Y. Sun, Y. Cao, R. Yang, Y. Wei, Q. Guo, Y. Ke, M. Yu, Y. Jin, Y. Liu, Q. Ding, D. Di, L. Yang, G. Xing, H. Tian, C. Jin, F. Gao, R.H. Friend, J. Wang, W. Huang, Perovskite light-emitting diodes based on solution-processed self-organized multiple quantum wells, Nat. Photonics. 10 (2016) 699–704, doi:10.1038/nphoton.2016.185.

[4] S.J. Pennycook, Z-contrast stem for materials science, Ultramicroscopy. 30 (1989) 58–69, doi:10.1016/0304-3991(89)90173-3.

[5] N.D. Browning, S.J. Pennycook, Direct experimental determination of the atomic structure at internal interfaces, J. Phys. D. Appl. Phys. 29 (1996) 1779–1798, doi:10.1088/0022-3727/29/7/013.

[6] C. Dwyer, C. Maunders, C.L. Zheng, M. Weyland, P.C. Tiemeijer, J. Etheridge, Sub-0.1 nm-resolution quantitative scanning transmission electron microscopy without adjustable parameters, Appl. Phys. Lett. (2012) 100, doi:10.1063/1.4711766.

[7] J.M. Lebeau, S. Stemmer, Experimental quantification of annular dark-field images in scanning transmission electron microscopy, Ultramicroscopy 108 (2008) 1653–1658, doi:10.1016/j.ultramic.2008.07.001.

[8] A. Rosenauer, K. Gries, K. Müller, M. Schowalter, A. Pretorius, A. Avramescu, K. Engl, S. Lutgen, Measurement of composition profiles in III-nitrides by quantitative scanning transmission electron microscopy, J. Phys. Conf. Ser. 209 (2010) 12009, doi:10.1088/1742-6596/209/1/012009.

[9] C. Dwyer, R. Erni, J. Etheridge, Measurement of effective source distribution and its importance for quantitative interpretation of STEM images, Ultramicroscopy. 110 (2010) 952–957, doi:10.1016/j.ultramic.2010.01.007.

[10] D.T. Nguyen, S.D. Findlay, J. Etheridge, The spatial coherence function in scanning transmission electron microscopy and spectroscopy, Ultramicroscopy. 146 (2014) 6–16, doi:10.1016/j.ultramic.2014.04.008.

[11] K. Kuramochi, T. Yamazaki, Y. Kotaka, M. Ohtsuka, I. Hashimoto, K. Watanabe, Effect of chromatic aberration on atomic-resolved spherical aberration corrected STEM images, Ultramicroscopy. 110 (2009) 36–42, doi:10.1016/j.ultramic.2009.09.003.

[12] K.A. Mkhoyan, S.E. Maccagnano-Zacher, E.J. Kirkland, J. Silcox, Effects of amorphous layers on ADF-STEM imaging, Ultramicroscopy. 108 (2008) 791–803, doi:10.1016/j.ultramic.2008.01.007.

[13] M.M.J. Treacy, The effects of elastic relaxation on transmission electron microscopy studies of thinned composition-modulated materials, J. Vac. Sci. Technol. B Microelectron. Nanom. Struct. 4 (1986) 1458, doi:10.1116/1.583473.

[14] L. De Caro, A. Giuffrida, E. Carlino, L. Tapfer, Elastic stress relaxation in HRTEM specimens of strained semiconductor heterostructures and its influence on the image contrast, Microsc. Microanal. Microstruct. 6 (1995) 465–472, doi:10.1051/mmm:1995137.

[15] V. Grillo, The effect of surface strain relaxation on HAADF imaging, Ultramicroscopy. 109 (2009) 1453–1464, doi:10.1016/j.ultramic.2009.07.010.

[16] L. De Caro, A. Giuffrida, E. Carlino, L. Tapfer, Effects of the elastic stress relaxation on the HRTEM image contrast of strained heterostructures, Acta Crystallogr. Sect. A Found. Crystallogr. 53 (1997) 168–174, doi:10.1107/S0108767396012378.

[17] A. Rosenauer, D. Gerthsen, V. Potin, Strain state analysis of InGaN/GaN - sources of error and optimized imaging conditions, Phys. Status Solidi. 203 (2006) 176–184, doi:10.1002/pssa.200563519.

[18] L. De Caro, L. Tapfer, A. Giuffrida, Finite-size effects in one-dimensional strained semiconductor heterostructures, Phys. Rev. B. 54 (1996) 10575–10584, doi:10.1103/PhysRevB.54.10575.

[19] Z. Yu, D.A. Muller, J. Silcox, Study of strain fields at a-Si/c-Si interface, J. Appl. Phys. 95 (2004) 3362–3371, doi:10.1063/1.1649463.

[20] A. Amali, P. Rez, J.M. Cowley, High angle annular dark field imaging of stacking faults, Micron 28 (1997) 89–94, doi:10.1016/S0968-4328(97)00001-2.

[21] D.D. Perovic, C.J. Rossouw, A. Howie, Imaging elastic strains in high-angle annular dark field scanning transmission electron microscopy, Ultramicroscopy. 52 (1993) 353–359, doi:10.1016/0304-3991(93)90046-Z.

[22] J.M. Cowley, Y. Huang, De-channelling contrast in annular dark-field STEM, Ultramicroscopy. 40 (1992) 171–180, doi:10.1016/0304-3991(92)90058-R.

[23] K. Huang, X-Ray Reflexions from Dilute Solid Solutions, Proc. R. Soc. A Math. Phys. Eng. Sci. 190 (1947) 102–117, doi:10.1098/rspa.1947.0064.

[24] A. Rosenauer, T. Mehrtens, K. Müller, K. Gries, M. Schowalter, P. Venkata Satyam, S. Bley, C. Tessarek, D. Hommel, K. Sebald, M. Seyfried, J. Gutowski, A. Avramescu, K. Engl, S. Lutgen, Composition mapping in InGaN by scanning transmission electron microscopy, Ultramicroscopy. 111 (2011) 1316–1327, doi:10.1016/j.ultramic.2011.04.009.

[25] E. H, K.E. MacArthur, T.J. Pennycook, E. Okunishi, A.J. D'Alfonso, N.R. Lugg, L.J. Allen, P.D. Nellist, Probe integrated scattering cross sections in the analysis of atomic resolution HAADF STEM images, Ultramicroscopy. 133 (2013) 109–119, doi:10.1016/j.ultramic.2013.07.002.

[26] P.N. Keating, Effect of invariance requirements on the elastic strain energy of crystals with application to the diamond structure, Phys. Rev. 145 (1966) 637–645, doi:10.1103/PhysRev.145.637.

[27] H. Döscher, P. Hens, A. Beyer, L. Tapfer, K. Volz, W. Stolz, GaP-interlayer formation on epitaxial GaAs(100) surfaces in MOVPE ambient, J. Cryst. Growth. (2016), doi:10.1016/j.jcrysgro.2016.10.055.

[28] T. Grieb, K. Müller, E. Cadel, A. Beyer, M. Schowalter, E. Talbot, K. Volz, A. Rosenauer, Simultaneous, quantification of indium and nitrogen concentration in InGaNAs using HAADF-STEM, Microsc. Microanal. 20 (2014) 1740–1752, doi:10.1017/S1431927614013051.

[29] I. Vurgaftman, J.R. Meyer, L.R. Ram-Mohan, Band parameters for III–V compound semiconductors and their alloys, J. Appl. Phys. 89 (2001) 5815, doi:10.1063/1.1368156.

[30] J. Belz, A. Beyer, T. Torunski, W. Stolz, K. Volz, Direct investigation of (sub-) surface preparation artifacts in GaAs based materials by FIB sectioning, Ultramicroscopy. 163 (2016) 19–30, doi:10.1016/j.ultramic.2016.01.001.

[31] S. Plimpton, Fast parallel algorithms for short-range molecular dynamics, J. Comput. Phys. 117 (1995) 1–19, doi:10.1006/jcph.1995.1039.

[32] T. Grieb, K. Müller, R. Fritz, V. Grillo, M. Schowalter, K. Volz, A. Rosenauer, Quantitative chemical evaluation of dilute GaNAs using ADF STEM: avoiding surface strain induced artifacts, Ultramicroscopy. 129 (2013) 1–9, doi:10.1016/j.ultramic.2013.02.006.

[33] R.F. Loane, P. Xu, J. Silcox, Thermal vibrations in convergent-beam electron diffraction, Acta Crystallogr. Sect. A Found. Crystallogr. 47 (1991) 267–278, doi:10.1107/S0108767391000375.

[34] J.O. Oelerich, L. Duschek, J. Belz, A. Beyer, S.D. Baranovskii, K. Volz, STEMsalabim: a high-performance computing cluster friendly code for scanning transmission electron microscopy image simulations of thin specimens, Ultramicroscopy. 177 (2017) 91–96, doi:10.1016/j.ultramic.2017.03.010.

[35] E.J. Kirkland, Advanced Computing in Electron Microscopy, Springer U.S, Boston, M.A., 2010, doi:10.1007/978-1-4419-6533-2.

[36] M. Schowalter, A. Rosenauer, J.T. Titantah, D. Lamoen, Computation and parametrization of the temperature dependence of Debye-Waller factors for group IV, III-V and II-VI semiconductors, Acta Crystallogr. A. 65 (2009) 5–17, doi:10.1107/S0108767308031437.

[37] A. Beyer, J. Belz, N. Knaub, K. Jandieri, K. Volz, Influence of spatial and temporal coherences on atomic resolution high angle annular dark field imaging, Ultramicroscopy. 169 (2016) 1–10, doi:10.1016/j.ultramic.2016.06.006.

[38] A. Lotnyk, D. Poppitz, U. Ross, J.W. Gerlach, F. Frost, S. Bernütz, E. Thelander, B. Rauschenbach, Focused high- and low-energy ion milling for TEM specimen preparation, Microelectron. Reliab. 55 (2015) 2119–2125, doi:10.1016/j.microrel.2015.07.005.

[39] F. Lelarge, C. Priester, C. Constantin, A. Rudra, K. Leifer, E. Kapon, Strain mapping of V-groove InGaAs/GaAs strained quantum wires using cross-sectional atomic force microscopy, Appl. Surf. Sci. 166 (2000) 290–294, doi:10.1016/S0169-4332(00)00410-4.

[40] F. Lelarge, O. Dehaese, E. Kapon, C. Priester, Strain relaxation at cleaved surfaces studied by atomic force microscopy, Appl. Phys. A Mater. Sci. Process. 69 (1999) 347–351, doi:10.1007/s003390051012.

[41] V. Grillo, K. Mueller, K. Volz, F. Glas, T. Grieb, A. Rosenauer, Strain, composition and disorder in ADF imaging of semiconductors, J. Phys. Conf. Ser. 326 (2011) 12006, doi:10.1088/1742-6596/326/1/012006.

[42] O. Rubel, I. Németh, W. Stolz, K. Volz, Modeling the compositional dependence of electron diffraction in dilute GaAs- and GaP-based compound semiconductors, Phys. Rev. B. 78 (2008) 75207, doi:10.1103/PhysRevB.78.075207.

[43] V. Grillo, E. Carlino, F. Glas, Influence of the static atomic displacement on atomic resolution Z-contrast imaging, Phys. Rev. B. 77 (2008) 54103, doi:10.1103/PhysRevB.77.054103.

[44] D.O. Klenov, S. Stemmer, Contributions to the contrast in experimental high-angle annular dark-field images, Ultramicroscopy. 106 (2006) 889–901, doi:10.1016/j.ultramic.2006.03.007.

[45] Y. Kotaka, Essential experimental parameters for quantitative structure analysis using spherical aberration-corrected HAADF-STEM, Ultramicroscopy. 110 (2010) 555–562, doi:10.1016/j.ultramic.2009.12.008.

[46] K. Watanabe, Y. Kotaka, N. Nakanishi, T. Yamazaki, I. Hashimoto, M. Shiojiri, Deconvolution processing of HAADF STEM images, Ultramicroscopy. 92 (2002) 191–199, doi:10.1016/S0304-3991(02)00132-8.

[47] C. Dwyer, Simulation of scanning transmission electron microscope images on desktop computers, Ultramicroscopy. 110 (2010) 195–198, doi:10.1016/j.ultramic.2009.11.009.

[48] T. Grieb, K. Müller, R. Fritz, M. Schowalter, N. Neugebohrn, N. Knaub, K. Volz, A. Rosenauer, Determination of the chemical composition of GaNAs using STEM HAADF imaging and STEM strain state analysis, Ultramicroscopy. 117 (2012) 15–23, doi:10.1016/j.ultramic.2012.03.014.

[49] K. Müller-Caspary, O. Oppermann, T. Grieb, F.F. Krause, A. Rosenauer, M. Schowalter, T. Mehrtens, A. Beyer, K. Volz, P. Potapov, Materials characterisation by angle-resolved scanning transmission electron microscopy, Sci. Rep. 6 (2016) 37146, doi:10.1038/srep3714.

Stemsalabim: a high-performance computing cluster friendly code for scanning transmission electron microscopy image simulations of thin specimens

J. O. Oelerich, L. Duschek, J. Belz, A. Beyer, S. D. Baranovskii, and K. Volz,

Ultramicroscopy, vol. 177, pp. 91–96, 2017

Abstract

We present a new multislice code for the computer simulation of scanning transmission electron microscope (STEM) images based on the frozen lattice approximation. Unlike existing software packages, the code is optimized to perform well on highly parallelized computing clusters, combining distributed and shared memory architectures. This enables efficient calculation of large lateral scanning areas of the specimen within the frozen lattice approximation and fine-grained sweeps of parameter space.

The authors' contributions

The simulation code was developed and written by J. O. Oelerich. My contribution was testing the code and giving feedback for the development. Furthermore I compared the results to results from existing software and provided sample data. The manuscript was written by J. O. Oelerich and all co-authors helped to improve the manuscript.

STEMsalabim: A high-performance computing cluster friendly code for scanning transmission electron microscopy image simulations of thin specimens

Jan Oliver Oelerich*, Lennart Duschek, Jürgen Belz, Andreas Beyer, Sergei D. Baranovskii, Kerstin Volz

Faculty of Physics and Material Sciences Center, Philipps-Universität Marburg, Germany

ARTICLE INFO

ABSTRACT

We present a new multislice code for the computer simulation of scanning transmission electron microscope (STEM) images based on the frozen lattice approximation. Unlike existing software packages, the code is optimized to perform well on highly parallelized computing clusters, combining distributed and shared memory architectures. This enables efficient calculation of large lateral scanning areas of the specimen within the frozen lattice approximation and fine-grained sweeps of parameter space.

© 2017 Elsevier B.V. All rights reserved.

1. Introduction

Since the early 1980s scanning transmission electron microscopy (STEM) has evolved into an indispensible tool for the structural analysis of thin crystalline specimen [1]. Using high-angle annular dark field (HAADF) detectors, chemically sensitive scattering of the focused electron probe can reveal valuable information about the sample, such as chemical composition, strain fields, thicknesses, etc [2–5]. In order to extract quantitative information from STEM images, however, often it is still necessary to compare measured data to computer simulations of the interaction between incident electron beam and the specimen.

Attempts to simulate such electron-specimen interaction numerically go back to the mid-1970s, when Goodman and Moodie [6] first implemented the multislice algorithm proposed earlier by Cowley and Moodie [7]. Since then, the multislice approach evolved into the most practical approach for the simulation of transmission electron microscopy (TEM) and STEM images and is widely applied today for the analysis of experimental (S)TEM im-

ages [2]. A brief description of the multislice algorithm is given in Section 2.

Although the basic algorithm of the multislice method is relatively simple and can be carried out very efficiently using highly optimized discrete fourier transform (DFT) packages [1], a typical STEM image simulation is still computationally demanding: For each lateral scan position of the focused electron probe, the full interaction between the incident electron wave and the specimen has to be simulated. For instance, modeling a STEM image with only 128 pixels × 128 pixels scan points requires more than 16k multislice simulations. This number grows significantly when taking into account thermal diffuse scattering (TDS) by applying the frozen lattice approximation [8] (see Section 2), requiring all simulations to be repeated a number of times with thermally displaced atomic positions. In order to further account for chromatic aberrations one needs to average over multiple probe defoci [9–12], each of which requires another repetition of the complete set of simulations. For typical values of 10 frozen lattice configurations (the necessary number for convergence depends on sample thickness) and a defocus series consisting of 7 defocus values, the total number of multislice simulations required for the 128 pixels× 128 pixels STEM image easily exceeds one million. Needless to say, systematic parameter variations or simulations of larger supercell sizes further drastically increase the computational demand.

---

* Corresponding author.
E-mail address: jan.oliver.oelerich@physik.uni-marburg.de (J.O. Oelerich).

Although there are many existing implementations of the multislice algorithm for the simulation of STEM images [1,13–23], almost all of them are designed for desktop computers with a single or very few processors or don't comply with common parallelization standards and are therefore not suited for realistic large-scale simulations, parameter sweeps, or iterative optimization. Particularly surprising is the lack of a freely available code for massive parallelization on high-performance computing (HPC) clusters, even though the many necessary multislice simulations for a single STEM image are independent from each other and therefore perfectly suited for efficient parallelization.

In this article we present *STEMsalabim*, a new implementation of the multislice algorithm that is built specifically for concurrent calculations on many computing nodes. The package uses a combination of the message passing interface (MPI) and (POSIX) threads for efficient parallelization while maintaining a small memory footprint, a feature that is not present in existing software packages but crucial for the simulation of large images. STEMsalabim supports TDS via the frozen lattice approximation [8], is able to simulate chromatic aberrations by means of defocus series [9–12], and implements lens aberrations of focused electron beams in STEM up to fifth order [24].

In Section 2 we summarize the multislice frozen lattice algorithm as implemented in STEMsalabim and give implementation details. Simulation results and comparison with experimental images are shown in Section 3, benchmarks and parallel scaling behaviour of the package are summarized in Section 4. Conclusions and acknowledgements are given in Section 5 and acknowledgement.

2. Algorithm and implementation

STEMsalabim implements the standard multislice algorithm as explained in great detail in the book of Kirkland [1]. In this approximation, the supercell is divided into slices of some thickness dz perpendicular to the direction of the electron beam z. Passing through a slice, the electronic wave function is first modified by interaction with the 2D projected potential of the slice's atoms, and is then propagated by a Fresnel propagator through empty space of thickness dz. This process is repeated for all slices in the supercell. Afterwards, the wave intensity is integrated and collected over some momentum range to simulate an HAADF ring detector. The multislice algorithm is repeated for each scan position of the incident focused electron probe, for varying atomic positions in order to resemble TDS, and for different defocus values to account for chromatic aberrations.

2.1. Multislice method

Let us briefly repeat the most important equations required for the multislice method as described by Kirkland [1].

The supercell is split into N consecutive slices of thickness dz perpendicular to the beam direction z. The projected potential $v_s(x, y)$ for each slice s is evaluated as the cumulative atomic potential of all atoms i in the slice:

$$v_s(x, y) = \sum_i \int V_i(x - x_i, y - y_i, z) dz. \tag{1}$$

The atomic potentials $V_i(|\vec{r}|)$ for the elements i are calculated from the atomic scattering amplitudes $f_i(\vec{k})$ by employing the first Born approximation

$$V_i(|\vec{r}|) \propto \mathcal{F}^{-1}\left(f_i(\vec{k})\right), \tag{2}$$

where $\mathcal{F}^{-1}$ is the inverse fourier transform. The scattering amplitudes $f_i(\vec{k})$ can be parametrized following Ref. [1] using tabulated

values for the element specific parameters $a_{i,j}$, $b_{i,j}$, $c_{i,j}$, and $d_{i,j}$:

$$f_i(\vec{k}) = \sum_{j=1}^{3} \frac{a_{i,j}}{|k|^2 + b_{i,j}} + \sum_{j=1}^{3} c_{i,j} \exp(-d_{i,j}|k|^2). \tag{3}$$

Note, that finding correct parametrizations of electron and X-ray scattering factors for a wide angle range is a field of research itself. With STEMsalabim, we stick to the parameters tabulated in Ref. [1], which are mostly based on the parametrizations published by Doyle and Turner [25] and Doyle and Cowley [26] but with a different basis (Lorentzian and Gaussian as opposed to the Gaussian-only basis of Doyle and Turner [25]). We are aware of more sophisticated ways to parametrize the scattering factors [27] and are considering them for future versions of the package. However, the one of Kirkland [1] works quite well and yields the same results as the STEMsim software [13].

From the slice potential given in Eq. (1), a weak phase object can be calculated for each of the N slices as

$$t_s(x, y) = \exp[i\sigma v_s(x, y)], \tag{4}$$

with the interaction parameter

$$\sigma = \frac{2\pi \gamma m_0 e \lambda}{h^2}. \tag{5}$$

Here, m_0 is the rest mass and e the charge of an electron, γ is the Lorentz factor, and h is Planck's constant. $t_s(x, y)$ is often referred to as the slice's *transmission function*. After the electron wave is modified by the transmission function, it is propagated to the next slice by applying a Fresnel propagator

$$p(k_x, k_y, dz) = \exp[-i\pi |k|^2 \lambda dz] \tag{6}$$

given in frequency space.

With Eqs. (4), 6, the total interaction between an incident wave function $\Psi_s(x, y)$ and slice s is given by

$$\Psi_{s+1}(x, y) = \mathcal{F}^{-1}\{p(k_x, k_y, dz)\mathcal{F}[t_s(x, y)\Psi_s(x, y)]\}, \tag{7}$$

which is iteratively applied for all slices of the supercell until the wave hits the detector (i.e., until the last layer of the supercell was passed).

The incident probe wave function $\Psi_0(x, y)$ for a focused electron beam resting at the scan position (x_p, y_p) is given by

$$\Psi_0(x, y, x_p, y_p) = B\mathcal{F}^{-1}(A(k_x, k_y) \exp[-i\chi(k_x, k_y) + 2\pi i(k_x x_p + k_y y_p)]), \tag{8}$$

with a normalization constant B, the aperture function $A(k_x, k_y)$, and the aberration phase error $\chi(k_x, k_y)$. The aperture function $A(k_x, k_y)$ is unity for all $\lambda |k| < \alpha_{max}$ and zero outside, with α_{max} being the maximal angle of the objective aperture. The aberration phase error $\chi(\vec{k})$ is given by

$$\chi(k_x, k_y) = \frac{\pi \alpha^2}{\lambda}\left(-\Delta f + C_a \cos(2\phi - 2\phi_a) + \frac{1}{2}C_s\alpha^2 + \frac{1}{3}C_5\alpha^4\right). \tag{9}$$

In Eq. (9), $\alpha = \lambda |k|$ is the polar angle, ϕ the azimuthal angle, and δf, C_a, ϕ_a, C_s, C_5 are the aberration coefficients defocus, two-fold astigmatism, two-fold astigmatism azimuthal angle, and spherical aberrations in third- and fifth-order, respectively.

Note, that both the transmission functions $t_s(x, y)$ as well as the atomic potentials $v_s(x, y)$ should be symmetrically bandwidth limited to $\min(k_{x, max}, k_{y, max})$ in order to ensure cylindrical symmetry inherent to electron microscopes [1].

2.2. Algorithm

The multislice method as outlined above yields the probe wave function after interaction with the supercell for a single lateral

probe position (x_p, y_p) and a single configuration of atomic coordinates $\vec{r}_i$. In order to simulate a full STEM image, this simulation needs to be repeated for the probe position at all scan points, for varying atomic coordinates in order to account for TDS in the frozen lattice approximation, and for different defoci Δf of the probe (see Eq. (9)) to include chromatic aberrations. The full algorithm is then as follows:

1. Displace atomic coordinates randomly following a Gaussian probability distribution (Einstein solid) to include TDS.
2. Divide the sample into N slices of thickness dz and calculate transmission functions $t_s(x, y)$ using Eqs. (2) and (4).
3. Generate the probe wave function $\Psi_0(x, y, x_p, y_p)$ with Eq. (8).
4. For each slice s, calculate $\Psi_{s+1} \leftarrow \Psi_s$ by applying Eq. (7).
5. Integrate $|\Psi|$ for the appropriate angle range to simulate the HAADF detector.
6. Repeat steps 3–5 for each scan point (x_p, y_p).
7. Repeat steps 1–6 for each frozen lattice configuration.
8. Repeat steps 1–7 for the each defocus Δf of the defocus series to model chromatic aberrations.
9. Appropriately average over frozen lattice configurations and defoci.

2.3. Implementation details

As shown in the introduction, a realistic STEM image simulation easily requires millions of single multislice simulations. Luckily, by parallelization and by reusing precalculated objects, one can reduce the computational demand significantly. In this section, we discuss some implementation details regarding MPI and threaded parallelization and a few caching mechanisms that are implemented in STEMsalabim.

The principle interaction between the supercell and the wave function $\Psi(x, y)$ is via each slice's transmission function $t_s(x, y)$ as described in Eq. (7), which, in turn, is built from the involved elements' atomic potentials $V_i(|\vec{r}|)$ via Eq. (1). While the atomic coordinates change between frozen lattice configurations and between slices, the atomic potentials need to be calculated only once for the distances $|\vec{r}| < r_{\text{cut}}$. Therefore, it is good practice to precalculate and cache $V_i(|\vec{r}|)$ for all elements involved in the simulation. The same holds true for the Fresnel propagator from Eq. (6), as it is constant as long as the slice thickness dz is kept unchanged.

The transmission function $t_s(x, y)$ for each slice s can be cached and reused within the same frozen lattice configuration for all STEM probe positions (x_p, y_p), since the slice potentials depend solely on the atomic coordinates. This requires the loop over probe positions to be carried out within the loop over frozen lattice configurations, as indicated in the algorithm in Section 2.2. Note, that caching the complex valued discretized transmission functions for all slices requires significant amounts of memory when calculating large lateral scan areas and/or thick supercells.

In principle, the transmission functions could be reused also for different defocus values Δf when simulating a defocus series, as these only influence the probe wave function Ψ_0 given by Eq. (8). However, it proved useful to generate a new set of configurations for each defocus value for convergence of the frozen lattice TDS method. (We consider a simulation as converged when the intensity differences between identical atomic columns become sufficiently small.) Generating new coordinates for each defocus allows significant reduction of required frozen lattice configuration to average over.

As mentioned above, most of the multislice iterations required for a full STEM image simulation are independent from each other and can therefore be parallelized very efficiently. In STEMsalabim, we opted for a hybrid parallelization scheme using MPI for communication between machines and a shared-memory threading architecture for parallelization within one machine. This scheme has some important benefits over pure MPI or threaded parallelization and is often applied for memory critical software [28]. First of all, message passing (MPI) allows us to parallelize across computers, which is crucial for running the program on highly concurrent HPC clusters. Using threads instead of MPI processes for concurrency within one machine greatly reduces the required memory, as the same set of transmission functions $t_s(x, y)$ can be used via shared memory for parallel multislice simulations. Moreover, the transmission functions for all slices can be calculated in parallel without the need of communicating large chunks of data between MPI processes, which is beneficial for performance. Second of all, reducing the number of involved MPI processes also reduces network activity when reporting simulation results to the MPI master process. Instead, result packages are gathered on each machine independently and are then passed to the master process as a single chunk of data for post-processing and input/output (I/O).

The basic steps of the parallel STEM image simulation as carried out by STEMsalabim, complementary to the algorithm Section 2.2, are as follows:

1. The master MPI process reads in atomic coordinates, randomly generates frozen lattice configurations and communicates the coordinates to the other MPI processes.
2. Each worker MPI process slices the specimen and calculates and caches atomic potentials $V_i(x, y)$, transmission functions $t_s(x, y)$, and the Fresnel propagator $p(k_x, k_y, dz)$.
3. Each worker MPI process queries the master for a work package of some probe positions (x_p, y_p), carries out the multislice calculations concurrently by threaded parallelization, and sends the packaged results back to the MPI master. This is repeated until all probe scan points (x_p, y_p) are processed.
4. Steps 1 - 3 are repeated for all frozen lattice configurations and defocus values Δf.

All processing of results, management of the queue of multislice simulations, and all I/O is carried out by the main thread of the master MPI process to prevent race conditions. The precision of all calculations can be chosen as single or double, depending on the desired level of accuracy.

Since the multislice method essentially consists only of a series of products and convolutions of discretized complex-valued wave functions, the bottle neck of the simulation are the forward and inverse fourier transforms. Fortunately, highly optimized implementations of the fast fourier transform (FFT) exist, that are the working horses of the STEM image simulations. The FFTs in STEMsalabim are carried out by the widely-applied FFTW library. While FFTW is written to run on conventional central processing units (CPUs), it would be easy to replace it with FFT codes that are capable of running on graphics processing units (GPUs), which would result in additional significant performance gain [14].

The input for a simulation with STEMsalabim consists of two files: One file describes the cell dimensions and contains (equilibrium) positions, elements and mean square displacements of all atoms present in the supercell. The second file contains all necessary configuration values for the simulation, e.g., characteristics of the microscope and detector, output file name, etc. Some configuration values can be overridden via command line parameters upon execution of the program.

Simulation results are stored as binary data using NetCDF, which is based on the HDF5 library. This has several advantages over the usual approach of storing data in structured ASCII files. First, the data volume is much smaller due to binary storage and is further compressed by HDF5. This is particularly useful for STEM image simulations where the amount of data produced in simulations can be large. Second, all results, simulation parameters, and

runtime information can be stored in a single result file, which is a much more portable approach than distributed ASCII files. Third, NetCDF/HDF5 bindings exist for all popular programming languages (MATLAB, for example, ships functions for reading binary HDF5 data) and data can be read selectively from the file, avoiding large memory requirements when processing big output files.

Other libraries used by STEMsalabim include libConfig for reading in simulation parameters, various of the Boost C++ libraries for utility functions, and CMake for the build process.

STEMsalabim is written in modern C++ using features of the latest language standards C++11 and C++14. The target platforms of the package are Unix based systems, however, it should work just as well on Microsoft Windows operating systems. The package can be used with both OpenMPI and Intel MPI implementations. Compilation was successfully tested with the GNU Compiler Collection (GCC), LLVM clang, and the Intel Compiler Collection (ICC).

3. Results and comparisons

Correctness of images simulated with our package was checked and confirmed by comparison to the well-established STEMsim code [13]. In what follows, we showcase a few examplary STEM image simulations carried out with STEMsalabim and compare some of the results to experimentally obtained images. The chosen examples show the necessity of TDS, chromatic aberrations, and large lateral supercell sizes in order to reach sufficient accuracy in the simulated images. Runtimes and performance of the simulations are discussed in Section 4.

All shown simulations were simulated with an acceleration voltage of 200 kV, a numerical aperture of 24 mrad, and spherical aberration coefficients $C_s = 2$ μm and $C_5 = 5$ mm. These parameters are chosen to match our microscope (JEOL JEM 2200). As astigmatism is corrected, it was disabled in the simulations. The detector angle range used to generate the micrographs was in all cases 74 mrad to 174 mrad.

3.1. GaP at 0K and room temperature

Let us start with a simple image simulation of pure gallium phosphide (GaP), at $T = 0K$ (i.e., all atoms rest at their equilibrium lattice positions) and at room temperature ($T = 300$ K, by including TDS via the frozen lattice approximation). By comparison of the two simulations we show the significant effects that TDS have on STEM images.

The simulated STEM images for the integrated detector angle range 72 mrad to 172 mrad are shown in Fig. 1(a) and (b), their dependences on detector angle $\alpha = |\vec{k}|\lambda$ is plotted in (c), along with the theoretical positions of the nine first higher order Laue zone (HOLZ) peaks. For both temperatures, a series of 7 defocus values distributed around $\Delta f = -2$ nm was calculated and averaged, similar to Refs. [12,29]. The simulated supercell had a lateral size of 9 × 9 unit cells, of which the center square of 3 × 3 unit cells was chosen as scanning area, and a thickness of about 50 nm. For the 300 K simulation, TDS was taken into account by calculating and averaging 15 configurations of atomic positions, according to the Einstein approximation.

It is clearly visible that including TDS smears out the atomic columns and reduces collected intensity. The homogeneous brightness and shape of the atomic columns indicates sufficiently large number of frozen lattice configurations for TDS. The intensity dependence on detector angle α in the diffraction plane of the images, shown in Fig. 1(c), exhibits a clear signature of the HOLZ peaks at their expected positions for the 0K sample. The first order Laue zone (FOLZ) is still visible as a small hump in the curve of
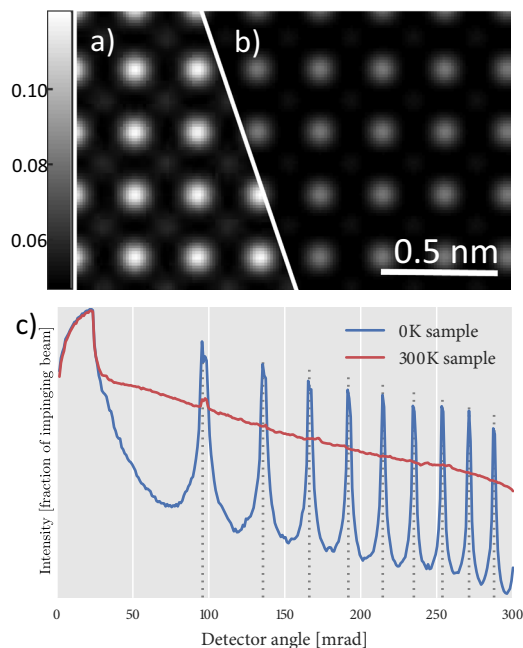

Fig. 1. Simulated gallium phosphide (GaP) STEM images at zero (a) and room temperature (b), beam direction [001]. The simulated scanning area was 3 × 3 unit cells, part of which is cropped in the upper figures. The dependences of the images on the detector angle ($\alpha = |\vec{k}|\lambda$) are shown in (c), with the expected positions of the higher order Laue zone (HOLZ) peaks up to 9th order marked by dotted vertical lines. Intensity values are displayed as fraction of impinging beam.

the 300 K sample. While the intensity of the former is almost exclusively collected at the HOLZ reflections, the latter sample shows a smooth, decaying angular dependence over the whole detector angle range.

Note, that the used number of 15 frozen lattice configurations per each of the 7 defoci results in 105 independent vibration configurations of the atomic positions. The homogeneity of the shape and intensity of the atomic columns indicates that generating new frozen lattice configurations for each defocus reduces the number of necessary configurations for a single defocus, as 15 configurations are usually not enough for convergence.

3.2. GaAsBi simulation in comparison to experiment

In Fig. 2, we show a STEM image of an approximately 32 nm thick gallium arsenide bismide (GaAsBi) sample with a bismuth (Bi) concentration of 4.8%, taken in a JEOL JEM 2200 TEM operating at 200 kV. A simulated GaAsBi image with equal sample and microscope parameters is shown in an overlay. The atomic positions of the supercell were relaxed prior to the simulation by valence force field (VFF) methods [30]. A series of 7 defoci with 10 frozen lattice configurations each was calculated to obtain the simulation results.

The excellent agreement between the images, both qualitatively and regarding background, group III, and group V intensities, is only possible by including chromatic aberrations. The group V columns with finite Bi content are nicely visible as bright spots in both results, with correct relative intensities to columns without Bi. Both the experimental and the simulated image are shown with the same colorbar, with intensities given in fractions of the impinging electron beam. The main differences left between experimental and simulated image are fly-back errors of the scanning microscope, that manifest as horizontal distortions in the experimental STEM image.
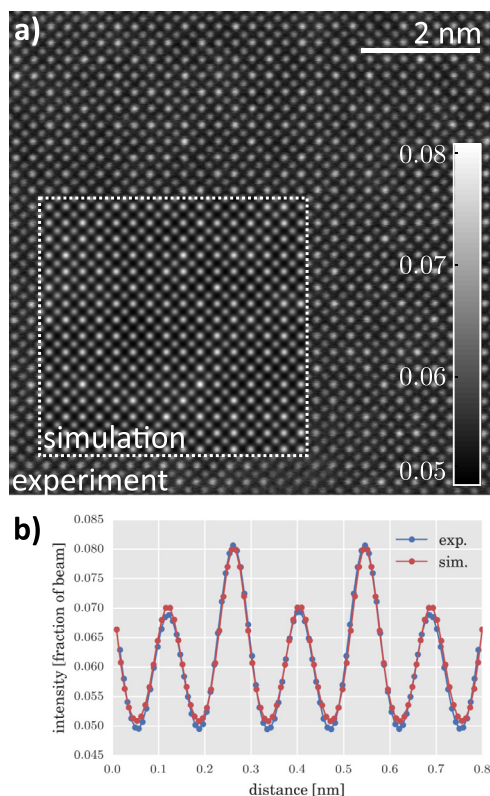
Fig. 2. (a) Experimentally obtained STEM image of an approximately 32 nm thin gallium arsenide (GaAs) sample with 4.8% bismuth (Bi). A corresponding sample simulated with STEMsalabim is shown as an overlay framed by a dotted, white line. Intensity values are displayed as fraction of impinging beam. In (b), diagonal line scans over both the simulated and experimentally obtained image are shown. The group III and group V peaks are clearly visible and exhibit quantitative agreement.

Fig. 3. STEM image simulation of a GaP/gallium arsenide (GaAs) heterojunction. The supercell dimensions were 55.88 nm × 1.37 nm × 24.68 nm in x, y, and beam direction, respectively. Scanning in y direction was confined to only 60% of the sample size to rule out boundary effects. The simulated image is continued periodically to five times its original size in y direction. The original supercell is framed by a red box. Below the image simulation, the intensity of the group III columns across the interface is plotted. (For interpretation of the references to color in this figure legend, the reader is referred to the web version of this article.)

3.3. Large simulation of GaP/GaAs heterojunction

A third example is displayed in Fig. 3, a simulation of a heterojunction between GaP and gallium arsenide (GaAs). The supercell morphology was relaxed prior to the simulation by means of finite element (FE) simulation in order to include lattice mismatch effects between the two materials. STEM image simulations allow for tracing the group III and V column intensity across the junction and thereby relate intensity to interface relaxation. In Fig. 3, the intensity on group III columns across the junction is plotted below the simulated STEM image.

It is clear from the plot, that a reduction of the group III intensity in the GaP bulk of up to 25% is induced by the lattice mismatch. The intensity recovers to its GaP bulk value more than 15 nm away from the junction, clearly showing the long-range nature of such effects. Especially for interfaces and structural phenomena on the scale of several nanometers, the calculations of large supercells is inevitable, for which efficient and well-parallelized software packages are required.

4. Benchmarks and scaling behaviour

The example simulations shown above were of very different complexity. Let us here briefly discuss the performance of the small GaP supercell (Fig. 1) and the GaP/GaAs heterojunction shown in Fig. 3. We will also show, how STEMsalabim scales with increasing number of computation cores.

As hinted in Section 1, the number of individual multislice simulations grows with number of frozen lattice configurations to account for TDS and required defocus values Δf for inclusion of chromatic aberration effects. The performance of a single multislice simulation depends linearly on the number of slices and on the size $N \times M$ of the k- and real-space grid[1], on which all wave functions are discretized.

The 300 K GaP simulation shown in Fig. 1 had a supercell size of $9 \times 9 \times 92$ unit cells. As the slice thickness dz was chosen to match the length of one unit cell (which is a reasonable thickness for [001] beam directions in crystals), the sample was split into 92 slices. A grid density of 360 nm^{-1} was used, resulting in a grid size of 1766×1766. A total of 65×65 probe positions were simulated (the scanning area was a center square of 3×3 unit cells), requiring an overall number of about 443 k multislice simulations for the room temperature simulation (15 frozen lattice configurations for each of the 7 defocus values). The simulation was carried out in parallel on 7×96 computation cores with a clock speed of 2.3 GHz each and finished within a runtime of approximately 20 h. All wave functions of the simulation were single precision complex-valued matrices of size 1766×1766. As the transmission functions $t_s(x, y)$ of all slices are cached (see Section 2.2), the required memory per machine involved in the computation was about 2.2 GB. The majority of simulation time is spent calculating (inverse) fourier transforms, of which for the GaP example more than 50 million are required.

The GaP simulation discussed above is small enough to still run in reasonable time on a desktop computer. In contrast, this becomes almost impossible for the heterojunction shown in Fig. 3. Here, a grid of size 20118×492 was used, resulting in much more expensive fourier transforms. The number of scan points calculated was 2012×29 and the sample was split into 46 slices. In total, including TDS and defocus series, over 4 million multislice simulations were executed, with required memory of about 5 GB per MPI process. The simulation finished within 4 days and 10 h running in parallel on 7×256 2.3 GHz CPUs.

As mentioned before, frozen lattice multislice simulations are parallelizable very efficiently, because the individual multislice simulations are independent from each other. The scaling behaviour with increasing number of processors should therefore be close to linear until the managing master process (I/O or postprocessing) becomes the bottle neck of the simulation. We checked the scaling behaviour of STEMsalabim by plotting runtime against number of processing units for single and double precision calculations. The results are displayed in Fig. 4. It is clearly visible that the speedup with increasing number of worker processors is linear, which is the desired behaviour. Double precision calculations are considerably slower than single precision, which is due to slower double precision FFTs.

---

[1] The precise scaling of the FFTs is governed by the FFT library used and usually depends on how well N and M can be factorized.
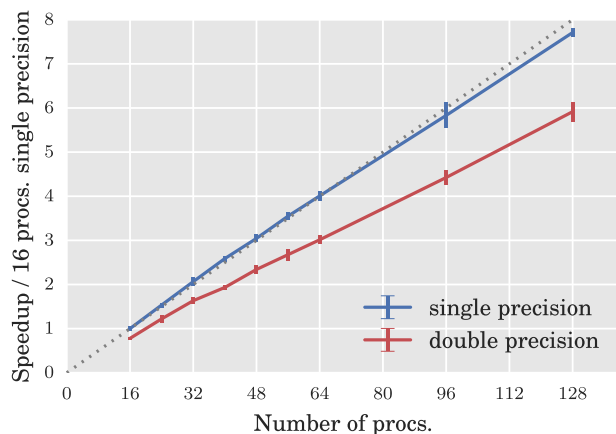
Fig. 4. Speedup relative to a single precision calculation on 16 processors for single and double precision calculations up to 128 processors.

5. Conclusion

We have presented a new implementation of the multislice algorithm for STEM image simulations, including chromatic aberrations via defocus series and TDS via the frozen lattice approximation, that is written specifically to run on highly parallelized HPC clusters. We briefly repeated the multislice algorithm and its implementation in Sections 2 and 2.2 and showed example calculations in Section 3. Performance, memory requirements, and scaling with number of processors was briefly discussed in Section 4. We have shown that our code runs successfully in parallel on computing clusters and have shown its computer time and memory efficiency. We have also shown, that the code scales well with increasing number of processors taking part in the simulations.

Acknowledgements

References

[1] E.J. Kirkland, Advanced Computing in Electron Microscopy, 2010, doi:10.1007/978-1-4419-6533-2.

[2] S.J. Pennycook, D.E. Jesson, High-resolution Z-contrast imaging of crystals, Ultramicroscopy 37 (1–4) (1991) 14–38, doi:10.1016/0304-3991(91)90004-P.

[3] A. Rosenauer, K. Gries, K. Müller, A. Pretorius, M. Schowalter, A. Avramescu, K. Engl, S. Lutgen, Measurement of specimen thickness and composition in Al$_x$Ga$_{1-x}$N/GaN using high-angle annular dark field images, Ultramicroscopy 109 (9) (2009) 1171–1182, doi:10.1016/j.ultramic.2009.05.003.

[4] V. Grillo, E. Carlino, F. Glas, Influence of the static atomic displacement on atomic resolution Z-contrast imaging, Phys. Rev. B 77 (5) (2008) 1–6, doi:10.1103/PhysRevB.77.054103.

[5] V. Grillo, The effect of surface strain relaxation on HAADF imaging, Ultramicroscopy 109 (12) (2009) 1453–1464, doi:10.1016/j.ultramic.2009.07.010.

[6] P. Goodman, a.F. Moodie, Beam wave functions in electron scattering by the multi-Slice method, Acta Crystallogr. Sect. A 30 (2) (1974) 280–290, doi:10.1107/S056773947400057X.

[7] J.M. Cowley, a.F. Moodie, The scattering of electrons by atoms and crystals. I. A new theoretical approach, Acta Crystallogr. 10 (1957) 609–619, doi:10.1107/S0365110X57002194.

[8] R.F. Loane, P. Xu, J. Silcox, Thermal vibrations in convergent-beam electron diffraction, Acta Crystallogr. Sect. A 47 (3) (1991) 267–278, doi:10.1107/S0108767391000375.

[9] Rolf Erni, High-resolution transmission electron microscopy, in: Aberration-Corrected Imaging Transmission Electron Microscopy, Imperial College Press, 2010, pp. 13–43, doi:10.1142/9781848165373_0002.

[10] C. Dwyer, C. Maunders, C.L. Zheng, M. Weyland, P.C. Tiemeijer, J. Etheridge, Sub-0.1 nm-resolution quantitative scanning transmission electron microscopy without adjustable parameters, Appl. Phys. Lett. 100 (19) (2012) 0–4, doi:10.1063/1.4711766.

[11] K. Kuramochi, T. Yamazaki, Y. Kotaka, M. Ohtsuka, I. Hashimoto, K. Watanabe, Effect of chromatic aberration on atomic-resolved spherical aberration corrected STEM images, Ultramicroscopy 110 (1) (2009) 36–42, doi:10.1016/j.ultramic.2009.09.003.

[12] A. Beyer, R. Straubinger, J. Belz, K. Volz, Local sample thickness determination via scanning transmission electron microscopy defocus series, J. Microsc. 262 (2) (2016) 171–177, doi:10.1111/jmi.12284.

[13] A. Rosenauer, M. Schowalter, STEMSIM—a New Software Tool for Simulation of STEM HAADF Z-Contrast Imaging, Springer Netherlands, Dordrecht, pp. 170–172. doi: 10.1007/978-1-4020-8615-1_36.

[14] I. Lobato, D. Van Dyck, MULTEM: A new multislice program to perform accurate and fast electron diffraction and imaging simulations using graphics processing units with CUDA, Ultramicroscopy 156 (2015) 9–17, doi:10.1016/j.ultramic.2015.04.016.

[15] Total Resolution, MacTempasX. http://www.totalresolution.com/MacTempasX.htm

[16] J.M. Zuo, J.C. Mabon, Web-based electron microscopy application software: Web-EMAPS, Microsc. Microanal. 10 (S02) (2004) 1000–1001, doi:10.1017/S1431927604884319.

[17] H.R. Inc., xHREM. https://www.hremresearch.com/Eng/simulation.html

[18] V. Grillo, E. Rotunno, STEM_CELL: a software tool for electron microscopy: Part I-simulations, Ultramicroscopy 125 (2013) 97–111, doi:10.1016/j.ultramic.2012.10.016.

[19] J. Barthel, Dr. Probe - STEM multislice image calculation program. http://www.er-c.org/barthel/drprobe/

[20] Christoph Koch, Determination of Core Structure Periodicity and Point Defect Density along Dislocations, Arizona State University, 2002 Dissertation.

[21] C. Dwyer, Simulation of scanning transmission electron microscope images on desktop computers, Ultramicroscopy 110 (3) (2010) 195–198, doi:10.1016/j.ultramic.2009.11.009.

[22] L.J. Allen, A.J. D'Alfonso, S.D. Findlay, Modelling the inelastic scattering of fast electrons, Ultramicroscopy 151 (2015) 11–22, doi:10.1016/j.ultramic.2014.10.011.

[23] J. Pizarro, P.L. Galindo, E. Guerrero, A. Yáñez, M.P. Guerrero, A. Rosenauer, D.L. Sales, S.I. Molina, Simulation of high angle annular dark field scanning transmission electron microscopy images of large nanostructures, Appl. Phys. Lett. 93 (15) (2008), doi:10.1063/1.2998656.

[24] M. Haider, S. Uhlemann, J. Zach, Upper limits for the residual aberrations of a high-resolution aberration-corrected STEM, Ultramicroscopy 81 (3–4) (2000) 163–175, doi:10.1016/S0304-3991(99)00194-1.

[25] P.A. Doyle, P.S. Turner, Relativistic HartreeFock X-ray and electron scattering factors, Acta Crystallogr. Sect. A 24 (3) (1968) 390–397, doi:10.1107/S0567739468000756.

[26] P.A. Doyle, J.M. Cowley, Scattering Factors for the Diffraction of Electrons by Crystalline Solids, International Tables for Crystallography, Kynoch Press, Birmingham, 1974.

[27] I. Lobato, D. Van Dyck, An accurate parameterization for scattering factors, electron densities and electrostatic potentials for neutral atoms that obey all physical constraints, Acta Crystallogr. Sect. A 70 (2014) 636–649, doi:10.1107/S205327331401643X.

[28] T. Hoefler, J. Dinan, D. Buntinas, P. Balaji, B. Barrett, R. Brightwell, W. Gropp, V. Kale, R. Thakur, MPI + MPI: a new hybrid approach to parallel programming with MPI plus shared memory, Computing 95 (12) (2013) 1121–1136, doi:10.1007/s00607-013-0324-2.

[29] A. Beyer, Influence of spatial and temporal coherences on atomic resolution high angle annular dark field imaging, Ultramicroscopy 169 (2016) 1–10, doi:10.1016/j.ultramic.2016.06.006.

[30] O. Rubel, I. Németh, W. Stolz, K. Volz, Modeling the compositional dependence of electron diffraction in dilute GaAs- and GaP-based compound semiconductors, Phys. Rev. B 78 (7) (2008) 1–8, doi:10.1103/PhysRevB.78.075207.

Further Publications

Efficient nitrogen incorporation in GaAs using novel metal organic As–N precursor di-tertiary-butyl-arsano-amine (DTBAA)

E Sterzer, A Beyer, L Duschek, L Nattermann, B Ringler, B Leube, A Stegmüller, R Tonner, C von Hänisch, W Stolz, K Volz

2016/4/1

Interface morphology and composition of Ga (NAsP) quantum well structures for monolithically integrated LASERs on silicon substrates

T. Wegele, A. Beyer, P. Ludewig, P. Rosenow, L. Duschek, K. Jandieri, R. Tonner, W. Stolz, K. Volz

2016/1/14

Quantitative characterization of the interface roughness of (GaIn) As quantum wells by high resolution STEM

H Han, A Beyer, K Jandieri, KI Gries, L Duschek, W Stolz, K Volz

2015/12/1

7. Zusammenfassung und Ausblick

Die erfolgreiche und kontinuierliche Verbesserung moderner Halbleiterbauelemente hängt wesentlich von der Fähigkeit ab, Materialeigenschaften so genau wie möglich beobachten und beschreiben zu können und dieses Verständnis als Grundlage für neue Entwicklungen nutzen zu können. Komplexe Halbleiterbauelemente, wie Mehrfachsolarzellen [2] und Laserbauelemente[3, 4], bestehen aus mehrschichtigen Strukturen und einer Kombination von verschiedenen Materialsystemen. Entscheidend für die Funktionalität des Bauelements ist es, sowohl die geometrischen Eigenschaften als auch die chemischen Eigenschaften genau zu charakterisieren. Das STEM bietet eine effektive Kombination aus lateraler Auflösung und quantitativen Methoden, um Einblicke in das Material zu gewinnen. Um quantitative Informationen aus der untersuchten Probenstruktur zu gewinnen, sind ergänzende Simulationen unerlässlich.

Im Rahmen dieser Arbeit wurde ein Workflow entwickelt um eine Elektronenmikroskopieprobe so präzise wie möglich zu modellieren. Dazu gehörte auch die Berücksichtigung der wichtigsten experimentellen Einflüsse auf die Multislice-Simulationen.

Eine Implementierung des häufig verwendeten Multislice-Algorithmus von Kirkland wurde im STEMsalabim-Softwarepaket [98] realisiert und in Kapitel 4.1 erläutert. Die Software wurde speziell für HPC-Cluster mit Multi-CPU-Architektur angepasst und optimiert. Dies ermöglicht es dem Anwender, Proben mit großen lateralen Dimensionen zu simulieren und wichtige Parameter-Sweeps in einem angemessenen Zeitrahmen durchzuführen.

Die Mischung verschiedener Halbleitermaterialsysteme in Mehrschichtstrukturen kann zu Spannungen an den Grenzflächen führen. Die Größe der Spannungen ist an die Differenz der Gitterkonstanten zwischen beiden Materialien gekoppelt. Bei sehr dünnen TEM-Proben wird die Spannung durch elastische Oberflächenrelaxation abgebaut. Die Oberfläche der Proben verformt sich elastisch und die atomaren Gitterebenen des Materials krümmen sich. Die daraus resultierenden gekrümmten Gitterebenen begünstigen das de-channelling der Elektronen und beeinflussen somit die gesammelte STEM-ADF-Intensität. Der Effekt selbst wird zusätzlich zu seinem Einfluss auf das STEM HAADF in Kapitel 4.2 vorgestellt und erläutert. Im Rahmen einer Simulationsstudie wurden Beispielproben auf Basis von *GaP/GaAs/GaP* mit unterschiedlichen geometrischen Parametern modelliert und die Strukturen durch einen FE-Algorithmus relaxiert. Anschließend wurden Multislice-Simulationen mit den relaxierten Superzellen als Ausgangsmaterial durchgeführt. Es konnte gezeigt werden, dass die mittlere quadratische Verschiebung der atomaren Gitterebenen direkt mit der STEM-ADF-Intensität verbunden ist. Auf diese Weise können rechenintensive Multislice-Simulationen mit weniger aufwendigen FE-Simulationen ersetzt werden. Dennoch erhält man einen genauen Überblick über die Auswirkung der Oberflächenrelaxation. Die Simulationsmethode wurde dann angepasst und auf eine experimentelle

Probe von *GaP/Ga(As,P)/GaP* angewendet. Die simulierte Struktur stimmte quantitativ mit den experimentellen Ergebnissen überein, was die Qualität und Präzision der FE-Simulationen unterstreicht. Mit dem Wissen, dass die Intensität von Multislice-Simulationen sehr gut mit experimentellen Intensitäten übereinstimmt, wurde eine bewährte Methode zur Zusammensetzungsbestimmung erweitert, um eine hohe laterale Auflösung und eine chemische Auflösung bis zu einem Atom zu erreichen. Die Grundlage der Methode ist der Vergleich von experimentellen Intensitäten mit einem simulierten Kompositionsset um die beste Übereinstimmung zu finden. Die Genauigkeit der Methode wurde im Detail in Kapitel 4.3 untersucht und es wurde festgestellt, dass eine perfekte Übereinstimmung nur mit sehr dünnen TEM-Proben erreicht werden kann. Dies ist darauf zurückzuführen, wie die Intensitäten aus Materialien mit unterschiedlichen Elementen erzeugt werden. Die statistische Verteilung der Substitutionsatome im Material führt zu einer Streuung der Intensitäten für eine gegebene Zusammensetzung, bedingt durch die unterschiedlichen möglichen Z-Höhenkonfigurationen für diese Atomsäule [116]. Da das Simulationsset die statistische Natur der Höhenverteilung der Substitutionsatome beinhaltet, wird der Einfluss auf die Streuung der STEM-Intensität berücksichtigt. Die Anwendung der Methode an drei technologisch relevanten Proben, nämlich *(Ga,In)As*, *Ga(P,As)* und *SiGe*, zeigte zudem eine sehr gute Übereinstimmung mit der weit verbreiteten HRXRD-Technologie. Durch die Erweiterung der Probe konnte eine verbesserte 2D-Auflösung des Resultats realisiert werden.

Weiterhin ist es möglich, die vorgestellte Methode zur Bestimmung unbekannter Halbleiterzusammensetzungen mittels STEM-Intensität auf quaternäre Halbleiter anzuwenden. Dies wurde an einem *Ga(N,As,P)*-Modellsystem in [109] und an *(Ga,In)(As,Bi)/GaAs* und *(Ga,In)(As,Bi)/InP* in [117] erfolgreich demonstriert. Die vorgestellt Methode nutzt die erhöhte STEM-Intensität in niedrigeren Winkelbereichen, die durch die Gitterverzerrung aufgrund von N-Atomen im Material erzeugt wird. Dadurch lassen sich Rückschlüsse auf den N-Gehalt des Materials ziehen. Die höhere Intensität in höheren Winkelbereichen ist überwiegend sensitiv gegenüber dem As-Gehalt, so dass die einzelnen chemischen Zusammensetzungen individuell bestimmt werden können.

Zusammenfassend lässt sich sagen, dass ein umfangreicher Workflow entwickelt und präsentiert wurde, der experimentelle Einflüsse wie elastische Oberflächenrelaxation, eine endliche Elektronenquelle und die Modellierung amorpher Materialien beinhaltet. All dies zusammen ermöglicht es, experimentelle STEM-Bilder mittels Multislice-Simulationen quantitativ zu untersuchen. Ein Vorteil dieser Technik ist, dass keine zusätzlichen Methoden verwendet werden müssen und nur STEM HAADF-Bilder sowie -Simulationen erforderlich sind.

Einige Verbesserungsvorschläge werden im folgenden Abschnitt präsentiert. Zunächst könnte die Simulation amorpher Materialien umgangen werden, wenn die amorphen Schichten auf den Proben

während der Präparation deutlich reduziert werden könnten. Dies würde die allgemeine Qualität der experimentellen Bilder deutlich verbessern [118].

Die Geschwindigkeit der Simulationen innerhalb des STEMsalabim-Softwarepakets könnte durch die Anpassung des Codes an die Ausführung auf Grafikkarten (GPU) verbessert werden. Ein Grafikprozessor ist für Grafikprobleme optimiert und besteht aus Tausenden kleineren, effizienten Kernen, die so konzipiert sind, dass sie mehrere Aufgaben gleichzeitig ausführen können. Die sehr hohe Anzahl von Fourier-Transformationen, die während einer Multislice-Simulation auftreten, könnte somit sehr effizient auf GPUs durchgeführt werden [96].

Simulierte STEM-Intensitäten weisen eine signifikante Diskrepanz in niedrigen Winkelbereichen in Bezug auf experimentelle Intensitäten auf [119], und es gibt einige Hinweise darauf, dass dies auf inelastische Streuung zurückzuführen sein könnte [34]. Derzeit wird von STEMsalabim nur elastische Streuung der Elektronen berücksichtigt. Techniken, mit denen inelastische Streuung berücksichtigt werden könnte, wurden bereits vorgestellt [88, 120] und könnten die Qualität der Simulationen hinsichtlich der Intensitätsverteilung im gesamten Winkelbereich verbessern.

Eine weitere Verbesserung wäre die Verwendung eines pixelbasierten Detektors, der anstelle der kumulativen inkohärenten Summe die komplette Winkelintensitätsverteilung jedes Scanpunktes erfasst. Wenn die winkelabhängige Intensitätsverteilung für jeden Scanpunkt der experimentellen Daten vorhanden sein würde, könnten verbesserte Algorithmen auf jedes Pixel angewendet werden. Dies würde die Präzision simulationsbasierter Bestimmung von Materialkompositionen erheblich erhöhen [121-123].

Jede Methode, die auf dem Vergleich simulierter Intensitäten mit experimentellen Bildern basiert, ist empfindlich gegenüber der angenommenen oder berechneten Probendicke. Insbesondere wenn es darum geht atomare Genauigkeit zu erreichen, kann eine falsch angenommene Probendicke einen signifikanten Einfluss haben. Mit dem Einsatz eines pixelbasierten Detektors könnten positionsgemittelte konvergente Elektronenbeugungsmuster (PACBED) ausgewertet und diese an jeder Abtastposition einfach aufgezeichnet werden, wodurch eine sehr genaue Dickenkarte der Probe entsteht [124].

Bibliography

[1] E. M.-N. Photonics and undefined 2010, "The semiconductor laser: Enabling optical communication," *nature.com*.

[2] E. Sterzer, "(Ga , In)(N , As , Sb) Solar Cells : N Incorporation using Novel Precursor in MOVPE Growth and Solar Cell Characteristics," 2018.

[3] C. Fuchs, A. Beyer, K. Volz, and W. Stolz, "MOVPE growth of (GaIn)As/Ga(AsSb)/(GaIn)As type-II heterostructures on GaAs substrate for near infrared laser applications," *J. Cryst. Growth*, vol. 464, pp. 201–205, Apr. 2017.

[4] C. Fuchs, C. Berger, C. Möller, M. Weseloh, S. Reinhard, J. Hader, J. V. Moloney, S. W. Koch, and W. Stolz, "Electrical injection type-II (GaIn)As/Ga(AsSb)/(GaIn)As single 'W'-quantum well laser at 1.2 μm," *Electron. Lett.*, vol. 52, no. 22, pp. 1875–1877, Oct. 2016.

[5] L. Bellaiche and A. Zunger, "Effects of atomic short-range order on the electronic and optical properties of GaAsN, GaInN, and GaInAs alloys," *Phys. Rev. B - Condens. Matter Mater. Phys.*, vol. 57, no. 8, pp. 4425–4431, Feb. 1998.

[6] E. P. O'Reilly, S. Schulz, D. Tanner, C. Coughlan, and M. A. Caro, "Impact of random composition fluctuations on electron and hole states in InAlN and InGaN alloys," in *Proceedings of the International Conference on Numerical Simulation of Optoelectronic Devices, NUSOD*, 2015, vol. 2015–May, pp. 111–112.

[7] M. K. Horton and M. A. Moram, "Alloy composition fluctuations and percolation in semiconductor alloy quantum wells," *Appl. Phys. Lett.*, vol. 110, no. 16, p. 162103, Apr. 2017.

[8] J. M. Tilli, H. Jussila, K. M. Yu, T. Huhtio, and M. Sopanen, "Composition determination of quaternary GaAsPN layers from single X-ray diffraction measurement of quasi-forbidden (002) reflection," *J. Appl. Phys.*, vol. 115, no. 20, 2014.

[9] O. L. Krivanek, M. F. Chisholm, V. Nicolosi, T. J. Pennycook, G. J. Corbin, N. Dellby, M. F. Murfitt, C. S. Own, Z. S. Szilagyi, M. P. Oxley, S. T. Pantelides, and S. J. Pennycook, "Atom-by-atom structural and chemical analysis by annular dark-field electron microscopy.," *Nature*, vol. 464, no. 7288, pp. 571–574, 2010.

[10] M. Haider, S. Uhlemann, E. Schwan, H. Rose, and B. Kabius, "Electron microscopy image enhanced," *Nature*, vol. 392, no. 6678, pp. 768–769, 1998.

[11] M. Haider, S. Uhlemann, and J. Zach, "Upper limits for the residual aberrations of a high-resolution aberration-corrected STEM," *Ultramicroscopy*, vol. 81, no. 3–4, pp. 163–175, 2000.

[12] O. L. Krivanek, N. Dellby, and A. R. Lupini, "Towards sub-Å electron beams," *Ultramicroscopy*, vol. 78, no. 1–4, pp. 1–11, 1999.

[13] S. J. Pennycook and D. E. Jesson, "High-resolution Z-contrast imaging of crystals,"

Ultramicroscopy, vol. 37, no. 1–4, pp. 14–38, 1991.

[14]   A. Singhal, J. C. Yang, and J. M. Gibson, "STEM-based mass spectroscopy of supported Re clusters," *Ultramicroscopy*, vol. 67, no. 1–4, pp. 191–206, Jun. 1997.

[15]   P. M. Voyles, D. A. Muller, J. L. Grazul, P. H. Citrin, and H.-J. J. L. Gossmann, "Atomic-scale imaging of individual dopant atoms and clusters in highly n-type bulk Si," *Nature*, vol. 416, no. 6883, pp. 826–829, Apr. 2002.

[16]   S. J. Pennycook and L. A. Boatner, "Chemically sensitive structure-imaging with a scanning transmission electron microscope," *Nature*, vol. 336, no. 6199, pp. 565–567, Dec. 1988.

[17]   J. M. LeBeau, S. D. Findlay, L. J. Allen, and S. Stemmer, "Quantitative Atomic Resolution Scanning Transmission Electron Microscopy," *Phys. Rev. Lett.*, vol. 100, no. 20, p. 206101, May 2008.

[18]   L. Jones, "Quantitative ADF STEM: acquisition, analysis and interpretation," *IOP Conf. Ser. Mater. Sci. Eng.*, vol. 109, no. 1, p. 012008, 2016.

[19]   J. M. LeBeau, S. D. Findlay, L. J. Allen, and S. Stemmer, "Standardless Atom Counting in Scanning Transmission Electron Microscopy," *Nano Lett.*, vol. 10, no. 11, pp. 4405–4408, Nov. 2010.

[20]   R. F. Loane, P. Xu, J. Silcox, and IUCr, "Thermal vibrations in convergent-beam electron diffraction," *Acta Crystallogr. Sect. A Found. Crystallogr.*, vol. 47, no. 3, pp. 267–278, May 1991.

[21]   J. M. LeBeau and S. Stemmer, "Experimental quantification of annular dark-field images in scanning transmission electron microscopy," *Ultramicroscopy*, vol. 108, no. 12, pp. 1653–1658, Nov. 2008.

[22]   S. I. Molina, D. L. Sales, P. L. Galindo, D. Fuster, Y. González, B. Alén, L. González, M. Varela, and S. J. Pennycook, "Column-by-column compositional mapping by Z-contrast imaging," *Ultramicroscopy*, vol. 109, no. 2, pp. 172–176, 2009.

[23]   A. Rosenauer, K. Gries, K. Müller, A. Pretorius, M. Schowalter, A. Avramescu, K. Engl, and S. Lutgen, "Measurement of specimen thickness and composition in Alx Ga1 - x N / GaN using high-angle annular dark field images," *Ultramicroscopy*, vol. 109, no. 9, pp. 1171–1182, Aug. 2009.

[24]   C. Dwyer, R. Erni, J. E.- Ultramicroscopy, and undefined 2010, "Measurement of effective source distribution and its importance for quantitative interpretation of STEM images," *Elsevier*.

[25]   D. T. Nguyen, S. D. Findlay, and J. Etheridge, "The spatial coherence function in scanning transmission electron microscopy and spectroscopy," *Ultramicroscopy*, vol. 146, pp. 6–16, 2014.

[26]   R. Erni, "High-Resolution Transmission Electron Microscopy," in *Aberration-Corrected Imaging in Transmission Electron Microscopy*, IMPERIAL COLLEGE PRESS, 2010, pp. 13–43.

[27]   K. Kuramochi, T. Yamazaki, Y. Kotaka, M. Ohtsuka, I. Hashimoto, and K. Watanabe, "Effect of chromatic aberration on atomic-resolved spherical aberration corrected STEM images," *Ultramicroscopy*, vol. 110, no. 1, pp. 36–42, 2009.

[28]   C. Dwyer, C. Maunders, C. L. Zheng, M. Weyland, P. C. Tiemeijer, and J. Etheridge, "Sub-0.1 nm-

resolution quantitative scanning transmission electron microscopy without adjustable parameters," *Appl. Phys. Lett.*, vol. 100, no. 19, p. 191915, May 2012.

[29] K. Mkhoyan, S. Maccagnano-Zacher, E. K.- Ultramicroscopy, and undefined 2008, "Effects of amorphous layers on ADF-STEM imaging," *Elsevier*.

[30] J. Belz, A. Beyer, T. Torunski, W. Stolz, and K. Volz, "Direct investigation of (sub-) surface preparation artifacts in GaAs based materials by FIB sectioning," *Ultramicroscopy*, vol. 163, pp. 19–30, 2016.

[31] N. Baladés, M. Herrera, D. L. Sales, M. P. Guerrero, E. Guerrero, P. L. Galindo, and S. I. Molina, "Influence of the crosstalk on the intensity of HAADF-STEM images of quaternary semiconductor materials," *Journal of Microscopy*, John Wiley & Sons, Ltd, 12-Nov-2018.

[32] P. Nellist, S. P.- Ultramicroscopy, and undefined 1999, "Incoherent imaging using dynamically scattered coherent electrons," *Elsevier*.

[33] J. F.- Optik and undefined 1981, "Resolution and contrast of crystalline objects in high-resolution scanning transmission electron microscopy," *ci.nii.ac.jp*.

[34] K. Müller-Caspary, O. Oppermann, T. Grieb, F. F. Krause, A. Rosenauer, M. Schowalter, T. Mehrtens, A. Beyer, K. Volz, and P. Potapov, "Materials characterisation by angle-resolved scanning transmission electron microscopy," *Sci. Rep.*, vol. 6, no. 1, p. 37146, Dec. 2016.

[35] L. De Broglie, "Recherches sur la théorie des quanta," 1924.

[36] C. Davisson and L. H. Germer, "Diffraction of Electrons by a Crystal of Nickel," *Phys. Rev.*, vol. 30, no. 6, pp. 705–740, Dec. 1927.

[37] G. T.-P. R. S. L. A and undefined 1928, "Experiments on the diffraction of cathode rays," *rspa.royalsocietypublishing.org*.

[38] E. Abbe, "Beiträge zur Theorie des Mikroskops und der mikroskopischen Wahrnehmung," *Arch. für Mikroskopische Anat.*, vol. 9, no. 1, pp. 413–418, Dec. 1873.

[39] M. Knoll and E. Ruska, "Das Elektronenmikroskop," *Zeitschrift für Phys.*, vol. 78, no. 5–6, pp. 318–339, May 1932.

[40] A. J. D'Alfonso, B. Freitag, D. Klenov, and L. J. Allen, "Atomic-resolution chemical mapping using energy-dispersive x-ray spectroscopy," *Phys. Rev. B*, vol. 81, no. 10, p. 100101, Mar. 2010.

[41] D. Bell and A. Garratt-Reed, "Energy dispersive X-ray analysis in the electron microscope," 2003.

[42] R. F. Egerton and M. Malac, "EELS in the TEM," *J. Electron Spectros. Relat. Phenomena*, vol. 143, no. 2–3, pp. 43–50, May 2005.

[43] D. B. Williams and C. B. Carter, *Transmission Electron Microscopy*. Boston, MA: Springer US, 2009.

[44] E. Rutherford, "LXXIX. The scattering of α and β particles by matter and the structure of the atom," *Philos. Mag. Ser. 6*, vol. 21, no. 125, pp. 669–688, May 1911.

[45] R. Brydson, *Aberration-corrected analytical transmission electron microscopy*. .

[46]   D. Van Dyck and M. Op de Beeck, "A simple intuitive theory for electron diffraction," *Ultramicroscopy*, vol. 64, no. 1–4, pp. 99–107, Aug. 1996.

[47]   J. M. Cowley and Y. Huang, "De-channelling contrast in annular dark-field STEM," *Ultramicroscopy*, vol. 40, no. 2, pp. 171–180, Feb. 1992.

[48]   V. Grillo, "The effect of surface strain relaxation on HAADF imaging," *Ultramicroscopy*, vol. 109, no. 12, pp. 1453–1464, Nov. 2009.

[49]   V. Grillo, K. Mueller, K. Volz, F. Glas, T. Grieb, and A. Rosenauer, "Strain, composition and disorder in ADF imaging of semiconductors," in *Journal of Physics: Conference Series*, 2011, vol. 326, no. 1, p. 012006.

[50]   V. Grillo, E. Carlino, and F. Glas, "Influence of the static atomic displacement on atomic resolution Z-contrast imaging," *Phys. Rev. B - Condens. Matter Mater. Phys.*, vol. 77, no. 5, 2008.

[51]   R. Fritz, "Quantitative Untersuchungen der Zusammensetzung von kubischen III/V-Verbindungshalbleitern mittels HAADF-STEM," 2013.

[52]   O. Rubel, I. Németh, W. Stolz, and K. Volz, "Modeling the compositional dependence of electron diffraction in dilute GaAs- and GaP-based compound semiconductors," *Phys. Rev. B - Condens. Matter Mater. Phys.*, vol. 78, no. 7, p. 075207, Aug. 2008.

[53]   T. Wegele, "Microstructural Characterization of Dilute N-Containing Semiconductor Alloys and Heterostructures by Scanning Transmission Electron Microscopy," Philipps-Universität Marburg, 2016.

[54]   O. Scherzer, "Sphärische und chromatische Korrektur von Elektronenlinsen," *Opt.*, vol. 2, pp. 114–132, 1947.

[55]   M. Haider, S. Uhlemann, E. Schwan, H. Rose, B. Kabius, and K. Urban, "Electron microscopy image enhanced," *Nature*, vol. 392, no. 6678, pp. 768–769, Apr. 1998.

[56]   J. Zach and M. Haider, "Aberration correction in a low voltage SEM by a multipole corrector," *Nucl. Inst. Methods Phys. Res. A*, vol. 363, no. 1–2, pp. 316–325, Sep. 1995.

[57]   J. M. Cowley and a. F. Moodie, "The scattering of electrons by atoms and crystals. I. A new theoretical approach," *Acta Crystallogr.*, vol. 10, no. 10, pp. 609–619, Oct. 1957.

[58]   P. Goodman and A. F. Moodie, "Numerical evaluations of *N* -beam wave functions in electron scattering by the multi-slice method," *Acta Crystallogr. Sect. A*, vol. 30, no. 2, pp. 280–290, Mar. 1974.

[59]   E. Kirkland, R. Loane, J. S.- Ultramicroscopy, and undefined 1987, "Simulation of annular dark field STEM images using a modified multislice method," *Elsevier*.

[60]   E. Kirkland, "Advanced computing in electron microscopy," 2010.

[61]   M. Schowalter, A. Rosenauer, J. T. Titantah, and D. Lamoen, "Computation and parametrization of the temperature dependence of Debye–Waller factors for group IV, III–V and II–VI

semiconductors," *Acta Crystallogr. Sect. A*, vol. 65, no. 1, pp. 5–17, 2009.

[62] H. Han, "Quantitative Evaluation of the Interfaces in III / V Semiconductors with Scanning Transmission Electron Microscopy," 2017.

[63] A. Beyer, J. Belz, N. Knaub, K. Jandieri, and K. Volz, "Influence of spatial and temporal coherences on atomic resolution high angle annular dark field imaging," *Ultramicroscopy*, vol. 169, pp. 1–10, 2016.

[64] J. Verbeeck, A. Béché, and W. Van den Broek, "A holographic method to measure the source size broadening in STEM," *Ultramicroscopy*, vol. 120, pp. 35–40, 2012.

[65] C. Y. Lee, Z. H. Stachurski, and T. Richard Welberry, "The geometry, topology and structure of amorphous solids," *Acta Mater.*, vol. 58, no. 2, pp. 615–625, 2010.

[66] L. T. To, D. J. Daley, and Z. H. Stachurski, "On the definition of an ideal amorphous solid of uniform hard spheres," *Solid State Sci.*, vol. 8, no. 8, pp. 868–879, 2006.

[67] A. Ourmazd, D. W. Taylor, J. Cunningham, and C. W. Tu, "Chemical Mapping of Semiconductor Interfaces at Near-Atomic Resolution," *Phys. Rev. Lett.*, vol. 62, no. 8, pp. 933–936, Feb. 1989.

[68] S. C. Anderson, C. R. Birkeland, G. R. Anstis, and D. J. H. Cockayne, "An approach to quantitative compositional profiling at near-atomic resolution using high-angle annular dark field imaging," *Ultramicroscopy*, vol. 69, no. 2, pp. 83–103, Sep. 1997.

[69] P. M. Voyles, D. A. Muller, J. L. Grazul, P. H. Citrin, and H.-J. J. L. Gossmann, "Atomic-scale imaging of individual dopant atoms and clusters in highly n-type bulk Si," *Nature*, vol. 416, no. 6883, pp. 826–829, Apr. 2002.

[70] R. Erni, H. Heinrich, and G. Kostorz, "Quantitative characterisation of chemical inhomogeneities in Al-Ag using high-resolution Z-contrast STEM," *Ultramicroscopy*, vol. 94, no. 2, pp. 125–133, Feb. 2003.

[71] D. Klenov, S. S.- Ultramicroscopy, and undefined 2006, "Contributions to the contrast in experimental high-angle annular dark-field images," *Elsevier*.

[72] J. M. LeBeau and S. Stemmer, "Experimental quantification of annular dark-field images in scanning transmission electron microscopy," *Ultramicroscopy*, vol. 108, no. 12, pp. 1653–1658, 2008.

[73] J. M. Lebeau, S. D. Findlay, L. J. Allen, and S. Stemmer, "Standardless atom counting in scanning transmission electron microscopy," *Nano Lett.*, vol. 10, no. 11, pp. 4405–4408, Nov. 2010.

[74] T. Grieb, K. Müller, R. Fritz, M. Schowalter, N. Neugebohrn, N. Knaub, K. Volz, and A. Rosenauer, "Determination of the chemical composition of GaNAs using STEM HAADF imaging and STEM strain state analysis," *Ultramicroscopy*, vol. 117, pp. 15–23, 2012.

[75] T. Grieb, K. Müller, R. Fritz, V. Grillo, M. Schowalter, K. Volz, and A. Rosenauer, "Quantitative chemical evaluation of dilute GaNAs using ADF STEM: Avoiding surface strain induced artifacts,"

Ultramicroscopy, vol. 129, pp. 1–9, 2013.

[76]   H. Kauko, T. Grieb, R. Bjørge, M. Schowalter, A. M.- Micron, and undefined 2013, "Compositional characterization of GaAs/GaAsSb nanowires by quantitative HAADF-STEM," *Elsevier*.

[77]   C. E. Pastore, M. Gutiérrez, D. Araújo, and E. Rodríguez-Messmer, "Quantification of InxGa1-xP composition modulation by nanometric scale HAADF simulations," in *Applied Surface Science*, 2013, vol. 269, pp. 138–142.

[78]   T. Mehrtens, K. Müller, M. Schowalter, D. Hu, D. M. Schaadt, and A. Rosenauer, "Measurement of indium concentration profiles and segregation efficiencies from high-angle annular dark field-scanning transmission electron microscopy images," *Ultramicroscopy*, vol. 131, pp. 1–9, 2013.

[79]   T. Grieb, K. M??ller, E. Cadel, A. Beyer, M. Schowalter, E. Talbot, K. Volz, and A. Rosenauer, "Simultaneous quantification of indium and nitrogen concentration in InGaNAs using HAADF-STEM," *Microsc. Microanal.*, vol. 20, no. 6, pp. 1740–1752, 2014.

[80]   S. Van Aert, J. Verbeeck, R. Erni, S. Bals, M. L.- Ultramicroscopy, and undefined 2009, "Quantitative atomic resolution mapping using high-angle annular dark field scanning transmission electron microscopy," *Elsevier*.

[81]   G. T. Martinez, A. Rosenauer, A. De Backer, J. Verbeeck, and S. Van Aert, "Quantitative composition determination at the atomic level using model-based high-angle annular dark field scanning transmission electron microscopy," *Ultramicroscopy*, vol. 137, pp. 12–19, Feb. 2014.

[82]   S. Van Aert, K. J. Batenburg, M. D. Rossell, R. Erni, and G. Van Tendeloo, "Three-dimensional atomic imaging of crystalline nanoparticles," *Nature*, vol. 470, no. 7334, pp. 374–377, Feb. 2011.

[83]   S. Bals, M. Casavola, M. A. Van Huis, S. Van Aert, K. J. Batenburg, G. Van Tendeloo, and D. Vanmaekelbergh, "Three-dimensional atomic imaging of colloidal core-shell nanocrystals," *Nano Lett.*, vol. 11, no. 8, pp. 3420–3424, Aug. 2011.

[84]   M. Alania, I. Lobato, and S. Van Aert, "Frozen lattice and absorptive model for high angle annular dark field scanning transmission electron microscopy: A comparison study in terms of integrated intensity and atomic column position measurement," *Ultramicroscopy*, vol. 184, pp. 188–198, Jan. 2018.

[85]   K. MacArthur, T. Pennycook, E. Okunishi, A. D.- Ultramicroscopy, and undefined 2013, "Probe integrated scattering cross sections in the analysis of atomic resolution HAADF STEM images," *Elsevier*.

[86]   T. Grieb, K. Müller, R. Fritz, M. Schowalter, N. Neugebohrn, N. Knaub, K. Volz, and A. Rosenauer, "Determination of the chemical composition of GaNAs using STEM HAADF imaging and STEM strain state analysis," *Ultramicroscopy*, vol. 117, pp. 15–23, Jun. 2012.

[87]   D. A. Muller, B. Edwards, E. J. Kirkland, and J. Silcox, "Simulation of thermal diffuse scattering including a detailed phonon dispersion curve," *Ultramicroscopy*, vol. 86, no. 3–4, pp. 371–380,

Feb. 2001.

[88] D. Van Dyck, "Is the frozen phonon model adequate to describe inelastic phonon scattering?," *Ultramicroscopy*, vol. 109, no. 6, pp. 677–682, May 2009.

[89] J. Barthel, "Dr. Probe: A software for high-resolution STEM image simulation," *Ultramicroscopy*, vol. 193, pp. 1–11, Oct. 2018.

[90] V. Grillo, F. R.- Ultramicroscopy, and undefined 2013, "STEM_CELL: A software tool for electron microscopy. Part 2 analysis of crystalline materials," *Elsevier*.

[91] V. Grillo, E. R.- Ultramicroscopy, and undefined 2013, "STEM_CELL: A software tool for electron microscopy: Part I—simulations," *Elsevier*.

[92] J. Zuo, J. M.-M. and Microanalysis, and undefined 2004, "Web-based electron microscopy application software: Web-EMAPS," *cambridge.org*.

[93] A. Rosenauer and M. Schowalter, "STEMSIM—a New Software Tool for Simulation of STEM HAADF Z-Contrast Imaging," in *Microscopy of Semiconducting Materials 2007*, Dordrecht: Springer Netherlands, pp. 170–172.

[94] "MacTempasX." [Online]. Available: http://www.totalresolution.com/MacTempasX.htm. [Accessed: 31-Jan-2019].

[95] "HREM Research - Simulation." [Online]. Available: https://www.hremresearch.com/Eng/simulation.html. [Accessed: 31-Jan-2019].

[96] I. Lobato, D. V. D.- Ultramicroscopy, and undefined 2015, "MULTEM: A new multislice program to perform accurate and fast electron diffraction and imaging simulations using Graphics Processing Units with CUDA," *Elsevier*.

[97] E. J. Kirkland, R. F. Loane, and J. Silcox, "Simulation of annular dark field stem images using a modified multislice method," *Ultramicroscopy*, vol. 23, no. 1, pp. 77–96, Jan. 1987.

[98] J. O. Oelerich, L. Duschek, J. Belz, A. Beyer, S. D. Baranovskii, and K. Volz, "STEMsalabim: A high-performance computing cluster friendly code for scanning transmission electron microscopy image simulations of thin specimens," *Ultramicroscopy*, vol. 177, pp. 91–96, 2017.

[99] A. Beyer, L. Duschek, J. Belz, J. O. Oelerich, K. Jandieri, and K. Volz, "Influence of surface relaxation of strained layers on atomic resolution ADF imaging," *Ultramicroscopy*, vol. 181, 2017.

[100] A. Beyer, L. Duschek, Jü. Belz, J. O. Oelerich, K. Jandieri, and K. Volz, "Surface relaxation of strained Ga(P,As)/GaP heterostructures investigated by HAADF STEM," *J. Microsc.*, vol. 268, no. 3, pp. 239–247, 2017.

[101] W. Hagen, "Tetragonal distortion in heteroepitaxial layers: Ge on GaAs," *J. Cryst. Growth*, vol. 43, no. 6, pp. 739–744, Jul. 1978.

[102] G. H. Olsen and R. T. Smith, "Misorientation and tetragonal distortion in heteroepitaxial vapor-Grown III–V structures," *Phys. Status Solidi*, vol. 31, no. 2, pp. 739–747, Oct. 1975.

[103] L. De Caro, A. Giuffrida, … E. C.-… S. A. F. of, and undefined 1997, "Effects of the elastic stress relaxation on the HRTEM image contrast of strained heterostructures," *scripts.iucr.org*.

[104] I. Vurgaftman, J. R. Meyer, and L. R. Ram-Mohan, "Band parameters for III–V compound semiconductors and their alloys," *J. Appl. Phys.*, vol. 89, no. 11, pp. 5815–5875, Jun. 2001.

[105] O. Rubel, I. Németh, W. Stolz, and K. Volz, "Modeling the compositional dependence of electron diffraction in dilute GaAs- and GaP-based compound semiconductors," *Phys. Rev. B - Condens. Matter Mater. Phys.*, vol. 78, no. 7, pp. 1–8, 2008.

[106] A. Beyer, L. Duschek, J. Belz, J. O. Oelerich, K. Jandieri, and K. Volz, "Surface relaxation of strained Ga(P,As)/GaP heterostructures investigated by HAADF stem," *J. Microsc.*, 2017.

[107] H. E, K. E. MacArthur, T. J. Pennycook, E. Okunishi, A. J. D'Alfonso, N. R. Lugg, L. J. Allen, and P. D. Nellist, "Probe integrated scattering cross sections in the analysis of atomic resolution HAADF STEM images," *Ultramicroscopy*, vol. 133, pp. 109–119, Oct. 2013.

[108] L. Duschek, P. Kükelhan, A. Beyer, S. Firoozabadi, J. O. Oelerich, A. Ballabio, G. Isella, and K. Volz, "Composition determination of semiconductor alloys towards atomic accuracy by HAADF-STEM," *Submitt. to Ultramicroscopy*, Feb. 2018.

[109] L. Duschek, A. Beyer, J. O. J. O. Oelerich, and K. Volz, "Composition determination of multinary III / V semiconductors via numerical STEM HAADF multislice simulations .," *Ultramicroscopy*, vol. 185, pp. 1–22, 2018.

[110] C. Rosenblad, H. R. Deller, A. Dommann, T. Meyer, P. Schroeter, and H. von Känel, "Silicon epitaxy by low-energy plasma enhanced chemical vapor deposition," *J. Vac. Sci. Technol. A Vacuum, Surfaces, Film.*, vol. 16, no. 5, pp. 2785–2790, Oct. 1998.

[111] K. T. Jacob, S. Raj, and L. Rannesh, "Vegard's law: A fundamental relation or an approximation?," *Int. J. Mater. Res.*, vol. 98, no. 9, pp. 776–779, Sep. 2007.

[112] W. Li, M. Pessa, and J. Likonen, "Lattice parameter in GaNAs epilayers on GaAs: Deviation from Vegard's law," *Appl. Phys. Lett.*, vol. 78, no. 19, pp. 2864–2866, May 2001.

[113] H. E, K. E. MacArthur, T. J. Pennycook, E. Okunishi, A. J. D'Alfonso, N. R. Lugg, L. J. Allen, and P. D. Nellist, "Probe integrated scattering cross sections in the analysis of atomic resolution HAADF STEM images," *Ultramicroscopy*, vol. 133, pp. 109–119, Oct. 2013.

[114] A. Beyer, L. Duschek, J. Belz, J. O. Oelerich, K. Jandieri, and K. Volz, "Influence of surface relaxation of strained layers on atomic resolution ADF imaging," *Ultramicroscopy*, vol. 181, pp. 8–16, 2017.

[115] P. Kükelhan, A. Beyer, L. Duschek, C. Fuchs, S. Firoozabadi, J. O. Oelerich, W. Stolz, and K. Volz, "Segregation at interfaces in 'W'-type quantum well heterostructures explored by atomic resolution STEM," *Submitt. Publ.*

[116] L. Duschek, A. Beyer, J. O. Oelerich, and K. Volz, "Composition determination of multinary III/V semiconductors via STEM HAADF multislice simulations," *Ultramicroscopy*, vol. 185, pp. 15–20,

Feb. 2018.

[117] P. Kükelhan, A. Beyer, S. Firoozabadi, M. Sarkar, T. Hepp, and K. Volz, "Composition determination for quaternary III-V semiconductors by aberration-corrected STEM," *Submitt. Publ.*

[118] K. H. W. van den Bos, L. Janssens, A. De Backer, P. D. Nellist, and S. Van Aert, "The atomic lensing model: New opportunities for atom-by-atom metrology of heterogeneous nanomaterials," *Ultramicroscopy*, Dec. 2018.

[119] P. Kükelhan, A. Beyer, S. Firoozabadi, M. Sarkar, T. Hepp, and K. Volz, "Composition determination for quaternary III-V semiconductors by aberration-corrected STEM," *Manuscr. Prep.*

[120] M. Schaffer, B. Schaffer, and Q. Ramasse, "Sample preparation for atomic-resolution STEM at low voltages by FIB," *Ultramicroscopy*, vol. 114, pp. 62–71, Mar. 2012.

[121] K. Müller-Caspary, O. Oppermann, T. Grieb, F. F. Krause, A. Rosenauer, M. Schowalter, T. Mehrtens, A. Beyer, K. Volz, and P. Potapov, "Materials characterisation by angle-resolved scanning transmission electron microscopy," *Sci. Rep.*, vol. 6, no. April, p. 37146, 2016.

[122] F. F. Krause, D. Bredemeier, M. Schowalter, T. Mehrtens, T. Grieb, and A. Rosenauer, "Using molecular dynamics for multislice TEM simulation of thermal diffuse scattering in AlGaN," *Ultramicroscopy*, vol. 189, pp. 124–135, Jun. 2018.

[123] L. Jones, "Quantitative ADF STEM: acquisition, analysis and interpretation," *IOP Conf. Ser. Mater. Sci. Eng.*, vol. 109, no. 1, p. 012008, Feb. 2016.

[124] H. Yang, L. Jones, H. Ryll, M. Simson, H. Soltau, Y. Kondo, R. Sagawa, H. Banba, I. MacLaren, and P. D. Nellist, "4D STEM: High efficiency phase contrast imaging using a fast pixelated detector," *J. Phys. Conf. Ser.*, vol. 644, no. 1, p. 012032, Oct. 2015.

[125] T. J. Pennycook, A. R. Lupini, H. Yang, M. F. Murfitt, L. Jones, and P. D. Nellist, "Efficient phase contrast imaging in STEM using a pixelated detector. Part 1: Experimental demonstration at atomic resolution," *Ultramicroscopy*, vol. 151, pp. 160–167, Apr. 2015.

[126] J. M. LeBeau, S. D. Findlay, L. J. Allen, and S. Stemmer, "Position averaged convergent beam electron diffraction: Theory and applications," *Ultramicroscopy*, vol. 110, no. 2, pp. 118–125, Jan. 2010.

Diese Seite enthält persönliche Angaben und ist nicht Bestandteil der Online-Version